University of Alberta

Repair of cracked steel structures by FRP patching

©

by

Chi Chiu Lam

A thesis submitted to the Faculty of Graduate Studies and Research
in partial fulfillment of the requirements for the degree of

Doctor of Philosophy
in
Structural Engineering

Department of Civil and Environmental Engineering

Edmonton, Alberta
Fall 2008

Library and
Archives Canada

Published Heritage
Branch

395 Wellington Street
Ottawa ON K1A 0N4
Canada

Bibliothèque et
Archives Canada

Direction du
Patrimoine de l'édition

395, rue Wellington
Ottawa ON K1A 0N4
Canada

Your file Votre référence
ISBN: 978-0-494-46353-6
Our file Notre référence
ISBN: 978-0-494-46353-6

NOTICE:
The author has granted a non-exclusive license allowing Library and Archives Canada to reproduce, publish, archive, preserve, conserve, communicate to the public by telecommunication or on the Internet, loan, distribute and sell theses worldwide, for commercial or non-commercial purposes, in microform, paper, electronic and/or any other formats.

The author retains copyright ownership and moral rights in this thesis. Neither the thesis nor substantial extracts from it may be printed or otherwise reproduced without the author's permission.

AVIS:
L'auteur a accordé une licence non exclusive permettant à la Bibliothèque et Archives Canada de reproduire, publier, archiver, sauvegarder, conserver, transmettre au public par télécommunication ou par l'Internet, prêter, distribuer et vendre des thèses partout dans le monde, à des fins commerciales ou autres, sur support microforme, papier, électronique et/ou autres formats.

L'auteur conserve la propriété du droit d'auteur et des droits moraux qui protège cette thèse. Ni la thèse ni des extraits substantiels de celle-ci ne doivent être imprimés ou autrement reproduits sans son autorisation.

In compliance with the Canadian Privacy Act some supporting forms may have been removed from this thesis.

While these forms may be included in the document page count, their removal does not represent any loss of content from the thesis.

Conformément à la loi canadienne sur la protection de la vie privée, quelques formulaires secondaires ont été enlevés de cette thèse.

Bien que ces formulaires aient inclus dans la pagination, il n'y aura aucun contenu manquant.

Canada

Abstract

Composite fiber patching techniques are being considered as alternatives to traditional methods of strengthening and fatigue crack repair in structures due to the growing use of fiber reinforced polymer (FRP) composite materials to different engineering structures. In the past few decades, most of the research studies focused mainly on the application of FRP on the repair of aluminum or titanium alloys, which are the common materials used in aircraft engineering, and also in strengthening and repair of reinforced concrete structures. However, there are relatively fewer studies of the application of FRP patching on the repair of steel structures. Therefore, an investigation of the application of FRP patching on repairing steel structures was carried out. The investigation includes three main parts: (1) a study of the tensile load transfer behaviour of FRP/steel double lap joints, (2) a study of the fracture behaviour of cracked steel plates repaired by FRP patching and (3) a study of the fatigue behaviour of cracked steel plates repaired by FRP patching.

An experimental and a numerical study of the static tensile strength of carbon fiber reinforced polymer (CFRP)/steel double lap joints were carried out and the results showed that loading could be transferred successfully from the parent steel plate to the CFRP plate. Finite element models were developed for predicting the stress intensity factor (SIF) of cracked steel plates with CFRP patching and the model was calibrated by the experimental results of Kennedy and Cheng (1998). The finite element results showed that for cracked steel plate with single-side CFRP patching, the SIF was reduced significantly on the patched side and increased slightly on the unpatched side. In addition,

the SIFs varied non-linearly across the thickness of the crack tip and as a result, different crack grow rate was expected through the thickness of the crack tip. To account for the variation of the SIFs through the thickness of the crack tip, a new set of finite element models was developed for the cracked plate with single-side FRP patching. Based on the finite element results, a set of equations was proposed for predicting the fatigue life of welded steel plates with cracks in the welded region repaired by Boron FRP patching. The analytical results compared well with the fatigue test results of welded steel plates with edge crack and single-side FRP patching (Roach and Rackow 2005). In addition, finite element parametric study of the SIF and prediction of fatigue life of cracked steel plates with FRP patching with different adherent stiffness ratio and different forms of crack and patching were carried out. It is shown that a higher efficiency of FRP patching was observed for the plates with edge crack than that of the central crack plate. It is also found that the increase in fatigue life was more pronounced for cracked plates with double-side patching. Lastly, based on the finite element model of the cracked plates with FRP patching, cracked steel circular tube structures with FRP patching were studied and the corresponding extension of the fatigue life was investigated.

Acknowledgement

The author would like to thank for the support and advice provided by Dr. Roger, J. J. Cheng who is the principle supervisor of this project. The author would also like to thank Dr. Michael, C. H. Yam of the Hong Kong Polytechnic University for providing suggestion and review of this thesis. The author would like to acknowledge the funding support from the Intelligent Sensing for Innovative Structures (ISIS) Canada research network and the Natural Sciences and Engineering Research Council of Canada (NSERC). The technical information provided by Syncrude Canada through Dr. Khaled Obaia is greatly appreciated.

The technical support provided by Larry Burden and Richard Helfrich of the I. F. Morrison Structural Laboratory at the University of Alberta is acknowledged. The contribution of Sika Canada for supplying the composite materials used in the experimental studies is gratefully acknowledged.

The author would like to thank his family, especially his wife, Sandy, M. I. Chan for their support and encouragement.

TABLE OF CONTENT

Page

1 INTRODUCTION 1

1.1 BACKGROUND 1

1.2 OBJECTIVE AND SCOPE 2

1.3 METHODOLOGY 3

1.4 THESIS ORGANIZATION 4

1.5 REFERENCES 6

2 LITERATURE REVIEW 8

2.1 INTRODUCTION 8

2.2 FIBER REINFORCED POLYMER (FRP) 8

2.3 FRP PATCHING IN AIRCRAFT ENGINEERING STRUCTURES 9

2.4 FRP PATCHING USED IN THE REPAIR OF CIVIL ENGINEERING STRUCTURES 15

2.5 REFERENCES 29

3 ADHESIVE CFRP/STEEL BONDED LAP JOINTS 33

3.1 INTRODUCTION 33

3.2 BACKGROUND 34

3.3 EXPERIMENTAL PROGRAM 36

3.3.1 Material properties of test specimens 36

3.3.2 Test specimen, instrumentation and test setup 37

3.4 TEST RESULTS 38

3.4.1 Effect of joint lap length 38

3.4.2 Effect of adherend stiffness ratio 40

3.4.3 Effect of tapering 40

3.5 FINITE ELEMENT ANALYSIS OF CFRP/STEEL DOUBLE LAP JOINT 41

3.5.1 Material properties used in the finite element analysis and the finite element analysis procedure 42

3.5.2 Comparison of axial strain distribution of CFRP plates of test and finite element results 44

3.5.3 Shear stress and strain of adhesive layer *46*
3.6 PREDICTION OF MAXIMUM STRENGTH AND MINIMUM LAP LENGTH OF ADHESIVE DOUBLE LAP JOINTS 47
3.6.1 Prediction of maximum strength of adhesive double lap joints *47*
3.6.2 Prediction of minimum lap length of adhesive double lap joints *50*
3.7 SUMMARY AND CONCLUSIONS 52
3.8 REFERENCES 71
4 FINITE ELEMENT STUDY OF STRESS INTENSITY FACTOR OF CRACKED STEEL PLATES WITH SINGLE-SIDE CFRP PATCHING 73
4.1 INTRODUCTION 73
4.2 BACKGROUND OF KENNEDY'S TEST PROGRAM 75
4.3 BACKGROUND TO THE DEVELOPMENT OF THE FINITE ELEMENT MODEL FOR CRACKED PLATES WITH FRP PATCHING 77
4.4 DEVELOPMENT OF A FINITE ELEMENT MODEL FOR CRACKED STEEL PLATES WITH SINGLE-SIDE CFRP PATCHING 79
4.4.1 Three layers model *81*
4.4.2 The modified three layers model *86*
4.5 DISCUSSION OF THE STRAIN RESULTS AND CRACK OPENING DISPLACEMENT 87
4.6 DISCUSSION OF THE SIF BASED ON THE MODIFIED THREE LAYERS MODEL AND THE THREE LAYERS MODEL 88
4.7 EFFECT OF PATCHING PARAMETERS ON THE SIF OF A CRACKED STEEL PLATE WITH A SINGLE-SIDE CFRP PATCHING 90
4.8 SUMMARY AND CONCLUSIONS 92
4.9 REFERENCES 111
5 FATIGUE REPAIR OF WELDED STEEL PLATES WITH BONDED COMPOSITE SINGLE-SIDE PATCHING 113
5.1 INTRODUCTION 113
5.2 BACKGROUND OF TEST PROGRAM AND RESULTS OF ROACH AND RACKOW (2005) 114
5.2.1 Test specimens *114*

5.2.2 *Test procedures* *116*
5.2.3 *Test results* *116*
5.2.4 *Fatigue analysis of the tested specimens* *118*
5.3 FINITE ELEMENT ANALYSIS OF SIF OF A CRACKED PLATE WITH SINGLE-SIDE FRP PATCHING 122
5.3.1 *Finite element models* *123*
5.3.2 *Modeling of fatigue crack growth* *124*
5.3.3 *Finite element results* *127*
5.4 DISCUSSION OF THE FINITE ELEMENT RESULTS OF SIF 132
5.5 ANALYSIS OF FATIGUE LIFE OF WELDED STEEL PLATE WITH EDGE CRACK AND SINGLE-SIDE FRP PATCHING 136
5.5.1 *Evaluation of the effective stress intensity factor and the corresponding crack opening stress of welded plates without FRP patching* *137*
5.5.2 *Prediction of the fatigue life of a welded steel plate with the edge crack repaired by single-side FRP patching* *140*
5.6 SUMMARY AND CONCLUSIONS 143
5.7 REFERENCES 167

6 PARAMETRIC STUDY OF CRACKED STEEL PLATES WITH FRP PATCHING – FINITE ELEMENT ANALYSIS 169

6.1 INTRODUCTION 169
6.2 FINITE ELEMENT MODEL 170
6.2.1 *Geometry and material properties of steel plate, crack pattern and form of FRP patching* *171*
6.2.2 *Finite element model of cracked plate with different crack pattern and form of FRP patching* *172*
6.3 FINITE ELEMENT RESULTS 174
6.3.1 *Plates with an edge crack and single-side patching* *174*
6.3.2 *Plate with an edge crack and double-side patching* *176*
6.3.3 *Central crack model with single-side patching* *176*
6.3.4 *Plate with a central crack and double-side patching* *178*

6.4 DISCUSSION OF THE RESULTS OF PLATES WITH SINGLE-SIDE PATCHING AND DOUBLE-SIDE PATCHING 179
6.5 PREDICTION OF FATIGUE LIFE OF PLATES WITH CFRP PATCHING 181
6.6 SUMMARY AND CONCLUSIONS 185
6.7 REFERENCES 210

7 FINITE ELEMENT STUDY OF CRACKED CIRCULAR STEEL TUBE REPAIRED BY FRP PATCHING 211

7.1 INTRODUCTION 211
7.2 OBJECTIVES 212
7.3 DEVELOPMENT OF A FINITE ELEMENT MODEL FOR CRACKED CIRCULAR TUBE STRUCTURES 212
7.3.1 Dimension and finite element model of cracked steel tube 212
7.3.2 Material properties of the steel tube, the adhesive and the CFRP patching 214
7.4 FINITE ELEMENT RESULTS OF THE CRACKED CIRCULAR TUBE STRUCTURE WITH AND WITHOUT CFRP PATCHING 214
7.4.1 Finite element results of SIF of cracked circular tube structure with and without CFRP patching 216
7.4.2 Finite element results of crack opening displacement of cracked circular tube structures with and without CFRP patching 218
7.4.3 Comparison of the finite element results of SIF of a circular tube structure and plate member 219
7.5 REDUCTION OF SIF OF CRACKED STEEL CIRCULAR TUBE STRUCTURE WITH DIFFERENT TYPE OF CFRP PATCHING 220
7.6 FATIGUE LIFE ANALYSIS OF CRACKED STEEL TUBE STRUCTURE WITH CFRP PATCHING 221
7.7 SUMMARY AND CONCLUSIONS 224
7.8 REFERENCES 239

8 SUMMARY, CONCLUSIONS AND RECOMMENDATIONS 240

8.1 SUMMARY 240

8.2 CONCLUSIONS ... 242
8.3 RECOMMENDATIONS FOR FUTURE WORK ... 246
8.4 REFERENCES ... 247

LIST OF TABLE

Page

TABLE 2.1 PROPERTIES OF TYPICAL COMMERCIAL FRP SYSTEMS 20

TABLE 2.2 SUMMARY OF FATIGUE TEST DATA OF CRACKED ALUMINUM PLATE................. 21

TABLE 2.3 SUMMARY OF FATIGUE TEST RESULTS OF CRACKED ALUMINUM PLATE............ 23

TABLE 2.4 SUMMARY OF FATIGUE TEST RESULTS OF BASSETTI ET AL. (2000) AND COLOMBI ET AL. (2003) 25

TABLE 2.5 SUMMARY OF FATIGUE TEST RESULTS OF JONES AND CIVJAN (2003) 26

TABLE 2.6 SUMMARY OF FATIGUE TEST RESULTS OF TAVAKKOLIZADEH AND SAADATMANESH (2003) 27

TABLE 3.1 MATERIAL PROPERTIES AND TEST RESULTS OF KENNEDY AND CHENG (1998). 54

TABLE 3.2 MATERIAL PROPERTIES OF STEEL PLATE, CFRP COMPOSITE AND EPOXY 55

TABLE 3.3 DIMENSION OF TEST SPECIMENS.. 56

TABLE 3.4 TEST RESULTS 57

TABLE 3.5 FINITE ELEMENT RESULTS OF MAXIMUM SHEAR STRESS AND STRAIN OF ADHESIVE.. 58

TABLE 3.6 COMPARISON OF TEST MAXIMUM JOINT STRENGTH WITH ANALYTICAL RESULTS 59

TABLE 4.1 SUMMARY OF TEST SPECIMEN VARIABLES (KENNEDY AND CHENG 1998) 94

TABLE 4.2 MATERIAL PROPERTIES OF STEEL PLATE, ADHESIVE AND CFRP PLATE FOR FINITE ELEMENT MODELING (KENNEDY AND CHENG 1998) 95

TABLE 4.3 SIF RESULTS OF THE THREE LAYERS MODEL AND THE MODIFIED THREE LAYERS MODEL 96

TABLE 4.4 RATIO OF SIF VALUE OF THE MODIFIED THREE LAYERS MODEL TO THE PLAIN STEEL MODEL 97

TABLE 4.5 SIF RESULTS OF FE MODELS WITH TAPERED AND NON-TAPERED END OF CFRP PATHCING... 98

TABLE 5.1 MATERIAL PROPERTIES (ROACH AND RACKOW, 2005).................................. 145

TABLE 5.2 FATIGUE TEST RESULTS OF SPECIMENS (ROACH AND RACKOW 2005)............ 146

TABLE 6.1 MATERIAL PROPERTIES FOR THE FINITE ELEMENT ANALYSIS (SIKA 2003)..... 188

TABLE 6.2 DETAILS OF THE PARAMETRIC STUDY 189

TABLE 6.3 NUMBER OF CYCLES AND INCREASE IN FATIGUE LIFE 190

TABLE 7.1 MATERIAL PROPERTIES OF STEEL, ADHESIVE AND CFRP OF TUBE MODEL 227

LIST OF FIGURE

Page

Figure 2.1 Cross section of Fiber Reinforced Polymer (FRP) material 28

Figure 3.1 Illustration of cracked steel plate repaired by bonded reinforcement 60

Figure 3.2 Load versus stroke curves of CFRP sheet/steel double lap joint specimens tested by Kennedy and Cheng (1998) 60

Figure 3.3 CFRP/steel double lap joint 61

Figure 3.4 Load versus stroke curve of specimens with different lap length and ETR = 0.17 61

Figure 3.5 Load versus stroke curve of specimens with different lap length and ETR = 0.34 and 1.03 62

Figure 3.6 Strain profile of CFRP of specimen with different lap length and ETR = 0.17 and 1.03 62

Figure 3.7 Load versus stroke curve of specimens with different ETR values and L_L =100mm and 150mm 63

Figure 3.8 Strain profile of CFRP of specimen with lap length = 50 mm and 150 mm 63

Figure 3.9 CFRP/steel double lap joint tapered specimens 64

Figure 3.10 Load versus stroke curve of specimens with and without tapered lap and ETR = 0.34 64

Figure 3.11 Load versus stroke curve of specimens with and without tapered lap and ETR = 1.03 65

Figure 3.12 Typical finite element model 66

Figure 3.13 Assumed shear stress-strain curve of adhesive 66

Figure 3.14 Finite element and test results of axial strain of CFRP plate (ETR = 0.17 and 1.03) 67

Figure 3.15 Finite element and test results of axial strain of CFRP plate (ETR = 0.34 and 1.03 taper and non-taper specimens) 68

FIGURE 3.16 SHEAR STRESS/STRAIN OF ADHESIVE OF SPECIMENS WITH ETR = 0.17 AND 0.34 AND L_L = 50 AND 150 MM 69

FIGURE 3.17 SHEAR STRESS/STRAIN OF ADHESIVE OF SPECIMENS WITH ETR = 1.03 AND L_L = 50 AND 150 MM AND THE SHEAR STRESS OF SPECIMEN P-3-50-1/2 70

FIGURE 4.1 THREE MODES OF STRESS PATTERN THAT CAN BE APPLIED TO A CRACK 99

FIGURE 4.2 THE STRESS FIELD IN THE VICINITY OF A CRACK TIP 99

FIGURE 4.3 TEST SETUP AND A TYPICAL GAUGED SPECIMEN TESTED BY KENNEDY AND CHENG (1998) 100

FIGURE 4.4 CRACK TIP COORDINATES AND TYPICAL CONTOUR Γ 100

FIGURE 4.5 THREE LAYERS FINITE ELEMENT MODEL 101

FIGURE 4.6 ILLUSTRATION OF THE THREE LAYERS FINITE ELEMENT MODEL AND THE DISPLACEMENT RELATIONSHIP ALONG THE X-DIRECTION 102

FIGURE 4.7 LONGITUDINAL DISPLACEMENT AND ROTATION OF NEAREST NODE TO THE CRACK TIP OF THE THREE LAYERS MODEL 103

FIGURE 4.8 THE MODIFIED THREE LAYERS MODEL (3-D BRICK AND SHELL MODEL) 104

FIGURE 4.9 DISPLACEMENT RELATIONSHIP OF THE MODIFIED THREE LAYERS MODEL ALONG THE X-DIRECTION 104

FIGURE 4.10 COMPARISON OF STRAIN RESULTS OF THREE LAYER MODEL AND SPECIMEN R116 105

FIGURE 4.11 COMPARISON OF STRAIN RESULTS OF THE MODIFIED THREE LAYERS MODEL AND SPECIMEN R116 105

FIGURE 4.12 COMPARISON OF STRAIN RESULTS OF THE MODIFIED THREE LAYERS MODEL AND SPECIMEN R224 106

FIGURE 4.13 COMPARISON OF STRAIN RESULTS OF THE MODIFIED THREE LAYERS MODEL AND SPECIMEN R324 106

FIGURE 4.14 COMPARISON OF STRAIN RESULTS OF THE MODIFIED THREE LAYERS MODEL AND SPECIMEN M216 107

FIGURE 4.15 COMPARISON OF STRAIN RESULTS OF THE MODIFIED THREE LAYERS MODEL AND SPECIMEN M316 107

FIGURE 4.16 DEFORMED SHAPE AND CRACK DISPLACEMENTS OF THE TWO TYPE OF FINITE ELEMENT MODEL (R116FE) 108

FIGURE 4.17 COMPARISON OF THE SIF ACROSS THE PLATE THICKNESS OF THE MODIFIED THREE LAYERS MODEL AND THE THREE LAYERS MODEL 109
FIGURE 4.18 RESULTS OF SIF RATIO VERSUS DIFFERENT PARAMETERS 109
FIGURE 4.19 MAGNIFIED DISPLACEMENT AT THE CRACK POSITION OF MODELS WITH PATCH LENGTH EQUAL TO 30 MM AND 100 MM 110
FIGURE 4.20 SUMMARY OF SIF RATIO OF SPECIMENS WITH CFRP PATCHING 110
FIGURE 5.1 TEST SPECIMEN WITH FRP (ROACH AND RACKOW, 2005) 147
FIGURE 5.2 CRACK LENGTH VERSUS FATIGUE CYCLE OF SPECIMENS (ROACH AND RACKOW, 2005) 148
FIGURE 5.3 FAILURE OF TYPICAL SPECIMEN (ROACH AND RACKOW, 2005) 149
FIGURE 5.4 CRACK GROWTH RATE VERSUS APPLY STRESS INTENSITY FACTOR RANGE OF UR-1-S1 150
FIGURE 5.5 CRACK GROWTH RATE VERSUS APPLY STRESS INTENSITY FACTOR RANGE OF UR-1-S3 AND UR-2-S3 150
FIGURE 5.6 GENERAL RESIDUAL STRESS FIELD PATTERN DUE TO WELDING PROCESS 151
FIGURE 5.7 ILLUSTRATION OF CRACK CLOSURE PRODUCED IN A COMPACT TENSION SPECIMEN BY LONGITUDINAL RESIDUAL WELDING STRESSES 151
FIGURE 5.8 COMPARISON OF CRACK GROWTH RATE OF SPECIMENS WITH AND WITHOUT FRP PATCHING 152
FIGURE 5.9 TYPICAL FINITE ELEMENT MODEL OF CRACKED STEEL PLATE WITH FRP PATCHING 153
FIGURE 5.10 STRAIN GAUGE LOCATION OF TEST SPECIMEN OF ROACH AND RACKOW (2005) 154
FIGURE 5.11 COMPARISON OF STRAIN RESULTS OF TEST AND FINITE ELEMENT ANALYSIS 154
FIGURE 5.12 ILLUSTRATION OF THE LOCAL INCREMENTS ALONG THE CRACK FRONT 155
FIGURE 5.13 FINITE ELEMENT MODELS WITH FOUR DIFFERENT CRACK LENGTH 155
FIGURE 5.14 CRACK OPENING DISPLACEMENT (COD) OF PATCHED AND UNPATCHED SIDES 156
FIGURE 5.15 LONGITUDINAL NORMALIZED STRESS AT POSITION A OF CRACKED PLATE .. 157
FIGURE 5.16 LONGITUDINAL NORMALIZED STRESS AT POSITION B OF CRACKED PLATE .. 158

FIGURE 5.17 LONGITUDINAL STRESS CONTOUR OF CRACKED PLATE WITH AND WITHOUT FRP PATCHING (A = 25.4 MM) 159
FIGURE 5.18 NORMALIZED LONGITUDINAL STRESS OF THE OUTER SURFACE OF TOP LAYER OF FRP AT POSITION C AND D 160
FIGURE 5.19 FINITE ELEMNT RESULTS OF CRACK PROPAGATION OF PATCHED AND UNPATCHED SIDES 161
FIGURE 5.20 THROUGH THICKNESS NORMALIZED SIF VERSUS CRACK LENGTH 161
FIGURE 5.21 RATIO OF ΔK OF PATCHED AND UNPATCHED SIDE 162
FIGURE 5.22 RATIO OF ΔK OF REPAIRED AND NON-REPAIRED SPECIMENS 162
FIGURE 5.23 F(A/B) VALUE OF REPAIRED AND NON-REPAIRED SPECIMENS 163
FIGURE 5.24 AN INFINITELY WIDE PLATE WITH BONDED REINFORCEMENTS 163
FIGURE 5.25 COMPARISON OF FINITE ELEMENT RESULTS WITH THE PREDICTIONS GIVEN BY EQS. 5.17 TO 5.20 164
FIGURE 5.26 CRACK GROWTH RATE VERSUS EFFECTIVE STRESS INTENSITY FACTOR RANGE OF WELDED SPECIMENS 164
FIGURE 5.27 ILLUSTRATION OF THE EFFECTIVE STRESS AND OPENING STRESS 165
FIGURE 5.28 ILLUSTRATION OF OPENING STRESS FOR SPECIMEN WITH FRP PATCHING ... 165
FIGURE 5.29 COMPARISON OF THE FATIGUE LIFE OF TEST AND PREDICTED RESULTS ($\Delta\sigma$ = 269 MPA) 166
FIGURE 6.1 STEEL PLATE WITH EDGE CRACK, SINGLE-SIDE / DOUBLE-SIDE CFRP PATCHING 191
FIGURE 6.2 STEEL PLATE WITH CENTRAL CRACK, SINGLE-SIDE / DOUBLE-SIDE CFRP PATCHING 192
FIGURE 6.3 FINITE ELEMENT MODEL OF EDGE CRACKED PLATE WITH SINGLE-SIDE CFRP PATCHING 193
FIGURE 6.4 FINITE ELEMENT MODEL OF CENTRAL CRACKED PLATE WITH SINGLE-SIDE CFRP PATCHING 193
FIGURE 6.5 FINITE ELEMENT MODEL OF EDGE CRACKED PLATE WITH DOUBLE-SIDE CFRP PATCHING 194
FIGURE 6.6 FINITE ELEMENT MODEL OF CENTRAL CRACKED PLATE WITH DOUBLE-SIDE CFRP PATCHING 194

FIGURE 6.7 TYPICAL FINITE ELEMENT MESH FOR THE PARAMETRIC STUDY 195

FIGURE 6.8 THROUGH THICKNESS NORMALIZED SIF ($\Delta K/\Delta\sigma$) VERSUS CRACK LENGTH OF EDGE CRACKED FE MODEL WITH SINGLE-SIDE CFRP PATCHING AND ETR = 0.33 196

FIGURE 6.9 THROUGH THICKNESS NORMALIZED SIF ($\Delta K/\Delta\sigma$) VERSUS CRACK LENGTH OF EDGE CRACKED FE MODEL WITH SINGLE-SIDE CFRP PATCHING AND ETR = 0.20 196

FIGURE 6.10 THROUGH THICKNESS NORMALIZED SIF ($\Delta K/\Delta\sigma$) VERSUS CRACK LENGTH OF EDGE CRACKED FE MODEL WITH SINGLE-SIDE CFRP PATCHING AND ETR = 0.13 197

FIGURE 6.11 NORMALIZED SIF ($\Delta K/\Delta\sigma$) OF PATCHED SIDE VERSUS (A/B) OF EDGE CRACKED FE MODEL WITH SINGLE-SIDE CFRP PATCHING AND ETR = 0.13, 0.20 AND 0.33 198

FIGURE 6.12 NORMALIZED SIF ($\Delta K/\Delta\sigma$) OF UNPATCHED SIDE VERSUS (A/B) OF EDGE CRACKED FE MODEL WITH SINGLE-SIDE CFRP PATCHING AND ETR = 0.13, 0.20 AND 0.33 198

FIGURE 6.13 NORMALIZED SIF ($\Delta K/\Delta\sigma$) OF PATCHED SIDE VERSUS (A/B) OF EDGE CRACKED FE MODEL WITH DOUBLE-SIDE CFRP PATCHING AND ETR = 0.13, 0.20 AND 0.33 199

FIGURE 6.14 NORMALIZED SIF ($\Delta K/\Delta\sigma$) OF PLANE OF SYMMETRY VERSUS (A/B) OF EDGE CRACKED FE MODEL WITH DOUBLE-SIDE CFRP PATCHING AND ETR = 0.13, 0.20 AND 0.33 199

FIGURE 6.15 THROUGH THICKNESS NORMALIZED SIF ($\Delta K/\Delta\sigma$) VERSUS CRACK LENGTH OF CENTRAL CRACKED FE MODEL WITH SINGLE-SIDE CFRP PATCHING AND ETR = 0.33 200

FIGURE 6.16 THROUGH THICKNESS NORMALIZED SIF ($\Delta K/\Delta\sigma$) VERSUS CRACK LENGTH OF CENTRAL CRACKED FE MODEL WITH SINGLE-SIDE CFRP PATCHING AND ETR = 0.20 200

Figure 6.17 Through thickness normalized SIF (ΔK/Δσ) versus crack length of central cracked FE model with single-side CFRP patching and ETR = 0.13 201
Figure 6.18 Normalized SIF (ΔK/Δσ) of patched side versus (a/b) of central cracked FE model with single-side CFRP patching and ETR = 0.13, 0.20 and 0.33 202
Figure 6.19 Normalized SIF (ΔK/Δσ) of unpatched side versus (a/b) of central cracked FE model with single-side CFRP patching and ETR = 0.13, 0.20 and 0.33 202
Figure 6.20 Normalized SIF (ΔK/Δσ) of patched side versus (a/b) of central cracked FE model with double-side CFRP patching and ETR = 0.13, 0.20 and 0.33 203
Figure 6.21 Normalized SIF (ΔK/Δσ) of plane of symmetry versus (a/b) of central cracked FE model with double-side CFRP patching and ETR = 0.13, 0.20 and 0.33 203
Figure 6.22 Value of f(a/b) versus crack length to plate width ratio (a/b) of edge cracked model with single-side CFRP patching 204
Figure 6.23 Value of f(a/b) versus crack length to plate width ratio (a/b) of edge cracked model with double-side CFRP patching 204
Figure 6.24 Crack mouth displacement of plate with single-side patching 205
Figure 6.25 Crack mouth displacement of plate with double-side patching 206
Figure 6.26 Value of f(a/b) versus crack length to plate width ratio (a/b) of central cracked model with single-side CFRP patching 207
Figure 6.27 Value of f(a/b) versus crack length to plate width ratio (a/b) of central cracked model with double-side CFRP patching 207
Figure 6.28 Number of cycle versus crack length of edge cracked model with single-side patching 208
Figure 6.29 Number of cycle versus crack length of central cracked model with single-side patching 208
Figure 6.30 Number of cycle versus crack length of edge cracked model with double-side patching 209

FIGURE 6.31 NUMBER OF CYCLE VERSUS CRACK LENGTH OF CENTRAL CRACKED MODEL WITH DOUBLE-SIDE PATCHING 209
FIGURE 7.1 DRAGLINE AT SYNCRUDE MINING SITE (COURTESY SYNCRUDE CANADA LTD.) 228
FIGURE 7.2 CLUSTER IN DRAGLINE BOOM (COURTESY SYNCRUDE CANADA LTD.) 228
FIGURE 7.3 WALL-THICKNESS TRANSITION IN DRAGLINE BOOM CHORD (COURTESY SYNCRUDE CANADA LTD.) 229
FIGURE 7.4 SECTION DIMENSION, CRACK AND CFRP DETAIL OF TUBE MEMBER 229
FIGURE 7.5 TYPICAL FINITE ELEMENT MESH OF CRACKED STEEL CIRCULAR TUBE MEMBER WITH CFRP PATCHING 230
FIGURE 7.6 GEOMETRY OF A CIRCULAR TUBE WITH A CIRCUMFERENTIAL THROUGH-WALL CRACK 230
FIGURE 7.7 COMPARISON OF F.E. RESULTS OF NORMALIZED SIF OF CRACKED STEEL CIRCULAR TUBE WITHOUT CFRP PATCHING TO THE PREDICTION OF LACIRE ET AL. (1999) 231
FIGURE 7.8 COMPARISON OF F.E. RESULTS OF NORMALIZED SIF OF CRACKED STEEL CIRCULAR TUBE WITH AND WITHOUT CFRP PLATE PATCHING FOR VARIOUS CIRCUMFERENTIAL HALF CRACK LENGTH 231
FIGURE 7.9 THE NORMALIZED SIFS OF CRACKED STEEL CIRCULAR TUBE WITH AND WITHOUT CFRP PLATE PATCHING VERSUS HALF CRACK LENGTH 232
FIGURE 7.10 COMPARISON OF CRACK OPENING DISPLACEMENT OF CRACK STEEL CIRCULAR TUBE WITH AND WITHOUT CFRP PLATE PATCHING 233
FIGURE 7.11 LONGITUDINAL CRACK OPENING DISPLACEMENT OF MODELS WITH AND WITHOUT CFRP PLATE PATCHING (HALF CRACK LENGTH OF 25.4 MM AND 63.5 MM) 234
FIGURE 7.12 COMPARISON OF NORMALIZED SIF OF CRACKED STEEL CIRCULAR TUBE AND CRACKED PLATE WITH CFRP PATCHING 234
FIGURE 7.13 TYPICAL CFRP PLATE AND CFRP SHEET 235
FIGURE 7.14 COMPARISON OF F.E. RESULTS OF NORMALIZED SIF OF CRACKED STEEL CIRCULAR TUBE WITH AND WITHOUT CFRP PATCHING FOR CIRCUMFERENTIAL HALF CRACK LENGTH, A, OF 25.4 MM 236

FIGURE 7.15 COMPARISON OF F.E. RESULTS OF NORMALIZED SIF OF CRACKED STEEL CIRCULAR TUBE WITH AND WITHOUT CFRP SHEET PATCHING FOR VARIOUS CIRCUMFERENTIAL HALF CRACK LENGTH 236
FIGURE 7.16 THE NORMALIZED SIFS OF CRACKED STEEL CIRCULAR TUBE WITH AND WITHOUT CFRP PATCHING VERSUS HALF CRACK LENGTH 237
FIGURE 7.17 GEOMETRICAL FACTORS OF CRACKED STEEL CIRCULAR TUBE WITH AND WITHOUT CFRP PATCHING 237
FIGURE 7.18 COMPARISON OF THE NUMBER OF CYCLES OF CRACKED STEEL CIRCULAR TUBE WITH AND WITHOUT CFRP PATCHING FOR CIRCUMFERENCE HALF CRACK LENGTH GREW FROM 25.4 MM TO 63.5 MM 238

LIST OF NOTATION

a = crack length
a_i = initial crack length
a_f = final crack length
C = material constant in Paris equation
da/dN = crack growth rate
da_i = local crack growth increment at an arbitrary point i
E_{Al} = elastic modulus of aluminum
E_{cfrp} = elastic modulus of CFRP composite
E_{frp} = elastic modulus of FRP composite
E_i = elastic modulus of inner adherend
E_o = elastic modulus of outer adherend
E_p = elastic modulus of plate
E_s = elastic modulus of steel plate
ETR = adherend stiffness ratio ($2E_{frp}\, t_{frp} / E_s\, t_s$) for double-side patching
= adherend stiffness ratio ($E_{frp}\, t_{frp} / E_s\, t_s$) for single-side patching
F_t = geometrical factors for axial load
$F_{t,CFRP}$ = geometrical factors for axial load of tube with CFRP patching
F_b = geometrical factors for bending moment
$f(a/b)^p$ = correction factor for the geometry of patched side
$f(a/b)^u$ = correction factor for the geometry of unpatched side
G_e = elastic shear modulus
G_{ep} = equivalent elastic-plastic shear modulus
J = J-integral
K_I = stress intensive factor for mode I fracture
K_m = stress intensive factor of reference plane
K_r = stress intensive factor of cracked plate with double side patching
K_p = stress intensive factor of patched side
K_u = stress intensive factor of unpatched side
$K^*_{patched}$ = stress intensive factor of patched side defined by Wang et al.

$K^*_{unpatched}$ = stress intensive factor of unpatched side defined by Wang et al.
ΔK = stress intensity factor range
ΔK_{app} = applied stress intensity factor
$\Delta K_{CFRP,eff}$ = effective stress-intensity range of tube with CFRP patching
ΔK_{eff} = effective stress-intensity range
ΔK_i = local stress intensity factor increment at an arbitrary point i
L = patch length
L_L = lap length
$L_{Practice}$ = practical design lap joint length
M = applied bending moment
m = material constant in Paris equation
N = fatigue cycle
N_p = number of layer of CFRP plate
N_{S1} = number of fatigue cycle applied at low stress range
N_{S2} = equivalent number of cycles for specimen loaded with medium
n = number of layer of CFRP sheet
P = applied axial force
P_{Adhv} = fully yield load of adhesive
P_{ANA} = predicted load
P_{Test} = test results
P_y = static yield load of steel plate
ΔP = load range
R = stress ratio ($\sigma_{max} / \sigma_{min}$)
R_m = mean radius of pipe
R_{SIF} = ratio of stress intensive factor defined by Wang et al.
S_1 = value of low stress range ($\Delta\sigma = 152$ MPa)
S_2 = value of medium stress range ($\Delta\sigma = 214$ MPa)
SIF = stress intensity factor (MPa$\sqrt{m}$)
t = wall thickness of tube
t_{Al} = thickness of aluminum

t_a, η = thickness of adhesive

t_{cfrp} = thickness of CFRP composite

t_{frp} = thickness of FRP composite

t_i = thickness of inner adherend

t_o = Thickness of outer adherend

t_p = thickness of plate

t_s = thickness of steel plate

$\bar{u}_a$ = mid-plane displacements of adhesive along the x direction

$\bar{u}_{frp}$ = mid-plane displacements of FRP along the x direction

$\bar{u}_s$ = mid-plane displacements of steel plate along the x direction

u_{frp}^b = displacement of bottom face of the FRP along the x direction

u_m = longitudinal displacement of reference plane of steel plate

u_p = longitudinal displacement of the patched face of steel plate

u_u = longitudinal displacement of the unpatched face of steel plate

$u_s{}^T$ = displacement of patched side of the steel plate along the x direction

$\bar{v}_a$ = mid-plane displacements of adhesive along the y direction

$\bar{v}_{frp}$ = mid-plane displacements of FRP along the y direction

$\bar{v}_s$ = mid-plane displacements of steel plate along the y direction

v_{frp}^b = displacement of bottom face of the FRP along the y direction

$v_s{}^T$ = displacement of patched side of the steel plate along the y direction

$\bar{w}_a$ = mid-plane displacements of adhesive along the z direction

$\bar{w}_{frp}$ = mid-plane displacements of FRP along the z direction

$\bar{w}_s$ = mid-plane displacements of steel plate along the z direction

w = patch width

β = geometry factor

ε = axial strain

Γ = arbitrary contour surrounding the crack tip

Λ = characteristic crack length of plate with bonded reinforcement

γ = shear strain

γ_e = limit of elastic shear strain

θ = half of the circumferential angle of crack

ν = Poisson's ratio

σ = axial stress

σ_b = applied bending stress

σ_{max} = maximum applied stress

σ_{op} = crack opening stress of plate without patching

σ_{op}^{p} = crack opening stress of plate with patching

σ_t = applied tensile stress

σ_{xx} = axial stress field at crack tip along x direction

σ_{yy} = axial stress field at crack tip along y direction

$\Delta\sigma$ = apply stress range

τ = shear stress

τ_e = limit of elastic shear stress

τ_{max} = maximum design shear stress of adhesive

τ_{xy} = shear stress field at crack tip

γ_p = plastic strain limit of adhesive

$\varphi_a{}^x$ = rotations of the cross section of adhesive along the x axis

$\varphi_{frp}{}^x$ = rotations of the cross section of FRP along the x axis

$\varphi_s{}^x$ = rotations of [illegible] cross section of steel plate along the x axis

$\varphi_a{}^y$ = rotations of the cross section of adhesive along the y axis

$\varphi_{frp}{}^y$ = rotations of the cross section of FRP along the y axis

$\varphi_s{}^y$ = rotations of the cross section of steel plate along the y axis

φ_m = rotation of reference plane of steel plate

1 INTRODUCTION

1.1 Background

Fatigue and fracture behavior are important considerations in determining the condition of metal structures subjected to cyclic loads. The existing microscopic cracks in structural members can propagate into large cracks due to repeated loading and the presence of large cracks will reduce the load-carrying capacity of a structural member. When the crack length reaches the critical crack length, the crack will propagate unstably and subsequently cause total failure of the members. There are several methods concerning the repair of fatigue cracks in steel members, such as hole drilling method, hole drilling and bolt pre-tensioning, hole expansion, overloading, crack bridging etc (Grondin et al. 2004). For the mentioned first three methods, a hole is drilled at the end of crack to 'blunt' the crack. By introducing a hole, the net section will be reduced. Therefore, the stresses at the net section should be re-evaluated after the repair to ensure that the repair is not detrimental to the integrity of the structures.

Crack growth rate can be slow down by introducing overloading to the structure. However, overloading of a structure requires careful consideration of other aspects of behavior such as instability of the structure or member or unstable fracture. Crack bridging method is one of the methods for repairing cracked structures. It is done by welding or bolting cover plates over the location of crack. When carrying out a repair by crack bridging method, some issues should be considered. For example, the stiffness of the cover plates may introduce a stress concentration and the repair may aggravate the situation and cause new cracks. Repairs must be designed to cause gradual transfer of loads and stresses. Besides, it is noticed that current techniques for strengthening steel structures have several drawbacks including the use of heavy equipment for installation, poor fatigue performance of the member after repair, the introduction of heat affected zones around welds, and the need for ongoing maintenance due to continued corrosion attack and crack growth (Karbhari and Shulley 1995).

Composite fiber patching techniques are being considered as alternatives to traditional methods of strengthening and fatigue crack repair in structures due to the growing use of fiber reinforced polymer (FRP) composite materials to different engineering structure. The use of fiber reinforced composite materials has several advantages such as lighter weight, higher strength and higher corrosion resistance than traditional structural materials such as steel. The advantages of composite patching include: (1) elimination of fastener holes or weld stress risers that produce new crack initiation sites, (2) good fatigue resistance, (3) high strength-to-weight ratio, (4) good durability, (5) ability to tailor strength to meet anisotropy needs thus eliminating the undesirable stiffening of a structure in directions other than those required, (6) corrosion resistance, and (7) formability to complex contours (Konur and Matthews 1989).

1.2 Objective and scope

Research studies have shown that the application of FRP patching on cracked structures for extending the fatigue life of the structures is effective. However, most of the studies focused mainly on the application of FRP on the repair of aluminum or titanium alloys which are the common materials used in aircraft engineering (Baker 1987, Callinan et al.

1996, Klug et al. 1999, Schubbe and Mall 1999) and reinforced concrete structures (Meier 1992, Deniaud and Cheng 2000, Karbhari and Seible 2000, Teng et al. 2004). There are relatively few studies of the application of FRP patching on the repair of cracked steel structures (Roberts 1995, Kennedy and Cheng 1998, Bassetti et al. 2000). Therefore, an investigation of the application of FRP patching on improving the fatigue performance of steel members is required. The objective of this project is to investigate the fatigue behavior of cracked steel structures repaired by FRP patching. In order to achieve this objective, following studies were carried out.

(1) Experimental and numerical studies of the strength and bond behavior of FRP/steel double lap joint.

(2) To examine the fracture behavior of cracked steel plates repaired by FRP patching by using the finite element analysis in order to determine the change of stress intensity factor due to various parameters of patching.

(3) To analyze the fatigue life of cracked steel plates repaired by FRP patching by mean of finite element method.

(4) To develop the prediction equation for determining the fatigue life of cracked steel plates with different crack pattern and form of patching.

(5) To apply the developed equation for determining the fatigue life of a cracked steel circular tube repaired by FRP patching.

1.3 Methodology

Since the behavior of a patching is highly dependent on the transfer of loads between the patching and adherend, an understanding of the static tensile behavior of FRP/steel double lap joint is essential. Kennedy and Cheng (1998) studied the bond behavior of CFRP/steel double lap joint experimentally. However, the adherend stiffness ratios of their specimens were relatively low. Therefore, additional study of the bond behavior of CFRP/steel double lap joint was first carried out by both experimental and numerical methods with a higher and wider range of adherend stiffness ratio. For the study of the fatigue crack growth behavior, since it is known that fatigue crack growth rate is related to the change of the stress intensity factor. Study of the stress intensity factors for cracked plates with single-side FRP patching was carried out next by the finite element method. The finite element model developed herein was then calibrated by the static and the fatigue test results obtained from literature. The calibrated finite element model was used to perform a parametric study for investigating the effect of various parameters on the reduction of the stress intensity factor of cracked steel plates with FRP patching. Based on the finite element results, equations which account for the effect of FRP patching was developed for determining the increase in fatigue life cracked steel plate with FRP patching. Lastly, the fatigue life of a cracked steel tube structure repaired with FRP patching was analyzed.

1.4 Thesis Organization

A brief review of the application of FRP patching to extend the fatigue life of aircraft and civil engineering structures is presented in Chapter 2. Experimental and numerical studies of the tensile behavior of FRP/steel double lap joints are presented in Chapter 3. After understanding the static behavior of FRP/steel lap joint, fracture behavior, such as, the reduction of stress intensity factor (SIF) of cracked plate repaired by applying FRP patching is presented in Chapter 4. Finite element study of the stress intensity factor of cracked steel plates with FRP patching at different crack length stage is presented in Chapter 5. Analytical solutions based on the finite element results are compared with the fatigue test results of welded steel plate with FRP patching in the same chapter. With the calibrated finite element models, a parametric study to examine the reduction of stress intensity factors and fatigue crack growth rate is presented in Chapter 6. Based on the finite element model of the cracked plates with FRP patching, cracked steel circular tube structures with FRP patching are studied and the reduction of the stress intensity factor of the tube structure is investigated and presented in Chapter 7. Summary, conclusions and discussions of the mentioned work is presented in Chapter 8.

1.5 References

Baker, A. A., 1987, "Fiber composite repair of cracked metallic aircraft components – practical and basic aspects", Composites, September, pp. 293 – 308

Bassetti, A., Nussbaumer, A. and Colombi, P., 2000, "Repair of riveted bridge members damaged by fatigue using CFRP materials", Advanced FRP Materials for Civil Structures, Bologna, Italy, 19th October 2000, pp. 33 – 42

Callinan, R., Sanderson, S. and Keeley, D. 1996, "3D FE Analysis of a bonded repair to an F-111 wing", Proceeding of Australian Conference on Applied Mechanics (ACAM 96), Institute of Engineers, Melbourne, Australia, May

Deniaud, C. and Cheng, J. J. R., 2000, "Behaviour of reinforced concrete beams strengthened in shear", Structural Engineering Report No. 234, University of Alberta, Department of Civil & Environmental Engineering

Grondin, Picard, Beaulieu, Tremblay and Massicotte, 2004, "Brittle Fracture and Fatigue", Limit States Design of Steel Structures, Ch. 8

Karbhari, V. M., and Shulley, S. B., 1995, "Use of Composites for Rehabilitation of Steel Structures – Determination of Bond Durability", Journal of Materials in Civil Engineering, Vol. 7, No. 4, ASCE, pp. 239 – 245

Karbhari, V. M. and Seible, F., 2000, "Fiber reinforced composites – advanced materials for the renewal of civil infrastructure", Applied Composite Materials, Vol. 7

Kennedy, G. D. and Cheng, J. J. R., 1998, "Repair of cracked steel elements using composite fiber patching", Structural Engineering Report No. 221, University of Alberta, Department of Civil & Environmental Engineering

Klug, J., Maley, S. and Sun, C. T., 1999, "Characterization of fatigue behaviour of bonded composite repairs", Journal of Aircraft, Vol. 36, No. 6, pp. 1016 - 1022

Konur, O., and Matthews, F. L., 1989, "Effect of the Properties of the Constituents on the Fatigue Performance of Composites: A review", Composites, Vol. 20, No. 4, pp. 317 - 328

Meier, U., Deuring, M., Meier, H. and Schwegler, G., 1993, "CFRP bonded sheets, Fibre-Reinforce-Plastic (FRP) Reinforcement for Concrete Structures: Properties and Applications, edited by A. Nanni, Elsevier Science, Amsterdam, The Netherlands.

Roberts, P. D., 1995, "Crack growth retardation by carbon fiber composite patching : An application to steel pressure vessel repair", Master of Science Thesis, University of Alberta, Department of Mechanical Engineering

Schubbe, J. J. and Mall, S., 1999, "Investigation of a cracked thick aluminum panel repaired with a bonded composite patch", Engineering Fracture Mechanics, Vol. 63, pp. 305 – 323

Teng, J. G., Lam, L and Chen, J. F., 2004, "Shear strengthening of RC beams with FRP composites", Processing of Structural Engineering Materials, 6, pp. 173 – 184

2 LITERATURE REVIEW

2.1 Introduction

Due to several properties such as lighter weight, higher strength and higher corrosion resistance of composite materials, composite materials have been using in different type of engineering aspect such as in aircraft engineering, automobile engineering, infrastructures etc in the past decades. In this chapter, a brief introduction about the fiber reinforced polymer (FRP) is presented. Then, several researches about the application of bonded FRP patching for fatigue repair of aluminum structure which is considered as the main structural material in aircraft engineering and steel structures are summarized.

2.2 Fiber Reinforced polymer (FRP)

The use of fiber reinforced polymer (FRP) for new construction and strengthening of older structures has increased steadily nowadays. Fiber reinforced polymers offer numerous advantages over steel including excellent corrosion resistance, good fatigue resistance, low coefficient of thermal expansion, as well as being lightweight. An additional advantage of FRP is in the endless ways in which polymers and fibers can be combined in a material to suit the specific needs of a structure (Meier 1992).

A composite is defined as a material system consisting of two chemically dissimilar phases that are separated by a distinct interface. The two different materials are usually referred as matrix and reinforcing material (Figure 2.1). The reinforcing material can be in different form (such as particulate or fiber form) for a composite material. If the reinforcement element were given a fiber-like shape characterized by a high aspect ratio, then the resulting composite is termed a 'fiber' reinforced composite. There are three commonly used fibers for producing FRP for civil engineering applications: glass, aramid and carbon/graphite. These are strong ceramic materials with that depict both a stiff and a brittle behavior. The cost of glass fiber is relatively lower than the other two fibers. However, its poor durability in alkaline cementitious environments has caused concern. Aramid fiber is an aromatic organic compound made of carbon, hydrogen, oxygen and nitrogen. Its advantages are low density, high tensile strength, and high impact resistance. Its drawbacks include its low compressive properties and degradation in sunlight. Carbon fiber is produced from one of the three precursors: polyacylonitrile (PAN), rayon and mesophase/isotropic pitches. These fibers, or their allotropic form graphite, have the most desired properties from the civil engineering applications view point (Kaw 1997). Mechanical properties of some commonly used FRPs are shown in Table 2.1 (ISIS Canada 2001).

2.3 FRP patching in aircraft engineering structures

Bonding of FRP materials to metallic structures was first used in mechanical engineering applications. In the past few decades, in order to restore the structural integrity of aging aircraft due to the damage from fatigue cracking and corrosion, the use of composite materials in aircraft structural components has increased gradually. Finite element analysis of cracked plate repaired by patching was initiated by Jones and Callinan (1979). Their main purpose was to develop the theoretical tools by mean of using finite element method to study the behavior of cracked structures repaired by patching. Rose (1982) developed the analytical model to study the crack extension force affected by bonded repair. Rose studied a plate with a semi-infinite crack which was repaired by bonding reinforcing sheets to its faces and was subjected to uniformly distribute tensile load at right-angle to the crack. It was shown that the crack extension force has a finite value, provided that the reinforced structure could still carry the load.

Baker (1987) summarizes the theoretical and experimental work of Australian work on fiber composite repair of cracked metallic aircraft components. In the paper, experimental results of the fatigue strength of 3.18 mm thick (t_{Al}) aluminum plate (2024-T3, elastic modulus (E_{Al}) equal to 72 GPa) with edge crack was presented. In the fatigue test, two similar specimens were simultaneously tested while joined together to form a honeycomb panel, with the patched sides facing outwards. Therefore, out of plane bending of the plates was prevented. The dimension of the plate was 300 mm long x 160 mm wide. Seven layers of boron/epoxy composite material with thickness equal to 0.13 mm/ply (t_{frp}/ply) and elastic modulus (E_{frp}) equal to 200 GPa was bonded on one side of the crack plate. With this configuration, the stiffness ratio of the composite to the plate ($ETR = E_{frp}t_{frp}/E_{Al}t_{Al}$) was about 0.8. Two specimens with composite patching were prepared with two different initial crack lengths (a_i = 5 mm and 25 mm respectively). The plates were loaded by tensile loading with a far end stress equal to 138 MPa. The test results showed that, (1) the fatigue life of the patching specimens was increased by more than 20 times when compared with the non-patched specimen; (2) significant retardation in crack growth is experienced with the longer (25 mm) starting crack, the crack did not propagated until about 180,000 cycles; and, (3) crack growth under the patch often follows a parabolic relationship.

Fatigue test involving thick metallic plates was performed by Jones and Chiu (1999). The specimens were aluminum alloy (2024-T4) with dimensions of 108.3 mm (width), 304 mm (length) and 11.1 mm (thickness) and the plate contained a centrally located surface crack. The surface length of the crack was 37 mm and was 6 mm deep. Five unrepaired specimens were tested under a constant amplitude stress of 65 MPa with stress ratio ($R = \sigma_{max} / \sigma_{min}$) equal to 0.01 and six specimens were repaired with a 10-ply thick boron fiber patch (t_{frp} = 1.27 mm) which was bonded on the crack using the 0.1 mm thick structural film adhesive FM73. The test results showed that the unpatched specimens lasted an average of 22,450 cycles and the patched specimens lasted an average of 527,000 cycles. The increase in fatigue life is about 23 times. Another group of test specimens (four unpatched and four patched specimens) were tested under the FALSTAFF (Fighter Aircraft Loading STAndard For Fatigue) loading with a peak stress of 138.9 MPa. Test results showed that the unpatched specimens lasted for an average of 354,117 cycles and the patched specimens lasted for an average of 2,052,557 cycles, an increase in fatigue life of about 5.8 times. This was significantly lower than the value obtained using constant amplitude loading. It was explained that the different result was due to the following effects: (1) Fatigue damage in the adhesive due to the higher loads; (2) growth of disbond/delamination directly over the crack; and, (3) load history effects due to the visco-plastic nature of the adhesive. Repair of aluminum lugs were also presented in the paper. Aluminum lugs (7075-T651) of 8 mm thick, 145 mm long and 50 mm wide containing a 20 mm diameter hole were tested. Those specimens had a 1 mm notch machined on one side of the hole. A fatigue crack was initiated from this notch and grown an average length of 1 mm to give a total crack length of 2 mm. Two specimens were tested without FRP patching and four specimens were tested with boron/epoxy composite patching. The patched specimens were further divided into groups, two specimens were repaired by bonding 0.8 mm thick (6 ply) boron/epoxy on each sides of the plate and the other two specimens were repaired with a combination of composite and a 1 mm thick steel-sleeve insert. The structure was loaded from 1 to 14.4 kN (stress range, $\Delta\sigma$ = 36 MPa) using a sinusoidal wave-form at a frequency of 5 Hz. The average fatigue life of the unpatched specimens, specimens with patched boron/epoxy only and specimens with patched boron/epoxy and steel-sleeve were 12,200 cycles, 149,000 cycles and 194,500 cycles respectively. The increases in fatigue life were about 12 times and 16 times, respectively.

Fatigue crack growth behavior of 6.35 mm thick aluminum panels (2024-T3) repaired with the asymmetrically bonded full width boron/epoxy composite patch was investigated experimentally by Schubbe and Mall (1999). The tested materials were aluminum sheet (2024-T3) of 3.175 mm thick and aluminum plate (2024-T351) of 6.35 mm thick and the length and width of the specimens were 508 mm and 153 mm, respectively. A 25.4 mm initial central crack was introduced to all the specimens before repair. Some of the specimens were repaired by bonding a unidirectional boron/epoxy composite along the loading direction. Different numbers of ply of composites were bonded to the plate to achieve the adherend stiffness ratios (ETR) of 1 and 1.3. Besides the two adherend stiffness ratios, three different patch lengths (51 mm, 68 mm and 102 mm) were chosen to investigate the effects of patch length. Fatigue testing of all repaired specimens was conducted at constant maximum stress equal to 120 MPa with stress ratio of 0.1 at 10 Hz.

Compared to the non-repaired specimens, test results showed that the average increase in fatigue life of the 6.35 mm thick and 3.175 mm thick specimens with ETR = 1 was about 4.2 times and 7.1 times, respectively. For those 6.35 mm thick and 3.175 mm thick specimens with ETR = 1.3, the average increase in fatigue life was about 5.3 times and 7.1 times. It was shown that by increasing the adherend stiffness ratio (ETR) from 1 to 1.3, the fatigue life of the 6.35 mm thick repaired specimens was increased by 26%, whilst for those 3.175 mm thick repaired specimens, the fatigue life did not increase with the increased adherend stiffness ratio. The effect of patch length to the fatigue life was found either no beneficial or even detrimental on the fatigue life for the thin specimens.

An examination of cracked aluminum plates repaired by single-side and double-side patching is presented by Klug et al. (1999). Aluminum plates (2024-T3) (dimension = 177.8 mm long, 88.9 mm wide and 3.1 mm thick) with initial edge crack (crack length = 12.7 mm) were repaired by bonding graphite/epoxy (AS4/3501-6) on either single-side or double- sides using FM73 adhesive (thickness = 0.1 mm). Two thicknesses of composite repairs were chosen for comparison of both the single and double sided repaired. Both four-ply (0.508 mm) and eight-ply (1.016 mm) repairs were used. The elastic modulus of the aluminum plate and the FRP are 72 GPa and 138 GPa (along the loading direction), respectively. Therefore, the corresponding adherend stiffnesses ratios (ETR) were 0.3 and 0.6, respectively, for single-side patching and 0.6 and 1.2 for double-side patching. The applied stress range for single-sided repaired specimens and double-sided repaired specimens were 68.5 MPa and 137.5 MPa respectively with R = 0. Test results showed that the fatigue life for the non-repaired specimen was 30,000 cycles. With the single-side patched repair (four-ply and eight-ply), the fatigue life was about 120,000 cycles and 140,000 cycles, respectively. For those specimens with double-sides patched repair (four-ply and eight-ply), the corresponding fatigue life was about 140,000 cycles and 330,000 cycles, respectively.

A case study involving repair to primary aircraft structures is presented by Chester et al. (1999). In order to repair a 48 mm long crack in the lower wing skin of an RAAF F-111 aircraft structure, two different sets of fatigue tests were carried out. The first set of specimens consisted of two box specimens (approximately 900 mm x 430 mm x 65 mm) which were constructed to simulate the wing structure as quasi-full scale test articles. The second set of specimens consisted of twenty panel specimens (approximately 300 mm x 190 mm), simulating the local geometry of the wing skin, which were designed as structural detail specimens. The repair technique applied to the aircraft structures consisted of a 14 ply boron/epoxy patch adhesively bonded to the wing skin with FM73 adhesive. The lay-up of the patch was $(0_2, \pm 45, 0_3)_s$, with the 0° fiber oriented along the wing axis and the 45° fiber presented for the local shear stresses and to resist the torsional loads. The wing skin thickness in the location of the crack initiation point was nominally 4 mm thick with the adjacent integral stiffener being 8 mm thick. Fatigue spectrum loading derived from multi-channel recorders fitted to an RAAF F-111 aircraft which was scaled from the results of the detailed finite element analysis (Callinan et al. 1996) was applied for testing the specimens. Test results showed that the unrepaired specimen suffered rapid crack growth and failed after 15.8 flight hours. However, the two repaired box specimens survived for more than 200 hours.

Aglan et al. (2001) summarize some of the research that deals with the development of composite repairs bonded to defective aircraft structures. In addition, fatigue crack growth behavior of a pre-cracked aluminum plate (7075-T6) repaired by bonding boron/epoxy using 3M adhesive (AF163-2K) was investigated experimentally and analytically. The dimension of the aluminum plate was 305 mm long, 51 mm wide and 1.6 mm thick. The elastic modulus of the aluminum plate and the FRP material were 72 GPa and 190 GPa, respectively. The specimens were repaired by bonding 2, 4 or 6 plies of FRP on only one side of the specimens. This resulted in an adherend stiffness ratio (ETR) of 0.429, 0.858 and 1.286 for the 2, 4 and 6 plies repaired specimens respectively. An initial crack (8 mm length) was introduced to the edge of the plates. All the specimens were loaded by 109 MPa uniformly distributed stress with a frequency of 3 Hz and at a stress ratio equal to 0.1. Test result showed that the fatigue life of the non-repaired specimen, specimens with 2, 4 and 6 plies bonded FRP were 4,245 cycles, 42,500 cycles, 63,200 cycles and 102,280 cycles, respectively. The increases in fatigue life were about 10, 15 and 24 times for the specimen with 2, 4 and 6 plies of boron/epoxy patching.

A summary of the above mentioned literature is shown in Table 2.2 and Table 2.3. The investigations listed involve the testing of aluminum plates which is the main material used in aircraft engineering.

2.4 FRP patching used in the repair of civil engineering structures

Application of FRP composites to strengthen reinforced concrete (RC) structures has become very popular during the last few years. Major application of FRP on strengthening RC structures include: (1) flexural strengthening of RC beams and slabs; (2) shear strengthening of RC beams; (3) strengthening of axially and eccentrically loaded RC columns; and, (4) seismic retrofit of RC columns. A state of the art summary of the application of FRP strengthening of RC structures can be found in several references (Meier et al. 1993, ACI 440R-96 1996, Karbhari and Seible 2000, Deniaud and Cheng 2000 and Teng et al. 2004). The application of FRP composites in strengthening and repair of steel structures is not as widespread as the strengthening of RC structures. One of the reasons is that the high strength and stiffness of steel make it more difficult material to strengthen. In addition, the FRP/adhesive bond is generally the weakest link and is likely to control the mode of failure.

Roberts (1995) carried out experimental work to examine the behavior of crack growth retardation in steel plates reinforced with carbon fiber composite patching. Fatigue tests of ASTM A-516 Gr 70 pressure steel vessel were carried out. The thickness of the steel specimens (t_s) was 15.9 mm and the width and length of the specimens were 120 mm and 144 mm, respectively. An initial machine notch (length = 52 mm) was introduced to the specimens. Fatigue loading was applied to introduce a pre-crack (length = 8 mm). Therefore, the initial crack length was about 60 mm. Then, the unpatched specimen was loaded with a cyclic tensile loading range (ΔP = 4.76 kN) and a stress ratio equal to 0.05. The test was terminated when the final crack length reached about 98 mm and the corresponding fatigue cycle number (N) was 5,345,000. Another specimen was repaired by carbon fiber reinforced polymer (CFRP) patching on both sides. The length of the CFRP plate was 140 mm and the width was 60 mm with the edge of the plate located at the tip of the machine notch (the CFRP plate covered the pre-crack only). Initially, the same fatigue loading which was used for loading the unpatched specimen was applied to the patched specimen. However, the crack did not propagate during this applied loading range. The cyclic loading range was increased to $\Delta P = 5.22$ kN under the same stress ratio of 0.05. Under this cyclic loading range, the fatigue life of the patched specimen was about 28,500,000. The increase in fatigue life was about 5 times. This testing showed that the patch slowed down the growth rate of the propagating crack and in some cases, arrested the crack altogether.

The repair of cracked steel elements using carbon fiber reinforced polymer (CFRP) material patching were examined by Kennedy and Cheng (1998). Steel plates (dimension = 750 mm x 400 mm x 6.5 mm) with a central crack (80 mm) were tested under uni-axial tensile loading (far end stress = 100 MPa). At the crack location, some of the specimens were reinforced with CFRP (4 or 6 layers) on one side. Other test parameters included the patch length, patch width, type of tapered end and patch pattern. In their study, the strain distribution in a cracked steel plate with and without CFRP patching was examined. It was shown that the strain at the cracked tip could be reduced by applying CFRP patching. Higher stiffness patches reduced the crack tip stresses while lower stiffness patches reduced the stress concentrations in the steel at the patch edge. Based on these experimental and numerical studies, minimum bond length for load transfer and for load redistribution were proposed.

The fatigue behavior of a riveted steel bridge repaired by bonding CFRP plates was studied by Bassetti et al. (2000) and Colombi et al. (2003). Fatigue tests on central notch steel specimens with a 30 mm initial crack length were carried out. The dimension of the steel plate specimens was 1000 mm x 300 mm x 10 mm. The notched steel plates were reinforced on both sides with CFRP plates (500 mm x 50 mm x 1.2 mm (or 1.4 mm)). Pre-stressing of the CFRP plate was introduced in some of the specimens. The CFRP plates were placed 10 mm from the crack tip symmetrically on both sides. The applied stress range ($\Delta\sigma$) was 80 MPa with R = 0.4. Compared to the fatigue life of unpatched specimen, test results showed that the increase in fatigue life for the patched specimens varied from 3.5 to 20 times. A summary of the test results is given in Table 2.4. In addition, fatigue tests on a cross-girder of the riveted steel bridge reinforced by CFRP plates were also performed in order to show the applicability of the technique to bridge reinforcement. It was shown that the application of pre-stress of CFRP plates prior to bonding introduces a compressive stress which prevents further cracking by promoting a crack closure effect.

Jones and Civjan (2003) carried out experimental and finite element studies to examine the fatigue behavior of cracked steel plates repaired with CFRP patching. Two different configurations of cracks were tested: the center crack and symmetric edge notched crack. The initial crack length for the center crack specimens ($2a_i$) and symmetric edge notched crack specimens (a_i) were 11.4 mm and 5.7 mm respectively. Different types of CFRP materials (CFRP plate and CFRP sheet) were used in the studies. It was shown that the maximum increase in fatigue life was less than 2 times. However, in most of the examined cases, the increase in fatigue life was less than 50%. It was reported that the epoxy performance was critical to the overall behavior and all specimen failures were initiated by CFRP debonding. A summary of test specimens and the test results is given in Table 2.5.

Fatigue tests of steel beam specimens repaired by CFRP patching were carried out by Tavakkolizadeh and Saadatmanesh (2003). Steel beams (S127 x 4.5) with an edge notch in the tensile flange were tested under cyclic loading at various stress levels. The length of the steel beams was 1.22 m and were tested under a two point loading (loads were 200 mm apart symmetrically located with respected to mid-span). CFRP patching was applied on the tensile flange of the steel beam. The width and length of the CFRP plate were 76 mm and 300 mm, respectively, and the thickness was 1.27 mm. The modulus of elasticity was 144 GPa. The fatigue life of the steel beams without CFRP patching was evaluated at various values of stress range (207, 241, 276, 310 and 345 MPa). For the steel beams with CFRP patching, one more stress range (379 MPa) was included in the study. The fatigue life of the non-repaired and repaired beams loaded at different stress range values is shown in Table 2.6. It was observed that the fatigue life of specimens with CFRP patching was increased by 2.5 to 3.4 times. This improvement was equivalent to upgrading the detail from the AASHTO category D to category C (AASHTO 2000).

Table 2.1 Properties of typical commercial FRP systems

FRP system	Areal Weight	Density	Thickness	Tensile Strength	Modulus in Tension	Elongation at Failure
	(g/m^2)	(g/cm^3)	(mm)	(MPa)	(GPa)	(%)
Replark (Mitsubishi)						
Type 30	300	1.8	0.167	3400	230	1.5
Type HM	200	2.1	0.143	1900	640	0.3
Mbrace (Master Builders)						
CF130	300	1.82	0.165	3480	227	1.5
Tyfo Fibrwrap (Composite Retrofit International)						
SHE51	930	0.72	1.3	552	27.6	2.0
Sika						
SikaWrap Hex 103C	618	1.8	1.0	960	73.1	1.3
CarboDur S	2240	1.6	1.2-1.4	2800	165	1.7

Table 2.2 Summary of fatigue test data of cracked aluminum plate

	Material			Specimens		
Ref.	**Cracked plate**	**Patch**	**Adhesive**	**Dimension (mm)**	**Repaired type**	**Stiffness ratio (ETR)**
Baker (1987)	2024-T3 Al $E_{Al} = 72$ GPa $t_{Al} = 3.18$ mm	Boron/epoxy $E_{frp} = 200$ GPa $t_{frp} = 0.91$ mm (7-ply, 0.13 mm/ply)	AF126 $G_a = 540$ MPa $t_a = 0.19$ mm	Plate: 300 x 160 Patch: R = 75 mm (semi-circle)	Single side Crack type: edge crack, $a_i = 5$ and 25 mm	0.8
Jones and Chiu (1999)	2024-T4 Al $E_{Al} = 72$ GPa $t_{Al} = 11.1$ mm	Boron/epoxy $E_{frp} = 208$ Gpa $t_{frp} = 1.23$ mm (10-ply, 0.123 mm/ply)	FM73 $G_a = 700$ MPa $t_a = 0.1$ mm	Plate: 510 x 108 Patch: 350 x 108	Single side Crack type: surface crack $a_i = 38$ mm long, 6 mm deep	0.32
Schubbe and Mall (1999)	2024-T3 Al $E_{Al} = 72$ GPa $t_{Al} = 3.175$ mm 2024-T351 Al $E_{Al} = 72$ GPa	Boron/epoxy $E_{frp} = 200$ GPa $t_{frp} = 9$ to 22 plies	FM73 $G_a = 700$ MPa $t_a = 0.1$ mm	Plate: 508 x 153 Patch: 138 x 153	Single side Crack type: Central crack $a_i = 25.4$ mm	1.0 1.3

Table 2.2 (cont'd) Summary of fatigue data of cracked aluminum plate

	Material			Specimens		
Ref.	**Cracked plate**	**Patch**	**Adhesive**	**Dimension (mm)**	**Repaired type**	**Stiffness ratio (ETR)**
Klug et al. (1999)	2024-T3 Al $E_{Al} = 72$ GPa $t_{Al} = 3.1$ mm	Graphite/epoxy $E_{frp} = 138$ GPa $t_{frp} = 0.508$ mm (4-ply) $t_{frp} = 1.016$ mm (8-ply)	FM73 $G_a = 700$ MPa $t_a = 0.1$ mm	Plate: 177.8 x 88.9 Patch: 50.8 x 76.2	Single side and double side Crack type: edge crack, $a_i = 12.7$ mm	Single side 0.3 (4-ply) 0.6 (8-ply) Double sides 0.6 (4-ply) 1.2 (8-ply)
Aglan et al. (2001)	7075-T6 Al $E_{Al} = 72$ GPa $t_{Al} = 1.6$ mm	Boron/epoxy $E_{frp} = 190$ GPa $t_{frp} = 0.26$ mm (2-ply) $t_{frp} = 0.52$ mm (4-ply) $t_{frp} = 0.78$ mm (6-ply) (0.13 mm/ply)	3M AF163-2K $G_a = 440$ MPa	Plate: 305 x 51 Patch: 117 x 51	Single side Crack type: edge crack $a_i = 6.4$ mm	0.429 (2-ply) 0.858 (4-ply) 1.286 (6-ply)

Table 2.3 Summary of fatigue test results of cracked aluminum plate

Ref.	**Stiffness ratio**	**Loading**	**Fatigue life (cycles)**		**Increase in fatigue life (times)**
			Unpatched	**Patched**	
Baker (1987)	0.8	$\sigma = 138$ MPa $R = 0.1$	12,000	258,000 ($a_i = 5$ mm)	21.5
				270,000 ($a_i = 25$ mm)	22.5
Jones and Chiu (1999)	0.32	$\sigma = 65$ MPa $R = 0.01$	22,450	527,000	23
		FALSTAFF Loading $\sigma_{max} = 138.9$ MPa	354,117	2,052,557	5.8
Schubbe and Mall (1999)	1.0	$\sigma = 120$ MPa $R = 0.1$	Not specified	99,412 ($t_{Al} = 3.175$ mm)	7.1
				36,235 ($t_{Al} = 6.35$ mm)	4.2
	1.3			99,721 ($t_{Al} = 3.175$ mm)	7.1
				46,375 ($t_{Al} = 6.35$ mm)	5.3

Table 2.3 (cont'd) Summary of fatigue test results of cracked aluminum plate .

Ref.	**Stiffness ratio**	**Loading**	**Fatigue life (cycles)**		**Increase in fatigue life (times)**
			Unpatched	**Patched**	
Klug et al.	Single side	Single side	30,000	Single side	
(1999)	0.3 (4-ply)	σ = 68.5 MPa		120,000 (4-py)	4
	0.6 (8-ply)			140,000 (8-ply)	4.7
	Double sides	Double sides		Double sides	
	0.6 (4-ply)	σ = 137.5 MPa		140,000 (4-ply)	4.7
	1.2 (8-ply)	R = 0		330,000 (8-ply)	11
Aglan et al.	0.429	σ = 109 MPa	4,245	42,500	10
(2001)	0.858	R = 0.1		63,200	14.9
	1.286			102,280	24

Table 2.4 Summary of fatigue test results of Bassetti et al. (2000) and Colombi et al. (2003)

	Material			**Specimens**		**Loading range**
	Crack plate	**Patch**	**Adhesive**	**Dimension (mm)**	**Repaired type**	
	Steel plate E_s = 210 GPa t_s = 10 mm	CFRP plate: Sika Carbodur S512 (E_{cfrp} = 155 GPa) M614 (E_{cfrp} = 210 GPa)	Sikadur 30 G_a = 270 MPa t_a = 0.3 mm	Plate: 1000 x 300 Patch: 500 x 50	Double sides Crack type: Central crack a_i = 30 mm	Δσ = 80 MPa R = 0.4
Specimens	**E_{cfrp} (GPa)**	**Pre-stress on CFRP plate (MPa)**	**t_{cfrp} (mm)**	**Stiffness ratio (ETR)**	**Number of cycles to failure**	**Increase in fatigue life (times)**
A	-------	--------	--------	-------	300,000	Control
C	155	0	1.2	0.18	1,062,000	3.5
D	155	632	1.2	0.18	1,609,000	5.4
E	155	632	1.4	0.20	2,681,000	8.9
G	210	632	1.4	0.28	6,015,000	20

Table 2.5 Summary of fatigue test results of Jones and Civjan (2003)

Specimens	Geometry	Type of CFRP	E_{cfrp} and t_{cfrp} (GPa, mm)	No. of CFRP		CFRP length (mm)	Loading range	Average fatigue life (cycles)	Increase in fatigue life (times)
				Front	Back				
H11, H12	Hole	None	-----	0	0	-----	$\Delta\sigma = 113$ R = 0.01	346,922	-----
H21, H22		Sika Wrap	65, 1	2	2	255		533,772	1.54
H31, H32		Sika Wrap	65, 1	2	2	255		432,127	1.25
H41, H42		Sika CarboDur	165, 1.2	2	2	255		336,455	0.97
N11 ~ N13	Notch	None	-----	0	0	-----	$\Delta\sigma = 113$ R = 0.01	173,418	-----
N21		Sika Wrap	65, 1	4	0	255		182,829	1.05
N31 ~ N35		Sika Wrap	65, 1	2	2	255		327,271	1.89
N41, N42		Sika Wrap	65, 1	2	2	255		302,818	1.75
N51, N52		Sika Wrap	65, 1	2	2	380		373,139	2.15
N61, N62		Sika Wrap	65, 1	2	2	255		255,504	1.47
N71 ~ N74		Sika Wrap	65, 1	2	2	255		218,967	1.26
N22		MBRACE CF30	38, 1	4	0	255		222,731	1.28
N36		MBRACE CF30	38, 1	2	2	255		200,851	1.16

Table 2.6 Summary of fatigue test results of Tavakkolizadeh and Saadatmanesh (2003)

	Material			Specimens		Loading range
	Steel Beam	Patch	Adhesive	Dimension (mm)	Repaired type	
	S127 x 4.5 with edge notch in tensile flange	CFRP plate: E_{cfrp} = 144 MPa t_{cfrp} = 1.27 mm	Not defined	Beam: 1220 mm long Patch: 300 x 760	Machine notch on tensile flange at the edge a_i = 12.7 mm	$\Delta\sigma$ = 207 to 379 MPa R = 0.1

Stress range (MPa)	Unpatched		Patched		Increase in life for crack initiation (times)	Increase in fatigue life (times)
	Crack initiation	Failure	Crack initiation	Failure		
207	69,760	119,140	152,414	379,824	2.2	3.2
241	32,495	71,278	92,687	241,965	2.9	3.4
276	14,511	35,710	35,966	105,345	2.5	2.9
310	10,019	30,216	21,655	75,910	2.2	2.5
345	7,606	19,068	16,786	54,300	2.2	2.8
379	-----	-----	7,146	35,356	-----	-----

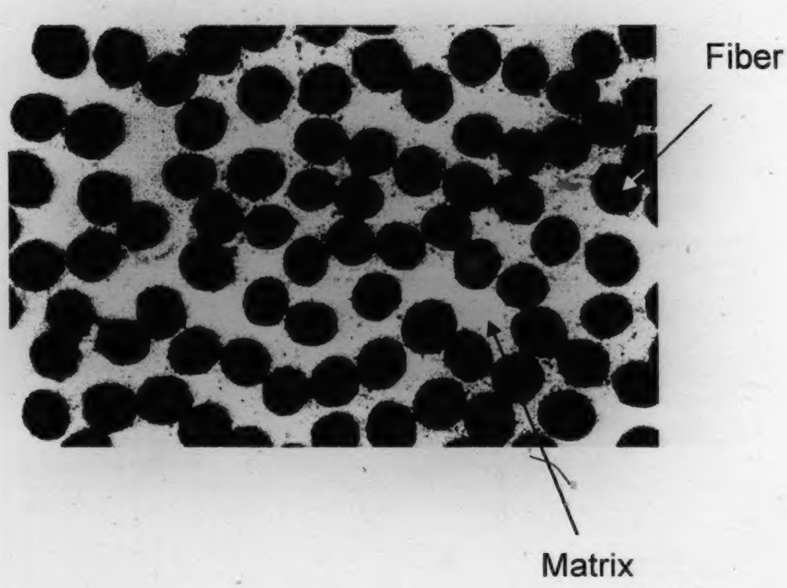
Fiber
Matrix

Figure 2.1 Cross section of Fiber Reinforced Polymer (FRP) material

2.5 References

American Association of State Highway and Transportation Officials (AASHTO), 2000, Standard Specifications for Highway Bridges, 16th Ed., Washington, D. C.

ACI 440R-96, 1996, "State-of-the Art Report on Fiber Reinforced Plastic (FRP) Reinforcement for Concrete Structures, American Concrete Institute (ACI) Committee 440, Farmington Hills, Michigan, USA.

Aglan, H., Wang, Q. Y., and Kehoe, M., 2001, "Fatigue behavior of bonded composite repairs", Journal of Adhesion Science and Technology, Vol. 15, No. 13, pp. 1621 – 1634

Baker, A. A., 1987, "Fiber composite repair of cracked metallic aircraft components – practical and basic aspects", Composites, September, pp. 293 – 308

Bassetti, A., Colombi, P. and Nussbaumer, A., 2000, "Finite element analysis of steel members repaired by prestressed composite patch", IGF 2000, XV Congresso Nazionale Del Gruppo Italiano Frattura, Bari

Bassetti, A., Nussbaumer, A. and Colombi, P., 2000, "Repair of riveted bridge members damaged by fatigue using CFRP materials", Advanced FRP Materials for Civil Structures, Bologna, Italy, 19th October 2000, pp. 33 – 42

Callinan, R., Sanderson, S. and Keeley, D. 1996, "3D FE Analysis of a bonded repair to an F-111 wing", Proceeding of Australian Conference on Applied Mechanics (ACAM 96), Institute of Engineers, Melbourne, Australia, May

Chester, R. J, Walker, K. F. and Chalkley, P. D. 1999, "Adhesively bonded repairs to primary aircraft structure" International Journal of Adhesion and Adhesives, 19, pp. 1 -8

Colombi, P., Bassetti, A. and Nussbaumer, A., 2003, "Crack growth induced delamination on steel members reinforced by prestressed composite patch", Fatigue Fract Engng Mater Struct 26, pp. 429 – 437

Colombi, P., Bassetti, A. and Nussbaumer, A., 2003, "Delamination effects on cracked steel members reinforced by prestressed composite patch", Theoretical and Applied Fracture Mechanics, 39, pp. 61 – 71

Colombi, P., Bassetti, A., and Nussbaumer, A., 2003, "Analysis of cracked steel members reinforced by pre-stress composite patch", Fatigue and Fracture Engineering of Materials and Structures, 26, pp. 59 – 66

Deniaud, C. and Cheng, J. J. R., 2000, "Behaviour of reinforced concrete beams strengthened in shear", Structural Engineering Report No. 234, University of Alberta, Department of Civil & Environmental Engineering

ISIS Canada, 2001, "Reinforcing concrete structures with fiber reinforced polymers, Manual No. 3", ISIS Canada Corporation, Winnipeg, Canada

Jones, R. and Callinan, R. J., 1979, "Finite element analysis of patched cracks", Journal of Structural Mechanics, 7(2), pp. 107 - 130

Jones, R. and Chiu, W. K., 1999, "Composite repairs to cracks in thick metallic components" Composite Structures, 44, pp. 17 - 29

Jones, S. C. and Civjan, S. A., 2003, "Application of Fiber Reinforced Polymer Overlays to Extend Steel Fatigue Life", Journal of Composites for Construction, Vol. 7, No. 4, pp. 331 – 338

Karbhari, V. M. and Seible, F., 2000, "Fiber reinforced composites – advanced materials for the renewal of civil infrastructure", Applied Composite Materials, Vol. 7

Kaw, A. K., 1997, "Mechanics of composite materials", CRC Press.

Kennedy, G. D. and Cheng, J. J. R., 1998, "Repair of cracked steel elements using composite fiber patching", Structural Engineering Report No. 221, University of Alberta, Department of Civil & Environmental Engineering

Klug, J., Maley, S. and Sun, C. T., 1999, "Characterization of fatigue behaviour of bonded composite repairs", Journal of Aircraft, Vol. 36, No. 6, pp. 1016 - 1022

Meier, U., 1992, "Carbon Fiber-Reinforced Polymers: Modern Materials in Bridge Engineering", Structural Engineering International, Vol. 1, No. 12, pp. 7 – 12

Meier, U., Deuring, M., Meier, H. and Schwegler, G., 1993, "CFRP bonded sheets, Fibre-Reinforce-Plastic (FRP) Reinforcement for Concrete Structures: Properties and Applications, edited by A. Nanni, Elsevier Science, Amsterdam, The Netherlands.

Roberts, P. D., 1995, "Crack growth retardation by carbon fiber composite patching : An application to steel pressure vessel repair", Master of Science Thesis, University of Alberta, Department of Mechanical Engineering

Rose, L. R. F., 1982, "A cracked plate repaired by bonded reinforcements", International Journal of Fracture, Vol. 18, No. 2, pp. 135 – 144

Schubbe, J. J. and Mall, S., 1999, "Investigation of a cracked thick aluminum panel repaired with a bonded composite patch", Engineering Fracture Mechanics, Vol. 63, pp. 305 – 323

Tavakkolizadeh, M. and Saadatmanesh, H., 2003, "Fatigue Strength of Steel Girders Strengthened with Carbon Fiber Reinforced Polymer Patch", Journal of Structural Engineering, Vol. 129, No. 2, pp. 186 – 196

Teng, J. G., Lam, L and Chen, J. F., 2004, "Shear strengthening of RC beams with FRP composites", Processing of Structural Engineering Materials, 6, pp. 173 – 184

3 ADHESIVE CFRP/STEEL BONDED LAP JOINTS

3.1 Introduction

It is shown in Chapter 2 that composite fiber patching techniques have been considered as alternatives to traditional methods of strengthening and fatigue crack repair in steel structures. As illustrated in Figure 3.1, by using the composite fiber patching techniques, some of the loadings can be transferred through the composite materials. In addition, the composite patching provides deformation constraint to the cracked mouth. The behavior of a patch is highly dependent on the transfer of load between the patch and adherend. This load transfer mechanism is best studied by using adhesive bonded joints. In order to understand the load transfer between composite patch and the base metal adherend, Kennedy and Cheng (1998) investigated the bond behavior of carbon fiber reinforced polymer (CFRP)/steel double lap joints. In their experiment, CFRP sheets with relatively thin thickness were used to form the CFRP/steel double lap joint. The corresponding adherend stiffness ratio (ETR) of CFRP to steel varied from 0.046 to 0.138. The experimental results showed that the axial strength of the CFRP/steel double lap joint increases with increasing ETR value. In this chapter, the experimental results of Kennedy and Cheng (1998) about the CFRP/steel double lap joint was summarized and discussed. In order to study the bond behavior of CFRP/steel double lap joint with higher ETR value, additional experimental and numerical studies were carried out. In the numerical study, non-linear finite element analysis was carried out to study the stress-strain

---

[1] A version of this chapter has been published in Dec., 2007 of the Canadian Journal of Civil Engineering.

behavior of adherend and adhesive of the double lap joint. Based on the finite element results, the analytical solution which was developed by Hart-Smith (1973) was applied to predict the maximum axial strength and minimum required lap length of the joint.

3.2 Background

Adhesive bonded joints have been used in the engineering industry such as the aircraft industry for several decades. A major advantage of the adhesive bond is that it enables dissimilar materials to be joined, even when one or both of these materials are non-metallic. Studies of adhesive bond strength were carried out by several researchers. Volkersen (1938) proposed a closed–form elastic equation to predict the elastic shear stress distribution of the adhesive of single lap joint. Goland and Reissner (1944) and Kutscha and Hofer (1969) made modifications on Volkersen's closed-form solution to consider other parameters such as the eccentricity of loading which would affect the strength of the joint. Hart-Smith (1973) studied the adhesive bonded joint more extensively. Both numerical and experimental studies of adhesively bonded composite joints were carried out. The studied parameters included: joint configurations, lap length, thickness of adherend, temperature effect etc. It was found that a better joint efficiency could be obtained by assigning suitable adherend stiffness ratio and lap length to the joint.

Uni-axial tensile tests of CFRP/steel double lap joint were carried out by Kennedy and Cheng (1998). Five specimens were prepared by bonding CFRP sheets (Mitsubishi Chemical Co. 1999) with a thickness of 0.11 mm/ply on both sides of steel plate. Before the application of CFRP sheet, all steel plates were sandblasted to provide a rough enough surface for bonding. The composite was applied using a hand lay-up procedure. The corresponding two-part epoxy was used as the matrix material of the composite and also as the adhesive between the steel plate and the composite. Different adherend stiffness ratios were achieved by increasing the number of layers (N_p) of CFRP composite material. Since hand lay-up procedure was used in patch fabrication, it was reported that the thickness of the resulting composite was highly variable. Therefore, the thicknesses of five CFRP sheets composite coupons were measured and an average composite thickness of 0.23 mm/layer was obtained with a coefficient of variation of 4%. The material properties, the average thickness and the detail dimensions of specimens, such as the lap length, number of layers and thickness of epoxy are shown in Table 3.1. All specimens were loaded with a uni-axial tensile loading up to failure. The load versus stroke curves of the five specimens are re-produced in Figure 3.2 and the corresponding maximum load and stroke at failure are summarized in Table 3.1. The results indicated that the maximum load increases with increasing adherend stiffness ratio (ETR). A finite element analysis was carried out to study the stress-strain behavior of the bond. Based on both experimental and numerical results, a minimum lap length (L_{min}) for load transfer was proposed, as follows:

$$L_{min} = 30\frac{E_{cfrp}t_{cfrp}}{E_s t_s} + 17 \qquad \text{(in mm)} \qquad (3.1)$$

where E_{cfrp} and t_{cfrp} are the elastic modulus and thickness of CFRP and E_s and t_s are the elastic modulus and thickness of steel plate. The above equation was developed for $E_{cfrp}t_{cfrp} / E_s t_s$ less than 0.25.

3.3 Experimental program

In order to investigate the tensile behavior of CFRP/steel double lap for a high adherend stiffness ratio (ETR), 14 CFRP/steel double lap joint specimens were designed and tested under static tensile loading. Major test parameters included the bonded lap length (L_L) and the adherend stiffness ratio ($ETR = 2E_{cfrp}t_{cfrp}/E_st_s$) in which E_{cfrp}, E_s, t_{cfrp} and t_s are the elastic module and thicknesses of the CFRP plate and steel plate, respectively.

3.3.1 Material properties of test specimens

A CFRP plate with a thickness of 1.2 mm/ply was used in preparing the specimens. The carbon fibers were placed in the longitudinal direction only. Tension coupons of the CFRP plates were prepared and tested to obtain the mechanical properties of the materials according to ASTM D3039/D3039M-00 (2000). The composites exhibited a linear stress versus strain relationship to failure, which was generally sudden and complete. The mean elastic modulus and ultimate strength of the composite materials are shown in Table 3.2. The steel test specimens were prepared using 300 mm long steel tabs (CSA 40.21-M 300W). Two different thicknesses of steel plate were used and the width of the steel plate was 50.8 mm for all specimens. Tension coupons of each type of steel plate were prepared and tested according to ASTM A370-02 (2002). The mean elastic modulus, the static yield strength, and the ultimate strength of the steel plates are also shown in Table 3.2. All of the steel plates were sandblasted in order to provide a rough enough surface for bonding (Roberts 1995). The Sika CFRP plates (Sika 2003), which were pre-fabricated and ready to use, were used in preparing the specimens. The corresponding two part epoxy, which was recommended by the manufacturer, was used as the adhesive between the steel plate and CFRP plate. The material properties of the adhesives provided by the manufacturer are shown in Table 3.2.

Different adherend stiffness ratios were achieved by increasing the number of layers (N_p) of CFRP composite material. Typical test specimens are illustrated in Figure 3.3. The average thickness and the detail dimensions of each test specimens such as the lap length, number of layers and thickness of epoxy are shown in Table 3.3.

3.3.2 Test specimen, instrumentation and test setup

The CFRP plates were cut into specified length and cleaned using acetone before bonding. The two-component epoxy paste adhesive was prepared according to the manual provided by the manufacturer and it was applied to the two sandblasted steel tabs by hand to both sides of the steel tabs. Subsequently, the specimens were allowed to cure at room temperature for a minimum of seven days before testing. Strain gauges were applied along the surface of the CFRP plates and steel plates to monitor the strain distribution as loading progressed. Strain gauges were applied primarily to one face of the specimen and a single gauge was applied to the other face for a symmetrical check. Specimens were tested in tension under stroke-controlled loading at a rate of 0.02 mm/min to failure in two of the four bonded surfaces. The applied load, stroke of the testing machine, and all the strain readings were recorded real time by a data acquisition system.

3.4 Test results

The test results, which included the maximum load, the stroke, and the maximum average shear stress of the adhesive, are shown in Table 3.4. The test results showed that all of the specimens failed by debonding of the CFRP in the adhesive. Linear load versus stroke behavior was observed in the early stage, then, nonlinear load versus stroke behavior was observed up to the maximum load. For specimens with long lap length, after the maximum load was reached, plateau stroke was observed up to the failure. The specimens with relatively short lap length failed without experiencing plateau stroke. Plateau stroke here is defined as the amount of stroke in which the change of loading is not significant (change of loading is less than 5% of the maximum load).

3.4.1 Effect of joint lap length

To study the effect of lap length, the specimens were divided into three groups. These three groups of specimens were prepared using CFRP plates with ETR 0.17, 0.34, and 1.03. The lap length varied from 50 mm to 150 mm for each group. The axial load versus stroke curve for these three groups of specimens are shown in Figure 3.4 and Figure 3.5. As shown in the figures, when the lap length was increased from 50 mm to 150 mm, the maximum load only increased marginally (less than 18%). However, much larger stroke was observed for specimens with longer lap length. The increase in stroke was more pronounced in specimens with lower adherend stiffness ratio (about 80% increases for specimens with ETR = 0.17 and 38% increase for with ETR = 1.03). Therefore, it can be seen that the axial load capacity of the bonded CFRP/steel double lap joint increased with increasing lap length. In addition, it was found that the increase in the axial load capacity of the double lap joint was not linearly proportional to the lap length. Once a certain lap length was achieved, the axial load capacity of the joint could not be increased further and the capacity was governed by the bond strength of the adhesive. Besides, when the lap length was increased; the corresponding stroke at failure was increased. This change of failure mode is compensated by the decrease of average shear stress of adhesive. The effect of increasing lap length to the shear stress of the adhesive is discussed in the section of finite element analysis.

The measured strains of the CFRP plate are shown in Figure 3.6 for specimens with ETR equal to 0.17 and 1.03. For each group of specimens, the strain results corresponding to two different loading stages (50% of maximum load and 100% of maximum load) are shown. It was observed that the maximum strain always occurs at the location of the gap. Since the steel plate was discontinuous at the gap, all the loading which was originally carried by the steel plate was transferred to the CFRP composite. As it was shown in Figure 3.6 the lower the adherend stiffness ratio, the higher the strain on CFRP composite was observed. The strain readings at locations other than the gap location were almost the same for either the short lap length or the long lap length specimens. This low strain implied that the additional lap length did not significantly contribute in load sharing of the joint. As a result, the capacity of the joint could not be increased significantly by increasing the lap length.

3.4.2 Effect of adherend stiffness ratio

The effect of relative stiffness ratio of the adherend can be shown by grouping the test results of the specimens with the same lap length. The plot of load versus stroke for the specimens with 100 mm and 150 mm lap length is shown in Figure 3.7. The results showed that the strength of the joint increased when the adherend stiffness ratio increased for the same lap length. The maximum loads obtained from each specimen are shown in Table 3.4. For the specimens with 50 mm lap length, test results showed that increasing the ETR by two and three times, the maximum loads were increased by about 36% and 59% respectively. For the 100 mm and 150 mm lap length specimens, test results showed that by increasing ETR by two times, the corresponding increase in the maximum strength was about 39% for both specimens.

Typical strain readings of CFRP composite corresponding to the maximum load level for specimens with different ETRs are shown in Figure 3.8. Maximum strain readings were obtained at the location of gap for all specimens. For specimens with lower ETR (=0.17), significant drop of strain was observed at those locations other than the location of the gap. For specimens with higher ETR (=1.03), strain readings along the lap length were more uniform. This implied that the load was shared more evenly on the CFRP composite for specimens with higher value of ETR. Hence, increasing the adherend stiffness ratio increases the load capacity of the joint.

3.4.3 Effect of tapering

Two specimens were prepared with tapered CFRP plates bonded to the steel plates. The dimensions of the tapered specimens are shown in Figure 3.9. The results of the tapered specimens were compared with those of the specimens with 50 mm and 150 mm lap length having the same ETR value. The corresponding loads versus stroke curves are shown in Figure 3.10 and Figure 3.11. The curves illustrate that the axial strength of the specimens did not decrease by using a tapering joint with 150 mm lap length and the same adherend stiffness ratio. It should be noted that the axial strength of the specimens with 3 layers of CFRP plates bonded to 6.09 mm steel plate reached the static yield load of the steel plate. The specimen with the non-taper lap pattern failed suddenly when the yielding capacity of the steel plate was reached. However, for the specimen with the taper lap pattern, ductile behavior was observed after the yielding capacity of the steel plate was reached. Strains reading at the same load level of the tapered specimens were compared with those of the non-tapered specimens with 150 mm lap length. The results showed that the strain reading of the strain gauges located at the gap were almost the same for tapered and non-tapered specimens. However, the strain readings of those strain gauges which were away from the gap of the tapered specimens were higher than those non-tapered specimens due to the reduced thickness of CFRP material at the tapered end.

3.5 Finite element analysis of CFRP/Steel double lap joint

In order to study the stress-strain behavior of the adhesive double lap joints, especially the stress-strain behavior of the adhesive, ten tested specimens which were prepared using the CFRP plates with adherend stiffness ratio (ETR) varied from 0.17 to 1.03, short and long lap length (L_L = 50mm and 150mm) and tapered pattern, were analyzed by using the finite element method. Specimens with intermediate lap length, as it was shown from the test results, failed at a maximum load that was almost the same as that of specimens with short and long lap length. Hence, the results from specimens with intermediate lap length were not included in the finite element study. The finite element package ABAQUS 6.4 (2004) was used to carry out the analysis. Since the specimens were subjected to axial tensile load only, it was assumed that the transverse behavior of the specimens were uniform. Therefore, two dimensional, plane strain, 4 nodes elements were used in the finite element models. The model represented one quarter of an experimental specimen, taking advantage of symmetry. Boundary conditions restrained the assembly from out-of-plane motion. A typical finite element model of a lap joint is shown in Figure 3.12.

3.5.1 Material properties used in the finite element analysis and the finite element analysis procedure

Based on the material test results, non-linear material properties were used for the steel plates and linear material property was used for the CFRP composite. For the adhesive, a theoretical adhesive shear stress-strain curve, which was proposed by Grant (1978), was used in the finite element analysis. Grant proposed that the nonlinear shear stress-strain relationship of adhesive could be represented by the following equations:

$$\tau = \gamma \, G_e \qquad \text{for} \qquad \gamma < \gamma_e \tag{3.2}$$

$$\tau = \tau_e + \left(\frac{\alpha\beta}{\alpha + \beta} \right) \qquad \text{for} \qquad \gamma > \gamma_e \tag{3.3}$$

where $\alpha = \gamma G_e - \tau_e$ and $\beta = \tau_{max} - \tau_e$

in which τ = shear stress, τ_{max} = maximum shear stress, τ_e = limit of elastic shear stress, γ = shear strain, γ_e = limit of elastic shear strain and G_e = elastic shear modulus. From the material properties provided by the manufacturer, the elastic modulus of the adhesive (Sikadur 30) is 4500 MPa. By assuming a Poisson's ratio of 0.34 for the adhesive (May and Hutchinson 1992), an elastic shear modulus (G_e) of 1680 MPa was used for the adhesive. The design maximum shear strength of the adhesive (τ_{max}) was 24.8 MPa, a value provided by the manufacturer. Assuming the properties of the adhesive is highly non-linear, the shear stress-strain relationship was assumed to be linear up 2.48 MPa (τ_e), which is 10% of the maximum shear stress. Therefore, the corresponding elastic shear strain (γ_e) could be obtained. The theoretical shear stress-strain curve is shown in Figure 3.13. The theoretical shear stress-strain curve of the adhesive was converted to axial stress-strain curve, which was needed in the finite element analysis. The following equations were used to convert the shear stress (τ) and strain (γ) to axial stress (σ) and strain (ε) (Bassetti et al. 2000)

$$\sigma = \sqrt{3}\tau \tag{3.4}$$

$$\varepsilon = \frac{\sqrt{3}}{2(1+\nu)}\gamma \tag{3.5}$$

Non-linear analysis was carried out by controlling the displacement of the inner steel plate of the model (to simulate stroke control). At each step of the displacement, stress of the inner steel plate was monitored. With the stress of the inner steel plate, the corresponding axial load was obtained. It was observed from the test results that progressive local failure occurred at part of the areas in the adhesive layer after the ultimate load of the specimen was reached. The progressive local failure of the adhesive could not be captured by the current finite element model. Therefore, it was decided to terminate the analysis at the maximum axial load level to obtain the maximum shear strain of the adhesive. At this maximum load level, the maximum shear strains of the adhesive were obtained. This maximum shear strain value will be used in the equations for predicting the maximum load and this will be discussed in the later section. Typical finite element result of load versus stroke curve is shown in Figure 3.4. The finite element results gave good prediction of the load versus stroke behavior in the elastic stage. Later on, stiffer behavior was observed for the finite element result up to the maximum load level.

3.5.2 Comparison of axial strain distribution of CFRP plates of test and finite element results

The axial strain distribution of CFRP plates obtained from the finite element analyses were compared with the experimental results at the maximum load level. Figure 3.14 shows the load versus strain results of 2 specimens with different adherend stiffness ratios (ETR = 0.17 and 1.03) and the axial strain distribution of CFRP plate of 2 sets of specimens with 2 different adherend stiffness ratios and 2 different lap lengths (L_L = 50 mm and 150 mm). It can be seen from the figure that the finite element results agreed well with the experimental results. The finite element results showed that the maximum axial strain in the CFRP plates decreased with increased axial stiffness of the plates. For specimens with short lap length (L_L = 50 mm), the axial strain distribution of CFRP plate decreased almost linearly from the gap location (x = 0 mm) to the end (x = L_L mm) of the lap. However, for specimens with a longer lap length (L_L = 150 mm), the maximum strain occurred at the gap location (x = 0 mm) followed by a plateau over the center of the lap and finally dropped to zero at the end of the lap (x = L_L mm). The difference between the maximum strain at the beginning of the lap and the plateau strain at the center region varied with different adherend stiffness ratios. It is shown from Figure 3.14 that when the adherend stiffness ratio was small, the difference between the maximum strain and the plateau strain was large. When the adherend stiffness ratio was close to unity, the difference between the maximum strain and the plateau strain was small.

The axial strain distributions of the tapered CFRP plate specimens were compared with the non-tapered specimens, as shown in Figure 3.15. Experimental results are also included in the figures and they are in good agreement with the finite element results. It can be seen from the figure that for the tapered joint, the axial strains at the tapered end were higher than those of the non-tapered specimens due to the reduction of axial stiffness of the CFRP plates at the tapered end. Although the axial stiffness of the CFRP plates at the tapered end was reduced, the axial strain of CFRP plates at the tapered end was still lower than the failure strain of the CFRP plate. This also agreed with the experimental failure mode that failure occurred in the adhesive layer.

3.5.3 Shear stress and strain of adhesive layer

In the experimental program, it was observed that failure occurred in the adhesive layer. Therefore, the shear stress/strain distribution of the adhesive, which was obtained from the finite element analysis, was examined. In the finite element model, two layers of elements were used for the adhesive layer. The shear stress/strain results at the top and bottom layer of the adhesive layer are shown in Figure 3.16 and Figure 3.17. These figures also show the shear stress/strain distribution of the adhesive between the steel and the CFRP plates of the specimens with adherend stiffness ratio equaled to 0.17, 0.34 and 1.03 and a lap length of 50 mm and 150 mm. As can be seen from the figures, the maximum shear stress/strain occurred at the ends of the lap. When the lap length increased, the maximum shear stress/strain did not decrease. For the long lap length specimens, the shear stress/strain at the center region of the lap was relatively low. Due to this low shear stress at the center region, increasing the lap length did not increase the axial capacity significantly. For the specimens with a low adherend stiffness ratio, the difference between the shear stress/strain at the ends of lap was large. For the specimens with the adherend stiffness ratio closed to unity, the shear stress/strain results at both ends were close to each other. This might imply that load was picked up at both ends (at the end of lap and at the location of the gap) of the lap for specimens with adherend stiffness ratio closed to unity. Therefore, specimens with higher adherend stiffness ratio have higher load transfer capacity than those specimens with lower adherend stiffness ratio.

The shear stress/strain distribution of the tapered and non-tapered specimens was also compared as shown in Figure 3.16 and Figure 3.17. It can be seen from the figures that the shear stress/strain of the tapered specimens was lower than that of the non-tapered specimens at the location where tapering started. However, higher shear stress/strain was observed at the second tapering step for specimen P-2-taper-1/2 and the second and third tapering steps for specimen P-3-taper-1/4. This might imply that a larger amount of loads was carried by the adhesive for the tapered joints within the stiffer region but a smaller amount of loads was carried up by the adhesive within the less stiff region. Therefore, the failure load did not decrease by using a tapered lap with the same adherend stiffness ratio.

3.6 Prediction of maximum strength and minimum lap length of adhesive double lap joints

It was shown from both the experimental and numerical results that the strength of the adhesive double lap joint was mainly affected by the adherend stiffness ratio and the strength of the adhesive. In order to develop the maximum strength, a minimum lap length should be provided for the joint. The prediction of maximum strength and minimum required lap length is shown in the following section.

3.6.1 Prediction of maximum strength of adhesive double lap joints

Hart-Smith (1973) extended the elastic analyses of Volkersen (1938) by considering the non-linear material behavior of adhesive. Hart-Smith proposed that the joint reached its maximum strength when the maximum shear strain of the adhesive reached its failure shear strain value. He also showed that for any arbitrary elastic-plastic curve representation of the shear behavior of an adhesive, its strain energy per unit bond area was the unique, necessary, and sufficient characterization defining the maximum attainable bond strength between two adherends. Hence, for any arbitrary elastic-plastic curve representation of the shear behavior of an adhesive in which the strain energy is the same will give the same maximum attainable bond strength between two adherends. For ductile adhesives, Hart-Smith (1973) proposed the following equations for predicting the maximum strength per unit width of adhesive bond double lap joint;

$$P = 2\tau_{av}L_L = \sqrt{4k\tau_p\eta(\gamma_e + \gamma_p)E_i t_i(1 + \frac{1}{ETR})} \qquad \text{for} \quad ETR \geq 1 \qquad (3.6)$$

$$P = 2\tau_{av}L_L = \sqrt{8k\tau_p\eta(\gamma_e + \gamma_p)E_o t_o(1 + ETR)} \qquad \text{for} \quad ETR < 1 \qquad (3.7)$$

where $k = \frac{(0.5\gamma_e + \gamma_p)}{(\gamma_e + \gamma_p)}$, E_i and E_o = elastic modulus of the inner and outer adherends respectively, L_L = lap length, t_i and t_o = thickness of inner and outer adherends respectively, τ_p = shear yield stress of adhesive, γ_e = elastic strain limit of adhesive, γ_p = plastic strain limit of adhesive, η = thickness of adhesive and $ETR = 2E_0t_0 / E_it_i$. By replacing the symbols in Eqs. 3.6 and 3.7 with the current symbols used with CFRP, the steel plate and the adhesive, Eqs. 3.6 and 3.7 were rewritten in the following format;

$$P = \sqrt{2\tau_{max}\eta(\gamma_e + 2\gamma_p)E_s t_s(1 + \frac{1}{ETR})} \qquad \text{for} \quad ETR \geq 1 \qquad (3.8)$$

$$P = 2\sqrt{\tau_{max}\eta(\gamma_e + 2\gamma_p)E_{cfrp}t_{cfrp}(1 + ETR)} \quad \text{for} \quad ETR<1 \tag{3.9}$$

where τ_{max} = maximum design shear stress of the adhesive.

Based on this condition, the non-linear shear stress-strain curve, which was used in the finite element analysis, was replaced by an elastic-plastic shear stress-strain curve. This required obtaining the maximum design shear stress and maximum design shear strain of the adhesive. From the finite element analysis results, the maximum shear stress and strain of the adhesive were obtained and is shown in Table 3.5. It was found that for specimens with steel plate thickness equal to 12.44 mm, the maximum shear strain at failure ranged from 0.1 to 0.135 and the maximum shear stress of the adhesive was close to the design shear stress (24.8 MPa) which was provided by the manufacturer. Therefore, by setting the maximum shear stress for the adhesive to 24.8 MPa and the maximum shear strain to 0.1, the non-linear shear stress-strain curve could be converted to an elastic-plastic shear stress-strain curve. This could be done by equating the area under the non-linear shear stress-strain curve and the elastic-plastic shear stress-strain curve. Therefore, based on the elastic-plastic shear stress-strain curve, the elastic shear strain (γ_e) and the plastic shear strain (γ_p) were found to be 0.0679 and 0.0321, respectively. By substituting the above values to Eqs. 3.8 and 3.9, the maximum joint strength per unit width of plate could be obtained.

The analytical results and the corresponding test results of the fourteen specimens tested are shown in Table 3.6. It can be seen from the table that the analytical predictions agreed well with the test results except for specimens with steel plate thickness equal to 6.09 mm and specimen P-3-50-1/2. The analytical predictions for the specimens with steel plate thickness equal to 6.09 mm were all greater than the static yield load of the 6.09 mm steel plate. Since Eqs. 3.8 and 3.9 did not take into account the effect of yielding of the adherend, the static yield load for the steel plate should be checked and the lower value (values predicted by Eqs. 3.8 or 3.9 and the static yield load) would give the maximum load. For specimen P-3-50-1/2, although the analytical prediction was lower than the static yield strength of the steel plate, the analytical prediction was found to be greater than the test result. The shear stress distribution of the adhesive which was obtained from the finite element result of specimen P-3-50-1/2 is shown in Figure 3.17. It is shown that the shear stress of the adhesive was almost uniform along the overall lap length. Therefore, for specimen with short lap length and ETR value closes to unity, the plastic shear strength of the adhesive, which is equal to 126 kN for this specimen should be used as the maximum strength for this specimen. It is shown in Table 3.6 that the modified analytical predictions were in better agreement with the test results. The test-to-predicted ratio varied from 0.88 to 1.14 with a mean of 1.00 and coefficient of variation of 8.43%.

3.6.2 Prediction of minimum lap length of adhesive double lap joints

Hart-Smith (1973) also suggested equations for predicting the minimum lap length of a double lap joint. The minimum lap length of double lap joints with adhesive can be predicted by using the following equation;

$$L_{min} \cong \frac{P}{2\tau_{max}} \qquad (3.10)$$

In practice, it is suggested that the practical lap length should be made longer in order to account for small fabrication tolerance and to provide enough residual strength for long-term environmental exposure. Therefore, the practical design lap joint length ($L_{Practice}$) should be,

$$L_{Practice} = \frac{P}{2\tau_{max}} + \frac{2}{\lambda} \qquad (3.11)$$

where $\lambda = \sqrt{\frac{G_{ep}}{\eta}\left(\frac{1}{E_{cfrp}t_{cfrp}} + \frac{2}{E_s t_s}\right)}$

The equivalent elastic-plastic shear modulus (G_{ep}) was 365.2 MPa in this study. The predictions of the practical design lap length of double lap joints with adhesive by Eq. 3.11 are shown in Table 3.6. The specimens which experienced plateau stroke and failed are marked with an asterisk in Table 3.6. The appearance of the plateau stroke implied that the applied lap length was more than enough for developing the maximum strength of the joint. For example, the test result of specimen P-2-50-1/2 with lap length equal to 50 mm did not show any plateau stroke but specimen P-2-150-1/2 with lap length equal to 75 mm did. The predicted design lap length is about 60 mm for this group of specimens. This prediction is in good agreement with the test results.

3.7 Summary and conclusions

In this chapter, the experimental results of the behavior of fourteen CFRP/steel double lap joint specimens subjected to axial loading were presented. The test parameters included: (1) lap length, (2) adherend stiffness ratio and (3) tapered and non-tapered lap joint pattern. Based on the experimental results, the following conclusions were made.

(1) All of the specimens failed by debonding of the adhesive.

(2) For specimens with short lap length, brittle failure behavior was observed.

(3) The axial capacity of the joint did not increase further once the lap length reached the required minimum lap length.

(4) Once the lap length reached the required minimum lap length, the axial load carrying capacity of the joint with the same adherend stiffness ratio could only be increased marginally by increasing the lap length. However, a larger failure deformation could be achieved before failure for specimens with longer lap length.

(5) With the same inner adherend thickness, specimens with higher adherend stiffness ratio showed a higher axial load carrying capacity.

(6) The axial capacities of the tapered lap joints with longer lap length were almost the same as the non-tapered lap joints. Higher shear strains were observed in the tapered lap joint specimens within the stiffer section.

A non-linear finite element analysis was carried out to study the stress-strain behavior of the adherend and the adhesive of a double lap joint. The finite element analysis results predicted well the experimental axial strain of the CFRP. Based on the finite element results, the analytical solution which was developed by Hart-Smith (1973) was applied to predict the maximum axial strength and minimum required lap length of the joint. The analytical solution provided good predictions of the test ultimate loads of the specimens. The test to predicted ratio of the maximum joint strength varied from 0.88 to 1.14 in this study. The corresponding minimum lap length of the joint can be predicted based on the prediction of the maximum joint strength. The prediction of minimum lap length agrees well with the test results in this study.

Table 3.1 Material properties and test results of Kennedy and Cheng (1998)

Specimen	**Thickness of CFRP sheet t_{cfrp} (mm)**	**Thickness of steel plate t_s (mm)**	**No. of layer of CFRP sheet N_p**	**Adherend stiffness ratio ETR**	**Lap length L_L (mm)**	**Maximum load (kN)**	**Stroke (mm)**
CM2-1	0.46	12.7	2	0.046	25.4	12.1	0.23
CM2-2	0.46	12.7	2	0.046	50.8	21.1	0.39
CM2-3	0.46	12.7	2	0.046	76.2	21.8	0.49
CM4-3	0.92	12.7	4	0.092	76.2	25.0	0.44
CM6-3	1.38	12.7	6	0.138	76.2	40.0	1.10

Material properties

Steel plate: Elastic modulus = 200000 MPa

CFRP composite sheet: Elastic modulus = 128093 MPa, Ultimate stress = 1063 MPa

Epoxy for CFRP sheet: Elastic modulus = 3000 MPa*

*Material properties provided by the manufactures

Table 3.2 Material properties of steel plate, CFRP composite and epoxy

Steel plate	Elastic modulus (MPa)	Static yield stress (MPa)	Ultimate stress (MPa)
Steel plate (t_s = 12.44mm)	203150	316.3	491.0
Steel plate (t_s = 6.09mm)	205700	328.7	474.7

CFRP composite	Elastic modulus (MPa)	Ultimate stress (MPa)
CFRP composite plates	176061	1618

Epoxy	Elastic modulus (MPa)	Shear strength (MPa)
Epoxy for CFRP plates	4500*	24.8*

*Material properties provided by the manufacturers.

Table 3.3 Dimension of test specimens

Specimen	Thickness of CFRP material t_{cfrp} (mm)	Thickness of steel plate t_s (mm)	Thickness of adhesive η (mm)	No. of layer of CFRP material N_p	Adherend stiffness ratio ETR	Lap length L_L (mm)
P-1-50-1/2	1.22	12.44	0.55	1	0.170	50
P-1-75-1/2	1.22	12.44	0.49	1	0.170	75
P-1-100-1/2	1.22	12.44	0.53	1	0.170	100
P-1-150-1/2	1.22	12.44	0.56	1	0.170	150
P-2-50-1/2	2.44	12.44	0.61	2	0.340	50
P-2-100-1/2	2.44	12.44	0.53	2	0.340	100
P-2-150-1/2	2.44	12.44	0.61	2	0.340	150
P-2-taper-1/2	2.44	12.44	0.66	2	0.340	150,100
P-3-50-1/2	3.66	12.44	0.59	3	0.510	50
P-2-50-1/4	2.44	6.09	0.60	2	0.680	50
P-3-50-1/4	3.66	6.09	0.65	3	1.030	50
P-3-100-1/4	3.66	6.09	0.55	3	1.030	100
P-3-150-1/4	3.66	6.09	0.71	3	1.030	150
P-3-taper-1/4	3.66	6.09	1.01	3	1.030	150,100,50

Designation of specimens: P-2-25-1/2 = Plates-N_p-L_L-t_s

The thickness of adhesive was obtained by subtracting the thickness of steel plate and composite from the total thickness of the lap joint.

Table 3.4 Test results

Specimen	Adherend stiffness ratio ETR	Maximum load (kN)	Average shear stress of adhesive (MPa)*	Stroke (mm)
P-1-50-1/2	0.170	70.32	13.84	0.49
P-1-75-1/2	0.170	70.91	9.31	0.56
P-1-100-1/2	0.170	71.25	7.01	0.67
P-1-150-1/2	0.170	78.65	5.16	0.88
P-2-50-1/2	0.340	95.48	18.79	0.57
P-2-100-1/2	0.340	98.72	9.72	0.62
P-2-150-1/2	0.340	109.38	7.18	0.76
P-2-taper-1/2	0.340	107.54	7.06	0.67
P-3-50-1/2	0.510	111.70	21.99	0.64
P-2-50-1/4	0.690	93.86	18.48	0.89
P-3-50-1/4	1.030	91.65	18.04	0.81
P-3-100-1/4	1.030	103.88	10.22	0.96
P-3-150-1/4	1.030	107.96	7.08	1.12
P-3-taper-1/4	1.030	110.68	7.26	5.57

*Average shear stress of adhesive = Maximum load / (2 x L_L x width)

Table 3.5 Finite element results of maximum shear stress and strain of adhesive

Specimens	Maximum shear stress (MPa)	Maximum shear strain (mm/mm)
P-1-50-1/2	21.89	0.1138
P-1-150-1/2	22.30	0.1350
P-2-50-1/2	22.12	0.1255
P-2-150-1/2	21.81	0.1115
P-2-taper-1/2	21.50	0.1000
P-3-50-1/2	23.03	0.2085
P-2-50-1/4	21.73	0.1080
P-3-50-1/4	20.98	0.0853
P-3-150-1/4	19.58	0.0615
P-3-taper-1/4	17.48	0.0424

Table 3.6 Comparison of test maximum joint strength with analytical results

Specimens	ETR	Test L_L (mm)	P_{Test} (kN)	P (kN)	P_{ANA} (kN)	$\frac{P_{Test}}{P_{ANA}}$	$L_{Practical}$ (mm)
P-1-50-1/2	0.17	50	70.32	68.32	68.32	1.03	60.39
P-1-75-1/2	0.17	75*	70.91	64.49	64.49	1.10	57.00
P-1-100-1/2	0.17	100*	71.25	67.07	67.07	1.06	59.28
P-1-150-1/2	0.17	150*	78.65	68.94	68.94	1.14	60.94
P-2-50-1/2	0.34	50	95.48	108.89	108.89	0.88	89.53
P-2-100-1/2	0.34	100*	98.72	101.50	101.50	0.97	83.46
P-2-150-1/2	0.34	150*	109.38	108.89	108.89	1.00	89.53
P-2-taper-1/2	0.34	150*	107.54	113.27	113.27	0.95	93.09
P-3-50-1/2	0.51	50	111.70	139.23	125.98	0.89	107.82
P-2-50-1/4	0.69	50	93.86	121.14	101.69	0.92	89.04
P-3-50-1/4	1.03	50	91.65	164.66	101.69	0.90	112.95
P-3-100-1/4	1.03	100	103.88	151.47	101.69	1.02	103.90
P-3-150-1/4	1.03	150*	107.96	172.09	101.69	1.06	118.05
P-3-taper-1/4	1.03	150*	110.68	205.26	101.69	1.09	140.74

P_{Test} = Test results, P_y = Static yield load of steel plate = 199.89 kN for 12.7 mm plate and 101.69 kN for 6.35 mm plate, P_{Adhv} = Fully yield load of adhesive = 24.8 x L_L x 50.8 x 2 kN, P = value obtained from Eq. 3.7 or 3.8 x width of specimen, P_{ANA} = smallest value of P (Eq. 3.7 or 3.8) x width of specimen, P_y and P_{Adhv}

The specimens which experienced plateau stroke and failed are marked with *.

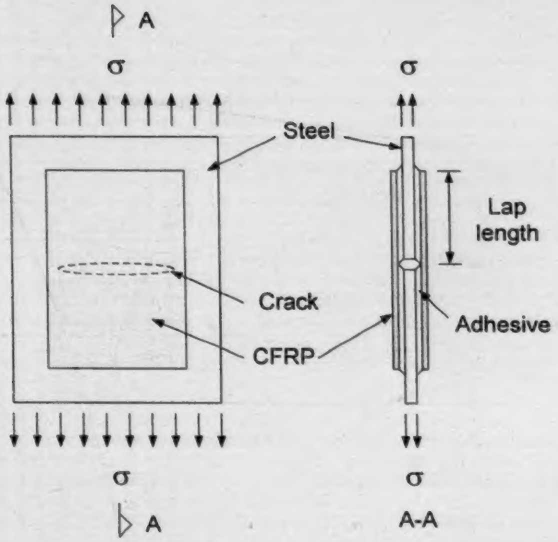
A
σ
σ
Steel
Lap length
Crack
Adhesive
CFRP
σ
σ
A
A-A

Figure 3.1 Illustration of cracked steel plate repaired by bonded reinforcement

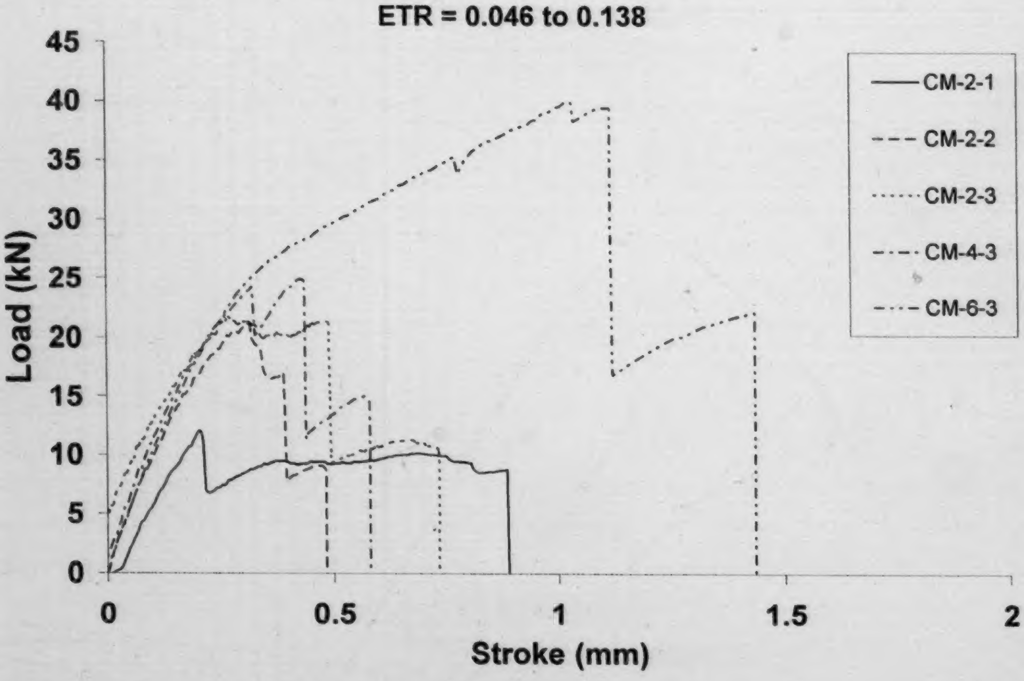

Figure 3.2 Load versus stroke curves of CFRP sheet/steel double lap joint specimens tested by Kennedy and Cheng (1998)

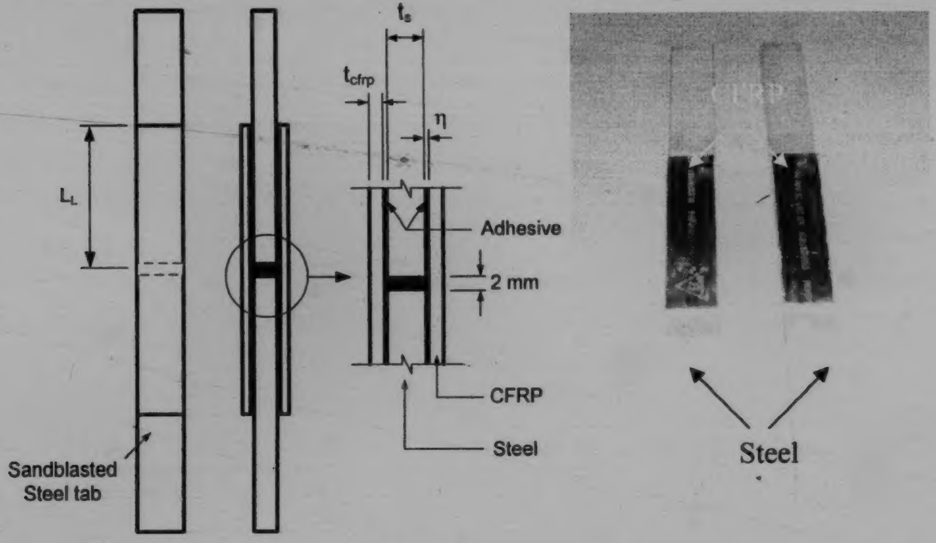
(a) Illustration of typical double lap joint specimen (b) Photo of CFRP/steel double lap joint

t_s
t_{cfrp}
η
L_L
Adhesive
2 mm
CFRP
Steel
Sandblasted Steel tab
CFRP
Steel

Figure 3.3 CFRP/steel double lap joint

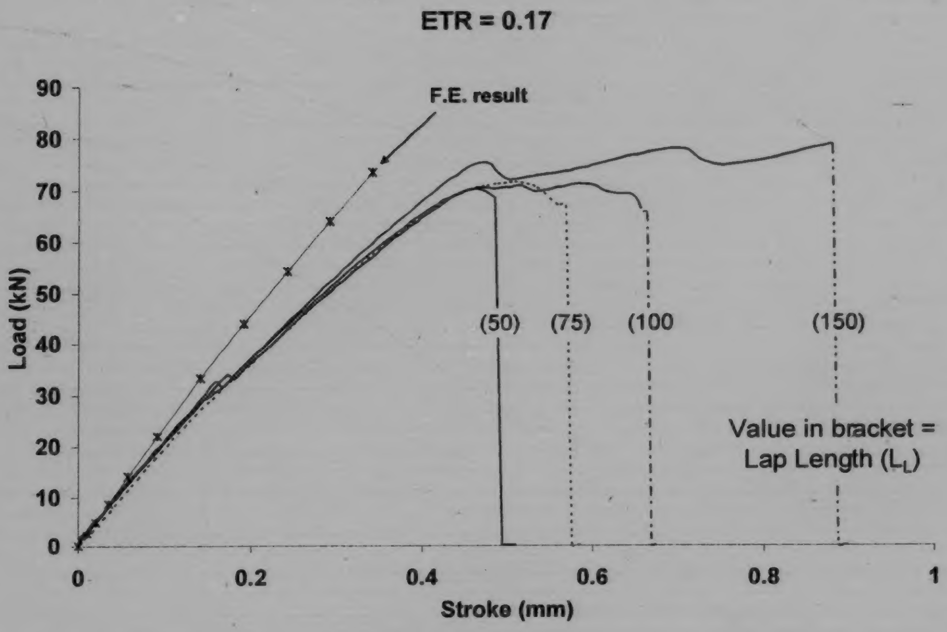

Figure 3.4 Load versus stroke curve of specimens with different lap length and ETR = 0.17

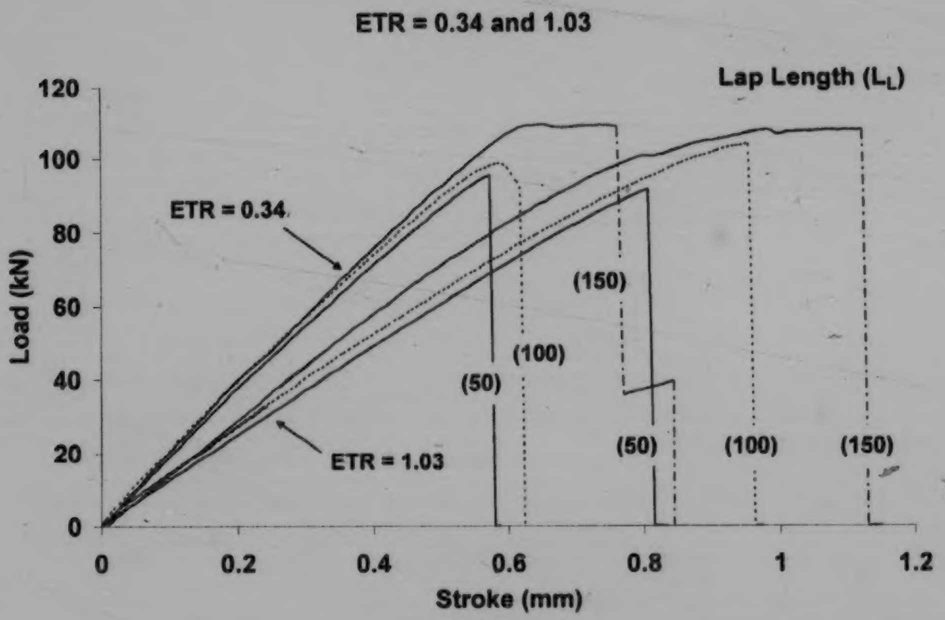

Figure 3.5 Load versus stroke curve of specimens with different lap length and ETR = 0.34 and 1.03

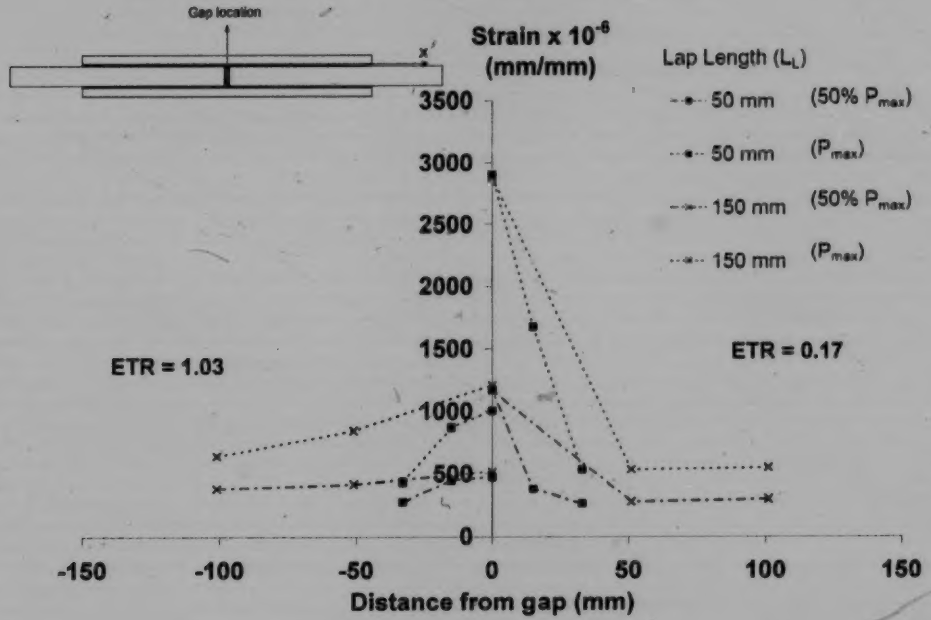

Figure 3.6 Strain profile of CFRP of specimen with different lap length and ETR = 0.17 and 1.03

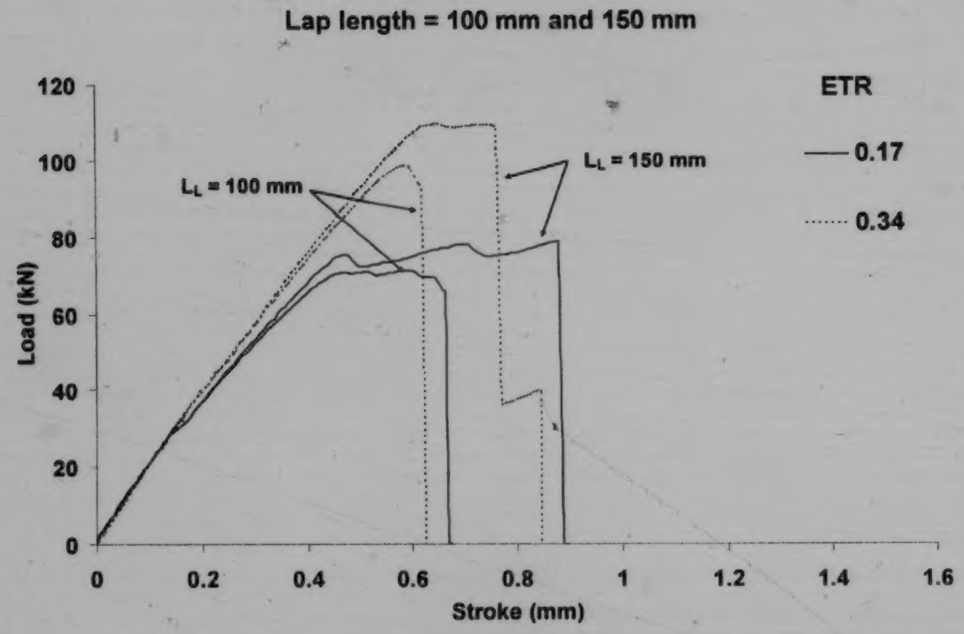

Figure 3.7 Load versus stroke curve of specimens with different ETR values and L_L =100mm and 150mm

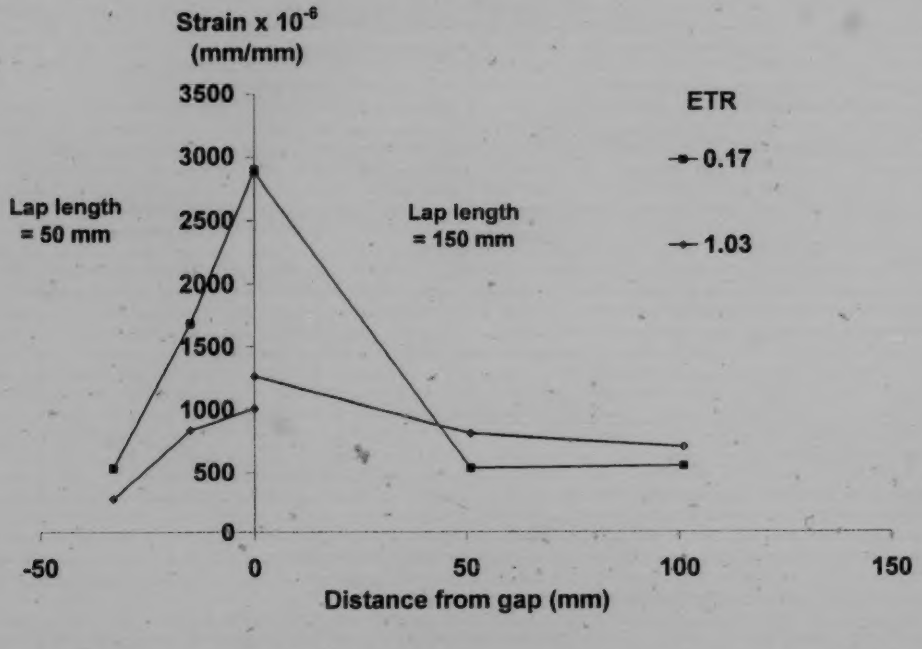

Figure 3.8 Strain profile of CFRP of specimen with lap length = 50 mm and 150 mm

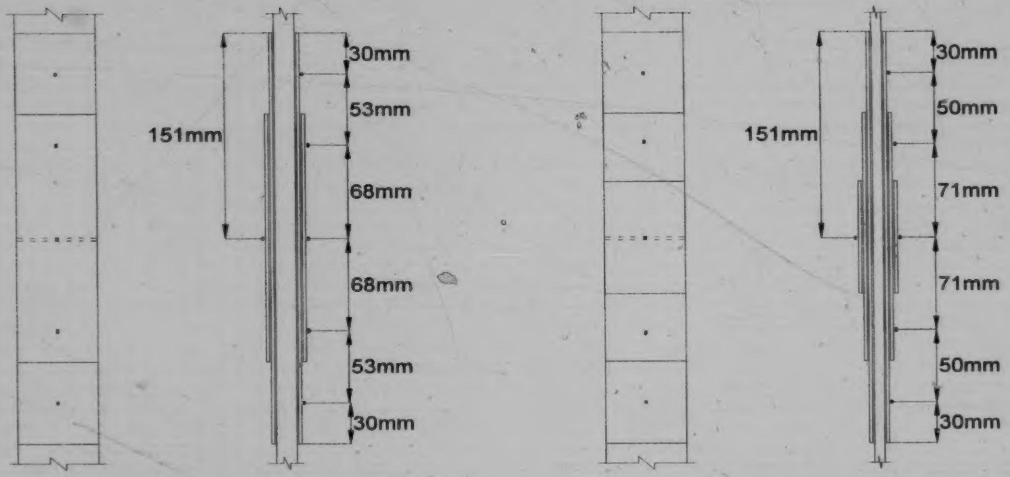
30mm
53mm
151mm
68mm
68mm
53mm
30mm
30mm
50mm
151mm
71mm
71mm
50mm
30mm

Two layers CFRP/steel
tapered specimen

Three layers CFRP/steel
tapered specimen

Figure 3.9 CFRP/steel double lap joint tapered specimens

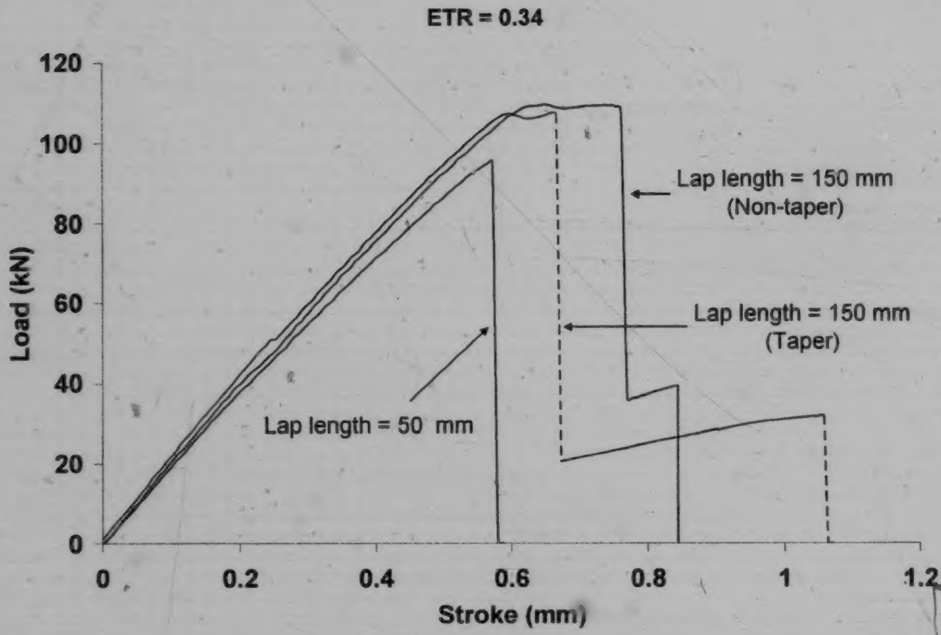

Figure 3.10 Load versus stroke curve of specimens with and without tapered lap and ETR = 0.34

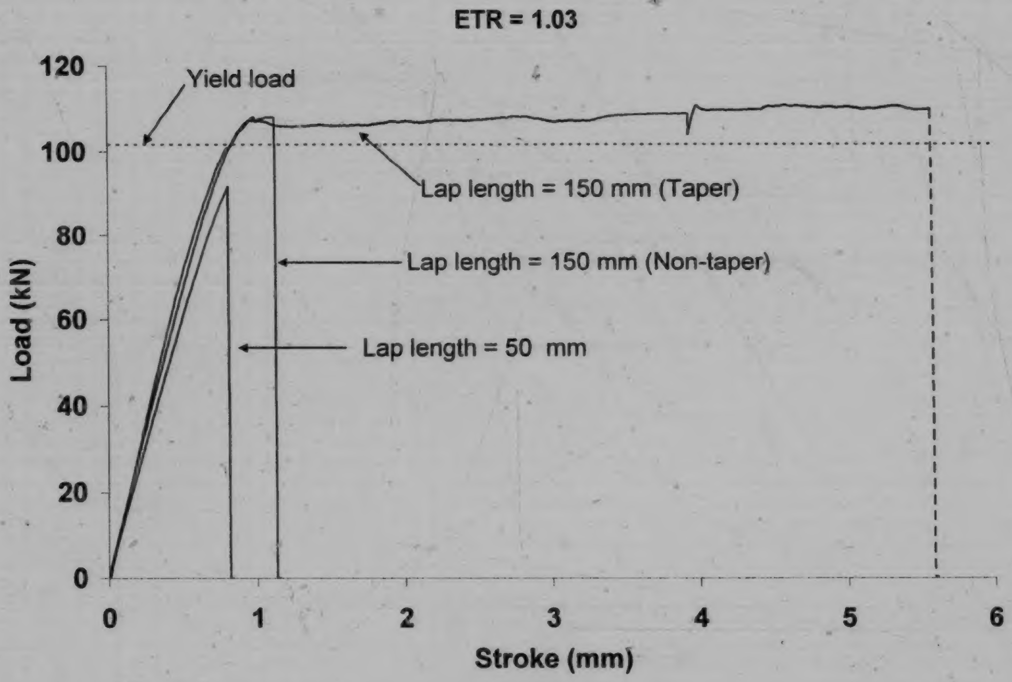

Figure 3.11 Load versus stroke curve of specimens with and without tapered lap and ETR = 1.03

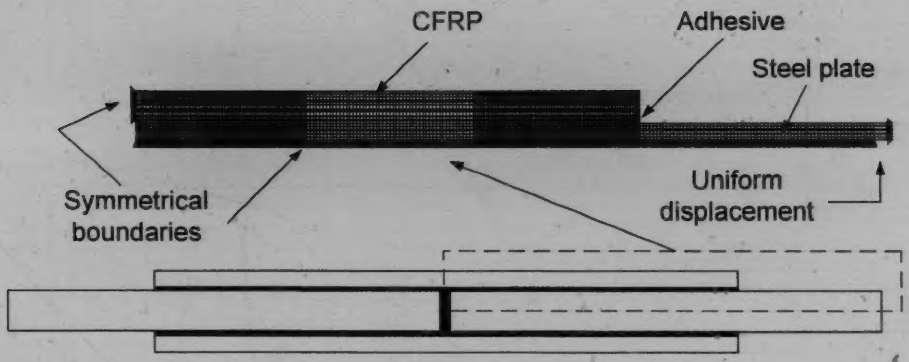
CFRP
Adhesive
Steel plate
Symmetrical boundaries
Uniform displacement

Figure 3.12 Typical finite element model

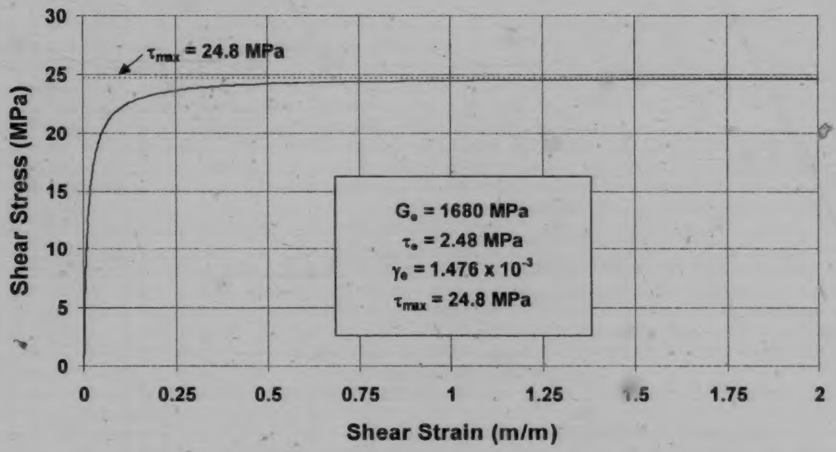

Figure 3.13 Assumed shear stress-strain curve of adhesive

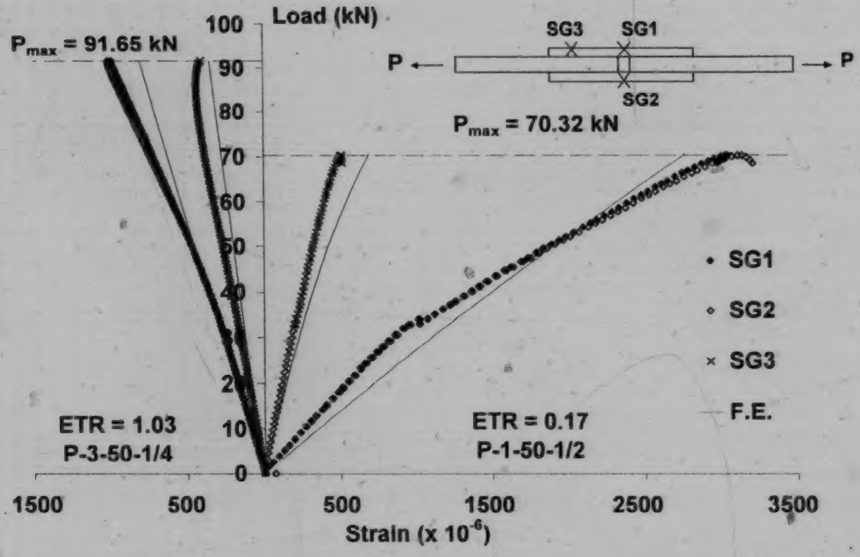

(a) Comparison of finite element and test results of load versus strain

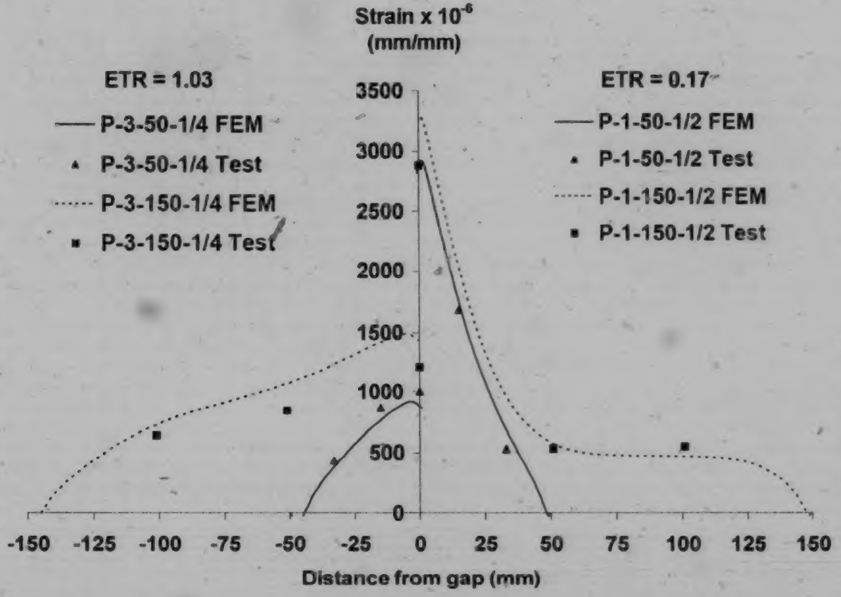

(b) finite element and test results of axial strain of CFRP plate at maximum load level

Figure 3.14 Finite element and test results of axial strain of CFRP plate (ETR = 0.17 and 1.03)

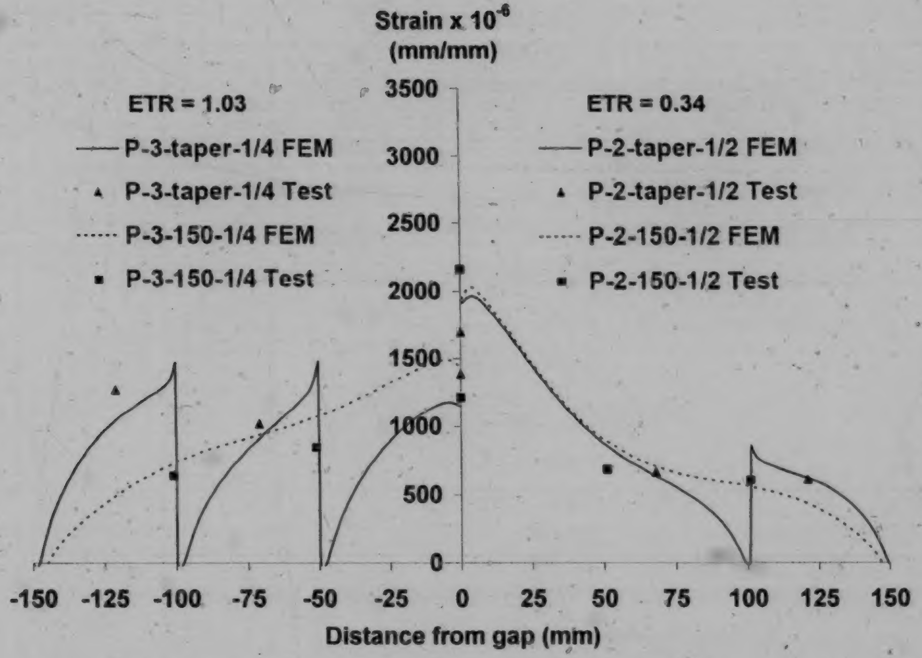

Figure 3.15 Finite element and test results of axial strain of CFRP plate (ETR = 0.34 and 1.03 taper and non-taper specimens)

(a) Shear stress distribution of adhesive

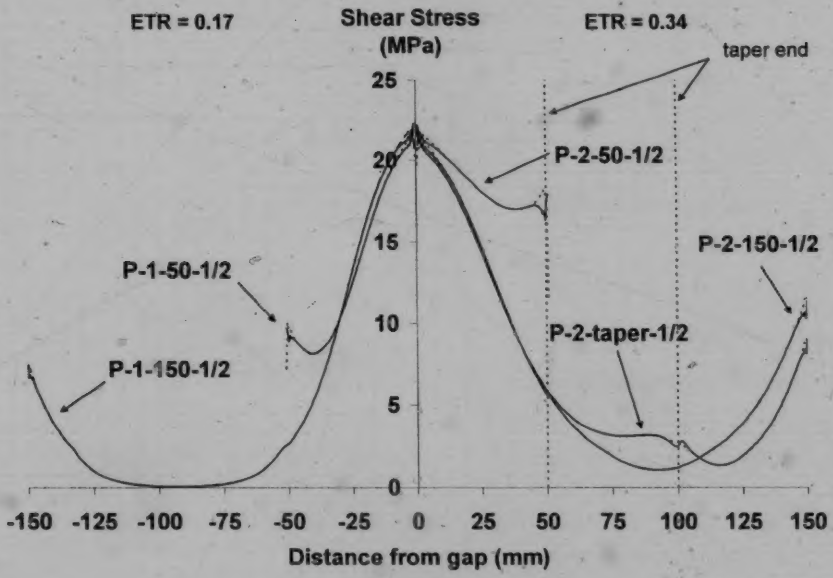

(b) Shear strain of adhesive

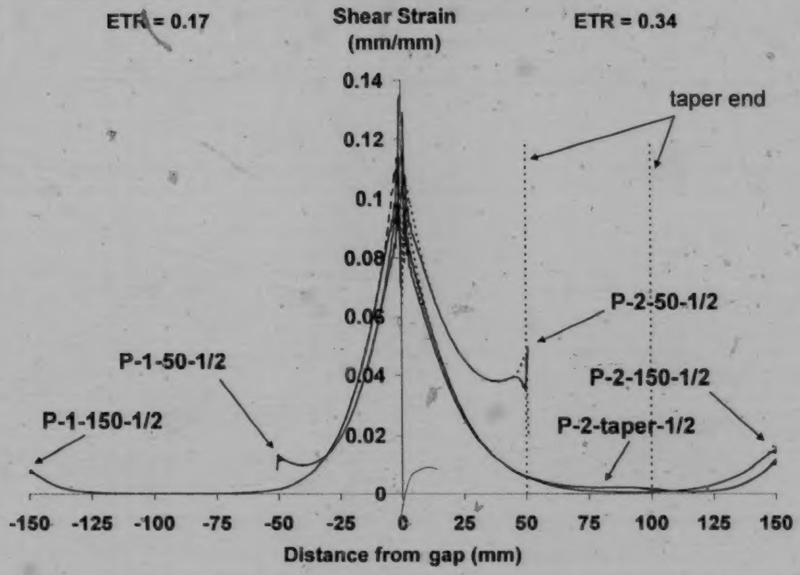

Figure 3.16 Shear stress/strain of adhesive of specimens with ETR = 0.17 and 0.34 and L_L = 50 and 150 mm

(a) Shear stress distribution of adhesive

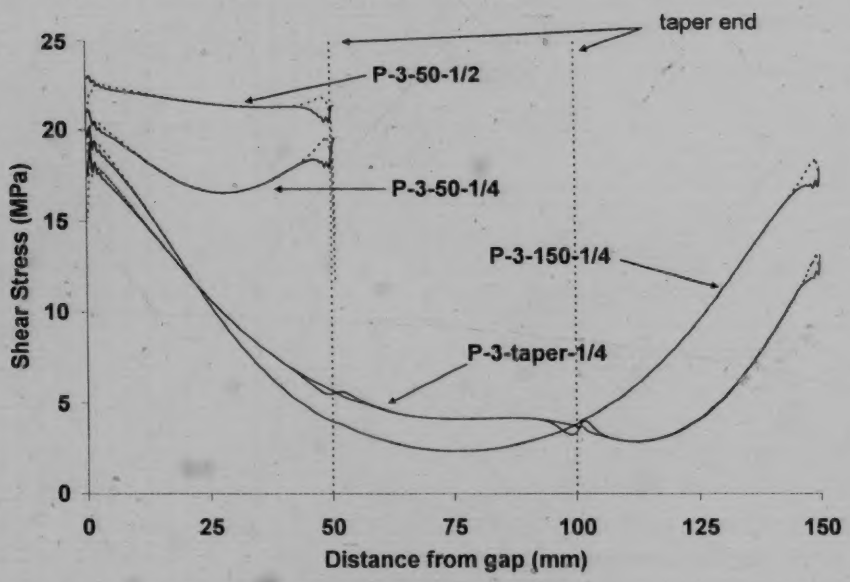

(b) Shear strain of adhesive

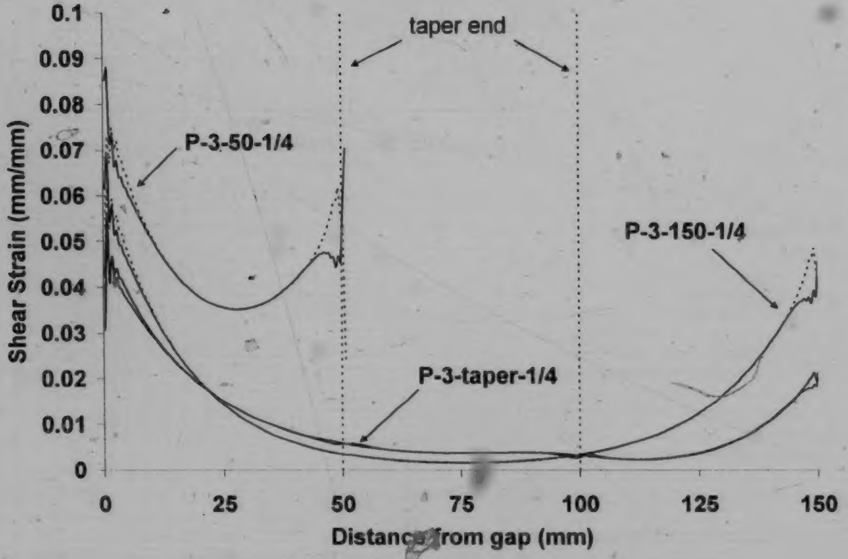

Figure 3.17 Shear stress/strain of adhesive of specimens with ETR = 1.03 and L_L = 50 and 150 mm and the shear stress of specimen P-3-50-1/2

3.8 References

ASTM A370-02. 2002. Standard Test Methods and Definitions for Mechanical Testing of Steel Products. American Society for Testing and Materials, West Conshohocken, PA, U.S.A.

ASTM D3039/3039M-00. 2000. Standard test method for tensile properties of polymer matrix composite materials. American Society for Testing and Materials, West Conshohocken, PA, U. S. A.

Bassetti, A., Colombi, P. and Nussbaumer, A., 2000. Finite element analysis of steel members repaired by prestressed composite patch, IGF 2000, XV Congresso Nazionale Del Gruppo Italiano Frattura, Bari

Goland, M. and Reissner, E. 1944. The stresses in cemented joints. Journal of Apply Mechanics, A.11, 17–27

Grant, P. 1978. Analysis of adhesive stresses in bonded joints, Symposium: Jointing in Fiber reinforced Plastics, Imperial College, London, I.P.C. Science and Technology Press Ltd, p. 41

Hart-Smith, L. J. 1973. Adhesive-bonded double-lap joints. National Aeronautics and Space Administration, CR-112235, Langley Research Centre

Hibbitt, Karlsson & Sorenson, Inc., 2004. ABAQUS Version 6.4, ABAQUS/Standard User's Manual Volumes I and II, Pawtucket, Rhode Island, U.S.A.

Kennedy, G. D. and Cheng, J. J. Roger. 1998. Repair of cracked steel elements using composite fiber patching, Structural Engineering Report No. 221, University of Alberta

Kutscha, D. and Hofor, K. E. 1969. Feasibility of joining advanced composite flight vehicle structures, AD 690616, ITT Research Inst.

Mays, G. C. and Hutchinson, A. R., 1992. Adhesive in civil engineering, Cambridge University Press

Mitsubishi Chemical Co. 1999. Carbon fiber prepreg sheet (Replark^{TM}). Available from http://www.m-kagaku.co.jp/english/aboutmcc/division/prod/carbonfiber/r-products.htm

Roberts, P.D. 1995. Crack growth retardation by carbon fiber composite patching: An application to steel pressure vessel repair. M.Sc. Thesis, Department of Mechanical Engineering, University of Alberta

Sika Carbodur Technical Data Sheet. 2003. Sika Canada Inc. http://www.sika.ca/con-tds-sikacarbodur-ca.pdf

Volkersen, O. 1938, Die Nietkraftverteilung in zugbeanspruchten Nietverbindungen mit konstanten Laschenquerschnitten, Luftfahrtforschung. 15, pp. 4–47

4 FINITE ELEMENT STUDY OF STRESS INTENSITY FACTOR OF CRACKED STEEL PLATES WITH SINGLE-SIDE CFRP PATCHING

4.1 Introduction

In the design of metal structures, such as steel structures, ductile fracture failure, which consists of exceeding the tensile strength of the material on the net section, or local or global instability of members or frames, is considered most often. However, when dealing with structures or mechanical equipment subjected to cyclic or impact loading, other modes of failure can take place at stress levels that can be substantially lower than the ultimate or yield strength of the material. These modes of failure either take the form of slow propagation of a crack under cyclic loading in a process called fatigue, or take the form of a sudden propagation of a crack when a critical stress is exceeded in a process called brittle fracture. Fracture is the result of cracks forming in a structural component either instantaneously as the stress reaches a critical value, or gradually under the action of repeated loading. In the presence of a crack, the behavior and safety of a structure or structural component can be compromised since cracks can lead to sudden fracture. The behavior of cracks in a structure is strongly dependent on the state of stress at the crack tip and ability of the material to resist propagation. Assuming a crack having a border defined by a simple curve or straight line, and crack extension in the crack plane, Irwin (1957) showed that the stress field in the region dominated by the singularity of stress can

---

[1] A version of this chapter has been prepared for publication in ASCE Journal of composites for construction.

be regarded as the sum of three invariant stress patterns taken in proportions which depend upon loads, dimensions and shape factors. The three stress patterns are due to (Figure 4.1): the opening mode (Mode I), the forward shear mode (Mode II) and the parallel or anti-plane shear mode (Mode III). An illustration of the stress field in the vicinity of a crack tip is shown in Figure 4.2. Based on the assumption that the material is linear elastic, the stress field (σ_{xx}, σ_{yy} and τ_{xy}) at the tip of a crack for Mode I fracture can be described by the following equations:

$$\sigma_{xx} = \frac{K_I}{\sqrt{2\pi r}} \cos\frac{\theta}{2}\left(1 - \sin\frac{\theta}{2}\sin\frac{3\theta}{2}\right) \tag{4.1}$$

$$\sigma_{yy} = \frac{K_I}{\sqrt{2\pi r}} \cos\frac{\theta}{2}\left(1 + \sin\frac{\theta}{2}\sin\frac{3\theta}{2}\right) \tag{4.2}$$

$$\tau_{xy} = \frac{K_I}{\sqrt{2\pi r}} \sin\frac{\theta}{2}\cos\frac{\theta}{2}\cos\frac{3\theta}{2} \tag{4.3}$$

where K_I is known as the stress intensity factor (SIF) for Mode I fracture. In general K_I is obtained from the following equation:

$$K_I = \beta\sigma\sqrt{\pi a} \tag{4.4}$$

where the geometry factor, β, accounts for factors such as the applied stress distribution, shape and location of the crack within the component and the size and shape of plate or component in which the crack is located and a is the crack length.

When composite patching is provided to the cracked surface of a steel member, the composite patching provides deformation constraint to the cracked mouth. The behavior of a patch is highly dependent on the transfer of load between the patch and adherend. This load transfer mechanism is best studied by using adhesive bonded joints. In Chapter 3, experimental study of the tensile behavior of CFRP/steel double lap joint is presented. It is shown from the experiments that load could be transferred successfully from a steel plate to a CFRP composite material through the adhesive. Therefore, it is believed that by applying CFRP patching, not only the crack mouth opening is constrained, but also the patching could help to share part of the loading. Experimental study of strain/stress distribution of cracked steel plate with single-side CFRP patching was carried out by Kennedy and Cheng (1998). The effects of single-side CFRP patching on strain/stress distribution through a cracked plate were investigated. Varying parameters such as the patch length, patch width and stiffness of patching were included. It was shown that the axial strain on the patched side was reduced significantly. However, the effect of CFRP patching on the stress intensity factor (SIF) was not studied. In this chapter, a finite element analysis was carried out to study the effect of single-side CFRP patching on the stress intensity factor (SIF) at crack tip. The results of the finite element analysis were compared to the experimental results obtained by Kennedy and Cheng (1998).

4.2 Background of Kennedy's test program

A total of ten tests were reported by Kennedy and Cheng (1998) in their test program. Of the ten specimens tested, five were bonded by CFRP patching on one side with a rectangular taper end, four were bonded by CFRP patching on one side with a mixed taper end and one served as the control specimen which was not bonded by any CFRP patching. All plate specimens were CAN/CSA-G40.21 300W steel had outside dimensions 400 mm x 750 mm and had a thickness of 6.4 mm. The gripping mechanism used in the test setup consisted of a 31.8 mm thick end plate gripped by the MTS testing machine and spliced to the specimen by two 12.7 mm thick plates at each end, as shown Figure 4.3. A uniform stress distribution was assumed to be developed across the width of the plate at a distance away from the bolted ends. A through-thickness crack of 80 mm long was saw-cut in the center of each plate. The saw-cut radiated from an 8 mm diameter hole drilled in the center of the plate. One plate was tested without CFRP patching for reference and the rest of the cracked plate specimens were patched on one side with carbon fiber sheets of various testing details. While, the total patch width was 2w, the total patch length was 2l, and the total crack length was 2a, but reference to patch dimensions is denoted by the "half-parameters"; namely, w, l, and a, as shown Figure 4.3. The x and y-axes represent the horizontal and vertical centerlines of the plate, respectively, as illustrated in the figure.

The carbon fiber sheet supplied by Mitsubishi Chemical Co. was applied to the steel plates using a hand lay-up procedure. The corresponding two-part epoxy was used as the matrix material of the CFRP and also as the adhesive between the steel plate and the CFRP. The average thickness of the CFRP was 0.23 mm/layer with an elastic modulus equal to 128,093 MPa. Six layers of carbon fiber sheet were applied to three of the specimens, providing a patch to adherend stiffness ratio, $E_{frp}t_{frp}/E_st_s$, of 0.16 where E_{frp} is the modulus of elasticity of the patch material, t_{frp} is the thickness of the patch material,

E_s is the elastic modulus of the steel material, and t_s is the thickness of the steel material. To obtain results for a different adherend stiffness ratio ($E_{frp}t_{frp}/E_st_s$ = 0.107), two specimens were patched with only four layers of fiber. Two different bond lengths (l = 30 mm and 100 mm) and three different patch widths (w = 80 mm, 120 mm and 160 mm) were studied. Three of the test patches has a 5 mm/layer (2.6^o) taper on both edges, perpendicular to the applied load. The remaining two specimens has a 3 mm/layer (4.4^o) taper on one of the edges and a 20 mm/layer (0.7^o) taper on the other, as shown in Table 4.1. The test specimens are designated with a four character label, Rwln, where R indicates a rectangular patch; w indicates the patch width (1 = 160 mm, 2 = 120 mm and 3 = 80 mm), l indicates the patch length (1 = 100 mm and 2 = 30 mm) and n is either 4 or 6 depending on the number of layers of composite applied. For example, R116 represents a specimen with 6 layers of CFRP patching and patch width and length equal to 160 mm and 100 mm, respectively. All the tension tests were conducted in the MTS 1000 machine. Each specimen was loaded at a stroke-controlled rate of 1 mm/min. A data acquisition system was used to collect the strain readings from the gauges mounted on the specimens.

4.3 Background to the development of the finite element model for cracked plates with FRP patching

In order to obtain a complete picture of the strain distribution and the stress intensity factor of the cracked steel plate with single-side CFRP patching, numerical models were developed. Chue et al. (1994) applied a 3-D finite element model to study the behavior of plates with an inclined central crack under biaxial loading repaired by patching. In the development of the 3-D finite element model, one of the challenges was to model the adhesive layer and the composite layer. Due to the very small thickness of the layers, very small elements were needed to model the adhesive and the composite layers. As a result, the computational time for the analysis was significantly increased. Sun et al. (1996) presented a simple analysis method using Mindlin plate theory in order to reduce the computational time. The researchers modeled the cracked plate and the fiber reinforced polymer (FRP) patching using the Mindlin plate elements and the adhesive layer was modeled with effective spring elements connecting the patch and the cracked plate. As the adhesive layer was modeled by spring elements, larger element size could be used for modeling the steel plate and the FRP patching so that the number of degrees of freedom could be reduced significantly. A similar plate model was also proposed by Naboulsi and Mall (1996). The only difference between the model developed by Sun et al. and the model developed by Naboulsi and Mall was that the Naboulsi and Mall modeled the adhesive layer using Mindlin plate elements (it is also known as the three layers technique). Suitable constraint conditions were applied to limit the displacement of the nodes in the cracked plate, the adhesive layer and the FRP patching layer. The numerical results obtained using Mindlin plate elements were compared with those using 3-D elements. It was shown that the three layers technique results in better prediction of SIF of the cracked plate than that obtained from the plate model with springs when compared with the 3-D finite element analysis results. Naboulsi and Mall (1996) concluded that the three layers technique provided an economic 2-D finite element model with a minimal difference to the 3-D model. Although it was shown that the 2-D three layers technique gave good predictions of SIF of the cracked plate with bonded FRP patching, the 2-D plate model could not capture the differential crack growth rate of the unpatched side and the patched side of a cracked plate with a single-side patching.

4.4 Development of a finite element model for cracked steel plates with single-side CFRP patching

In this study, the three layers technique developed by Naboulsi and Mall (1996) was used to model the test specimens which were tested by Kennedy and Cheng (1998). In the three layers finite element model, the cracked steel plate, the adhesive layer and the CFRP patching are modeled using the shell elements based on the Mindlin plate assumption. Static analysis is carried out to obtain the strain results and the SIF around the crack tip is obtained using the contour integral method. The contour integral method is an energy method employing the J-integral and is defined as (Rice 1968):

$$J = \int_{\Gamma} \left(W dy - T \frac{\delta u}{\delta x} ds\right) \tag{4.5}$$

where Γ is an arbitrary contour surrounding the crack tip as shown in Figure 4.4, W is strain energy density, T is the traction vector, u is the displacement vector and, ds is the differential distance along the contour. For a linear elastic condition, the J-integral is proportional to the square of the stress intensity factor (K_I). For plane stress conditions, the stress intensity factor (K_I) can be predicted by

$$K_I = \sqrt{JE} \tag{4.6}$$

where E is the elastic modulus of the material. Since Mindlin plate elements are used to model the cracked steel plate, it is assumed that the SIF varies linearly through the thickness of the plate. With this assumption, the SIF of the unpatched side and patched side can be obtained. The equations for evaluating the SIF of the unpatched side and patched side are shown in the following section. In order to examine this assumption, a modified three layers model with the cracked steel plate being modeled using 3-D brick elements, and the adhesive layer as well as the CFRP patching using shell elements based on the Mindlin plate assumption are proposed. There are two advantages in using the modified three layers model. Firstly, since only the cracked plate is modeled by 3-D brick elements and the adhesive layer and CFRP patching modeled by shell elements, the computational and modeling time is reduced significantly compared to a traditional 3-D model with the cracked plate, adhesive layer and CFRP patching being modeled by 3-D elements. Secondly, as the cracked steel plate is modeled using the 3-D brick elements, the SIF around the crack tip through the thickness of the plate can be directly obtained from the analysis results. In the following section, cracked steel plates with a single-side CFRP patching are modeled by the three layers technique and the modified three layers models. The SIFs of the patched side and the unpatched side are predicted assuming that the SIF varies linearly through the thickness of the plate for the three layers model. Then, the SIFs of the patched side and unpatched side of the three layers model are compared with the SIF results obtained from the modified three layers model. The effects of various patch parameters on the SIF at the patched and the unpatched side are discussed based on the results of the modified three layers model.

4.4.1 Three layers model

The three layers technique was used to model the test specimens using the finite element program ABAQUS Version 6.4-1 (Hibbitt et al. 2004). Eight node shell elements (S8R, 8 nodes general purpose shell element in ABAQUS) were used in the modeling and the model represents one quarter of a patched plate with an internal through-thickness crack. A typical finite element model of the steel plate with the adhesive layer and the CFRP patching is shown in Figure 4.5. Due to the singularity properties of stress and strain at the crack tip, collapsed node elements were used at the crack tip to simulate the singularity properties of stress and strain around the crack tip numerically. As shown in Figure 4.5, three of the nodes of the original eight nodes element are collapsed at the crack tip and two mid nodes are moved to the quarter point of the sides. With such arrangement of the nodes, singularity properties of strain exist within the elements (Barsoum 1976). Therefore, the singularity properties of stress and strain can be captured by the collapsed node elements around the crack tip. In general, the shell element is assigned to represent the mid-plane of the corresponding plate. In this study, since a tapered end condition is used in the CFRP patching of the test specimens, the reference face of the patching is set at the bottom face of the patching in the finite element model by including a parameter "offset = -0.5" in the command statement "*Shell section" in the input file of ABAQUS. Hence, different thicknesses can be assigned to different layers of the CFRP patching. The reference faces for the adhesive layer and steel plate layer are set at the mid-plane of the plate in the through thickness direction. Illustrations of the shell elements for modeling the CFRP patching, the adhesive layer and the steel plate are shown in Figure 4.6. Constraints are used to enforce compatibility between the plate-adhesive and the adhesive-CFRP patching interface based on Mindlin assumptions. The Mindlin plate theory (Timoshenko and Woinowsky-Kriege 1959) assumes a linear displacement field in the plate thickness and allows for the transverse shear deformation of the plate. In the three layers technique proposed by Naboulsi and Mall (1996), the cracked plate layer, the adhesive layer and the CFRP patching layer are assumed to have a linear displacement field across the thickness which satisfy the following relations:

$$u_{frp} = \bar{u}_{frp} + \varphi_{frp}^{y} z_{frp} \qquad u_a = \bar{u}_a + \varphi_a^{y} z_a \qquad u_s = \bar{u}_s + \varphi_s^{y} z_s \qquad (4.7\ a, b, c)$$

$$v_{frp} = \bar{v}_{frp} + \varphi_{frp}^{x} z_{frp} \qquad v_a = \bar{v}_a + \varphi_a^{x} z_a \qquad v_s = \bar{v}_s + \varphi_s^{x} z_s \qquad (4.8\ a, b, c)$$

$$w_{frp} = \bar{w}_{frp} \qquad w_a = \bar{w}_a \qquad w_s = \bar{w}_s \qquad (4.9\ a, b, c)$$

where $\bar{u}, \bar{v}, \bar{w}$ are the mid-plane displacements along the x, y and z directions (x and y are in the plane of the plate and z is in the thickness direction), respectively, φ^x, φ^y are the rotations of the cross section along the x and y axis. The subscript symbols frp, a, and s are used to denote the composite patching, the adhesive, and the steel plate, respectively. The symbols representing the longitudinal displacements in the x-direction and the rotations are also shown in Figure 4.6. According to Naboulsi and Mall (1996), at the plate-adhesive interface where the z co-ordinates for the cracked plate and the adhesive are equal and at the adhesive-composite patching interface where the z co-ordinates for the adhesive and the composite patching are equal, the displacement field's equations reduce to:

$$u_{frp} = u_a \qquad v_{frp} = v_a \qquad w_{frp} = w_a \qquad (4.10\ a, b, c)$$

$$u_a = u_s \qquad v_a = v_s \qquad w_a = w_s \qquad (4.11\ a, b, c)$$

Therefore, for the plate-adhesive interface, the relationships between the mid-plane displacements are:

$$\bar{u}_s - \bar{u}_a - \varphi_a^y \frac{t_a}{2} - \varphi_s^y \frac{t_s}{2} = 0 \quad \text{and} \quad \bar{v}_s - \bar{v}_a - \varphi_a^x \frac{t_a}{2} - \varphi_s^x \frac{t_s}{2} = 0 \qquad (4.12\ a, b)$$

For the composite-adhesive interface, the relationships between the mid-plane displacements are:

$$\bar{u}_a - \bar{u}_{frp} - \varphi_{frp}^y \frac{t_{frp}}{2} - \varphi_a^y \frac{t_a}{2} = 0 \quad \text{and} \quad \bar{v}_a - \bar{v}_{frp} - \varphi_{frp}^x \frac{t_{frp}}{2} - \varphi_a^x \frac{t_a}{2} = 0 \qquad (4.13\ a, b)$$

However, it has been mentioned that the reference face for the composite is at the bottom face location, the relationship between the displacements of mid-plane and the bottom face of the composite are:

$$u^b_{frp} = \bar{u}_{frp} + \varphi^y_{frp}\frac{t_{frp}}{2} \qquad \text{and} \qquad v^b_{frp} = \bar{v}_{frp} + \varphi^x_{frp}\frac{t_{frp}}{2} \qquad (4.14\text{ a, b})$$

where u^b_{frp} and v^b_{frp} are the displacement of bottom face of the composite patching. Therefore, for the composite-adhesive interface, the displacement relationships become:

$$\bar{u}_a - u^b_{frp} - \varphi^y_a\frac{t_a}{2} = 0 \qquad \text{and} \qquad \bar{v}_a - v^b_{frp} - \varphi^x_a\frac{t_a}{2} = 0 \qquad (4.15\text{ a, b})$$

Symmetric boundary conditions are applied to the edges. According to the test set up, the steel plate was connected to two splice members at both ends by bolting and the splice members were connected to the MTS machine. Since the thickness of each splice member is two times the thickness of the tested steel plates, therefore, rotational and out of plane displacements were assumed to be restrained at the loading edge of the steel plate in the finite element models. Suitable axial displacement was applied to the loading edge so that a far end mean axial stress in the steel plate of 100 MPa was obtained.

The material properties which are shown in Table 4.2 (Kennedy and Cheng 1998) are used in the finite element analysis. The thickness of the steel plate (t_s), the adhesive layer (t_a), and the CFRP patching (t_{frp}) are 6.35 mm, 0.06 mm and 0.23 mm/ply, respectively. Static analysis is carried out to obtain the strain distributions and the SIF is obtained using the contour integral function in ABAQUS. This SIF represents the SIF value of the mid-plane of the cracked steel plate. The SIF of the unpatched side and patched side are calculated assuming that the SIF varies linearly across the thickness of the plate as mentioned above. In addition, the SIF is assumed to be linearly proportional to the deformation of the steel plate near the crack tip. The longitudinal displacement of the steel plate and the rotation of the nearest node to the crack tip are obtained from the finite element analysis. Since this longitudinal displacement represents the displacement of the mid-plane of the plate, the longitudinal displacement of the patched side (u_p) and unpatched side (u_f) of the plate is evaluated using the following relations:

$$u_p = u_m - \frac{t_s \varphi_m}{2} \quad \text{and} \quad u_f = u_m + \frac{t_s \varphi_m}{2} \tag{4.16 a, b}$$

where u_m and φ_m are the longitudinal displacement and rotation of the nearest node to the crack tip of reference plane as shown in Figure 4.7 and t_s is the thickness of the plate. It is assumed that the SIF varies linearly across the thickness and is proportional to the longitudinal displacement. Therefore, with the SIF of the mid-plane of the cracked plate (K_m), the SIF of the patched face (K_p) and unpatched face (K_f) are:

$$K_p = K_m\left(\frac{u_p}{u_m}\right) = K_m\left(1 - \frac{t_s \varphi_m}{2u_m}\right) \quad \text{and} \quad K_f = K_m\left(\frac{u_f}{u_m}\right) = K_m\left(1 + \frac{t_s \varphi_m}{2u_m}\right) \tag{4.17 a, b}$$

4.4.2 The modified three layers model

In the three layers finite element model discussed above, a linear relationship relating the SIF to the longitudinal displacement near the crack tip was assumed in the prediction of the SIF of the unpatched and the patched side of the cracked plate. In order to examine this assumption, a modified three layers finite element model is proposed. The modified model uses 3-D brick elements to model the cracked plate and shell elements to model both the CFRP patching and the adhesive layer. Since the cracked plate is modeled by the 3-D brick elements, the SIF at the crack tip through the thickness direction can be obtained numerically. A typical 3-D brick element (C3D20, 20 nodes brick element in ABAQUS) model is shown in Figure 4.8. As shown in the figure, the 3-D brick elements with collapsed nodes are assigned at the crack tip location. The SIFs at the crack tip through the thickness direction of the plate are obtained using the contour integral function in the ABAQUS program. The boundary conditions and material properties used in the three layers model are also applied to the modified three layers model. Similar to the three layers model, the reference faces for the adhesive layer are set at the mid-plane of the plate in the through thickness direction and the reference face for the composite is at the bottom face location. Therefore, the displacement constraints used in the three layers model are also applied to the modified three layers model to enforce the compatibility along the adhesive-CFRP patching interface. Since the 3-D brick elements are used to model the steel plate, the displacements of the nodes on the patched side of the steel plate are made compatible with the displacement of the nodes of the adhesive layer as follows:

$$u_s{}^T - \bar{u}_a - \varphi_a^y \frac{t_a}{2} = 0 \qquad \text{and} \qquad v_s{}^T - \bar{v}_a - \varphi_a^x \frac{t_a}{2} = 0 \qquad (4.18\text{ a, b})$$

where $u_s{}^T$ and $v_s{}^T$ are the displacements of the patched side of the steel plate and the description of $u_s{}^T$ is shown schematically in Figure 4.9.

4.5 Discussion of the strain results and crack opening displacement

In the finite element analysis, the tapered end of all the specimens with CFRP patched are modeled with rectangular tapered end. As shown in Table 4.3, the first four characters of the FE models' designation are assigned in the same format as that of the test specimens. The strain results obtained from the two types of finite element models at the section of the crack level of steel plate with CFRP patching (R116FE) and plain steel specimen are compared with the test data as shown in Figure 4.10 and Figure 4.11. The axial strain results obtained from the two types of finite element model compare well with the test data and the strain results obtained from the three layers shell model are similar to those obtained from the modified three layers model. As can be seen from the figures, for the cracked steel plates with single-side CFRP patching, the strains near the crack tip on the patched side are reduced effectively. On the other hand, the strains on the unpatched side of specimen R116 are increased. This increase is due to the bending of the plate caused by the unsymmetrical CFRP patching. Comparison of axial strain of the modified three layers model results and test results of other four specimens (R224FE, R324FE, M216FE and M316FE) are shown in Figure 4.12 to Figure 4.15.

The deformed shapes at the crack level of the three layer model and the modified three layer model (R116FE corresponds to specimen R116) are shown Figure 4.16 (the patching is not shown in the figure for clarity). It can be seen from the figure that the displacement of the three layers model is close to the mid-plane displacement of the modified three layers model. In addition, the crack opening displacement of the three layer model of the patched side (u_p) and the unpatched side (u_f) based on the linear assumption according to Eqs. 4.16a and 4.16b are shown in the same figure. Compared to the results of the modified three layer model, it is shown that Eqs. 4.16a and 4.16b overestimate the crack opening displacement on the patched side and underestimate the displacement on the unpatched side by 6% and 3%, respectively.

4.6 Discussion of the SIF based on the modified three layers model and the three layers model

The crack opening displacements of the patched side and the unpatched side of the three layers model predicted by Eqs. 4.16a and 4.16b are shown to be close to the results of the modified three layers model. In this section, the prediction of the SIF of the three layers model according to Eqs. 4.17a and 4.17b are compared to the results from the modified three layers model. The SIFs at the crack tip across the thickness of the steel plate of R116FE of the three layers model and the modified three layers model together with the SIF of the plain steel model are shown in Figure 4.17. For the plain steel model, the brick model gives almost the same value of SIF as that of the three layers model on the unpatched surface, but a slightly higher value of SIF is observed for the region across the thickness of the plate. This higher value of SIF is expected due to the presence of a plane strain condition in that region. Figure 4.17 also shows that the SIF reduces significantly on the patched side, but increases slightly on the unpatched side when comparing the SIF of the plain steel model to that of both models with single-side CFRP patching. In addition, the modified three layers model gives a slightly smaller value of SIF when compared to that of the three layers model on the patched side, but a higher value of SIF is observed on the unpatched side for the modified three layers model. In general, the three layers model underestimates the SIF across the thickness of the plate when compared to those of the modified three layers model.

The results of the SIF obtained from both the three layers model and the modified three layers model and the SIF_{3-D} / SIF_{3-L} ratios are shown in Table 4.3. With the finite element results of the modified three layers model as a reference, it is shown in the table that the three layers model overestimates the SIF on the patched side of the plate and underestimates the SIF on the unpatched side by about 10% on average. It is shown from the results of the modified three layers model (Figure 4.17) that the SIF varies non-linearly through the thickness of the crack tip, and the predictions of SIF based on the three layers model on the patched side and the unpatched side cannot reflect the SIF variation through the thickness properly. Therefore, even though the SIF obtained from the three layers model gives a slightly conservative prediction on the patched side, it is suggested that the modified three layers model should be adopted when evaluating the through thickness SIF of cracked steel plate with single-sided patching.

4.7 Effect of patching parameters on the SIF of a cracked steel plate with a single-side CFRP patching

The effect of patching parameters on the SIF is shown in Table 4.4 and Figure 4.18. The SIF ratios as shown in the table represent the ratio of the SIF based on the modified three layers model ($SIF_{3\text{-}D}$) to the SIF based on the plain steel model (SIF_{steel}). The SIF ratios of the patched side vary from 0.37 to 0.50, whereas the ratios for the unpatched side vary from 1.11 to 1.18. Hence, it is shown that the CFRP patching can reduce the SIF of the patched side of the cracked plate substantially. The effect of patch length on the SIF is obtained, for example, by comparing the SIF results of models R116FE, R216FE and R316FE. It is shown that when the patch width decreases from 160 mm to 80 mm, the ratio of SIF only increases from 0.38 to 0.42 on the patched side and decreases from 1.14 to 1.12 on the unpatched side, respectively. Therefore, the SIF on the patched side slightly decreases with decreasing patch width. Similar behaviour is observed for models with 4 layers of CFRP patching. For the effect of patch length, it is shown that by increasing the patch length from 30 mm (R226FE) to 100 mm (R216FE), the ratio of the SIF on the patched side increases from 0.37 to 0.40, but decreases from 1.18 to 1.13 on the unpatched side, respectively. A magnified displacement at the crack position of models R226FE and R216FE with patch length equal to 30 mm and 100 mm, respectively, is shown in Figure 4.19. The figure shows that the model with shorter length of CFRP patching provided relatively stiffer localized constraint to the crack on the patched side than to the unpatched side. As a result, the SIF of the patched side is reduced more than that of the unpatched side for the model with shorter patch length. Although more reduction of the SIF on the patched side can be achieved by increasing the patch width and/or reducing the patch length, the SIF on the unpatched side will also be increased. In addition, for the models studied, it is also shown that the patch width and patch length have only a marginal effect on the SIF. However, the effect of the number of layers of CFRP patching on the reduction of the SIF is more pronounced. Table 4.4 shows that the average SIF ratio is 0.39 (representing a 61% decrease) for specimens with 6 layers of CFRP patching and 0.47 (representing a 53% decrease) for specimens with 4 layers of CFRP patching. In addition, the SIF on the unpatched side of the cracked plate is on average about 14% higher than that of the plain steel model. A summary of the ratio of SIF is shown in Figure 4.20. Compared the SIF of the plain steel model to the model with CFRP patching, in general, the reduction of the SIF on the patched side for models with 6 layers of CFRP patching is about 20% more than that for models with 4 layers of CFRP patching.

In the test program, tapered end of CFRP patching was designed for all the specimens with CFRP patching. Study of the effect of the tapered end of CFRP patching on the SIF was carried out numerically. The modified three layers model of the specimens was used by assigning equal thickness to the shell elements of the CFRP patching. Hence, the thickness of CFRP patching is constant along the patch length in order to form a non-tapered end. The SIF results of specimens with and without tapered end are compared and shown in Table 4.5. It is shown that for models with non-tapered end of CFRP patching, SIF increases about 4 to 5% on the patched side and 3 to 4% on the unpatched side when compared to the results of the models with the tapered end of CFRP patching. Hence, it is shown that the effect of tapered end of CFRP patching on the SIF is also marginal.

However, it is recommended that tapered end patching should be used not only to reduce the stress concentration at the end of the patching, but also to reduce the shear stress of the adhesive at the end of the patching.

4.8 Summary and conclusions

In this chapter, a finite element model was developed and used for the analysis of the result from specimens tested by Kennedy and Cheng (1998). The three layers model (shell elements with Mindlin plate assumptions were used to model the cracked steel plate, the adhesive layer and the CFRP patching) and a modified three layers model are proposed in this study (shell elements with Mindlin plate assumptions were used to model the adhesive layer and the CFRP patching and 3D brick elements were used to model the cracked steel plates) were used to examine the strain distributions in the vicinity of the crack. In general, the strain distributions of the specimens were predicted well by the finite element analyses using either model. An investigation of the stress intensity factors (SIFs) of cracked steel plates with single-side CFRP patching was subsequently conducted based on the calibrated finite element models. It should be noted that a linear relationship of SIF through the plate thickness was assumed in the three layers model, whereas the SIF through the thickness of the plate of the modified three layers model could be obtained numerically since 3D brick elements were used to model the cracked steel plate. The SIF results obtained from the three layers model and the modified three layers model were compared and the results showed that the three layers model overestimated the SIF on the patched side and underestimated the SIF on the unpatched side by about 10% on average compared to those of the modified three layers model. It was also observed that the modified three layers model was capable of capturing the nonlinear SIF variation through the thickness of a cracked steel plate with single-side patching.

Based on the finite element analysis results of the modified three layers model, it is shown that the patch width, the patch length, as well as the tapered and non-tapered end conditions of patching had only marginal effect on the SIF. On the other hand, the effect of the number of layers of CFRP patching on the reduction of SIF was more pronounced. Compared to the plain steel plate model, the finite element results of SIF showed that, an average, the reduction of SIF on the patched side was about 61% for specimens with 6 layers of CFRP patching and 53% for specimens with 4 layers of CFRP patching. However, the presence of the single-side CFRP patching caused the SIF of the unpatched side to increase by about 14% compared to that of the plain steel model. It was observed that this increase of SIF only localized on the unpatched side, and in general a significant reduction of SIF at the crack tip through the plate thickness was observed.

Table 4.1 Summary of test specimen variables (Kennedy and Cheng 1998)

Specimen	Width w (mm)	Length L (mm)	Layer n	Taper (mm)		Shape of patching
				Top	Bottom	
Unpatched	---	---	---	---	---	---
R116	160	100	6	5	5	Rectangular
M216	120	100	6	5	5	Mixed
M214	120	100	4	5	5	Mixed
M316	80	100	6	5	5	Mixed
M314	80	100	4	5	5	Mixed
R226	120	30	6	3	20	Rectangular
R224	120	30	4	5	5	Rectangular
R326	80	30	6	5	5	Rectangular
R324	80	30	4	3	20	Rectangular

Table 4.2 Material properties of steel plate, adhesive and CFRP plate for finite element modeling (Kennedy and Cheng 1998)

Steel plate	Elastic modulus	$E_s =$	200000 MPa
	Poisson's ratio	$\nu_s =$	0.3
Adhesive	Elastic modulus	$E_a =$	3000 MPa
	Poisson's ratio	$\nu_a =$	0.34
CFRP composite	Longitudinal elastic modulus	$E_{frp1} =$	128093 MPa
	Transverse elastic modulus	$E_{frp2} =$	6900 MPa
	Poisson's ratio	$\nu_{frp} =$	0.17
	Shear modulus	$G_{frp} =$	4480 MPa

Table 4.3 SIF results of the three layers model and the modified three layers model

Specimens	Width w (mm)	Length l (mm)	Layer n	Taper (mm)	Three layers model SIF (K) MPa $\sqrt{m}$		Modified three layers model SIF (K) MPa $\sqrt{m}$		SIF $_{3\text{-}D}$ / SIF $_{3\text{-}L}$	
					Patch	Unpatch	Patch	Unpatch	Patch	Unpatch
Plain Steel	---	---	---	---	36.71	36.71	36.59	36.59	1.00	1.00
R116FE	160	100	6	5	15.25	37.31	13.99	41.65	0.92	1.12
R216FE	120	100	6	5	15.90	37.02	14.58	41.24	0.92	1.11
R316FE	80	100	6	5	16.89	37.00	15.50	41.01	0.92	1.11
R226FE	120	30	6	3	14.79	38.62	13.48	43.01	0.91	1.11
R326FE	80	30	6	5	15.60	38.03	14.05	42.47	0.90	1.12
R214FE	120	100	4	5	18.74	37.73	17.32	40.76	0.92	1.08
R314FE	80	100	4	5	19.76	38.06	18.12	40.57	0.92	1.07
R224FE	120	30	4	5	18.10	39.28	16.34	42.12	0.90	1.07
R324FE	80	30	4	3	18.55	39.03	16.85	41.71	0.91	1.07
								Average	**0.91**	**1.10**

Table 4.4 Ratio of SIF value of the modified three layers model to the plain steel model

Specimens	Width w (mm)	Length l (mm)	Layer n	Taper (mm)	Modified three layers model SIF (K) MPa √m		SIF $_{3\text{-D}}$ / SIF $_{\text{steel}}$	
					Patch	Unpatch	Patch	Unpatch
Plain Steel	---	---	---	---	36.59	36.59	1.00	1.00
R116FE	160	100	6	5	13.99	41.65	0.38	1.14
R216FE	120	100	6	5	14.58	41.24	0.40	1.13
R316FE	80	100	6	5	15.50	41.01	0.42	1.12
R226FE	120	30	6	3	13.48	43.01	0.37	1.18
R326FE	80	30	6	5	14.05	42.47	0.38	1.16
				Average	**14.32**	**41.88**	**0.39**	**1.15**
R214FE	120	100	4	5	17.32	40.76	0.47	1.11
R314FE	80	100	4	5	18.12	40.57	0.50	1.11
R224FE	120	30	4	5	16.34	42.12	0.45	1.15
R324FE	80	30	4	3	16.85	41.71	0.46	1.14
				Average	**17.16**	**41.29**	**0.47**	**1.13**

Table 4.5 SIF results of FE models with tapered and non-tapered end of CFRP pathcing

Specimens	Width w (mm)	Length l (mm)	Layer n	Non-taper end SIF (K) MPa √m		Taper end SIF (K) MPa √m		Non-taper / Taper	
				Patch	Unpatch	Patch	Unpatch	Patch	Unpatch
R116FE	160	100	6	14.60	42.99	13.99	41.65	1.04	1.03
R216FE	120	100	6	15.32	42.86	14.58	41.24	1.05	1.04
R316FE	80	100	6	16.23	42.52	15.50	41.01	1.05	1.04
R226FE	120	30	6	14.08	44.24	13.48	43.01	1.04	1.03
R326FE	80	30	6	14.72	43.59	14.05	42.47	1.05	1.03
							Average	**1.05**	**1.03**
R214FE	120	100	4	18.03	42.20	17.32	40.76	1.04	1.04
R314FE	80	100	4	18.87	42.04	18.12	40.57	1.04	1.04
R224FE	120	30	4	16.97	43.42	16.34	42.12	1.04	1.03
R324FE	80	30	4	17.53	42.96	16.85	41.71	1.04	1.03
							Average	**1.04**	**1.04**

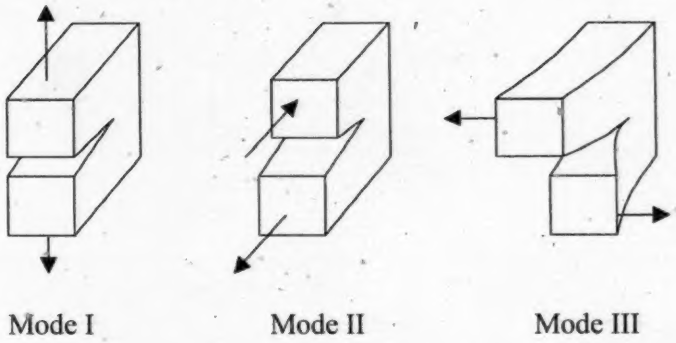
Mode I
Mode II
Mode III

Figure 4.1 Three modes of stress pattern that can be applied to a crack

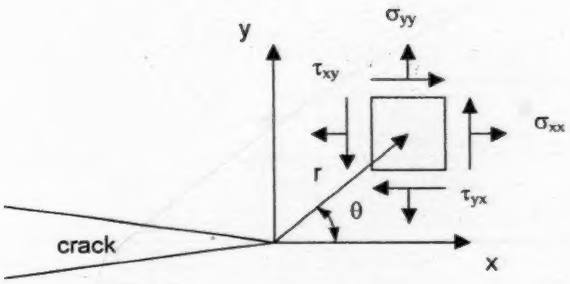
y
σyy
τxy
σxx
r
θ
τyx
crack
x

Figure 4.2 The stress field in the vicinity of a crack tip

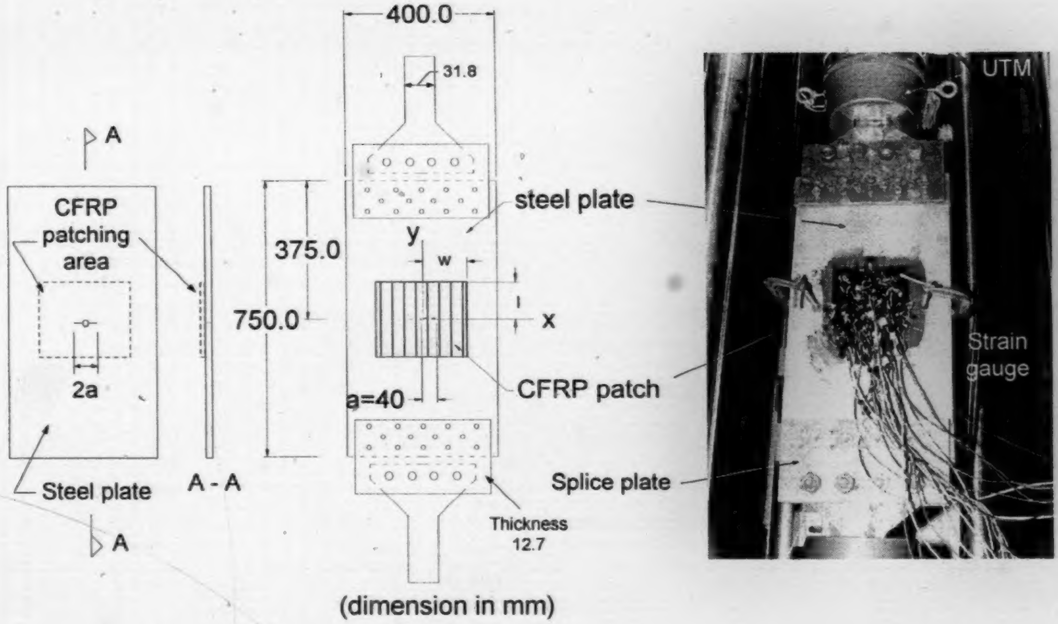
A
CFRP patching area
2a
Steel plate
A
A - A
375.0
750.0
400.0
31.8
steel plate
y
w
l
x
CFRP patch
a=40
Splice plate
Thickness 12.7
(dimension in mm)
UTM
Strain gauge

Figure 4.3 Test setup and a typical gauged specimen tested by Kennedy and Cheng (1998)

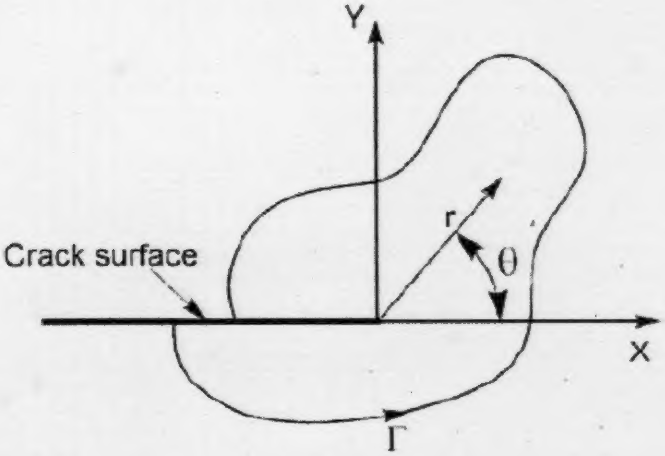
Y
X
Crack surface
r
θ
Γ

Figure 4.4 Crack tip coordinates and typical contour Γ

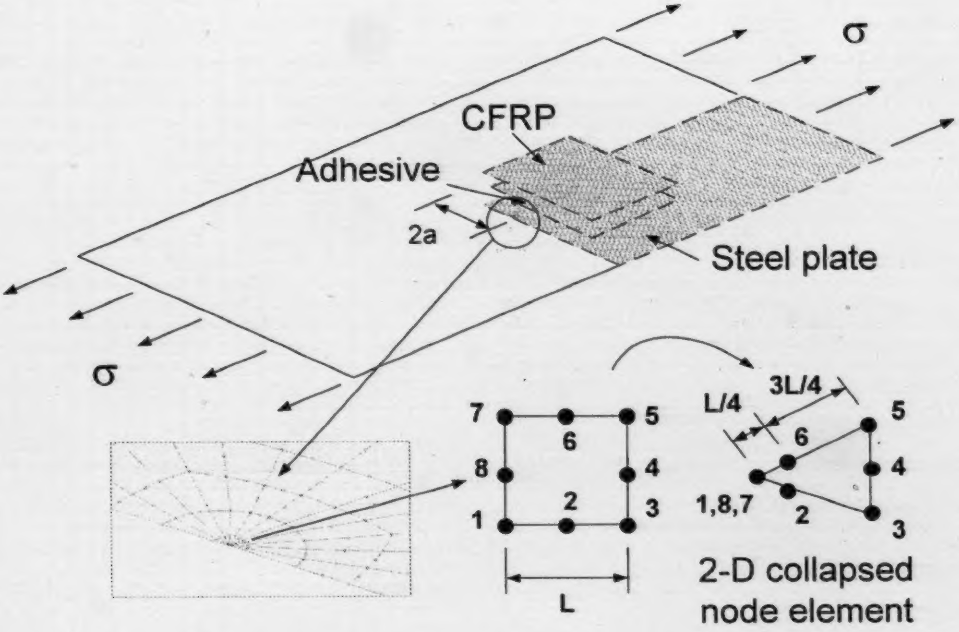
σ
CFRP
Adhesive
2a
Steel plate
σ
7
6
5
8
4
1
2
3
L
L/4
3L/4
5
6
4
1,8,7
2
3
2-D collapsed
node element

Figure 4.5 Three layers finite element model

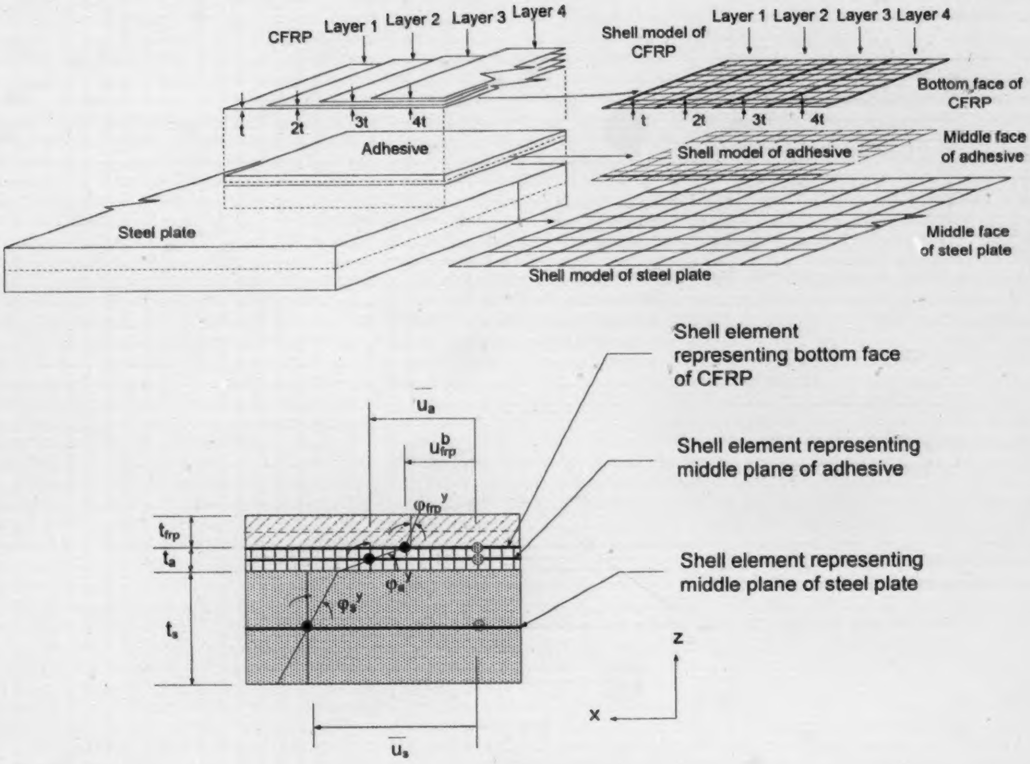
CFRP
Layer 1
Layer 2
Layer 3
Layer 4
t
2t
3t
4t
Adhesive
Steel plate
Shell model of CFRP
Layer 1
Layer 2
Layer 3
Layer 4
Bottom face of CFRP
t
2t
3t
4t
Shell model of adhesive
Middle face of adhesive
Middle face of steel plate
Shell model of steel plate
Shell element representing bottom face of CFRP
Shell element representing middle plane of adhesive
Shell element representing middle plane of steel plate
$\overline{u_a}$
u_{frp}^b
φ_{frp}^y
φ_a^y
φ_s^y
t_{frp}
t_a
t_s
$\overline{u_s}$
z
x

Figure 4.6 Illustration of the three layers finite element model and the displacement relationship along the x-direction

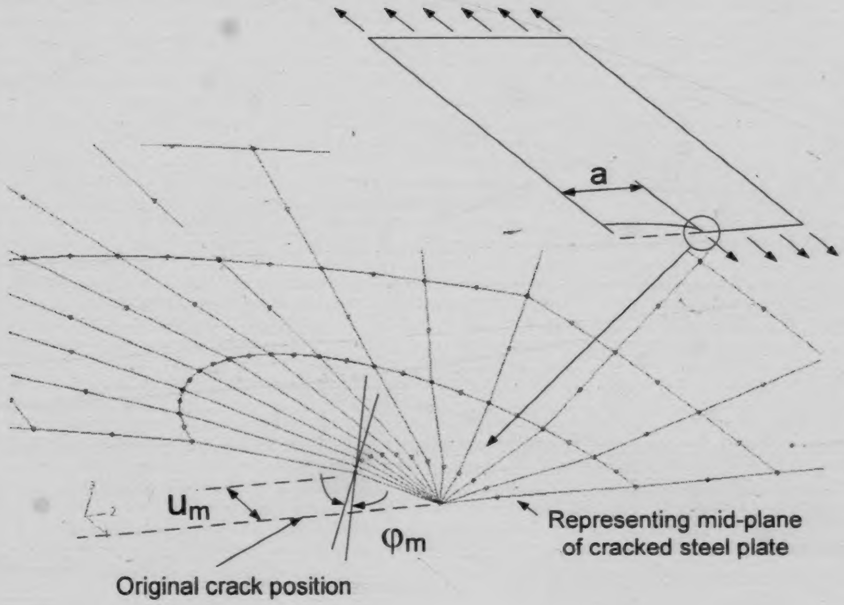
a
u_m
φ_m
Representing mid-plane of cracked steel plate
Original crack position

Figure 4.7 Longitudinal displacement and rotation of nearest node to the crack tip of the three layers model

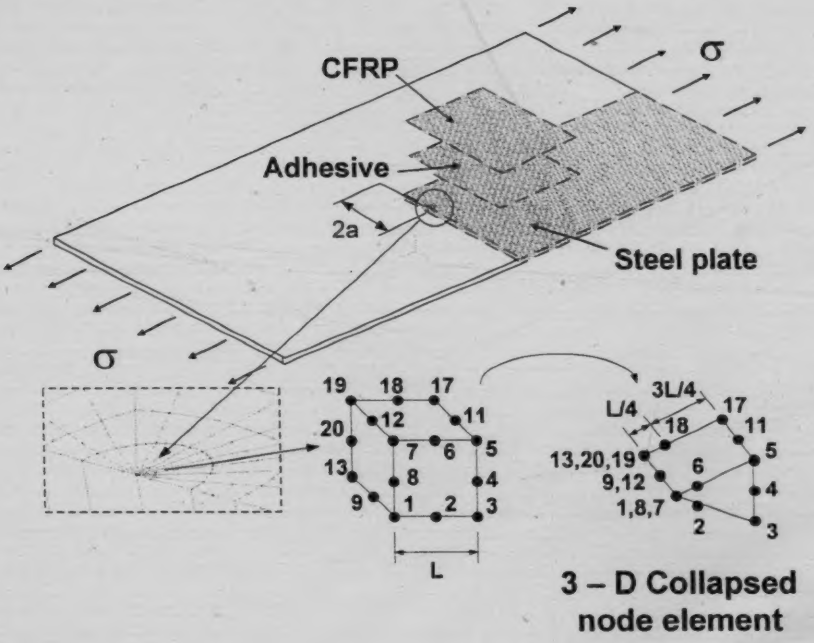
CFRP
Adhesive
2a
Steel plate
σ
σ
19
18
17
12
11
20
7
6
5
13
8
4
9
1
2
3
L
3L/4
L/4
17
18
11
13,20,19
6
5
9,12
4
1,8,7
2
3
3 – D Collapsed node element

Figure 4.8 The modified three layers model (3-D brick and shell model)

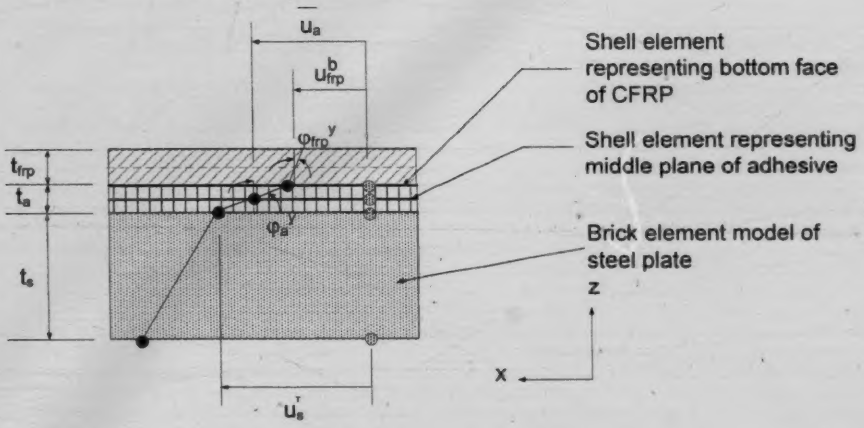
$\overline{u}_a$
u_{frp}^{b}
φ_{frp}^{y}
φ_{a}^{y}
t_{frp}
t_a
t_s
u_s^{τ}
Shell element representing bottom face of CFRP
Shell element representing middle plane of adhesive
Brick element model of steel plate
z
x

Figure 4.9 Displacement relationship of the modified three layers model along the x-direction

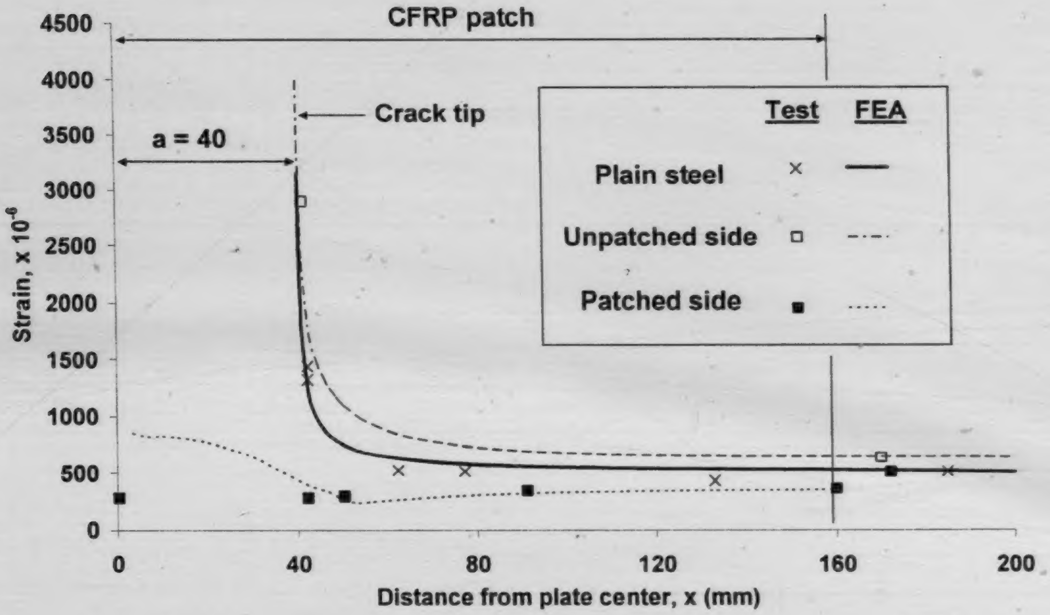

Figure 4.10 Comparison of strain results of three layer model and specimen R116

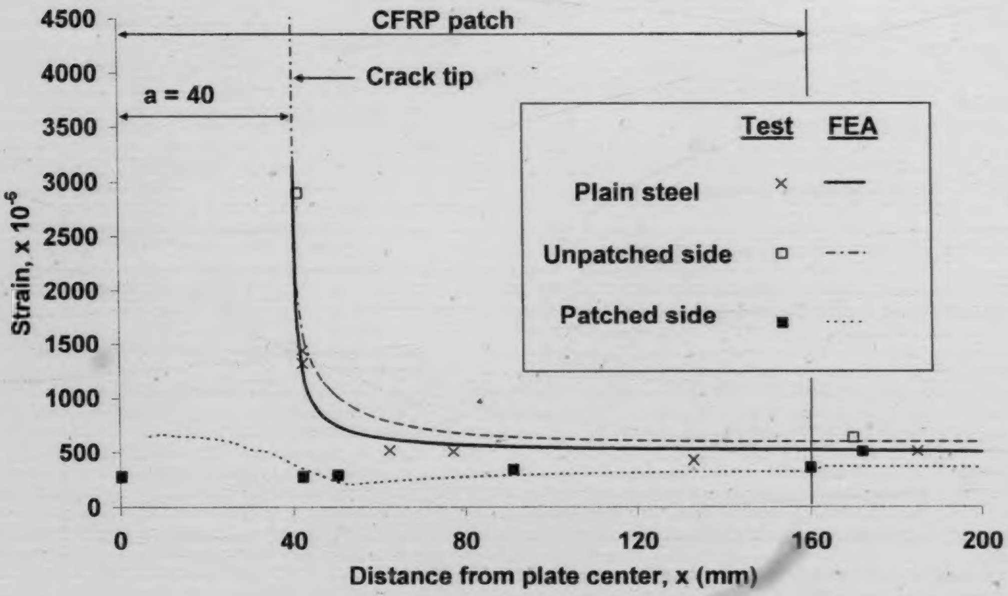

Figure 4.11 Comparison of strain results of the modified three layers model and specimen R116

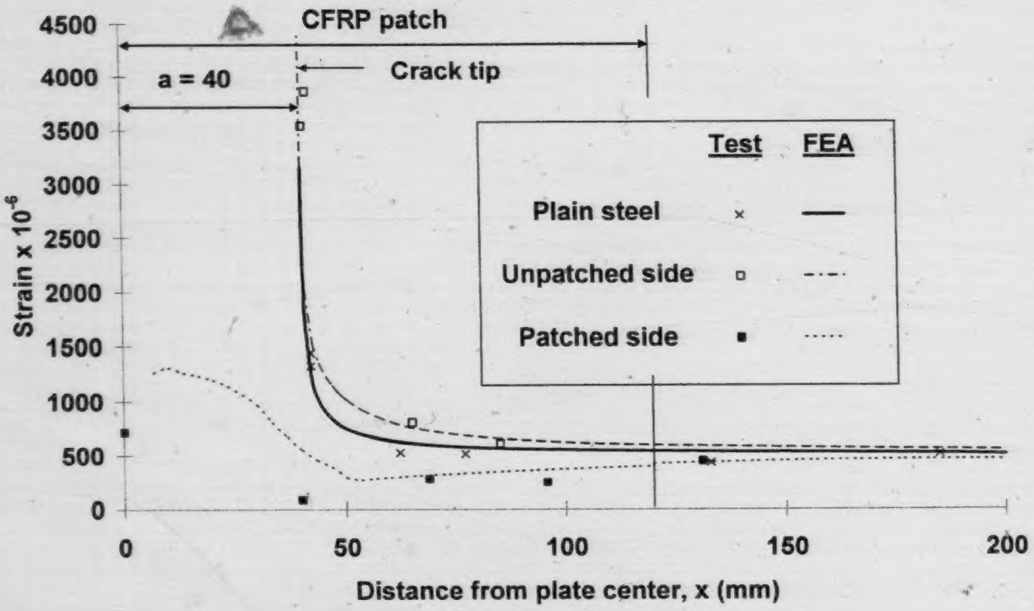

Figure 4.12 Comparison of strain results of the modified three layers model and specimen R224

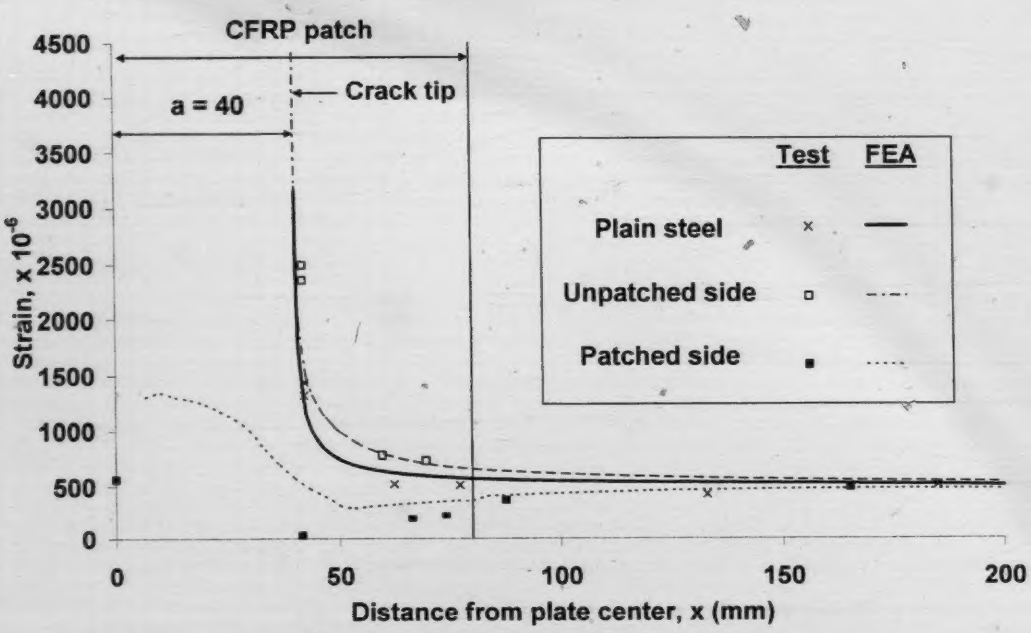

Figure 4.13 Comparison of strain results of the modified three layers model and specimen R324

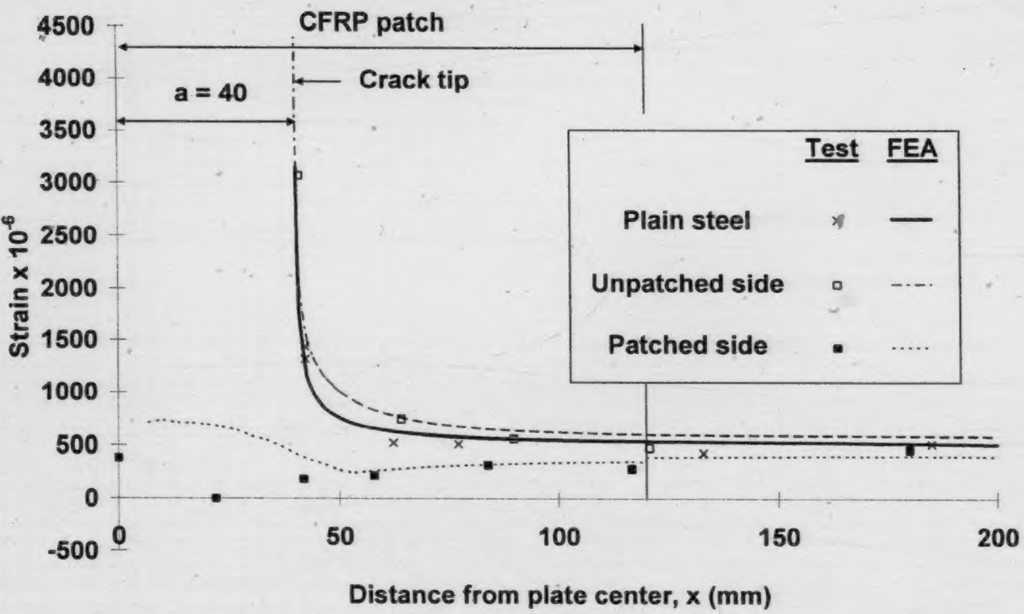

Figure 4.14 Comparison of strain results of the modified three layers model and specimen M216

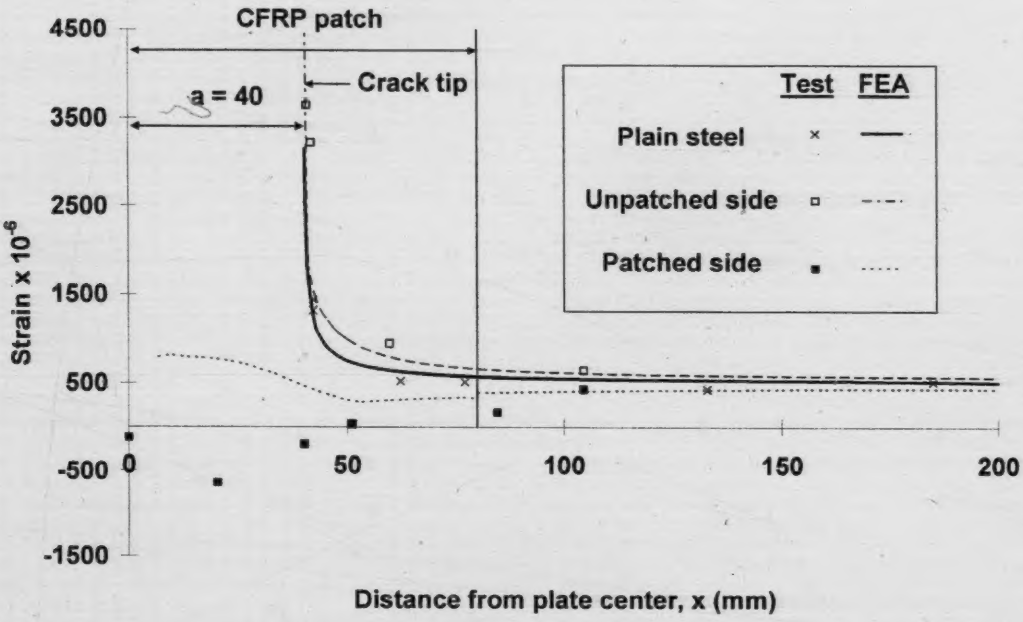

Figure 4.15 Comparison of strain results of the modified three layers model and specimen M316

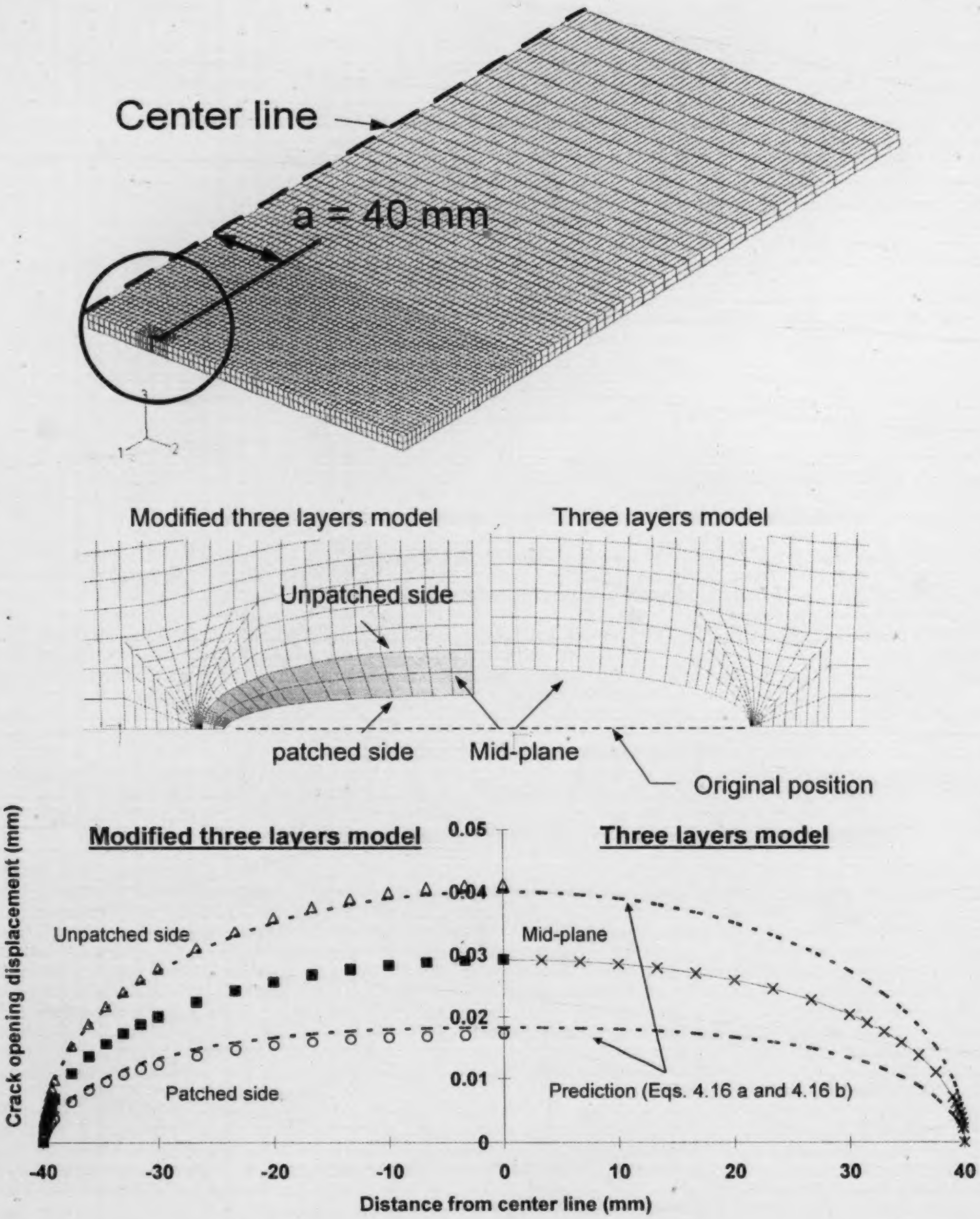

Figure 4.16 Deformed shape and crack displacements of the two type of finite element model (R116FE)

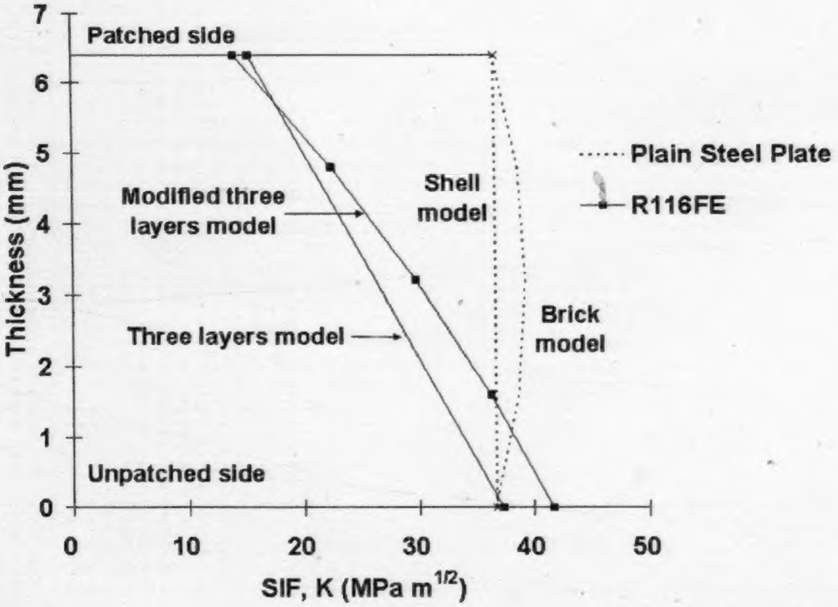

Figure 4.17 Comparison of the SIF across the plate thickness of the modified three layers model and the three layers model

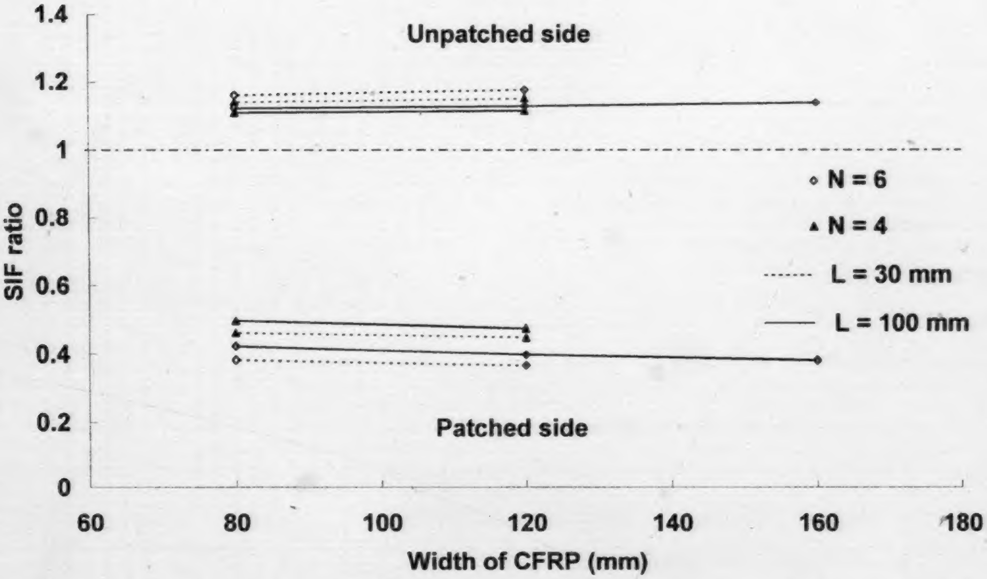

Figure 4.18 Results of SIF ratio versus different parameters

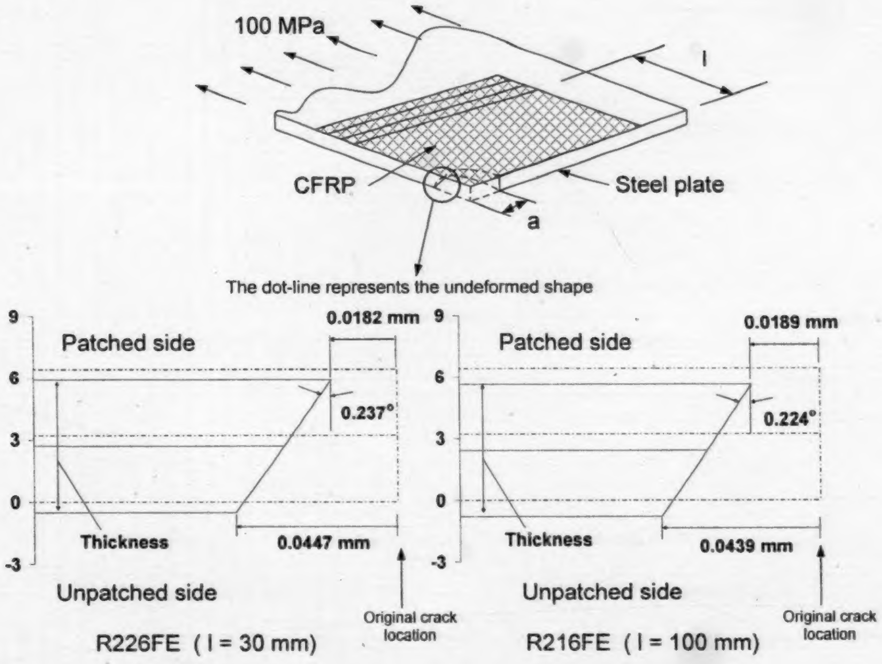
100 MPa
l
CFRP
Steel plate
a
The dot-line represents the undeformed shape
9
6
3
0
-3
Patched side
0.0182 mm
0.237°
Thickness
0.0447 mm
Unpatched side
Original crack location
R226FE (l = 30 mm)
Patched side
0.0189 mm
0.224°
Thickness
0.0439 mm
Unpatched side
Original crack location
R216FE (l = 100 mm)

The dotted line represents the undeformed shape

Figure 4.19 Magnified displacement at the crack position of models with patch length equal to 30 mm and 100 mm

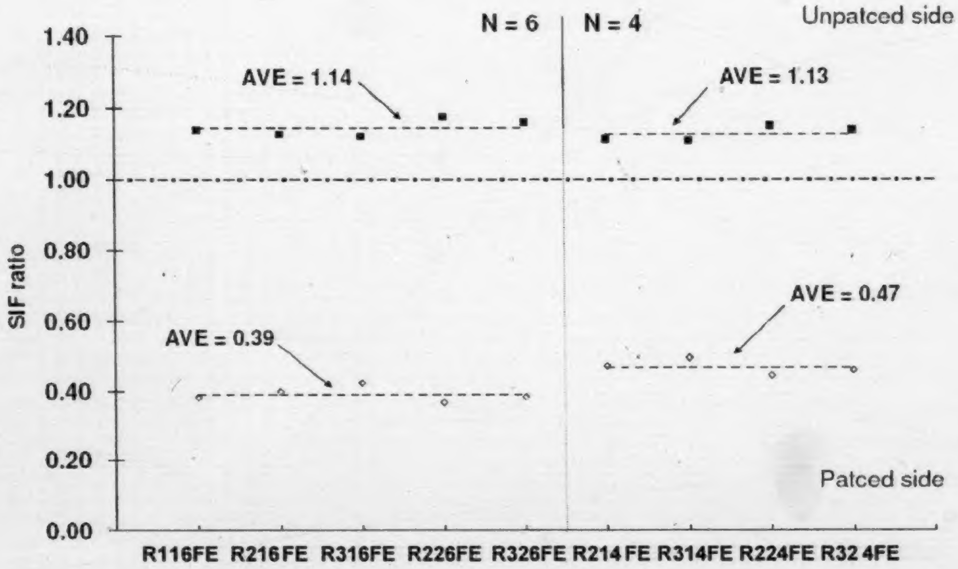

Figure 4.20 Summary of SIF ratio of specimens with CFRP patching

4.9 References

Barsoum, R. S., 1976. On the use of isoparametric finite elements in linear fracture mechanics. International Journal for Numerical Methods in Engineering, Vol. 10, 25-37

Chue, C. H., Chang, L. C., and Tsai, J. S. 1994. Bonded repair of a plate with inclined central crack under biaxial loading. Composite structure, Vol. 28, No. 1, pp. 39-45

Hibbitt, Karlsson & Sorenson, Inc. 2004. ABAQUS Version 6.4-1, ABAQUS/Standard User's Manual Volumes I and II, Pawtucket, Rhode Island, U.S.A.

Irwin, G.R. 1957, Analysis of stresses and strains near the end of a crack transversing a plate, Journal of Apply Mechanics, 24, pp. 361

Kennedy, G.D. and Cheng, J.J. 1998. Repair of cracked steel elements using composite fiber patching. Structural Engineering Report No. 221, Department of Civil & Environmental Engineering, University of Alberta

Mitsubishi Chemical Co. 1999. Carbon fiber prepreg sheet (Replark^{TM}). Available from http://www.m-kagaku.co.jp/english/aboutmcc/division/prod/carbonfiber/r-products.htm

Naboulsi, S. and Mall, S. 1996. Modeling of a cracked metallic structure with bonded composite patch using the three layer technique. Composite structures, Vol. 35, pp. 295-308

Rice, J. R. 1968. A path independent integral and approximate analysis of strain concentration by notches and cracks. Journal of Applied Mechanics, Vol. 35, pp. 379-386

Sun, C.T., Klug, J. and Arendt, C. 1996. Analysis of cracked aluminum plates repaired by bonded composite patches. AIAA Journal, Vol. 34, No. 2, pp. 369-374

Timoshenko, S. and Woinowsky-Kriege, S., 1959. Theory of plates and shells, McGraw-Hill Publishing Co.

5 FATIGUE REPAIR OF WELDED STEEL PLATES WITH BONDED COMPOSITE SINGLE-SIDE PATCHING

5.1 Introduction

Crack bridging is one of the methods for repairing cracked structures. It is done by welding or bolting cover plates over the location of crack. Another method of repair is to re-weld the cracked section again. The method of re-welding the cracked section involves the removal of the fatigue crack by gouging of the material in the vicinity of the crack and subsequently replaces the material using a fill-weld process. Usually, the strength of the welded material is higher than that of the parent metal; hence, the stiffness of the section is not reduced. However, in most instances, fatigue cracks reappear in the weld fill areas.

In the previous chapter, experimental and numerical investigations of the stress/strain distribution and the stress intensity factor (SIF) of cracked steel plates with carbon fiber reinforced polymer (CFRP) patching were discussed. It was shown that the strains at the cracked tip on the patched side could be reduced by applying CFRP patching. In addition, SIF could be reduced significantly on the patched side due to the presence of the CFRP patching. As mentioned in Chapter 2, most of the research has focused on the application of FRP patching to repair fatigue cracks in aluminum structures. There is relatively little research concerning the application of FRP patching for the repair of fatigue cracks in

---

[1] A version of chapter 5, 6 and 7 has been prepared for publication of the Canadian Journal of Civil Engineering.

steel structures. The extension of fatigue life of welded steel plates with single-side Boron-Epoxy composite patching was investigated by Roach and Rackow (2005). In this chapter, some of the fatigue test results of Roach and Rackow (2005) are presented and discussed. In addition, the modified three layers finite element model which was developed and discussed in the previous chapter is applied to investigate the progress of crack growth and the corresponding through thickness SIF of cracked steel plate with single-side FRP patching.

5.2 Background of test program and results of Roach and Rackow (2005)

A testing program on the fatigue repair of welded steel plates with single-sided FRP patching was conducted by Roach and Rackow (2005) at the Sandia National Laboratories in the U.S.A. on behalf of Syncrude Canada, Ltd. The objective of the testing program was to study the viability of using FRP patching to repair equipment used in the oil recovery industry. The details of the testing program and some of the test results which are presented in the report prepared by Roach and Rackow (2005) are summarized in the following section. Necessary information such as the dimensions and material properties of specimens are adopted for the finite element analysis that follows.

5.2.1 Test specimens

Fatigue tests were performed on steel plate specimens with a crack in the welded region at the Sandia National Laboratories. The base steel plate used in the testing program is ASTM 572-50 material. The plate thickness was 9.5 mm (0.375 in) with a plate width of

165 mm (6.5 in). In order to simulate a weld repair of the cracked region, a through-thickness weld repair region was installed in the parent plate before the composite materials were applied. This was done by cutting the original plate into two halves and welding them together using a typical V-shape full-penetration weld profile. A fatigue crack was introduced in the weld region of the test specimen prior to bonding the composite material in place. The fatigue crack was formed by introducing a 19 mm (0.75 in) saw cut in the welded region at the edge of the specimen as a starter notch. Then, tension-tension fatigue loads were applied until a 6.4 mm (0.25 in) fatigue crack was formed. Therefore, a total initial crack length of approximately 25.4 mm (1 in) was formed for the specimens. A typical fatigue test specimen is shown in Figure 5.1. There were three specimens which were referred to as the baseline un-repaired specimens (UR-1-S1, UR-1-S2 and UR-1-S3). For these three specimens, no composite materials were bonded. The other four specimens were prepared by bonding the composite materials on one side of the cracked steel plate over the cracked region. Boron-Epoxy composite material used in these tests (Specialty Materials Inc. 2002). The Boron-Epoxy composite material is a multi-ply, multi-directional lay-up of 24 plies [0,0,0,0,45,-45,0,0,0,0,-45,0,0,45,0,0,0,0,-45,45,0,0,0,0] with a post-cure adhesive thickness approximately equal to 0.15 mm. The plies were cut to different lengths in the tension load direction in order to taper the thickness of the edges. The taper pattern at the edge of composite produced a more gradual load transfer between the steel and the composite materials. The ply taper pattern was approximately 5 mm step every 2 plies. The properties of the steel plate and the average Boron-Epoxy laminate properties as reported by the supplier, are shown in Table 5.1. The stiffness ratio of the Boron-Epoxy laminate to the steel plate (ETR =

$E_{frp}t_{frp}$ / E_st_s) was approximately equal to 0.3 where E_{frp} and t_{frp} are the elastic modulus and thickness of the Boron-Epoxy laminate and E_s and t_s are the elastic modulus and thickness of the steel plate.

5.2.2 Test procedures

All of the specimens were tested under cyclic tensile loading. Three different levels of maximum stress (166 MPa (24 ksi), 228 MPa (33 ksi) and 283 MPa (41 ksi)) were applied to different groups of specimens. A minimum tensile stress of 13.8 MPa (2 ksi) was maintained in each stress range. As a result, the cyclic tensile stress range ($\Delta\sigma$) for each group was 152 MPa (22 ksi), 214 MPa (31 ksi) and 269 MPa (39 ksi). All fatigue tests were conducted at a test frequency of 3 – 5 Hz. Strain gauges were mounted to the specimens to monitor the strain on the composite and the steel specimens. Crack growth gages (Figure 5.1) with a resolution of 5 mm per filament were mounted on the back side of the specimens (steel surface) to measure the sequential growth of the seeded fatigue crack.

5.2.3 Test results

The results from the fatigue tests are summarized in Table 5.2 (Roach and Rackow 2005). The number of cycle versus crack length curves for all the specimens are shown in Figure 5.2. It can be seen from Table 5.2 and Figure 5.2 that for the non-repaired specimens the average number of fatigue cycles were 129,044 and 11,197 corresponding to the low stress range loading ($\Delta\sigma$ = 152 MPa) and the high stress range loading ($\Delta\sigma$ = 269 MPa), respectively. For these specimens, the fatigue crack grew from 25.4 mm to slightly over 60 mm. For the specimen repaired with the FRP patching and subjected to the low stress range loading, no fatigue crack growth was observed up to 251,011 cycles. Subsequently, the same specimen was tested using the medium stress range loading ($\Delta\sigma = 214$ MPa). The equivalent fatigue cycles accumulated in the low stress range were calculated for the medium stress range case according to Miner's Rule and the DOE-B curve (Roach and Rackow 2005). The equation for calculating the equivalent number of cycles is as following (Eq. 5.1).

$$N_{S2} = N_{S1}\left\{\frac{S_1}{S_2}\right\}^4 \tag{5.1}$$

where N_{S2} = equivalent number of cycles for specimen loaded with medium stress range

N_{S1} = number of fatigue cycle applied at low stress range

S_1 = value of low stress range ($\Delta\sigma = 152$ MPa)

S_2 = value of medium stress range ($\Delta\sigma = 214$ MPa)

According to Eq. 5.1 with the fatigue cycle of low stress range specimen equal to 251,011, the equivalent fatigue cycle of specimen subjected to medium stress range is about 63,887. Then, additional cyclic loading of medium stress range was applied to the repaired specimen until a final crack length of about 50 mm was observed. The total number of the fatigue cycle, which is the sum of the equivalent fatigue cycle and additional fatigue cycle, is about 188,703 as shown in Table 5.2. For those specimens which were repaired by composite patching and subjected to high stress range loading, the average number of fatigue cycles is about 109,950 with the corresponding average fatigue crack length grew from 25 mm to 62 mm. Comparing this fatigue life with the non-repaired specimens subjected to the same stress range of loading, the increase in fatigue life is about 9.8 times. A typical failed specimen is shown in Figure 5.3.

5.2.4 Fatigue analysis of the tested specimens

In the report prepared by Roach and Rackow (2005), the crack length versus number of cycle of loading of repaired and non-repaired specimens is presented; however, no fatigue analysis of the repaired and non-repaired specimens is presented. Therefore, fatigue analysis of the test specimens was carried out and discussed in the following section.

Paris and Erdogan (1960) proposed the following power law relationship for fatigue crack growth prediction.

$$\frac{da}{dN} = C\Delta K^{m} \qquad (5.2)$$

where a is the crack length, N is the number of cycles, ΔK is the stress intensity factor range, and C and m are material constants. The above equation is known as the Paris-Erdogan equation. The applied stress intensity factor range (ΔK) is obtained by using the specimen geometry and applied stress range and the general form of ΔK is as follows (Anderson 2005).

$$\Delta K = f(a/b)\Delta\sigma\sqrt{\pi a} \tag{5.3}$$

where f (a/b) is a correction factor for the geometry of the specimen. The change of SIF (ΔK) of steel plate with edge crack subjected to uniform far end stress can be predicted by Eq. 5.4 with f(a/b) equal to the following (Gross and Srawley 1964):

$$f(a/b) = 1.12 - 0.231\left(\frac{a}{b}\right) + 10.55\left(\frac{a}{b}\right)^2 - 21.72\left(\frac{a}{b}\right)^3 + 30.39\left(\frac{a}{b}\right)^4 \tag{5.4}$$

where a is the edge crack length and b is the plate width. By using the crack length versus fatigue cycle data, the da/dN value can be obtained. The applied stress intensity factor range (ΔK_{app}) is calculated based on the specimen geometry and the applied stress range. After the da/dN and applied ΔK_{app} are obtained, the data can be plotted to evaluate the corresponding material constants, C and m, which are described by Paris's equation (Eq. 5.2).

The da/dN versus ΔK curves for three of the specimens without FRP patching are shown in Figure 5.4 and Figure 5.5 in log-log scale. The corresponding da/dN versus ΔK curve of the fatigue test results of G40.12 350WT plain steel (Yin et al. 2006) is also included in the figures for comparison. It is shown from the figures that slower crack growth rate is obtained for specimens with crack in the welding region. Similar behavior was reported by Link (1990) and it was stated that during the process of welding (heating and cooling of welding and base material), residual stress is formed within the specimen. The general form of residual stress for a butt-welded specimen is shown in Figure 5.6. Link explained that a specimen notch by removing metal that is under residual weld tensile stresses could induce compressive residual stresses at the notch tip in the weld materials (Figure 5.7). Fatigue tests of compact tension (CT) specimen of ASTM A710 steel with and without weldment were carried out by Link (1990) and the result of crack growth rate (da/dN) versus applied stress intensity range (ΔK_{app}) of specimens with and without weldment was discussed. It was shown that the specimen with weldment seemed to have a slower crack growth rate when the applied stress intensity range was used in the plot. However, from the load versus crack opening displacement (COD) plot, it was found that significant crack closure behavior existed. Plot of the crack growth rate (da/dN) versus applied stress intensity factor range of both base steel plate and welded steel plate were compared and it was shown that the material constants C and m of the Paris equation (Eq. 5.2) for welded steel plate are within 1.05×10^{-18} and 2.18×10^{-18} m/cycle for C and within 4.95 and 4.96 for m. Since crack closure behavior existed for steel plate with crack on the weldment region, the corresponding material constants are not the same as those of plain steel plate when the crack growth rate (da/dN) was plotted versus applied stress intensity factor range. The crack closure behaviour was studied by Elber (1971) who reported that when the closure load is greater than the minimum applied load, the stress intensity calculated using applied loads would be greater than those that actually exist at the crack tip. Elber introduced the concept of effective stress intensity range (ΔK_{eff}), which assumes that crack propagation is controlled by the stress intensity only if the crack tip is opened. According to Elber's concept about the effective stress intensity range, Link took into account those closure measurements to predict the effective stress intensity range (ΔK_{eff}) and plotted da/dN versus ΔK_{eff}. The results showed that the growth rate of the welded specimen shifted close to the plain plate data.

The evaluation of the effective stress intensity range (ΔK_{eff}) involves the measurement of the crack tip displacement versus the applied loading and the corresponding crack opening stress is obtained by examining the change of the stiffness of the crack tip. For the current specimens studied, since there is no data about the crack tip opening displacement versus the applied loading, an alternative method for evaluating the effective stress intensity range is proposed in section 5.5.

The crack growth rate versus the applied stress intensity factor, which is predicted by Eqs. 5.3 and 5.4, for the specimens with FRP patching subjected to 269 MPa stress range are plotted in Figure 5.8. The data of the specimens without FRP patching are also plotted on the same figure for comparison. It is shown in the figure that for the same applied stress intensity factor, a slower crack growth rate is obtained for the specimens with FRP patching. Moreover, it is recognized that the presence of the FRP patching helps to share part of the loading and provide constraint to the crack mouth opening. As a result, the stress intensity factor at crack tip is reduced. Therefore, the actual stress intensity factor of the cracked plate with bonded FRP should be evaluated and used to plot the crack growth rate versus stress intensity factor.

It is shown in the previous chapter that due to the single-side FRP patching, the stress intensity factor is reduced significantly for the patched side and increased for the unpatched side. Hence, the crack growth rate on the patched side and unpatched side would be different. Due to the unequal crack growth rate, the crack tip shape would no longer be uniform. This change of geometry of the crack tip would affect the stress intensity factor across the crack tip. The interaction between the change of stress intensity factor and the change of geometry of crack tip is studied by the finite element method and is discussed in the following section.

5.3 Finite element analysis of SIF of a cracked plate with single-side FRP patching

To obtain the stress intensity factor (SIF) of cracked steel plates with single-side FRP patching, the modified three layers model which was discussed in the previous chapter is adopted for modeling the test specimens reported by Roach and Rackow (2005). The finite element model which is discussed in the previous chapter is setup by assigning a uniform crack length on the patched side and unpatched side. In this chapter, further modification of the finite element model is made by considering the different crack growth rate of the patched side and unpatched side of the cracked plate with single-side FRP patching according to the numerical procedures proposed by Lee and Lee (2004). Detail discussion regarding the finite element model and the procedures for obtaining the crack length and the corresponding stress intensity factor of patched side and unpatched side is given in the following section.

5.3.1 Finite element models

Finite element analyses of cracked steel plates with single-side FRP patching were carried out to study the effect of single-side FRP patching on the change of stress intensive factor across crack tip at different stage of crack propagation. Finite element models were set up using the commercial finite element program ABAQUS (Hibbitt et al. 2004). The modified three layers model which was discussed in the previous charter is used to model the tested steel specimens with single-side FRP patching. Eight node shell elements (S8R, 8 nodes general purpose shell element in ABAQUS) were used to model the adhesive and the FRP plates and 20 node brick elements (C3D20, 20 nodes brick element in ABAQUS) were used to model the steel plates. As it was mentioned previously, the Boron-Epoxy composite materials were applied in multi-direction lay-up of 24 plies on only one side of the cracked steel plate, composite shell element with plies direction according to the specimen detail were used for the FRP materials. The composite material was defined in the shell element property by including a keyword "composite" in the input file. By introducing the parameter "composite" in the input file, the elements associated with the FRP could be modeled as a material which was made up of several layers of material with predefined orientation. The adhesive layer between the steel plate and composite material was modeled by the homogeneous shell element. In order to obtain the SIF through the thickness of the plate, three dimensional brick elements were used to model the cracked steel plate. The number of elements used in the finite element models was about 6000, 650 and 800 for the steel plate, adhesive, and the FRP, respectively. Suitable constraints were used to enforce the compatibility along the plate-adhesive and the adhesive-FRP interface. The condition of constraints which were discussed in section 4.4.1 and 4.4.2 were applied to the current finite element models.

Due to symmetry, only half of the specimen was modeled and suitable boundary conditions were applied to the edge of the model. A typical model of the steel plate with FRP patching is shown in Figure 5.9. At the location of the crack tip, collapsed node elements with mid nodes located at quarter point were used in order to obtain the stress intensity factor at crack tip by mean of contour integration methods. The initial finite element model was setup by assuming that the initial crack tip shape is uniform across the thickness of the plate with crack length of 25.4 mm (1 in) on both patched and unpatched side. The finite element model was verified by comparing the strain results from the finite element analysis with the test results. The strain gauge location in a specimen with FRP patching is shown in Figure 5.10, as reported by Roach and Rackow (2005). The strain results from the test specimen, corresponding to a far end stress of 100 MPa, are shown along with the finite element results in Figure 5.11. It is shown that the finite element strain results compared well with the test results. Similar strain behaviour as discussed in the previous chapter for cracked steel plate with single-side patching, which is higher strain occurred on the unpatched side and lower strain occurred on the patched side, is observed.

5.3.2 Modeling of fatigue crack growth

The finite element model of a cracked steel plate with single-side FRP patching showed that higher strain is observed on the unpatched side and lower strain is observed on the patched side. It is also shown from the finite element results that the SIF on the patched side is 22.3 MPa√m and 57.9 MPa√m on the unpatched side. Due to the various values of SIF across the thickness of the plate, different crack propagation length at crack tip across the thickness of the plate is expected. The numerical procedures proposed by Lee and Lee (2004) for evaluating different crack propagation length at crack tip across the thickness of the plate and the corresponding SIF is adopted in the current finite element analysis. According to the Paris law (Eq. 5.2), the number of cycles for a crack to grow from the initial crack length (a_i) to the final crack length (a_f) can be predicted by the following equation.

$$N = \int_{a_i}^{a_f} \frac{1}{C(\Delta K)^m} da \tag{5.5}$$

where N is the number of cycles required for the initial crack (a_i) to grow to the size of the final crack length (a_f). Since ΔK varies with the crack growth in practical situations, the Euler algorithm is often used and the corresponding number of cycles (N) in the j + 1 term is shown in the following equation (Lee and Lee 2004),

$$N^{(j+1)} = N^{(j)} + \Delta N^{(j)} = N^{(j)} + \frac{\Delta a^{(j)}}{C\left[\Delta K(a^{(j)})\right]^m} \qquad j = 0, 1, 2, \ldots, n \tag{5.6}$$

where n is the number of intervals.

In the finite element analysis, a model with uniform initial crack length ($a_i = 25.4$ mm) was used as a starting analysis. FRP patching was applied at one side of the cracked steel plate. As was discussed in the previous chapter, since the SIF varies across the crack front in the case of single-sided repairs, different crack growth rates of the patched side and un-patched side should be considered. In this study, local increments across the crack front are considered, as shown in Figure 5.12. The Paris law can be used at any points along the crack front as follows,

$$\frac{da_i}{dN} = C(\Delta K_i)^m \tag{5.7}$$

where da_i and ΔK_i are the local crack growth increment and stress intensity factor range at an arbitrary point i along the crack front, respectively. Similarly, the following equation can be derived from Eq. 5.7 at j term,

$$\text{with} \qquad \Delta N = \frac{\Delta a_i^{(j)}}{C(\Delta K_i^{(j)})^m} = \frac{\Delta a_{max}^{(j)}}{C(\Delta K_{max}^{(j)})^m}$$

$$\Delta a_i^{(j)} = \left(\frac{\Delta K_i^{(j)}}{\Delta K_{max}^{(j)}}\right)^m \Delta a_{max}^{(j)} \qquad i = 1, 2, \ldots. \tag{5.8}$$

where $\Delta a_{max}^{(j)}$ is the maximum crack growth increment at the point where the maximum stress intensity factor range, $\Delta K_{max}^{(j)}$, across the crack front occurs. Equation 5.8 can be used to calculate the local increment of crack growth at each point along the crack front. As the advanced crack tip shape is depended on the SIF range, a very fine crack growth value is assigned during the analysis. A maximum crack growth value ($\Delta a_{max}^{(j)}$) of the unpatched side equal to 1.5875 mm (1/16 in) was used in the analysis. This crack growth value is about 6.25% of the length of the initial crack length. After the first successive analysis of the SIF across the uniform initial crack front, the crack growth values through the thickness of the plate were calculated by Eq. 5.8 with the material constants (m) equal to 3 (Barsom and Rolfe 1999). Then, another finite element model was set up by using the updated non-uniform crack length and the corresponding SIF across the crack tip was analyzed. This procedure was repeated until the crack length of the unpatched side reached 63.5 mm. The finite element models which represent four different crack lengths are shown in Figure 5.13. Maximum and minimum far end stresses which were used in the testing program were assigned in the finite element analysis accordingly for the evaluation of the corresponding SIF range.

5.3.3 Finite element results

The finite element results of the effect of FRP patching on reducing the crack opening displacement (COD) are presented first. As it is shown in Figure 5.14, the crack opening displacement (COD) of the cracked steel plate with FRP patching for four different crack lengths of unpatched side (a = 25.4 mm, 38.1 mm, 50.8 mm and 63.5 mm) are compared with the COD of the plain cracked steel plate. As shown in this figure, the reduction of the COD on the patched side is about 50% compared to the COD of plain steel. However, there was almost no reduction of COD on the unpatched side for the short crack length (a = 25.4 mm). It is believed that the significant reduction of the COD in the patched side might cause the SIF of the patched side to reduce significantly as well. As the crack length increased, a reduction of the COD on the unpatched side became significant. When the crack length of the unpatched side was 63.5 mm, the COD on the unpatched side was reduced by 50%. It should be noted that for the plate with FRP patching, when the crack length of the unpatched side was 63.5 mm, the crack length of the patched side was about 45 mm. Therefore, for cracked plate with single-side FRP patching, the reduction of the COD on the unpatched side is affected by not only the presence of the FRP patching, but also the reduced crack length of the patched side.

The longitudinal stress pattern across the thickness of the a plate at two locations for plate with FRP patching (crack length a = 25.4 mm and 63.5 mm) is shown in Figure 5.15 and Figure 5.16. Location A is chosen close to the crack and location B is chosen at the edge where the tapered end starts. The longitudinal stress was normalized by dividing the stress by the applied far end stress. For the stress pattern at position A, it is shown from the figures that significant bending of the FRP patching was observed. Since position A is chosen close to the crack, all the loading was transferred from the steel plate to the FRP patching at that location. As FRP patching was applied to only one side of the cracked plate, the FRP patching was subjected to not only axial loading, but also bending due to the eccentricity of the applied loading at the far end. As noted previously, certain layers of the FRP laminas were placed at ±45° with respect to the loading direction. According to the bending stress pattern of the FRP patching, the stresses at the ±45° layers were relatively lower due to the lower stiffness of ±45° layers along the loading direction. In addition, the bending stress of the FRP patching at position A was more significant for the plate with a longer crack length. The higher bending stress indicated that more loading was attracted by the FRP patching since the stiffness of the steel plate was reduced more when the crack length was long. The stress patterns of FRP patching and steel plate at position B are shown in Figure 5.16. As position B is not located near the crack, the stress pattern at this position shows that part of the loading is shared by the steel plate. It is also shown in Figure 5.16 that more loading was attracted by the FRP patching in the cracked plate with longer crack length. As the crack length increases, the stiffness of the steel plate decreases. Therefore, the effect of the FRP patching on the constraint to the crack displacement becomes more significant and more loading is transferred to the FRP patching.

With a far end applied stress of 166 MPa, the longitudinal stress contour of cracked plate (a = 25.4 mm) with and without FRP patching is shown in Figure 5.17. Examining the stress around the crack tip region (area within the dash-line), it is noted that significant reduction in longitudinal stress takes place on the patched side for the plate with FRP patching. The normalized longitudinal stress of the outer surface of the FRP along position C and position D are shown in Figure 5.18. Position C was chosen close to the location of the crack and position D was chosen at the edge where the tapered end starts. For the stress pattern along position C, as shown in the figure, a higher stress was observed at the crack region. The stress decreased and became more uniform on the uncracked region. For the stress pattern along position D, it is shown that the highest stress was not observed at the crack region. Instead, the stress at the free edge was a bit lower than that within the uncracked region. Since the crack is location at the free edge of the plate, the stress near the free edge of the cracked steel plate is lower than that on the uncracked region due to the present of the crack. As a result, the loading shared by the FRP near the free edge is lower than that within the uncracked region.

The crack growth propagation through the thickness of the plate of every two steps of crack growth is shown in Figure 5.19. The normalized SIF range ($\Delta K/\Delta\sigma$) is shown in Figure 5.20. As was discussed previously, a uniform crack length (a_i = 25.4 mm) was used as a starting analysis. With this assigned uniform crack length, the variation of the SIF is slightly nonlinear through the thickness of the crack (Figure 5.20). As a result, the crack grows at a different rate on the patched side and on the unpatched side. Crack propagation was then calculated through the thickness of the plate according to Eq. 5.8 and the original uniform crack shape changed to a non-uniform crack shape. The change of SIF was then predicted according to the non-uniform crack shape. With the non-uniformly propagation of the crack tip, as shown in Figure 5.20, the through thickness values of $\Delta K / \Delta\sigma$ became more uniform as the crack length increased. The ratio of ΔK of the patched side to ΔK of the unpatched side as a function of the crack length to plate width ratio (a/b) is shown in Figure 5.21. It is shown that the ΔK of the unpatched side is about 2.5 times larger than that on the patched side when the crack length is short (a_i = 25.4 mm). As the crack length increased, significant drop of the ratio of ΔK of patched and unpatched side was observed. When the crack length of unpatched side reached 50.8 mm (2 times a_i), the difference in ΔK between the patched and unpatched side is less than 10%. As the crack length increases, ΔK of the unpatched side is close to the value of ΔK of the patched side.

The SIF range (ΔK) of the steel plate with the edge crack subjected to uniform far end stress can be obtained from Eqs. 5.3 and 5.4. For a crack length, a, equal to 25.4 mm and a plate width, b, equal to 165.1 mm, f(a/b) obtained from Eq. 5.4 is 1.272. Comparing this value to $\Delta K / \Delta\sigma\sqrt{\pi a}$, where ΔK is obtained from the finite element analysis, $\Delta\sigma$ is the applied stress range, and a is defined as the crack length of the unpatched side of patched specimen, it is shown that $\Delta K / \Delta\sigma\sqrt{\pi a}$ of a patched plate is reduced by about 41% on the patched side and is increased by about 6% on the unpatched side. The variation of ΔK for a non-repaired and a repaired plate is shown in Figure 5.22. It is shown in Figure 5.22 that significant reduction of ΔK is observed for the patched side when the crack length is short. However, there is almost no reduction of ΔK on the unpatched side when the crack length is short. As the crack length increases, the ratio of ΔK of the non-repaired and repaired plate decreases on unpatched side but increases on patched side. When the crack length increases to 50.8 mm (2 times a_i, corresponding to a/b = 0.31), the ratio of ΔK of the non-repaired and repaired plate on the patching side starts to decrease slightly. As the crack length increases to 63.5 mm (corresponding to a/b = 0.38), a reduction of about 45% of ΔK is observed. The correction factor for the geometry for the patched and unpatched side, $f(a/b)^p$ and $f(a/b)^u$, are calculated based on the results of ΔK for the patched side and unpatched side from the finite element analysis and the equations are shown as follow:

$$f(a/b)^p = 1267(a/b)^4 - 1407.2(a/b)^3 + 561.5(a/b)^2 - 92.044(a/b) + 5.792 \qquad (5.9)$$

$$f(a/b)^u = 134.25(a/b)^4 - 223.41(a/b)^3 + 135.29(a/b)^2 - 34.74(a/b) + 4.2524 \qquad (5.10)$$

The results of $f(a/b)^p$ and $f(a/b)^u$ are shown along with the results obtained from Eq. 5.4 for a non-repaired plate and the f(a/b) values as a function of crack length- to- plate width ratio (a/b) are shown in Figure 5.23. As shown in the figure, the values of $f(a/b)^p$ and $f(a/b)^u$ for the patched and unpatched sides convert to around 1.1 as the crack length increases. Compared to the f(a/b) values of a plate without patching, a reduction of 85% was obtained for the specimen with patching on one side when the crack length of the unpatched side was to 63.5 mm.

5.4 Discussion of the finite element results of SIF

In order to verify the finite element results, an analytical solution of a cracked plate with bonded reinforcement was studied and the predictions were compared with the finite element results. Rose (1982) carried out an analytical study of estimating the reduction of the crack extension force when a cracked plate is repaired by reinforcing patches bonded to its faces. Rose pointed out that there are two main effects of the bonded reinforcing patches on the cracked surface: (1) to reduce the stress in the uncracked plate at the prospective location of the crack and (2) to restrain the opening of the crack. Rose considered two extreme cases of an infinitely wide plate. One involved an uncracked plate with bonded reinforcement and one involved a cracked plate with bonded reinforcement (Figure 5.24). With a far end applied stress equal to σ, Rose showed that the stress in the uncracked plate, σ_0, with bonded reinforcement is:

$$\sigma_0 = \left(\frac{E_s t_s}{E_s t_s + E_{frp} t_{frp}} \right) \sigma \qquad (5.11)$$

For a cracked plate with bonded reinforcement, the vertical displacement of the cracked surface is

$$u_y = \sigma_0 t_s \beta \left(\frac{t_a}{G_a} \right) \tag{5.12}$$

where
$$\beta = \sqrt{\frac{G_a}{t_a} \left(\frac{1}{E_s t_s} + \frac{1}{E_{frp} t_{frp}} \right)} \tag{5.13}$$

E_s and t_s are the elastic modulus and half thickness of plate with double sides patching, respectively; E_{frp} and t_{frp} are the elastic modulus and thickness of FRP patch, respectively; and G_a and t_a are the shear modulus and thickness of adhesive, respectively. Therefore, the crack extension force, G, which is the work extracted (per unit thickness, per unit crack advance) on the plate allowing the stress σ_0 to relax to zero through the displacement u_y on both crack faces is:

$$G = 2\left(\frac{1}{2} \sigma_0 u_y \right) = \frac{\sigma_0^{\ 2}}{E_s} (\pi \Lambda) \tag{5.14}$$

where
$$\pi \Lambda = \beta \frac{E_s t_s t_a}{G_a} \tag{5.15}$$

For a plane stress problem, the stress intensive factor (SIF), K_r, can be related to the G in the following way:

$$G = \frac{K_r^{\ 2}}{E_s} \tag{5.16}$$

Therefore,

$$K_r = \sigma_0 \sqrt{\pi \Lambda} \tag{5.17}$$

In Eq. 5.17, Λ is known as the characteristic crack length of a plate with bonded reinforcement. It was shown that the SIF of a cracked plate with bonded reinforcement approaches a constant value which is independent of the actual crack length.

For the plate with only single-side patching, the out-of-plane bending of the plate due to the load-path eccentricity should be considered for the prediction of the SIF. Wang et al. (1998) proposed a modified equation for predicting the SIF of a plate with only single-side patching. Based on the assumption that the SIF at the crack tip of a plate with single-side patching varies linearly across the thickness of the plate, the SIF at the crack tip on the patched and the unpatched side are obtained by the following equations:

$$K^{*}_{\text{unpatched}} = \left(\frac{3}{1 + R_{SIF} + R_{SIF}^{\ 2}} \right)^{1/2} K^{*}_{\text{rms}} \tag{5.18}$$

$$K^{*}_{\text{patched}} = \left(\frac{3}{1 + R_{SIF} + R_{SIF}^{\ 2}} \right)^{1/2} R_{SIF} K^{*}_{\text{rms}} \tag{5.19}$$

where R_{SIF} is the ratio of the SIF of the patched side to the SIF of the unpatched side and is depended on the geometry and material properties of the plate and reinforcement.

The K^*_{rms} is the root-mean-square SIF for a plate with single-side patching and is expressed as:

$$K^*_{rms} = K_r \omega \tag{5.20}$$

where K_r denotes the SIF for double-sides patching and ω is the bending correction factor which is related to the geometry and material properties of the plate and the reinforcement. The equations for calculating the values of R_{SIF} and ω are shown in Appendix A.

The normalized ΔSIF ($\Delta K/\Delta\sigma$) of the finite element analysis results of the patched and the unpatched sides is shown in Figure 5.25 along with the values obtained by Eqs. 5.17 to 5.20. It is shown that the values obtained from these equations for double-side patching (Eq. 5.17) is close to the finite element values of the patched side when the crack length is short. Equation 5.17 gives the lower bound value for SIF since the effect of out-of-plane bending on the SIF is eliminated for a cracked plate with double-side patching. As the crack length increases, the finite element values of $\Delta K/\Delta\sigma$ increase for both patched and unpatched sides. The values obtained through Eqs. 5.18 to 5.20 for single-side patching overestimate ΔK, especially for the unpatched side. As was shown in the finite element study, with a uniform crack tip the SIF varies almost linearly through the thickness of the plate with single-side patching. The same assumption was applied to Eqs. 5.18 to 5.20. However, it was shown in the finite element study that in the case of a plate with single-side patching, the crack propagation on the patched and the unpatched sides was not the same. As a result, the crack tip is not uniform across the thickness of the plate. As the crack length increases, the SIF across the thickness of the plate become almost uniform through the thickness of the plate due to the non-uniform shape of the crack tip. Since Eqs. 5.18 to 5.20 do not account for the effect of the non-uniform crack propagation through the thickness of the plate, overestimated values were obtained using Eqs. 5.18 to 5.20. Since, the finite element results are shown to be within the prediction between the K^{*}_{rms} (the root-mean-square SIF for plate with single-side patching) and the prediction of K_r (the SIF for plate with double-side patching), it is concluded that the current finite element results are within a reasonable range of SIF for cracked plate with single-side patching.

5.5 Analysis of fatigue life of welded steel plate with edge crack and single-side FRP patching

The analysis of the fatigue life of the test specimens by Roach and Rackow (2005), was carried out for specimens subjected to a high stress range loading. The Paris equation (Eq. 5.2) was used as the fundamental equation in the fatigue analysis. As was discussed in Section 5.2.4 a slower crack growth rate was observed in a cracked plate with a crack in the welded region when the crack growth data were plotted against the applied stress intensity factor range. This slower crack growth rate behaviour is due to the crack closure effect, as described by Elber (1971). In order to eliminate the crack closure effect in the analysis of crack growth rate, Elber (1971) suggested that the crack growth rate data should be plotted against the effective stress intensity factor range. Therefore, in this section, the crack growth data of the welded specimens without FRP patching are analyzed first to obtain a reasonable effective stress intensity factor range. With the prediction of the effective stress intensity factor range, the corresponding crack opening stress is evaluated. Then, this crack opening stress is used to determine the effective stress intensity factor range of the welded specimens with single-side FRP patching. Detail procedures are discussed in the following sections.

5.5.1 Evaluation of the effective stress intensity factor and the corresponding crack opening stress of welded plates without FRP patching

As it is mentioned previously, the presence of residual stress due to welding causes slower crack growth rate. This is evident when the crack growth rate is plotted as a function of the applied stress intensity factor. Elber (1971) explained that the observed slower crack growth rate is due to the crack closure behaviour and he suggested that the crack growth rate should be plotted as a function of the effective stress intensity factor instead of the applied stress intensity factor. Link (1990) showed that when the crack growth rate data are plotted as a function of the effective stress intensity factor, the crack growth rate data of a welded plate shift to the crack growth rate data of the base metal. Therefore, with the crack growth rate data of a welded plate and the effective stress intensity factor, similar material constants, C and m, in the Paris equation for the welded plate and plain plate should be obtained. A plot of the crack growth rate versus the applied stress intensity factor of plate without FRP patching subjected to 269 MPa stress range is shown in Figure 5.5. The corresponding crack growth rate equation of welded plate (Roach and Rackow 2005) and the plain plate (Yin et al. 2006) are shown below:

For plain plate: $$da/dN = 8.88 \times 10^{-12}(\Delta K_{app})^{3.03} \tag{5.21}$$

For welded plate: $$da/dN = 5.44 \times 10^{-19}(\Delta K_{app})^{6.04} \tag{5.22}$$

where da/dN is the crack growth rate per cycle (m/cycle) and ΔK_{app} is the applied stress intensity factor range (MPa√m).

It is assumed that with the crack growth rate in a welded plate when plotted as a function of the effective stress intensity factor, the material constants, C and m, in the Paris equation, should be close to or the same as the material constants of the plain plate. Therefore, by using the material constants, C and m, of the base metal and introducing the effective stress intensity factor range (ΔK_{eff}) for a welded plate into Eq. 5.21, the crack growth rate (da/dN) of the welded plate can be expressed as a function of the effective stress intensity factor range (ΔK_{eff}) as following equation:

For a welded plate: $$\frac{da}{dN} = 8.88 \times 10^{-12}(\Delta K_{eff})^{3.03} \tag{5.23}$$

This crack growth rate should be the same as that obtained by Eq. 5.22. Therefore, by equaling Eq. 5.22 and 5.23, the effective stress intensity factor range (ΔK_{eff}) for a welded plate could be obtained as follows:

$$8.88 \times 10^{-12}(\Delta K_{eff})^{3.03} = 5.44 \times 10^{-19}(\Delta K_{app})^{6.04}$$

$$(\Delta K_{eff}) = 4.16 \times 10^{-3} (\Delta K_{app})^{1.99} \tag{5.24}$$

The crack growth rate versus effective stress intensity factor range of welded plate is shown in Figure 5.26 along with the fatigue test data of the plain plate.

The definition of the effective stress intensity factor range (ΔK_{eff}) is defined as the difference between the maximum stress intensity factor (K_{max}) and the opening stress intensity factor (K_{op}). Once the effective stress intensity factor range is known, the corresponding crack opening stress (σ_{op}) could be obtained by the following equations.

$$\Delta K_{eff} = K_{max} - K_{op} \tag{5.25}$$

$$\Delta K_{eff} = (\sigma_{max} - \sigma_{op}) f(a/b)\sqrt{\pi a} \tag{5.26}$$

$$\sigma_{op} = \sigma_{max} - \frac{\Delta K_{eff}}{f(a/b)\sqrt{\pi a}} \tag{5.27}$$

where σ_{max} is the maximum applied stress, a is the edge crack length and f(a/b) is defined in Eq. 5.4. With the predicted effective stress intensity factor range (Eq. 5.24) of the welded plate without FRP patching, the crack opening stress, σ_{op} (MPa) versus crack length is obtained from the following equation (Eq. 5.28)

$$\sigma_{op} = \sigma_{max} - \frac{4.16 \times 10^{-3} (\Delta K_{app})^{1.99}}{f(a/b)\sqrt{\pi a}} \tag{5.28}$$

where a is the edge crack length in mm which varies from 25 mm to 64 mm and

$$\Delta K_{app} = \Delta\sigma\, f(a/b)\sqrt{\pi a}$$

An illustration of the effective stress and the opening stress is shown in Figure 5.27.

5.5.2 Prediction of the fatigue life of a welded steel plate with the edge crack repaired by single-side FRP patching

The Paris equation is used as the basis for predicting the fatigue life of a welded steel plate with edge crack repaired by single-side FRP patching. The resulting equation takes the following form

$$N = \int_{a_i}^{a_f} \frac{1}{C(\Delta K_{eff})^m} da \qquad (5.29)$$

where N is the number of cycle; a_i is the initial crack length; a_f is the final crack length; ΔK_{eff} is the effective stress intensity factor range; and, C and m are the material constants of steel. The initial and final crack lengths are taken as 25.4 mm and 63.5 mm, respectively in this study. The material constants, C and m, are taken as 8.88×10^{-12} m/cycle and 3.03, respectively, in this study, according to the material constant of G40.12 350WT steel (Yin et al. 2006). The prediction of the effective stress intensity factor range (ΔK_{eff}) is obtained from Eqs. 5.3, 5.4 and 5.24 for the plate without FRP patching. For the specimens with single-side FRP patching, Eq. 5.26 is modified using the crack opening stress and the geometry factor, as follows:

$$\Delta K_{eff} = (\sigma_{max} - \sigma_{op}^{p}) f(a/b)^{u} \sqrt{\pi a} \tag{5.30}$$

For this study, a maximum stress (σ_{max}) of 283 MPa was used and $f(a/b)^{u}$ is the equation of the modification factor (Eq. 5.10) accounting for the effect of geometry of crack and the presence of the single-side FRP patching. Equation 5.10 is repeated as follows:

$$f(a/b)^{u} = 134.25(a/b)^{4} - 223.41(a/b)^{3} + 135.29(a/b)^{2} - 34.74(a/b) + 4.2524 \tag{5.10}$$

For a plate with FRP patching, illustrated in Figure 5.28, part of the loading is shared by the FRP patching. Therefore, the far end stress which is needed to cause the crack to open for the specimen with FRP patching should be larger the crack opening stress for plate without FRP patching. The far end opening stress for the plate with FRP patching (σ_{op}^{p}) is obtained by combining Eqs. 5.11 and 5.28 with σ in Eq. 5.11 replaced by σ_{op} from Eq. 5.28. The combined equation becomes:

$$\sigma_{op}^{p} = \left(\frac{E_s t_s + E_{frp} t_{frp}}{E_s t_s} \right) \sigma_{op} \tag{5.31}$$

where σ_{op} is obtained from Eq. 5.28; E_s and t_s are the elastic modulus and thickness of steel plate, respectively, and E_{frp} and t_{frp} are the elastic modulus and thickness of the FRP plates, respectively.

The fatigue lives is obtained by carrying out a numerical iteration based on Eq. 5.29. The continuous integration of Eq. 5.29 is converted to discrete summation, as follows:

$$N_{j+1} = N_j + \Delta N \tag{5.32}$$

where $\Delta N = \dfrac{\Delta a}{C(\Delta K_{eff})^m}$ and $\Delta a = 0.1 \text{ mm}$

Based on the above procedures, the fatigue life of the plain welded steel plate and the welded steel plate with single-side FRP patching for crack grows from 25.4 mm to 63.5 mm on the unpatched side are 111,498 and 13,284 cycles, respectively. The corresponding test and theoretical results are shown in Figure 5.29. The average test-to-predicted ratio for non-repaired and repaired specimens are 0.84 and 0.99, respectively. The test results showed that the average increase in fatigue life of specimens with single-side FRP patching is about 9.8 times, while the prediction showed that the increase in fatigue life of the plates with single-side FRP patching is about 8.4 times.

5.6 Summary and conclusions

Fatigue test results of steel plate with crack in welded region repaired by single-side FRP patching by Roach and Rackow (2005) were analyzed by finite element method. Uniform initial crack front was assigned as the starting analysis and the stress intensive factors, SIF, (K) through the thickness of the plate were obtained by means of contour integration. The finite element results showed that with uniform initial crack front, the through thickness SIF increases on the unpatched side and decreases on the patched side for plate with single-side patching. According to the predicted SIF through the thickness of the plate, different crack grow rates of the crack front were obtained through the thickness of the plate using the Paris equation. As a result, for an assigned advance crack length at the unpatched side, non-uniform crack front were formed and the SIF through the thickness were obtained by contour integration. This procedure was repeated until the crack length at the unpatched side reached the target final crack length. The finite element results showed that the through thickness SIF becomes more uniform across the thickness of the plate as the crack length grows gradually. The finite element results of the through thickness SIF were compared to the results obtained by using the equations proposed by Wang et al. (1998) for cracked plate with single-side patching. Since the equations proposed by Wang et al. do not account for the effect of the non-uniform crack propagation through the thickness of the plate, the predicted SIF on the patched and unpatched side were overestimated. With the test results of the crack growth rate of welded specimens and base metal, equations for obtaining the crack opening stress was obtained. This crack opening stress equation is modified for the welded specimens with single-side FRP patching according to the adherend stiffness of the FRP patching and the steel plate. Together with the SIF obtained in the finite element analysis, equation for determining the fatigue life of repaired and non-repaired welded steel plates with edge crack was developed. Test results of Roach and Rackow (2005) showed that the increase in fatigue life is 9.8 times for specimens subjected to high stress range loading ($\Delta\sigma$ = 269 MPa) and with the adherend stiffness ratio of composite materials to steel plate ($E_{frp}t_{frp}$ / E_st_s) equal to 0.3. The fatigue life obtained from the proposed equations of the repaired and non-repaired welded steel plates are 111,498 and 13,284 cycles, respectively. The average test-to-predicted ratios are 0.84 and 0.99, respectively. According to the fatigue life obtained from current proposed equations, the values show that the increase in fatigue life is about 8.4 times.

Table 5.1 Material properties (Roach and Rackow, 2005)

Material		**Material properties**	**Thickness**
Steel plate	Elastic modulus	E_s = 205000 MPa	t_s = 9.5 mm
Boron-Epoxy laminate*	Elastic modulus	E_{frp} = 173,754 MPa	t_{frp} = 3.6 mm
	Shear modulus	G_{frp} = 25,994 MPa	
	Poisson's ratio	ν_{frp} = 0.32	

		Shear Modulus	**Thickness**
Adhesive (AF-163)		G_a = 413.7 MPa	t_a = 0.15 mm

*Note: the Boron-Epoxy lamina properties are: E_{11} = 193,060 MPa, E_{22} = 18,616 MPa, G_{12} = 5,516 MPa, ν_{12}= 0.21 and t_{ply} = 0.145mm

Table 5.2 Fatigue test results of specimens (Roach and Rackow 2005)

Specimen No.	Condition	Stress Range $\Delta\sigma$ (MPa)	Number of Fatigue Cycles (N)	Total crack length (mm)
UR-1-S1	Non-repaired	152	129,044	62
R-1-S1	Repaired	152	251,011	None
R-1-S2*	Repaired	214	188,703	50
UR-1-S3	Non-repaired	269	12,651	61
UR-2-S3	Non-repaired	269	9,743	61
R-1-S3	Repaired	269	109,004	60
R-2-S3	Repaired	269	110,897	64

*The equivalent fatigue cycles accumulated in the low stress range were calculated for this specimen according to Eq. 5.1.

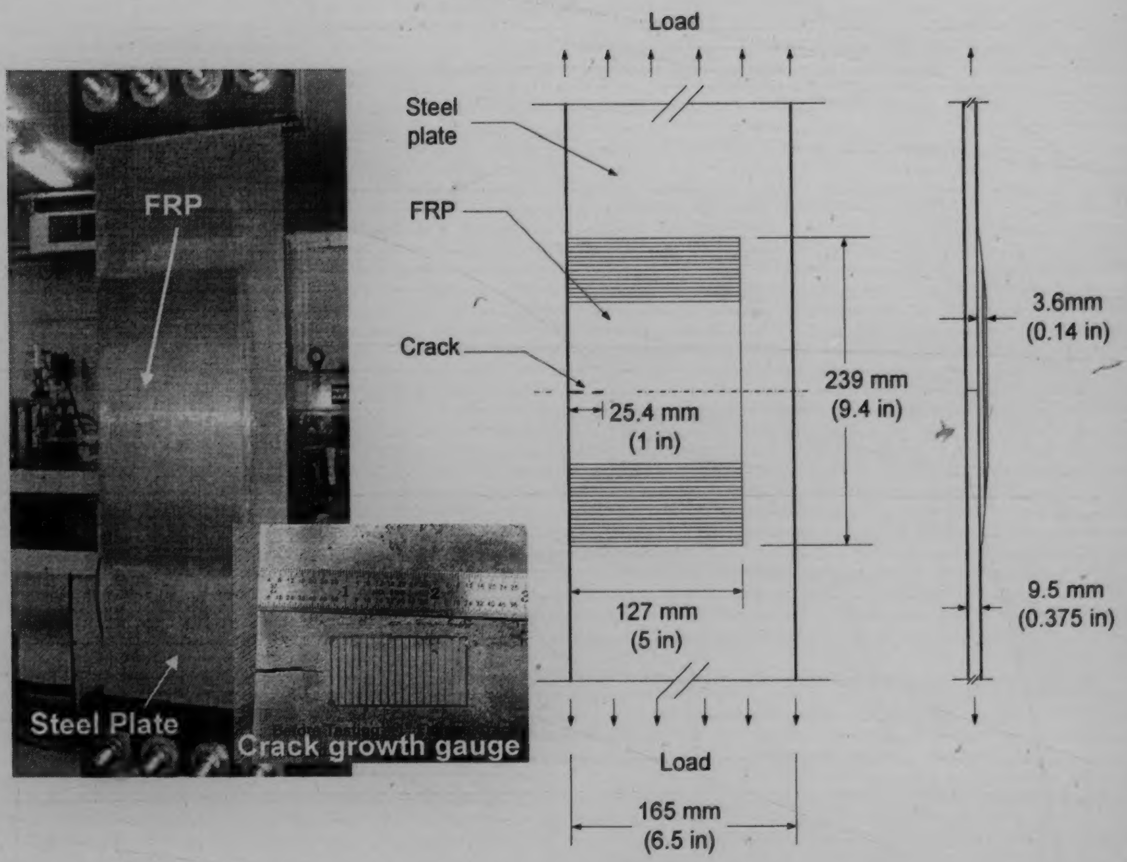
FRP
Steel Plate
Crack growth gauge
Load
Steel plate
FRP
Crack
25.4 mm
(1 in)
239 mm
(9.4 in)
127 mm
(5 in)
Load
165 mm
(6.5 in)
3.6mm
(0.14 in)
9.5 mm
(0.375 in)

Figure 5.1 Test specimen with FRP (Roach and Rackow, 2005)

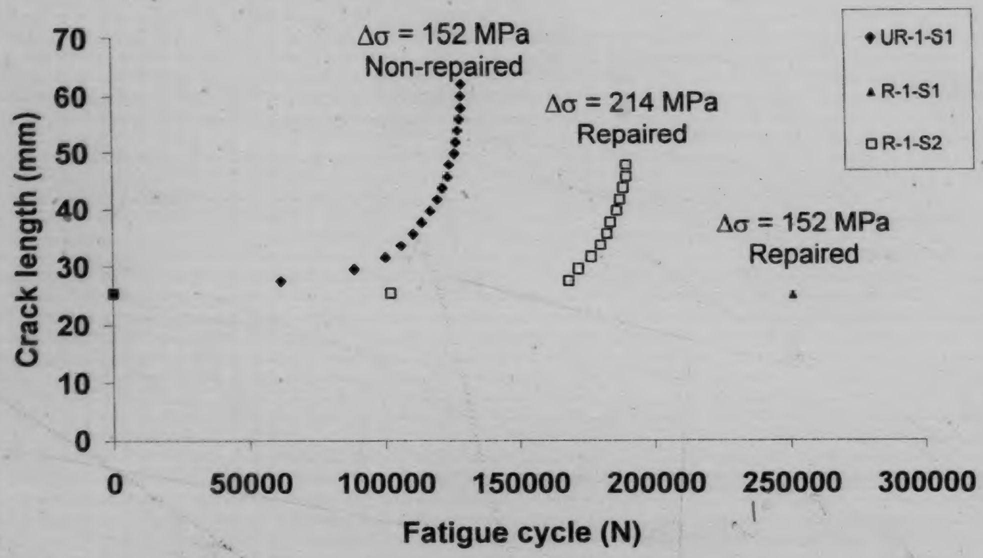

(a) specimens subjected to low and medium stress range (Δσ = 152 MPa and 214 MPa)

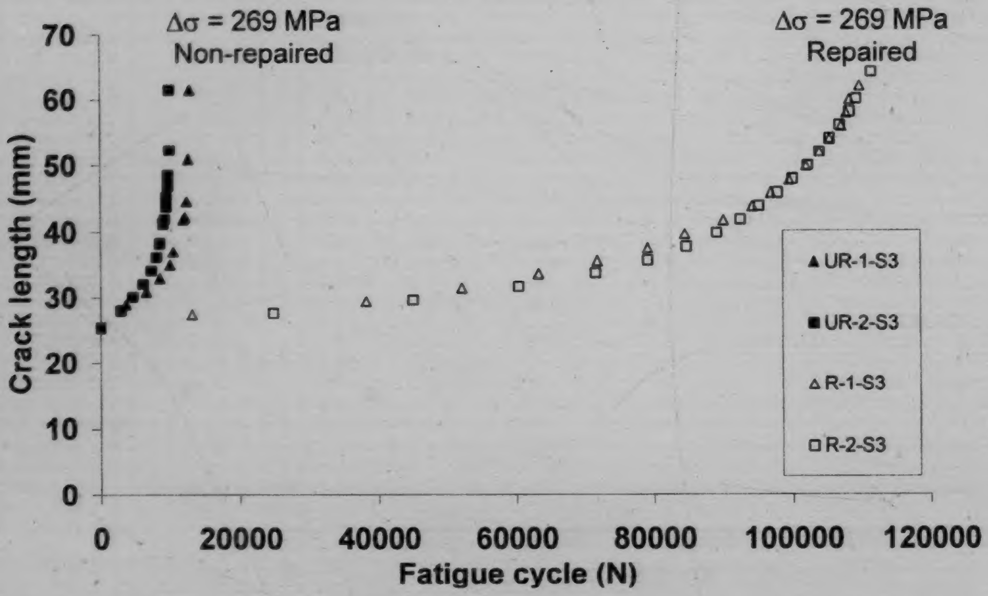

(b) Specimens subjected to high stress range (Δσ = 269 MPa)

Figure 5.2 Crack length versus fatigue cycle of specimens (Roach and Rackow, 2005)

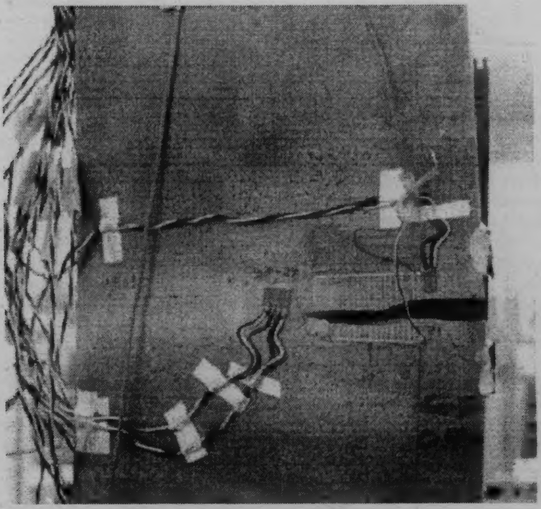

Figure 5.3 Failure of typical specimen (Roach and Rackow, 2005)

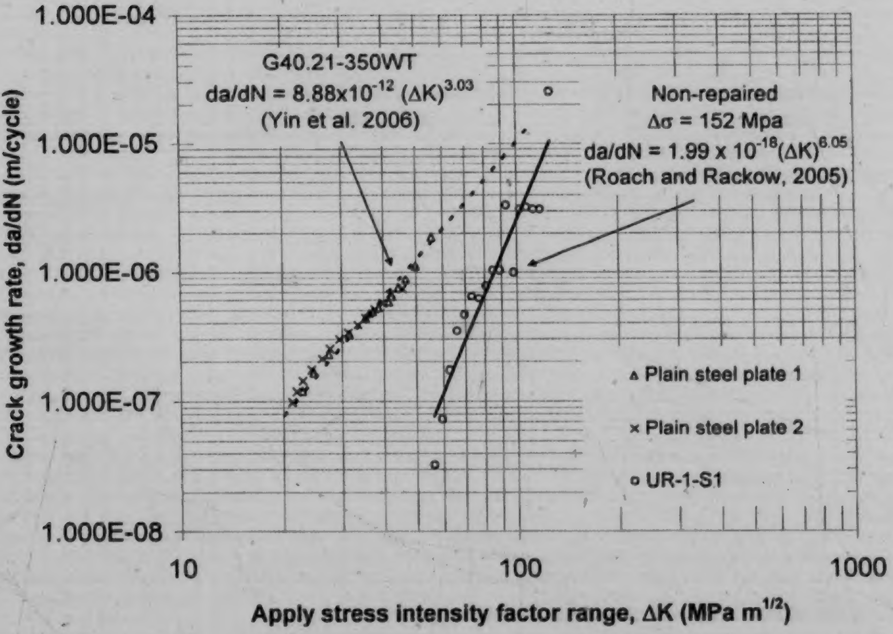

Figure 5.4 Crack growth rate versus apply stress intensity factor range of UR-1-S1

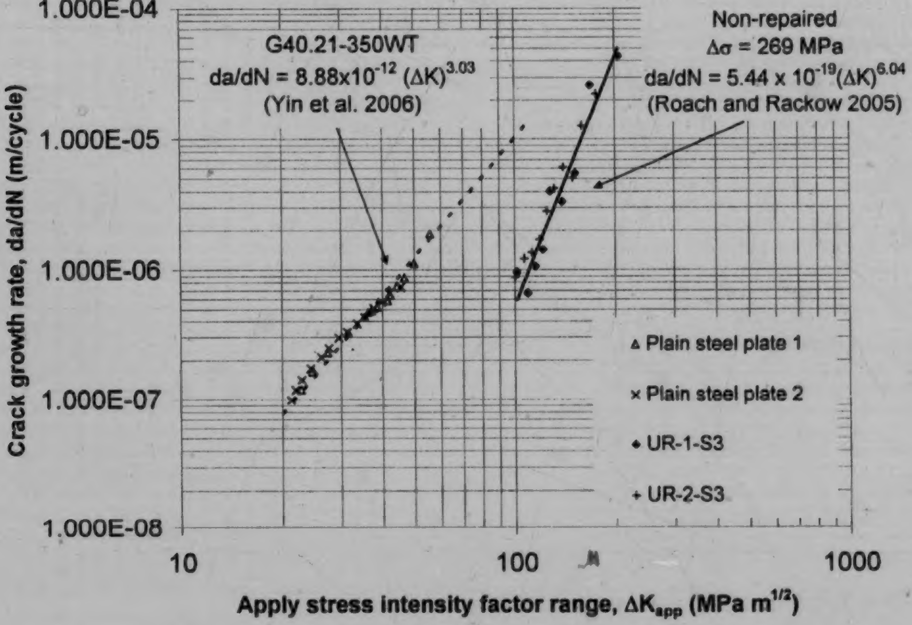

Figure 5.5 Crack growth rate versus apply stress intensity factor range of UR-1-S3 and UR-2-S3

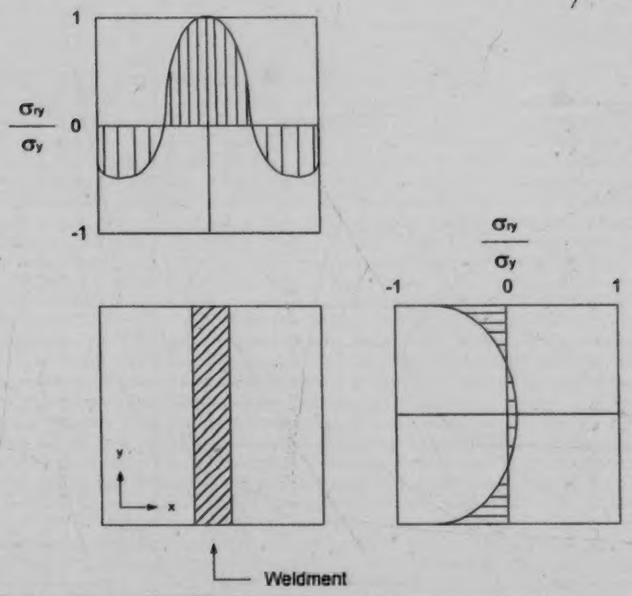
1
σry / σy
0
-1
σry / σy
-1
0
1
y
x
Weldment

Figure 5.6 General residual stress field pattern due to welding process

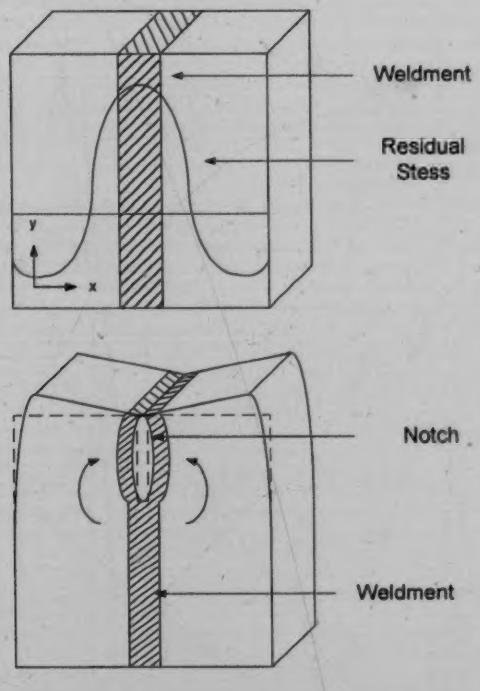
Weldment
Residual Stess
y
x
Notch
Weldment

Figure 5.7 Illustration of crack closure produced in a compact tension specimen by longitudinal residual welding stresses

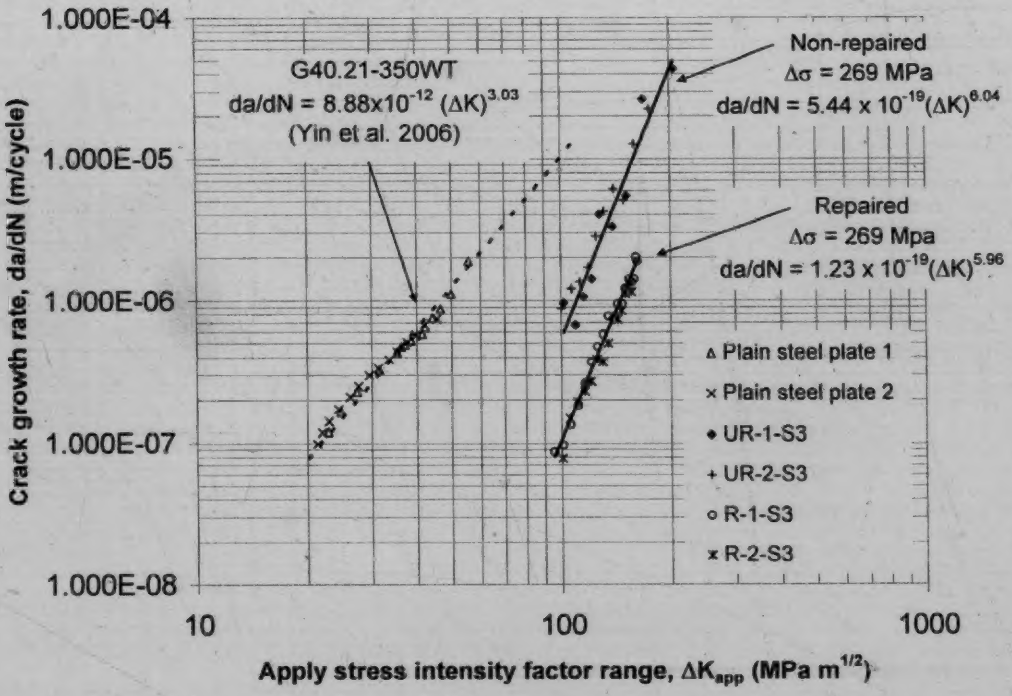

Figure 5.8 Comparison of crack growth rate of specimens with and without FRP patching

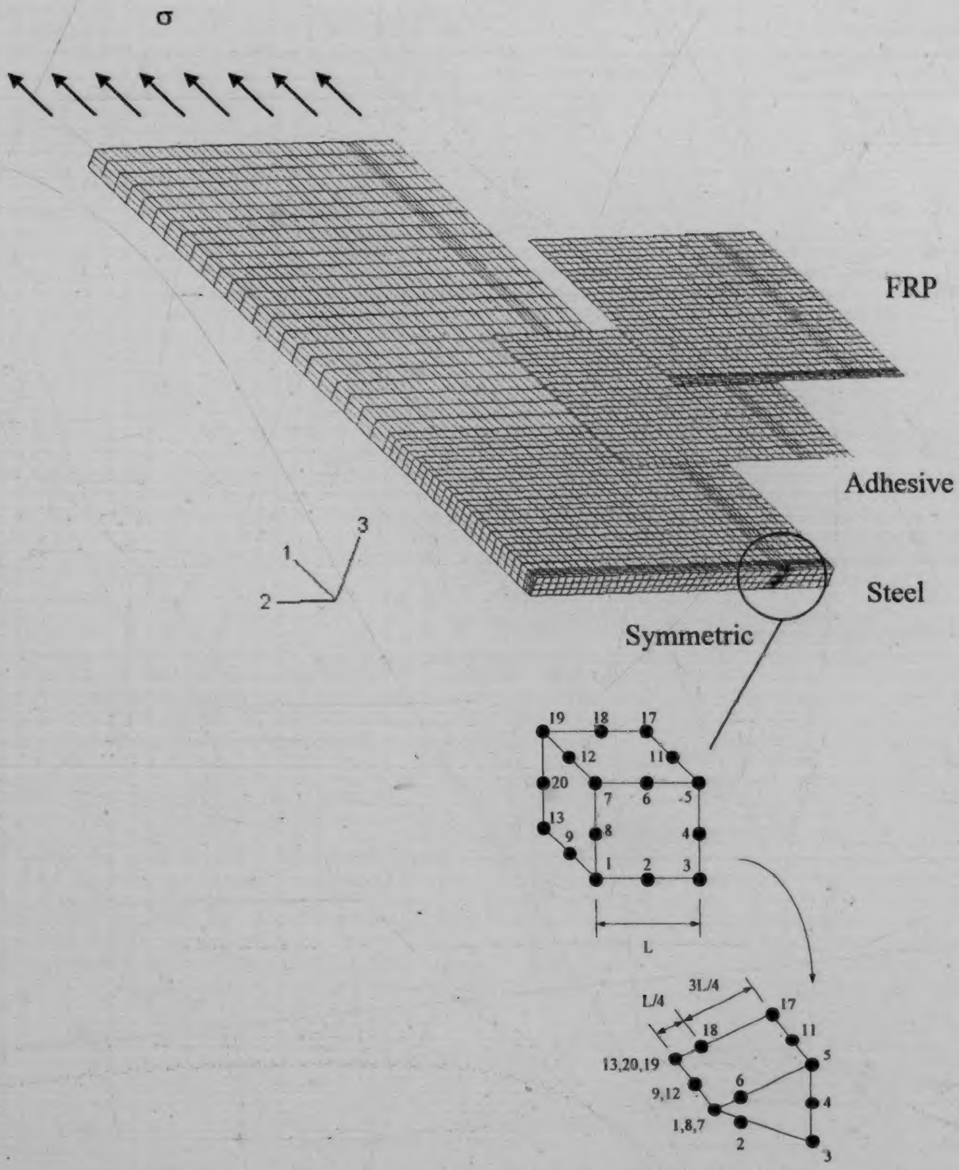
σ
FRP
Adhesive
Steel
Symmetric
1
2
3
19
18
17
12
11
20
7
6
5
13
9
8
4
1
2
3
L
L/4
3L/4
17
18
11
13,20,19
5
6
9,12
4
1,8,7
2
3

Figure 5.9 Typical finite element model of cracked steel plate with FRP patching

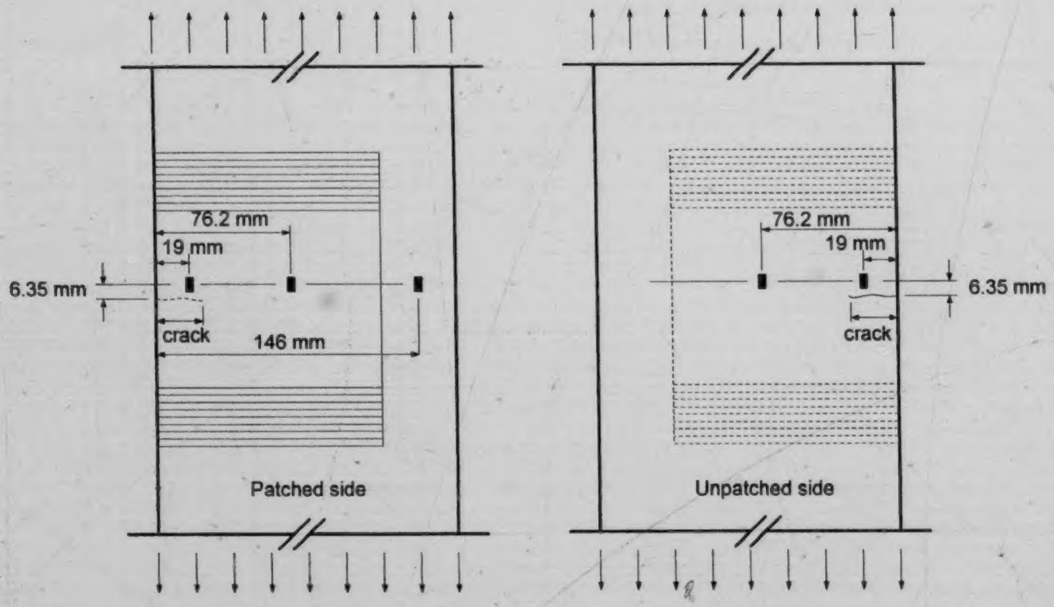
76.2 mm
19 mm
6.35 mm
crack
146 mm
Patched side
76.2 mm
19 mm
6.35 mm
crack
Unpatched side

Figure 5.10 Strain gauge location of test specimen of Roach and Rackow (2005)

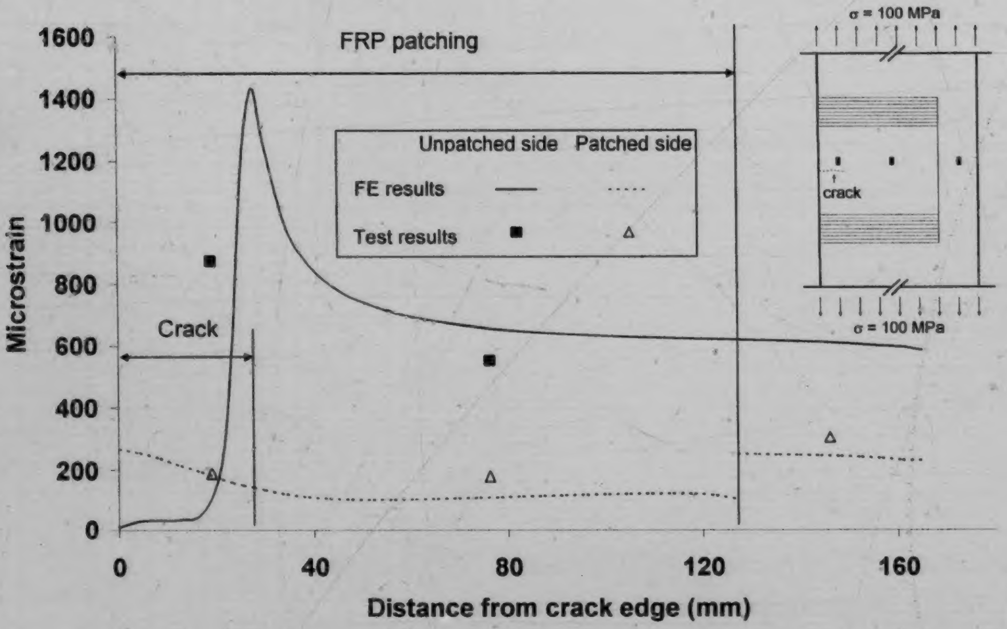

Figure 5.11 Comparison of strain results of test and finite element analysis

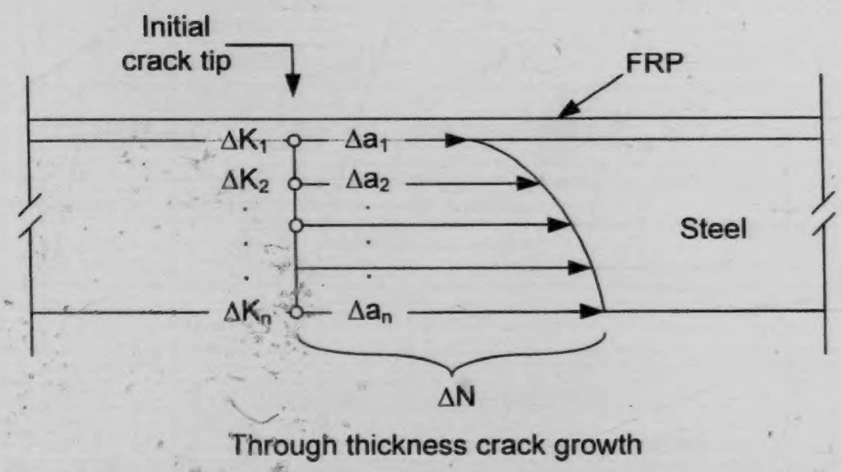
Initial crack tip
FRP
ΔK1
Δa1
ΔK2
Δa2
Steel
ΔKn
Δan
ΔN
Through thickness crack growth

Figure 5.12 Illustration of the local increments along the crack front

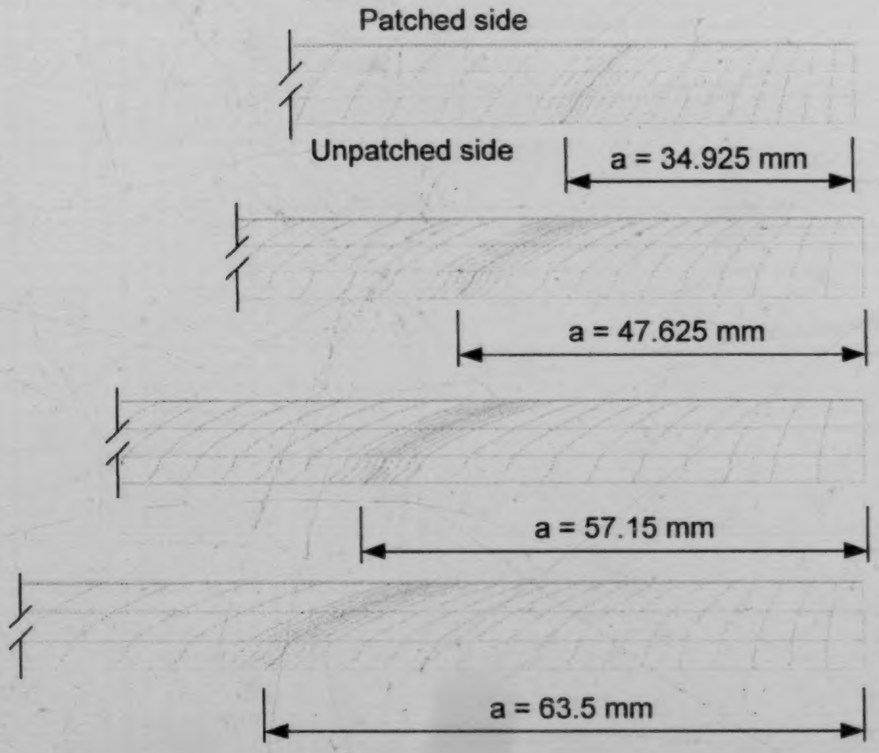
Patched side
Unpatched side
a = 34.925 mm
a = 47.625 mm
a = 57.15 mm
a = 63.5 mm

Figure 5.13 Finite element models with four different crack length

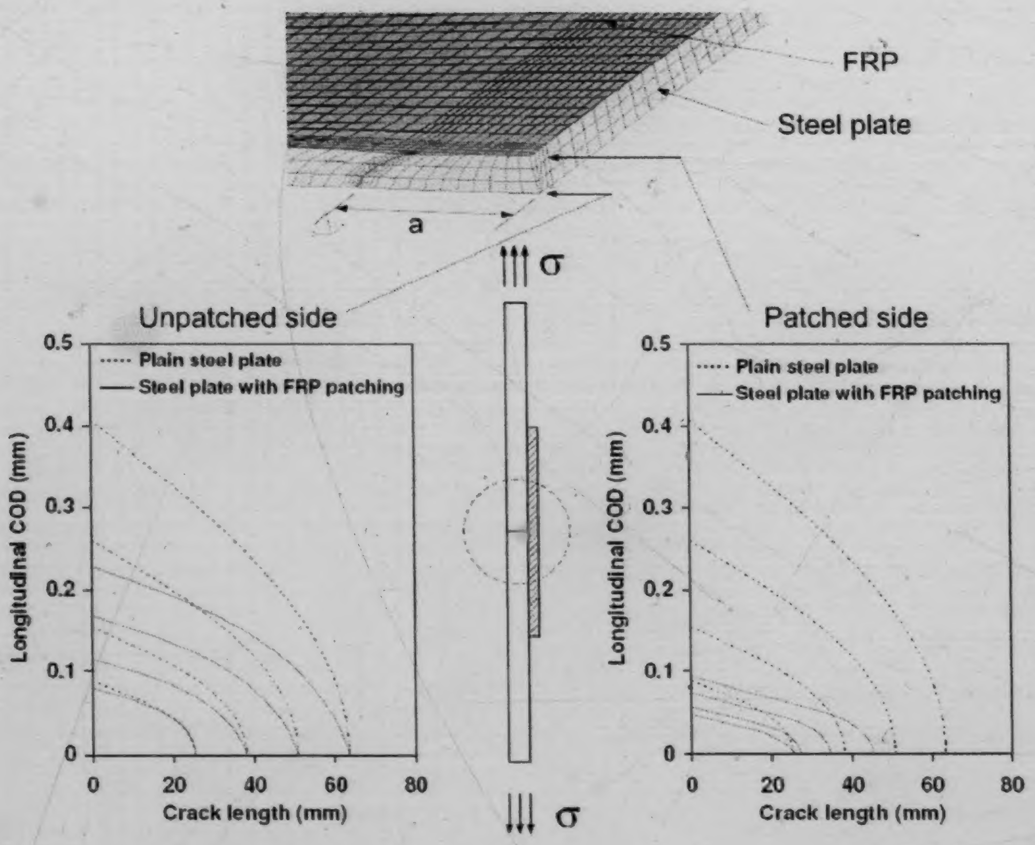

Figure 5.14 Crack opening displacement (COD) of patched and unpatched sides

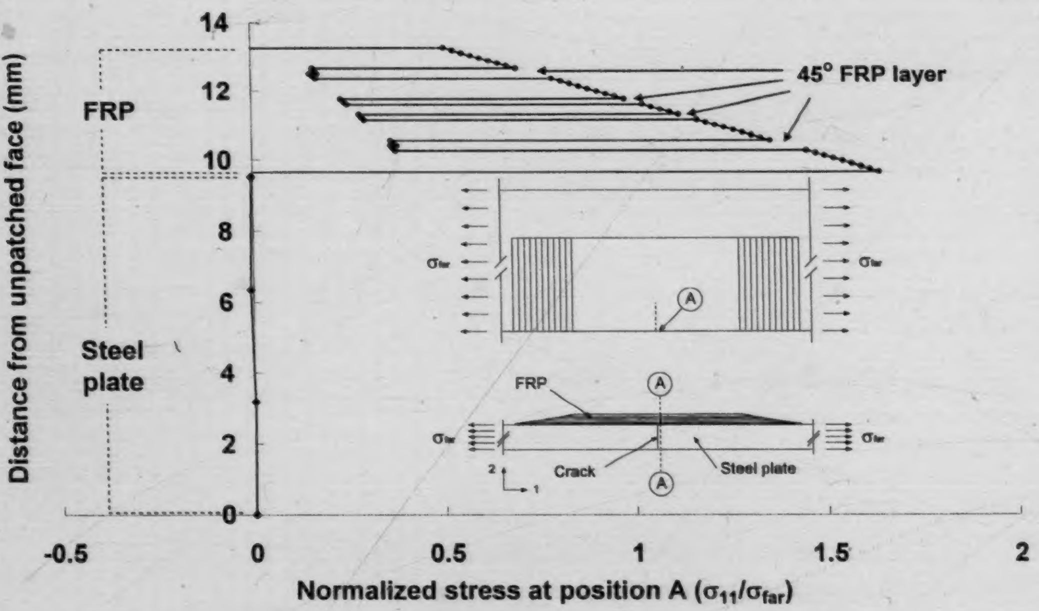

(a) Normalized stress at position A of plate with 25.4 mm crack length

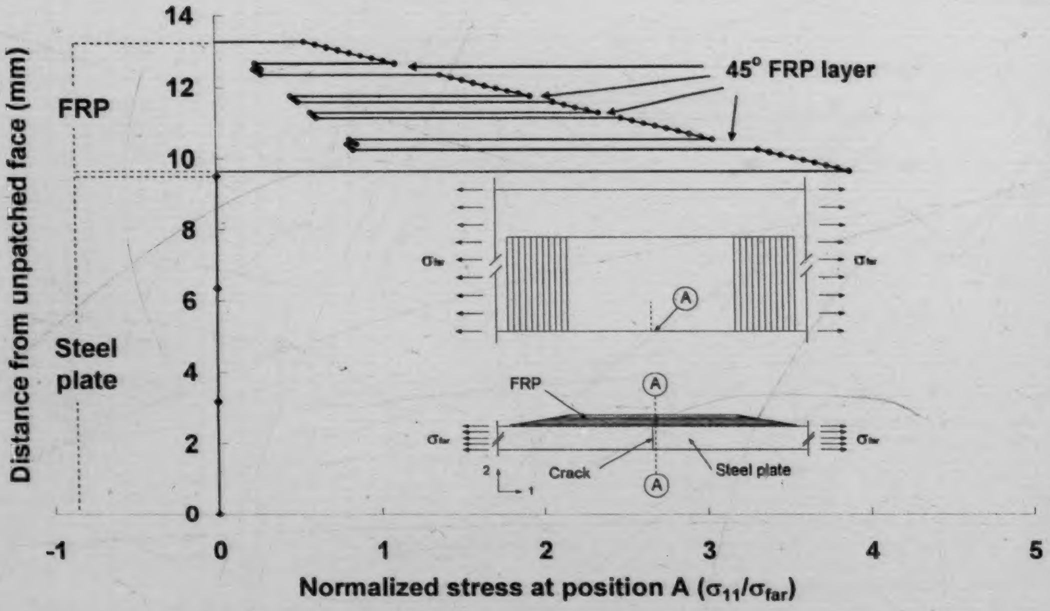

(b) Normalized stress at position A of plate with 63.5 mm crack length

Figure 5.15 Longitudinal normalized stress at position A of cracked plate

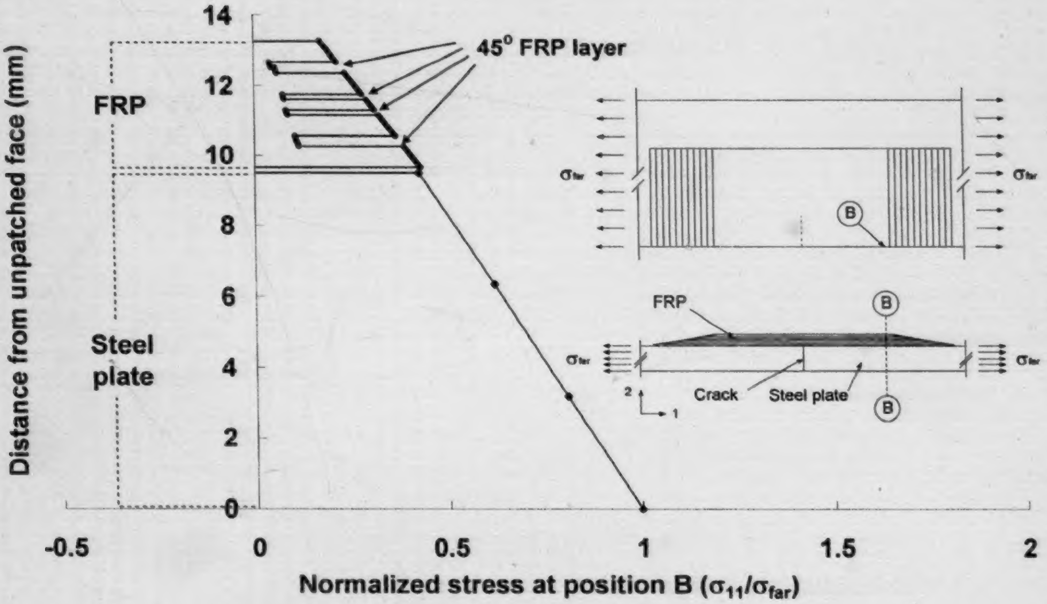

(a) Normalized stress at position B of plate with 25.4 mm crack length

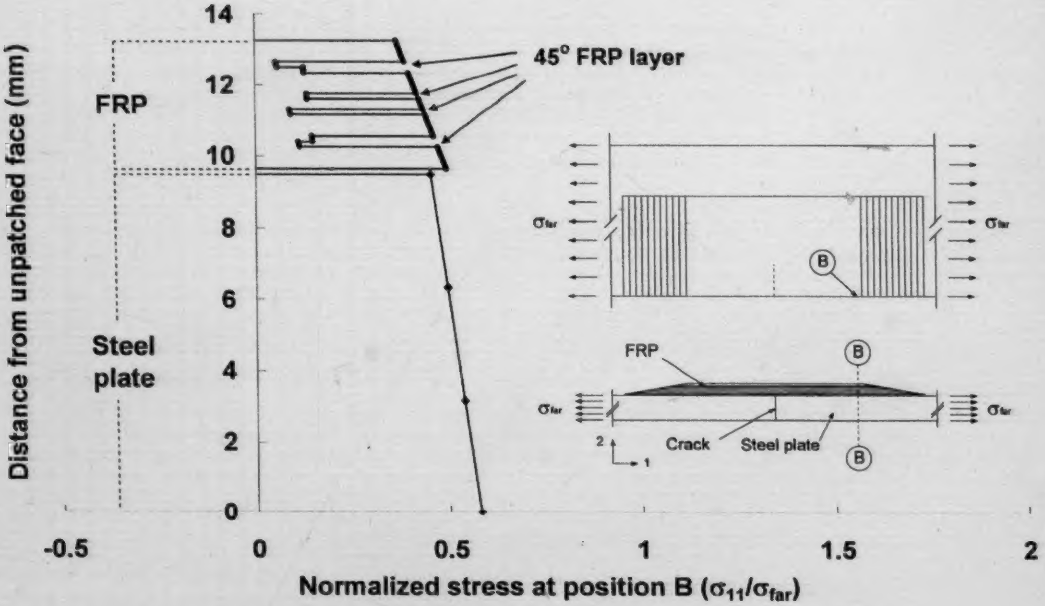

(b) Normalized stress at position B of plate with 63.5 mm crack length

Figure 5.16 Longitudinal normalized stress at position B of cracked plate

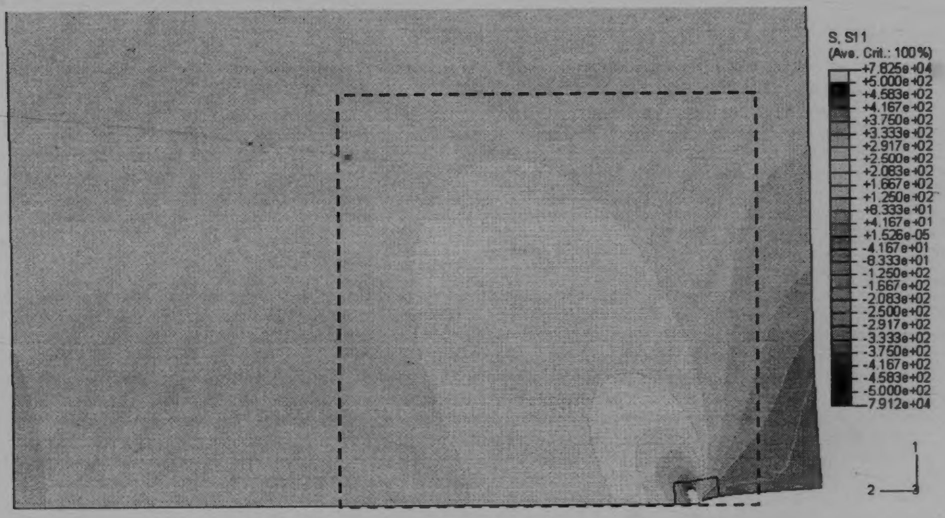

(a) cracked plate without FRP patching

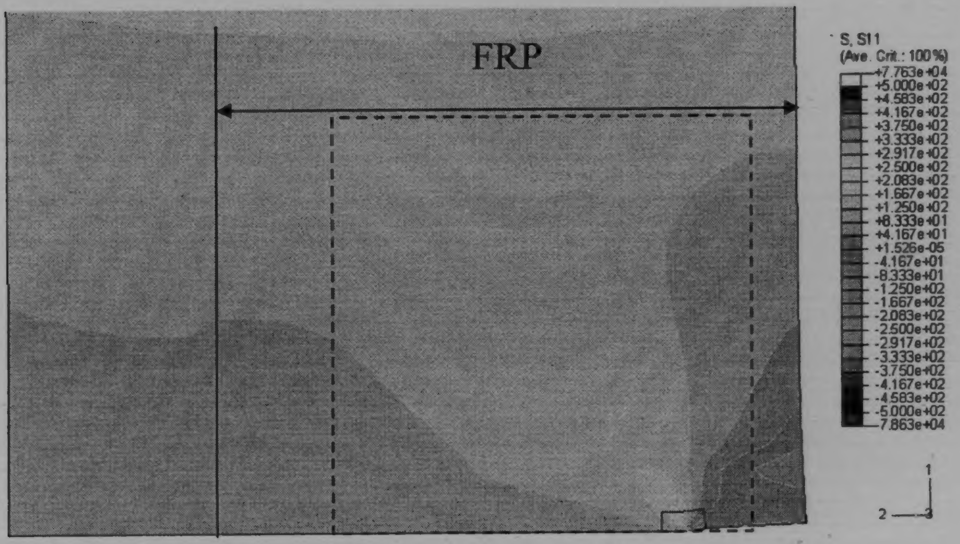

(b) cracked plate with FRP patching (stress contour on patched side)

Figure 5.17 Longitudinal stress contour of cracked plate with and without FRP patching (a = 25.4 mm)

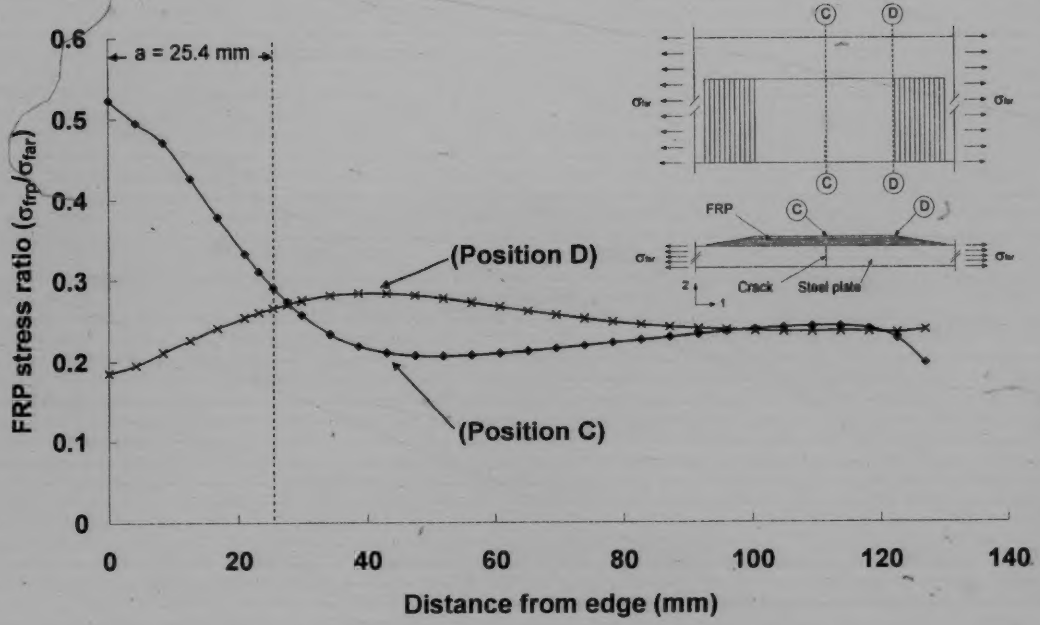

Figure 5.18 Normalized longitudinal stress of the outer surface of top layer of FRP at position C and D

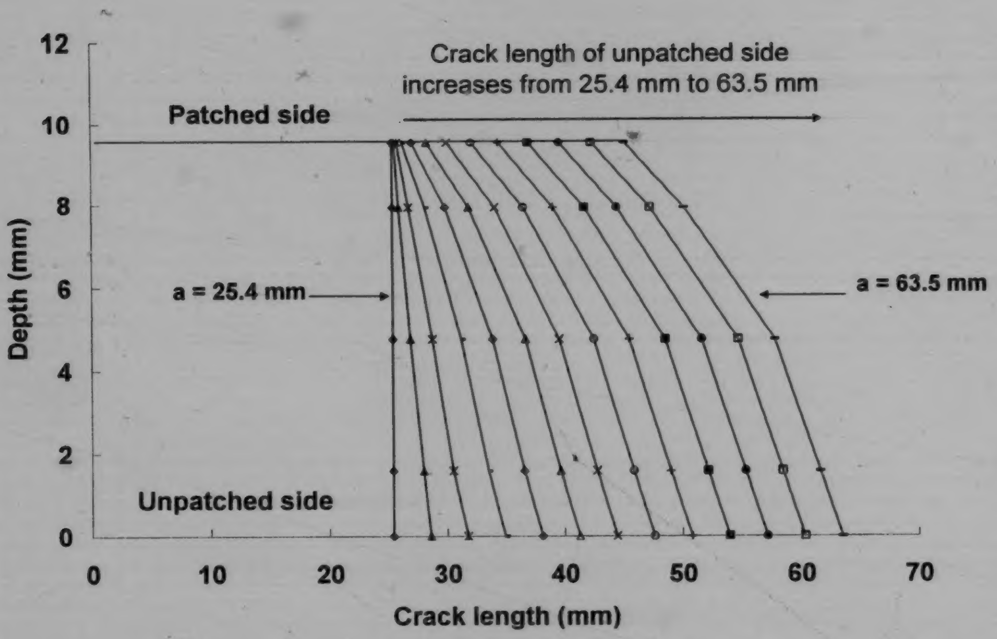

Figure 5.19 Finite elemnt results of crack propagation of patched and unpatched sides

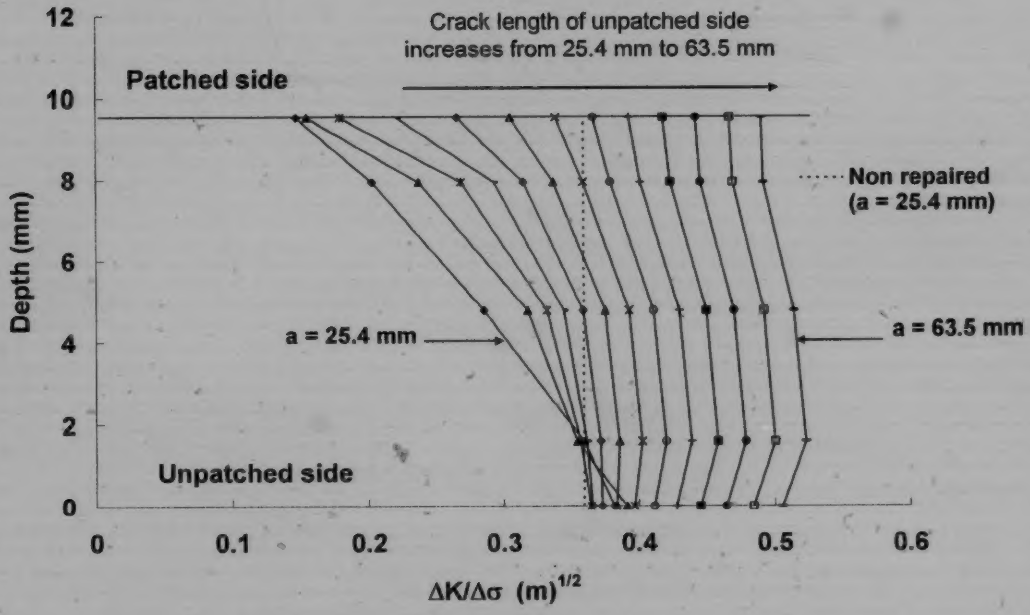

Figure 5.20 Through thickness normalized SIF versus crack length

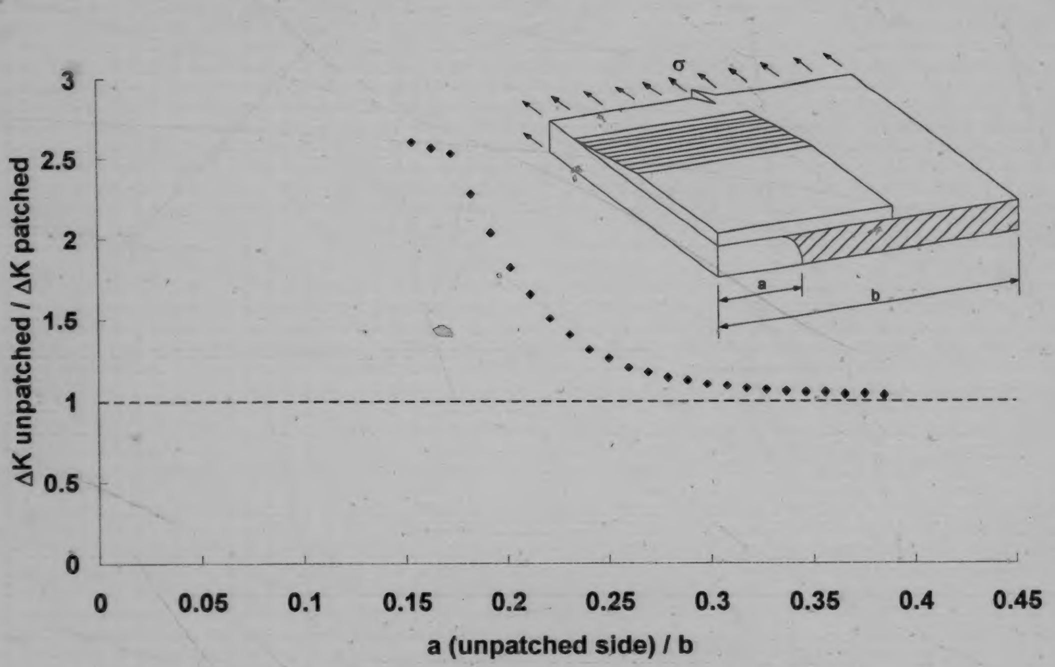

Figure 5.21 Ratio of ΔK of patched and unpatched side

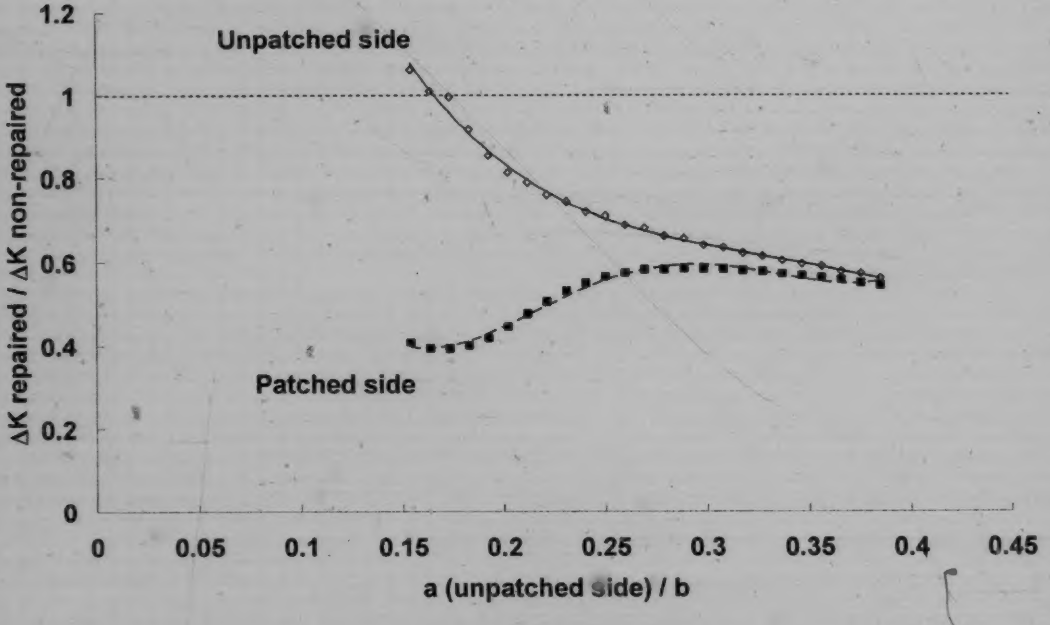

Figure 5.22 Ratio of ΔK of repaired and non-repaired specimens

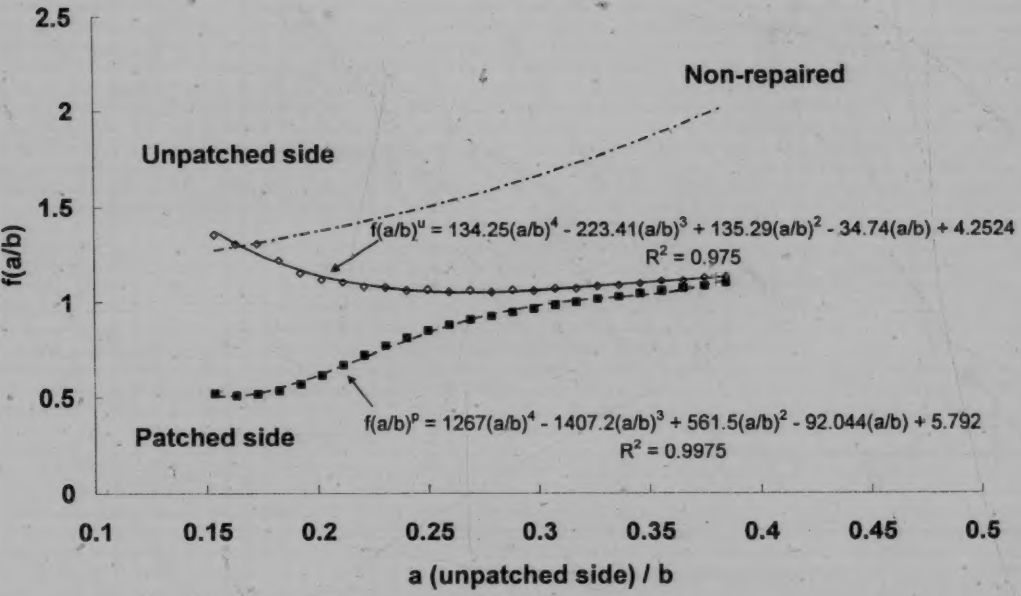

Figure 5.23 f(a/b) value of repaired and non-repaired specimens

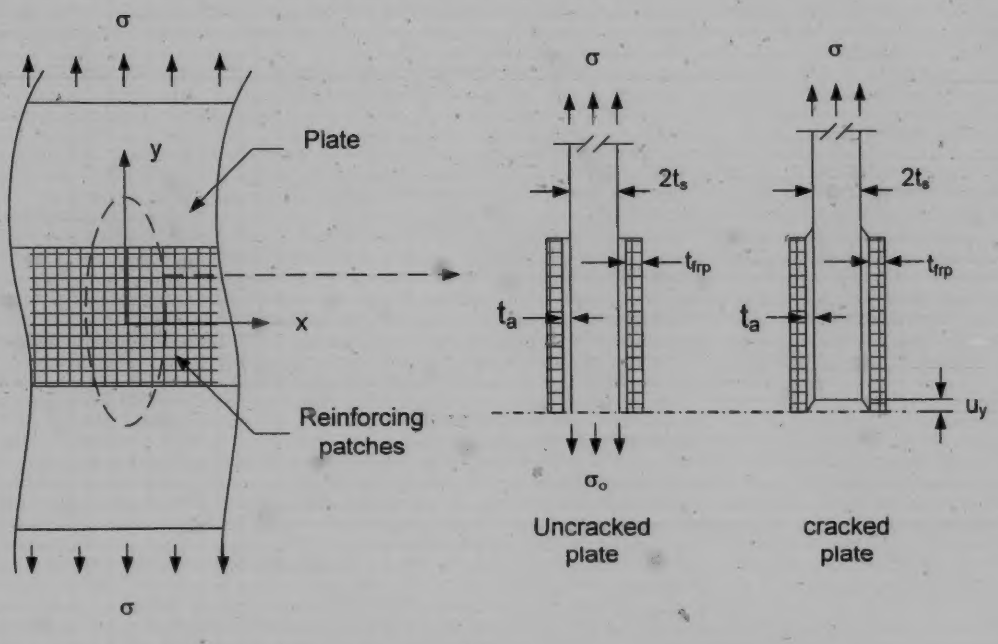
σ
Plate
y
x
Reinforcing patches
σ
σ
$2t_s$
t_{frp}
t_a
σ_o
Uncracked plate
σ
$2t_s$
t_{frp}
t_a
u_y
cracked plate

Figure 5.24 An infinitely wide plate with bonded reinforcements

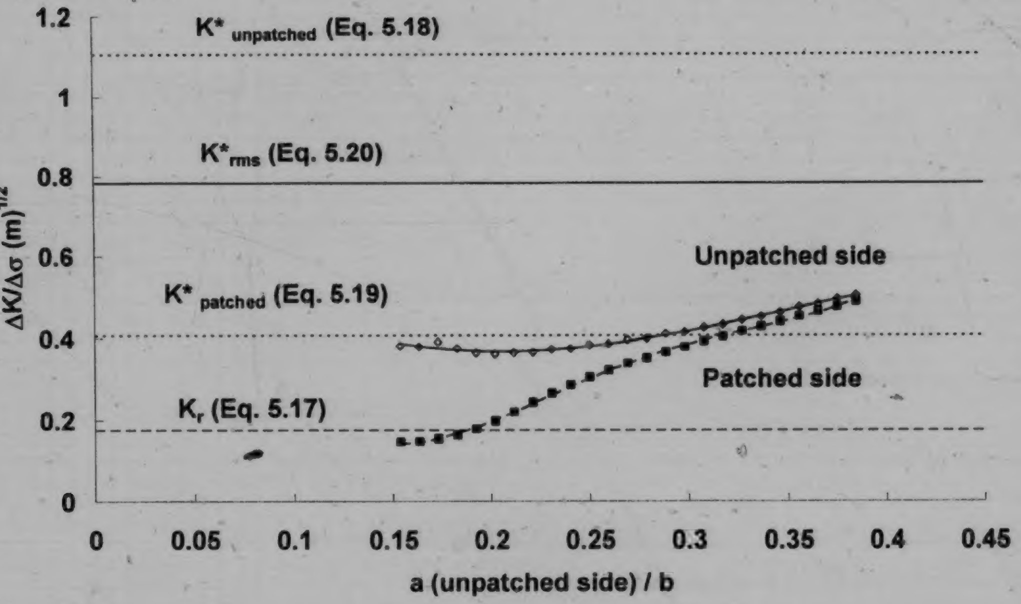

Figure 5.25 Comparison of finite element results with the predictions given by Eqs. 5.17 to 5.20

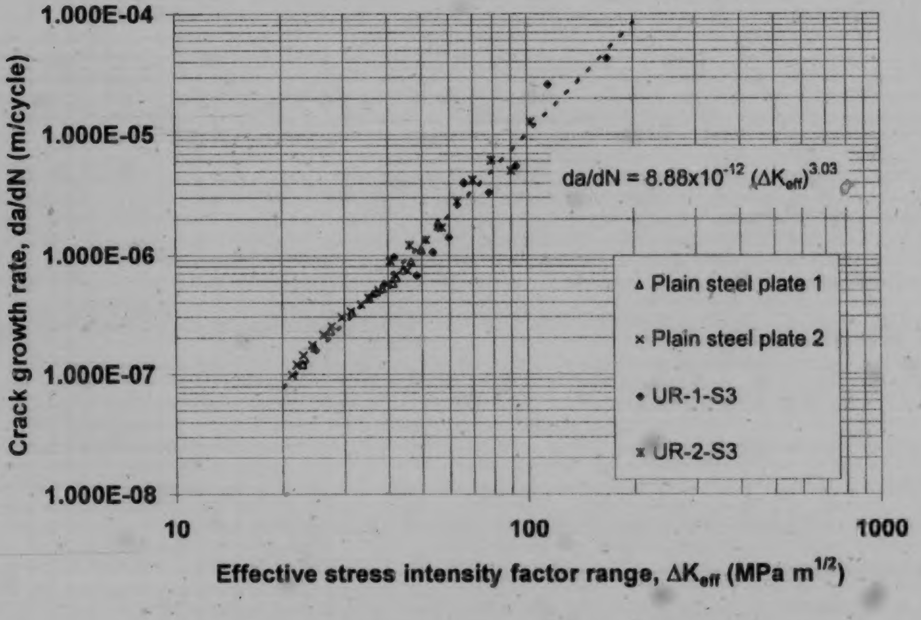

Figure 5.26 Crack growth rate versus effective stress intensity factor range of welded specimens

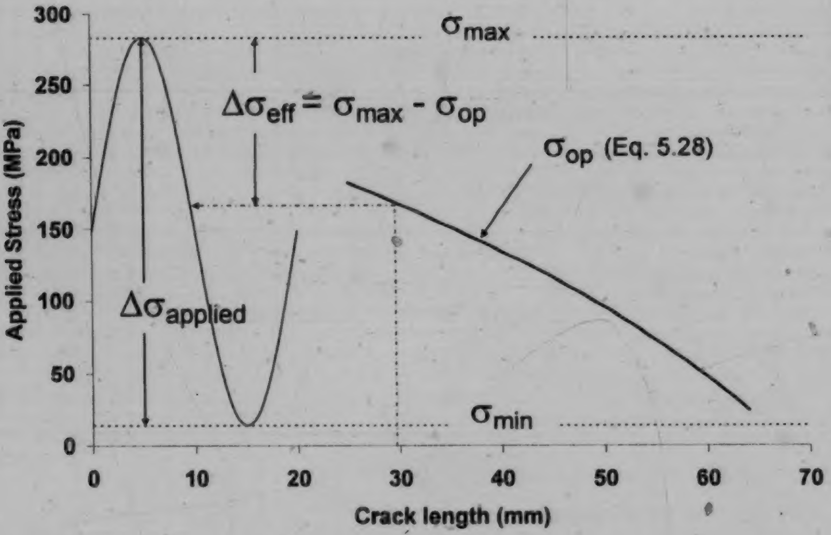

Figure 5.27 Illustration of the effective stress and opening stress

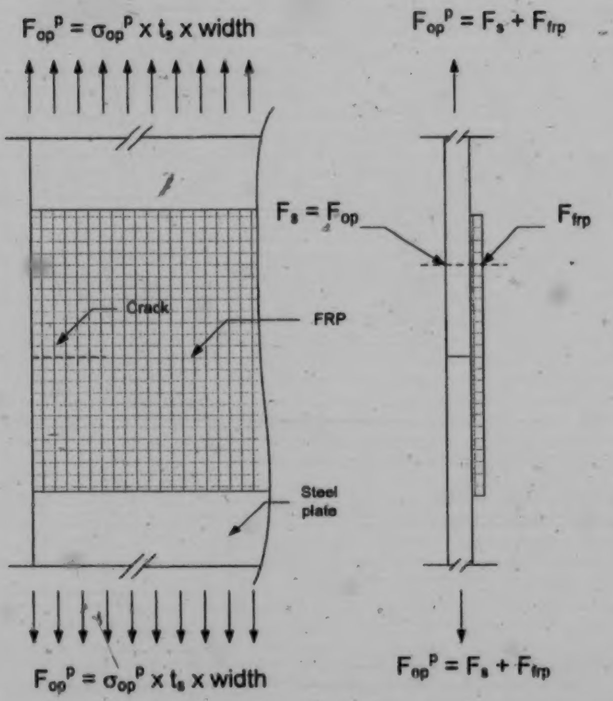
$F_{op}^{P} = \sigma_{op}^{P} \times t_s \times$ width
$F_{op}^{P} = F_s + F_{frp}$
$F_s = F_{op}$
F_{frp}
Crack
FRP
Steel plate
$F_{op}^{P} = \sigma_{op}^{P} \times t_s \times$ width
$F_{op}^{P} = F_s + F_{frp}$

Figure 5.28 Illustration of opening stress for specimen with FRP patching

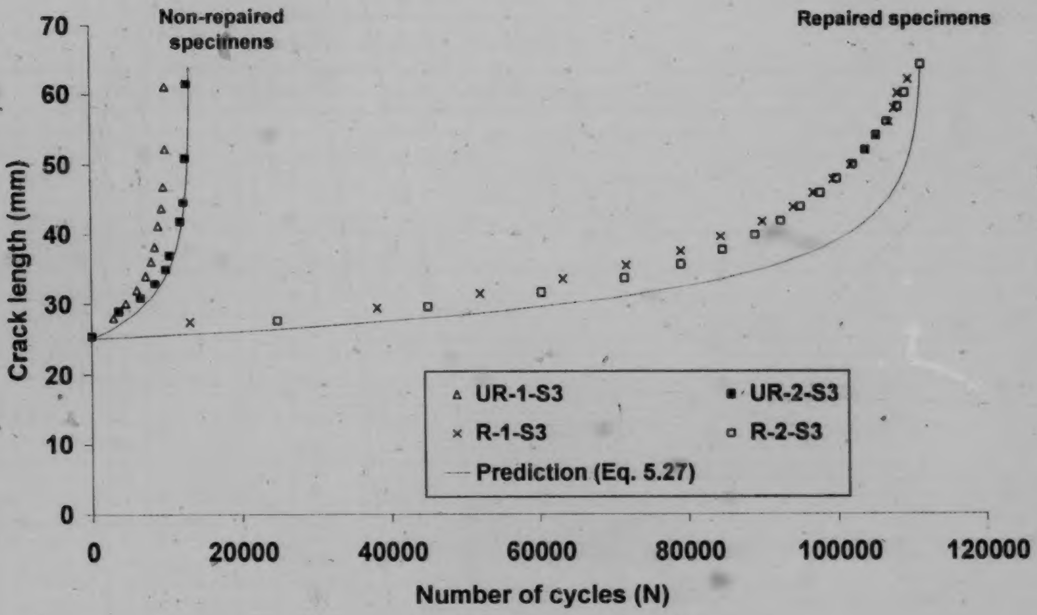

Figure 5.29 Comparison of the fatigue life of test and predicted results ($\Delta\sigma$ = 269 MPa)

5.7 References

Anderson, T. L., 2005, Fracture Mechanics, CRC Press - Taylor and Francis Group, pp. 334

Barson, J. M. and Rolfe, S. T., 1999, Fracture and fatigue control in structures, ASTM manual series: MNL 41, pp. 213

Elber, W., 1971, The significance of fatigue crack closure, ASTM STP 486, American Society for Testing and Materials, pp. 230-242

Gross, B. and Srawley, J. E., 1964, "Stress intensity factors for a single notch tension specimen by boundary collocation of a stress function", NASA TN D-2395

Hibbitt, Karlsson & Sorenson, Inc., 2004, "ABAQUS Version 6.4", ABAQUS/Standard User's Manual Volumes I and II, Pawtucket, Rhode Island, U.S.A.

Lee, W-Y and Lee, J-J, 2004, "Successive 3D FE analysis technique for characterization of fatigue crack growth behavior in composite-repaired aluminum plate", Composite Structures, 66, pp. 513 - 520

Link, L. R., 1990, "Fatigue crack growth of weldments", Fatigue and Fracture Testing of Weldments, ASTM STP 1058, pp. 16 – 33

Paris, P.C. and Erdogan, F., 1960 "A critical analysis of crack propagation laws", Journal of Basic Engineering, Vol. 85, pp. 528-534

Roach, D. and Rackow, K., 2005, "Development of bonded composite doublers for the repair of oil recovery equipment", Sandia National Laboratories, Sandia report, Sand2005-3195

Rose, L. R. F., 1982, "A cracked plate repaired by bonded reinforcements", International Journal of Fracture, Vol. 18, No. 2, pp. 135 – 144

Specialty Materials Inc., 2002, Lowell, MA, U.S. A., 5521 Boron Epoxy Prepreg Tape. Available from http://www.specmaterials.com/5521site.htm.

Wang, C. H., Rose, L. R. F. and Callinan, R., 1998, "Analysis of out-of-plane bending in one-sided bonded repair", International Journal of Solids and Structures, Vol. 35, No. 14, pp. 1653 – 1675

Yin, Y., Grondin, G. Y. and Elwi, A. E. 2006. "Fatigue crack behaviour in Mine Excavator", Structural Engineering Report No. 265, University of Alberta, Department of Civil & Environmental Engineering, pp. 35

6 PARAMETRIC STUDY OF CRACKED STEEL PLATES WITH FRP PATCHING – FINITE ELEMENT ANALYSIS

6.1 Introduction

In the previous chapter, finite element models were developed for determining the stress intensive factor (SIF) of edge cracked steel plates with single-side fiber reinforced polymer (FRP) patching. The finite element results showed that a reduction of SIF is observed on the patched side. However, the SIF on the unpatched side is increased marginally when the crack tip shape is uniform. As the SIF varies along the crack front in the case of single-side repairs, it implies that the crack will grow at a different rate on the patched side than on the unpatched side. Based on the various values of SIF along the crack front, simulation of the non-uniform crack propagation along the crack front was carried out by means of a finite element method and the SIF of both the patched and unpatched side were obtained. The finite element results showed that the through thickness SIF becomes more uniform across the thickness of the plate as the crack length grows gradually.

In the finite element study presented in the previous chapter, the adherend stiffness ratio (ETR) of the FRP-to-the steel plate was assigned as 0.3 and only the case of a steel plate with edge crack and with single-side FRP patching was studied in the finite element analysis. In order to investigate the effect of different adherend stiffness ratios (ETR) of FRP-to-steel plate, type of patching, such as single-side or double-side, and the form of crack, such as edge crack or central crack, a parametric study of cracked steel plates with FRP patching is carried out in this chapter. Four different cases were examined: (a) a steel plate with edge crack and single-side FRP patching; (b) a steel plate with central crack and single-side FRP patching; (c) a steel plate with edge crack and double-side patching; and, (d) a steel plate with central crack and double-side patching. Three different parent plate thicknesses were considered with a constant adherend stiffness of FRP patching. The numerical crack grow procedure which was discussed in Section 5.3 for determining the crack length and the corresponding SIF across the thickness of the plate was adopted for each finite element parametric analysis.

6.2 Finite element model

The finite element model which was developed in the previous chapter for determining the SIF of the test specimens is used in the parametric study. The modified three layers finite element models consisted of 3-D brick element for modeling the cracked steel plate and 3-D shell element for modeling the adhesive and FRP patching. Suitable constraint conditions were assigned for constraining the relative movement of the steel plate, adhesive and FRP patching. Details of the finite element model and constraint condition are described in Chapter 4. The FRP patching of the finite element model was modeled by assigning the material properties of Sika Carbodur (Sika 2003) for the carbon fiber reinforced polymer (CFRP). Detail of the parameters is discussed in the following section.

6.2.1 Geometry and material properties of steel plate, crack pattern and form of FRP patching

In the finite element parametric study presented here, several parameters were included. They included the thickness of the steel plate, the edge crack/central crack pattern and single-side/double-side FRP patching. For modeling the FRP patching, the material properties of the CFRP plates (Sika 2003) which were used for the lap joint tests reported in Chapter 3 were used in the finite element models. The Sika CFRP is a pre-fabricated composite plate with thickness of 1.2 mm. Three layers of the Sika CFRP plate were used in the finite element models. Therefore, the total thickness of the CFRP plate was 3.6 mm. The material properties of the Sika CFRP plate are listed in Table 6.1. One of the parameters used in this study is the adherend stiffness ratio of steel plate-to-CFRP which is defined as ETR (= $E_{frp}E_{frp}$ / E_st_s). In order to achieve three different adherend stiffness ratios of CFRP patching to steel plate (ETR = 0.33, 0.2 and 0.13), three different steel plate thicknesses (t_s = 9.5 mm, 16 mm and 25 mm for single-side patching models and t_s = 19 mm, 32 mm and 50 mm for double-side patching models) were used. The thickness of the CFRP patching was kept the same for all models. The geometry of the steel plate with edge crack, single-side and double-side CFRP patching is shown in Figure 6.1. The geometry of the steel plate with a central crack, single-side and double-side CFRP patching is shown in Figure 6.2. The width of the steel plate used in the F.E. models with edge crack was 165 mm, which is the same as that of the test specimens reported by Roach and Rackow (2005). In order to maintain the same crack length to plate width ratio (a/b), the width of the steel plate model with central crack was taken as 330 mm. The width of the CFRP patching was 100 mm which is about 4 times the length of the initial crack length for edge crack models. Similarly, the width of the CFRP patch was designed to be 200 mm, which is also about 4 times the length of the initial crack length for the central crack models. The length of the CFRP patching was 120 mm for the non-tapered region and 60 mm each for the tapered ends. Therefore, the total length of the CFRP patching was 240 mm. The material properties which were assigned in the finite element model for the steel plate, adhesive, and CFRP patching, are listed in Table 6.1 while the combination of the parameters used are shown in Table 6.2.

6.2.2 Finite element model of cracked plate with different crack pattern and form of FRP patching

For the models of edge crack steel plate with single-side CFRP patching, only half of the plate was modeled due to symmetry of geometry. For the central crack steel plate with single-side CFRP patching models and the edge crack steel plate with double-side CFRP patching models, a quarter of the plate was modeled by assigning symmetrical boundary condition to the edge for central crack steel plates and to the unpatched face for edge crack steel plate with double-side patching. For the central crack steel plate models with double-side CFRP patching, one eighth of the plate was modeled by assigning symmetrical boundary condition to both the edge and the unpatched face. Illustrations of the finite element models for the various cases are shown in Figure 6.3 to Figure 6.6. At the location of crack tip, collapsed elements with middle nodes located at quarter point were used in order to obtain the stress intensity factor at the crack tip by means of contour integration methods. The adhesive and the CFRP patching were modeled using shell elements. Composite shell elements were used to model the CFRP plates and the adhesive between the CFRP plates. As illustrated in Figure 6.7, there are three layers of CFRP plate each 1.2 mm thick and two layers of adhesive of 0.5 mm thick. These five layers of materials were modeled by using the composite shell element. The material properties of each layer of the materials were assigned to the shell element by introducing the key word "composite" in the input file of ABAQUS (Hibbitt et al. 2004). The numerical fatigue crack growth technique which was discussed in Chapter 5; was applied to the finite element model used in the parametric study. The initial crack length, defined as a_i for edge crack models was 25.4 mm and $2a_i$ for the central crack models is 50.8 mm. The SIF of the crack front according to two far end stress levels (σ_{min} = 14 MPa and σ_{max} = 283 MPa), defined as the high stress range spectrum were obtained. Therefore, the corresponding stress range ($\Delta\sigma$) was 269 MPa and the SIF range (ΔK) was defined as the difference between K_{max} and K_{min}. After the first successive analysis of the SIF along the uniform initial crack front, the crack growth values through the thickness of the plate were calculated using Eq. 5.8 with the material constant, m equal to 3 (Barsom and Rolfe 1999). Then, another finite element model was set up by using the updated non-uniform crack front and the corresponding SIF along the crack. With a maximum crack growth value ($\Delta a_{max}^{(j)}$) of the unpatched side equal to 1.5875 mm, 24 finite element models for each case were formed according to the results of the SIF to achieve a final crack length of 63.5 mm which is defined as a_f for edge crack models and 127 mm which is defined as $2a_f$ for central crack models.

6.3 Finite element results

The finite element results are presented in the following section according to the form of patching (single-side or double-side) and the crack pattern (edge crack or central crack). For those models with single-side patching, the profile of the normalized stress intensity factor ($\Delta K/\Delta\sigma$) along the crack front is presented. Then, comparisons of the normalized stress intensity factor ($\Delta K/\Delta\sigma$) of plates with and without FRP patching are shown. For plates with the same crack pattern, the results are further compared to examine the effect of single-side/double-side CFRP patching on the reduction of the SIF on the patched and unpatched sides. Based on the results of the SIF, correction factors for the geometry of each model with different crack patterns and form of patching are proposed and compared with correction factors of the cracked steel plate without CFRP patching.

6.3.1 Plates with an edge crack and single-side patching

The crack growth propagation and the normalized stress intensity factor ($\Delta K/\Delta\sigma$) through the thickness of the crack of every two steps are shown in Figure 6.8 to Figure 6.10 for the edge crack models with various ETR values (ETR = 0.13, 0.2 and 0.33). As shown in those figures, for models with different ETR values, significant reduction of the values of $\Delta K/\Delta\sigma$ were observed on the patched side for models with initial crack length a_i = 25.4 mm. Larger reduction of $\Delta K/\Delta\sigma$ was observed for models with larger ETR values. Values of $\Delta K/\Delta\sigma$ versus the ratio of crack length of unpatched sides to the width of the steel plate (a/b) of non-repaired model were obtained from Eq. 6.1.

$$\Delta K / \Delta\sigma = f(a/b)\sqrt{\pi a} \quad (6.1)$$

where f (a/b) is a correction factor for the geometry of the specimen. For plate with edge crack subjected to uniform far end stress, f(a/b) is calculated according to Eq. 6.2 (Gross and Srawley 1964).

$$f(a/b) = 1.12 - 0.231\left(\frac{a}{b}\right) + 10.55\left(\frac{a}{b}\right)^2 - 21.72\left(\frac{a}{b}\right)^3 + 30.39\left(\frac{a}{b}\right)^4 \quad (6.2)$$

where a is the edge crack length and b is the width of plate. With a = 25.4 mm and b = 165 mm, the corresponding ΔK/Δσ was calculated for the non-repaired model according to Eqs. 6.1 and 6.2 and the values are shown in Figure 6.8 to Figure 6.10. Comparing the values of ΔK/Δσ of plates with single-side CFRP patching and the non-repaired plates, the reduction in ΔK/Δσ is 62%, 52% and 42% for plates with ETR value equal to 0.33, 0.2 and 0.13, respectively. On the other hand, almost no reduction in the value of ΔK/Δσ was observed on the unpatched side for those plates.

The value of ΔK/Δσ versus a/b for models with various ETR values is shown in Figure 6.11 and Figure 6.12. As shown in the figures that for an edge crack plate with single-side patching, as the crack length becomes longer, the value of ΔK/Δσ is almost the same for plates with different ETR values. As the crack becomes longer, the value of ΔK/Δσ of the patched side increases and approaches the value of the unpatched side. Values of ΔK/Δσ of the non-repaired plates were shown in the figures for comparison. It is shown that when a/b is equal to 0.38 (crack length corresponding to the final crack length), the reduction of ΔK/Δσ is about 55% on the patched side and 40% on the unpatched side.

6.3.2 Plate with an edge crack and double-side patching

For the plates with an edge crack plate and with double-side patching, the plot of the values of ΔK/Δσ versus the ratio of crack length-to-width of the steel plate (a/b) of the patched side and the plane of symmetry are shown in Figure 6.13 and Figure 6.14 for plates with various values of ETR. The figures show that a larger reduction of ΔK/Δσ is observed for models with larger ETR value. The values of ΔK/Δσ at the plane of symmetry are about 13% larger than those at the patched side. However, the trend of the ΔK/Δσ values for the patched side is similar to that of the plane of symmetry. Compared to the non-repaired plate, in plates with initial crack length a_i equals to 25.4 mm, the reduction of ΔK/Δσ on the patched side are 47%, 36% and 29% for models with ETR value equal to 0.33, 0.2 and 0.13, respectively. As the crack length increases, the reduction of the values of ΔK/Δσ for plates with different ETR values becomes larger. It was found that for plates with final crack length a_f equals to 63.5 mm, the reduction of ΔK/Δσ are 72%, 62% and 53% for plates with ETR values equal to 0.33, 0.2 and 0.13, respectively.

6.3.3 Central crack model with single-side patching

The crack growth propagation and the normalized stress intensity factor (ΔK/Δσ) through the thickness of the crack of every two steps are shown in Figure 6.15 to Figure 6.17 for plates with various ETR values (ETR = 0.13, 0.2 and 0.33). Similar to the case of plates with an edge crack and with single-side patching, it is shown from the figures that for plates with a central crack and various ETR values, significant reduction of the normalized stress intensity factor ($\Delta K/\Delta\sigma$) are observed on the patched side for plates with initial crack length a_i equals to 25.4 mm. Larger reduction of $\Delta K/\Delta\sigma$ was observed for models with larger ETR value. The value of $\Delta K/\Delta\sigma$ of non-repaired plates with initial crack length ($2a_i$) equal to 50.8 mm and steel plate width (2b) equal to 330mm, was calculated according to Eq. 6.1 with the correction factor f(a/b) obtained according to Eq. 6.3 (Tada et al. 1985), as follows.

$$f(a/b)=\left(1-0.025\left(\frac{a}{b}\right)^2+0.06\left(\frac{a}{b}\right)^4\right)\sqrt{\sec\left(\frac{\pi a}{2b}\right)} \tag{6.3}$$

where a is half of the crack length and b is half of the width of cracked plate.

Compared to the non-repaired plates, the reduction of $\Delta K/\Delta\sigma$ is 58%, 46% and 36% for plates with ETR values equal to 0.33, 0.2 and 0.13, respectively. However, the values of $\Delta K/\Delta\sigma$ on the unpatched side were observed to be larger than those of the non-repaired plates. The increase of $\Delta K/\Delta\sigma$ on the unpatched side is 14%, 10% and 8% for plates with ETR value equal to 0.33, 0.2 and 0.13, respectively. The values of $\Delta K/\Delta\sigma$ versus the ratio of crack length-to-width of the steel plate (a/b) are shown in Figure 6.18 to Figure 6.19 for plates with various ETR values along with the computed value of $\Delta K/\Delta\sigma$ of non-repaired plates. As shown in the figures, for plates with a central crack and with single-side patching, when the crack length increases, the value of $\Delta K/\Delta\sigma$ is almost the same for models with different ETR values. As the crack becomes longer, the value of $\Delta K/\Delta\sigma$ of the patched side increases and approaches the value of the unpatched side. When a/b is equal to 0.38 (crack length corresponding to final crack length), the reduction of $\Delta K/\Delta\sigma$ is about 27% on the patched side and 16% on the unpatched side.

6.3.4 Plate with a central crack and double-side patching

For the plates with a central crack and double-side patching, the plot of the value of $\Delta K/\Delta\sigma$ of patched side and plane of symmetry versus the ratio of crack length to the width of the steel plate (a/b) are shown in Figure 6.20 and Figure 6.21 for plates with various ETR values. The figures show that a larger reduction of $\Delta K/\Delta\sigma$ is observed for models with larger ETR values. Similar to the plates with an edge crack and double-side patching, the stress intensity factor of the plane of symmetry is about 11% larger than that of the patched side. However, the trend of the $\Delta K/\Delta\sigma$ of the plane of symmetry is similar to that of the patched side. Compared to the non-repaired plates, for plates with an initial crack length a_i equals to 25.4 mm, the reduction of $\Delta K/\Delta\sigma$ on the patched side is 36%, 25% and 18% for plates with ETR values equal to 0.33, 0.2 and 0.13, respectively. As the crack length increases, the reduction of the values of $\Delta K/\Delta\sigma$ for plates with various ETR values becomes larger. It is found that for plates with final crack length a_f equals to 63.5 mm, the reduction of $\Delta K/\Delta\sigma$ is 52%, 40% and 32% for plates with ETR values equal to 0.33, 0.2 and 0.13, respectively.

6.4 Discussion of the results of plates with single-side patching and double-side patching

As discuss in previous section, the stress intensity factor (SIF) was reduced by applying either single-side or double-side CFRP patching. However, the efficiency of reducing the SIF is different for different cases of patching. In order to examine the efficiency of reducing the SIF for different patching details, the results of plates with single-side patching are compared to the results of plates with double-side patching in the following section.

The normalized stress intensity factor range ($\Delta K/\Delta\sigma$) can be obtained according to Eq. 6.1 where f(a/b) is the correction factor which accounts for the geometry of the specimen. From the finite element results, the stress intensity factor, K, is obtained for plates with different crack patterns and patching conditions. Therefore, with Eq. 6.1, the corresponding value of f(a/b) could be obtained according to Eq. 6.4 which based on the finite element results.

$$f(a/b) = \frac{\Delta K}{\Delta\sigma\sqrt{\pi a}} \tag{6.4}$$

The results of f(a/b) for the unpatched side of plates with an edge crack and single-side patching and the results of f(a/b) for the plane of symmetry of plates with double-side patching are shown in Figure 6.22 and Figure 6.23 along with the results of the non-repaired model. As shown in Figure 6.22 that for plates with an edge crack and single-side patching, the values of f(a/b) of unpatched side is almost the same as that of the non-repaired plates when the crack length is short. However, as the crack length increases, the values of f(a/b) of the plates with single-side patching were reduced significantly. Meanwhile, the effect of adherend stiffness ratio (ETR) is not obvious as shown in the figure for plates with an edge crack and single-side patching. On the other hand, it is shown from Figure 6.23 that for plates with an edge crack and double-side patching, the values of f(a/b) on the plane of symmetry are relatively constant and the values of f(a/b) decrease with increasing ETR values. It implies that the effect of adherend stiffness ratio is more significant for plates with double-side patching.

As the SIF range is related to the stress field around the crack tip and also to the deformation of the crack mouth, the crack mouth displacement of plates with different adherend stiffness ratios are examined and shown in Figure 6.24. The stiffness of the patching is the same for all finite element models in the parametric study. Therefore, different adherend stiffness ratio, (ETR) are achieved by varying the thickness of the steel plate. As shown in Figure 6.24, a plate with low ETR value, the out-of-plane displacement of the crack mouth is relatively small compared to that of the plates with large ETR value. A larger out-of-plane displacement implies a larger out-of-plane bending of the cracked plate. Although it is expected that the crack mouth displacement should be reduced more for a plate with larger ETR value, the larger ETR value also increases the out-of-plane bending and rotation at the crack location of the cracked plate. Therefore, the crack mouth displacements of the unpatched side for plates with larger ETR values are almost the same as those with lower ETR value. As a result, the adherend stiffness ratio does not affect the SIF of the unpatched side of plates with single-side patching only.

For plate with double-side patching, the crack mouth displacement of the plate with different adherend stiffness ratios is shown in Figure 6.25. It is worth noting that for a plate with double-side patching, the out-of-plane bending of the cracked plate is eliminated. As shown in this figure, the crack mouth displacement decreases with increasing adherend stiffness ratios. Therefore, the SIF decreases with increasing adherend stiffness ratio in plates with double-side patching.

For plate with a central crack, the results of f(a/b) of plates with single-side patching and plates with double-side patching are shown in Figure 6.26 and Figure 6.27. As shown in these figures, for plates with a central crack and single-side patching, the values of f(a/b) are a bit larger than that of the non-repaired plates when the crack length is short. As the crack length increases, the values of f(a/b) are reduced. However, the reduction is not as much as that found in the plates with an edge crack. For the plates with double-side patching, Figure 6.27 showed that the values of f(a/b) on the plane of symmetry are relatively constant and the values of f(a/b) decrease with increasing ETR values as shown in Figure 6.27. This behaviour is similar to that observed for plates with an edge crack.

6.5 Prediction of fatigue life of plates with CFRP patching

In order to examine the fatigue life of plates with CFRP patching, prediction of the fatigue life of plates with different crack pattern and patching details was carried out based on the procedure discussed in Section 5.5.2 of Chapter 5. The Paris equation (Paris and Erdogan 1960) is taken as the basic format of the equation for predicting the fatigue life of the welded steel plate according to Eq. 5.29. The equation is repeated below.

$$N = \int_{a_i}^{a_f} \frac{1}{C(\Delta K_{eff})^m} da \tag{5.29}$$

where N is the number of cycles, a_i is the initial crack length, a_f is the final crack length, ΔK_{eff} is the effective stress intensity factor range, and, C and m are the material constants of steel. In this study, the initial and final crack lengths are taken as 25.4 mm and 63.5 mm, respectively. The material constants, C and m, are taken as 8.88 x 10^{-12} m/cycle and 3.03 according to the material constant of G40.12 350WT steel (Yin et al. 2006). It should be noted that the effective stress intensity factor (ΔK_{eff}) is used in Equation 5.29 to account for the crack closure effect due to the presence of residual stress at the welded location. The prediction of the effective stress intensity factor range is based on Eq. 5.26 for welded steel plate without FRP patching and Eq. 5.30 for welded steel plate with FRP patching. These equations are repeated below.

$$\Delta K_{eff} = (\sigma_{max} - \sigma_{op}) f(a/b) \sqrt{\pi a} \tag{5.26}$$

$$\Delta K_{eff} = (\sigma_{max} - \sigma_{op}^{p}) f(a/b)^{u} \sqrt{\pi a} \tag{5.30}$$

For this parametric study, a maximum stress (σ_{max}) of 283 MPa was assigned, σ_{op} is the crack opening stress for welded steel plate without FRP patching and it is obtained from the fatigue test results discussed in Chapter 5. $\sigma^{P}{}_{op}$ is the crack opening stress for welded steel plates with FRP patching and it is related to the adherend stiffness ratio of the FRP and the plate as defined by Eq. 5.31. The correction factor f(a/b) for plain plates with an edge crack is defined in Eq. 6.2 and for plain plates with a central crack is defined in Eq. 6.3. The $f(a/b)^{u}$ is the equation of the modification factor accounting for the effect of geometry of crack and the presence of the FRP patching. Values of this correction factor for plates with CFRP patching were obtained from the finite element results of the SIF. As it is shown in Figure 6.22 and Figure 6.26, for plates with single-side CFRP patching, the values of $f(a/b)^{u}$ for plates with various ETR values are almost the same. Therefore, based on regression analysis of the data, a single equation which takes the form similar to the equation for non-repaired model was developed for determining the value of $f(a/b)^{u}$ for plates with single-side patching and the correction functions are:

(a) For plates with an edge crack and single-side patching:

$$f(a/b)^{u} = 1.65 - 1.42\left(\frac{a}{b}\right) - 17.35\left(\frac{a}{b}\right)^{2} + 81.60\left(\frac{a}{b}\right)^{3} - 90.3\left(\frac{a}{b}\right)^{4} \qquad (6.5)$$

(b) For plates with a central crack and single-side patching:

$$f(a/b)^{u} = 1.96 - 8.82\left(\frac{a}{b}\right) + 26.55\left(\frac{a}{b}\right)^{2} - 33.55\left(\frac{a}{b}\right)^{3} + 15.06\left(\frac{a}{b}\right)^{4} \qquad (6.6)$$

For plates with double-side patching, the values of $f(a/b)^u$ were found to be dependent on the ETR values (Figure 6.23 and Figure 6.27). Therefore, different equations of $f(a/b)^u$ were developed for plates with double-side patching and various ETR values. The correction factors are:

(a) For plates with an edge crack and double-side patching:

For ETR = 0.13

$$f(a/b)^u = 0.26 + 11.29\left(\frac{a}{b}\right) - 59.67\left(\frac{a}{b}\right)^2 + 142.7\left(\frac{a}{b}\right)^3 - 127.31\left(\frac{a}{b}\right)^4 \qquad (6.7)$$

For ETR = 0.20

$$f(a/b)^u = 0.49 + 6.64\left(\frac{a}{b}\right) - 36.75\left(\frac{a}{b}\right)^2 + 86.99\left(\frac{a}{b}\right)^3 - 77.02\left(\frac{a}{b}\right)^4 \qquad (6.8)$$

For ETR = 0.33

$$f(a/b)^u = 0.91 - 1.57\left(\frac{a}{b}\right) + 5.21\left(\frac{a}{b}\right)^2 - 11.43\left(\frac{a}{b}\right)^3 + 9.53\left(\frac{a}{b}\right)^4 \qquad (6.9)$$

(b) For plates with a central crack and double-side patching:

For ETR = 0.13

$$f(a/b)^u = 0.83 + 1.41\left(\frac{a}{b}\right) - 10.09\left(\frac{a}{b}\right)^2 + 26.19\left(\frac{a}{b}\right)^3 - 24.18\left(\frac{a}{b}\right)^4 \qquad (6.10)$$

For ETR = 0.20

$$f(a/b)^u = 0.88 + 0.05\left(\frac{a}{b}\right) - 4.85\left(\frac{a}{b}\right)^2 + 15.82\left(\frac{a}{b}\right)^3 - 16.33\left(\frac{a}{b}\right)^4 \qquad (6.11)$$

For ETR = 0.33

$$f(a/b)^{u} = 0.77 + 0.45\left(\frac{a}{b}\right) - 9.04\left(\frac{a}{b}\right)^{2} + 27.64\left(\frac{a}{b}\right)^{3} - 27.43\left(\frac{a}{b}\right)^{4} \qquad (6.12)$$

The fatigue life of non-repaired plates and repaired plates with an initial crack length (a_i) equal to 25.4 mm and a final crack length (a_f) equal to 63.5 mm were determined according to procedure discussed in Section 5.2.2 in Chapter 5. Plots showing the number of cycles versus crack length for plates with various crack patterns are given in Figure 6.28 to Figure 6.31. The corresponding number of cycles at the final crack length is listed in Table 6.3 for all plates studied. For plates with ETR equals to 0.13, 0.20 and 0.33, the fatigue life is increased by 2.62, 3.76 and 9.2 times, respectively for plates with an edge crack and single-side patching and 1.73, 2.46 and 5.90 times, respectively for plates with a central crack and single-side patching. For plates with double-side patching, the increase in fatigue life is about 3.82, 8.59 and 41.7 times for plates with an edge crack and 2.79, 5.38 and 21.4 times for plates with a central crack with ETR equal to 0.13, 0.20 and 0.33, respectively. Therefore, it is shown that higher efficiency of FRP patching is observed for plates with edge crack than that of the plates with central crack. It is also found that the increase in fatigue life is more pronounced in cracked plates with double-side patching.

6.6 Summary and conclusions

In this chapter, a parametric study of the stress intensity factor of cracked plates with single-side or double-side CFRP patching based on the finite element analysis was presented. In the finite element parametric study, several parameters such as thickness of steel plate, edge crack/central crack pattern and single-side/double-side CFRP patching pattern were considered. One of the main parameters considered in this study is the adherend stiffness ratio of a steel plate to a CFRP plate (ETR = $E_{frp}E_{frp}$ / E_st_s). In order to achieve three different adherend stiffness ratios of CFRP to steel plate (ETR = 0.33, 0.2 and 0.13), three different steel plate thicknesses (t_s = 9.5 mm, 16 mm and 25 mm for single-side patching model and t_s = 19 mm, 32 mm and 50 mm for double-side patching model) were used while the thickness of the CFRP plate was kept constant. The finite element results showed that for plates with single-side CFRP patching, the stress intensity factor of the patched side is reduced significantly whilst the stress intensity factor of the unpatched side is reduced only marginally when the crack length is short. As the crack length becomes longer, the stress intensity factor are almost the same for plates with different ETR values. For plates with double-side patching, similar trend of stress intensity factor is observed on the patched side and the plane of symmetry. Unlike the plates with single-side patching, larger reduction of the stress intensity factor was obtained for plates with larger ETR values.

Based on the finite element results of the stress intensity factor, equations of the correction factor which take into account the crack pattern as well as the patching pattern were developed for plates with different form of crack pattern and patching pattern. With the correction factor of different form of crack pattern and patching pattern, fatigue life of each plates with CFRP patching was determined according to the procedure discussed in Section 5.2.2 for re-welded steel plate. The results showed that higher efficiency of FRP patching is observed for plates with an edge crack than that of the plates with a central crack. It was also found that the increase in fatigue life is more pronounced in cracked plates with double-side patching.

Table 6.1 Material properties for the finite element analysis (Sika 2003)

Steel plate	E_s	200,000 MPa
	ν_s	0.3
CFRP plate	E_{frp1}	175,000 MPa
	E_{frp2}	9,000 MPa
	ν_{frp}	0.28
	G_{frp}	4,500 MPa
Adhesive	E_a	4,500 MPa
	ν_a	0.34
	G_a	1,680 MPa

Note: E_{frp1} is the elastic modulus along the loading direction and E_{frp2} is the elastic modulus along the transverse direction

Table 6.2 Details of the parametric study

			Number of CFRP plate $N_p = 3$	Adherend stiffness ratio $E_{frp}\, t_{frp} / E_s\, t_s$
Edge crack	Single-side patching	$t_s = 9.5$ mm	$t_{frp} = 3.6$ mm	0.33
		$t_s = 16$ mm	$t_{frp} = 3.6$ mm	0.20
		$t_s = 25$ mm	$t_{frp} = 3.6$ mm	0.13
	Double-side patching	$2t_s = 19$ mm	$t_{frp} = 3.6$ mm	0.33
		$2t_s = 32$ mm	$t_{frp} = 3.6$ mm	0.20
		$2t_s = 50$ mm	$t_{frp} = 3.6$ mm	0.13
Central crack	Single-side patching	$t_s = 9.5$ mm	$t_{frp} = 3.6$ mm	0.33
		$t_s = 16$ mm	$t_{frp} = 3.6$ mm	0.20
		$t_s = 25$ mm	$t_{frp} = 3.6$ mm	0.13
	Double-side patching	$2t_s = 19$ mm	$t_{frp} = 3.6$ mm	0.33
		$2t_s = 32$ mm	$t_{frp} = 3.6$ mm	0.20
		$2t_s = 50$ mm	$t_{frp} = 3.6$ mm	0.13

Table 6.3 Number of cycles and increase in fatigue life

	Edge crack plate		Central crack plate	
	N*	Increase in fatigue life	N	Increase in fatigue life
Non-repaired	12343	----	29707	-----
Single-side patching				
ETR = 0.13	32359	2.62	51530	1.73
ETR = 0.20	46383	3.76	73225	2.46
ETR = 0.33	113111	9.2	175307	5.90
Double-side patching				
ETR = 0.13	47089	3.82	82885	2.79
ETR = 0.20	106035	8.59	159903	5.38
ETR = 0.33	514378	41.7	635522	21.4

* number of cycles (N) is predicted based on the development of crack length from initial crack length (a_i) equal to 25.4mm to final crack length (a_f) equal to 63.5mm.

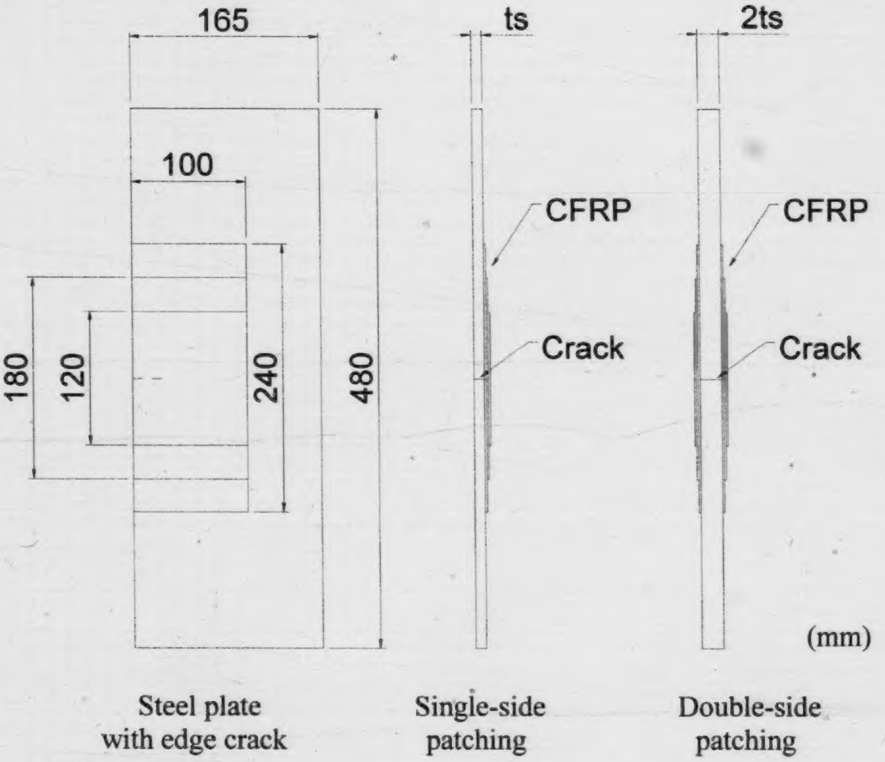
165
100
180
120
240
480
ts
2ts
CFRP
Crack
CFRP
Crack
(mm)
Steel plate with edge crack
Single-side patching
Double-side patching

Figure 6.1 Steel plate with edge crack, single-side / double-side CFRP patching

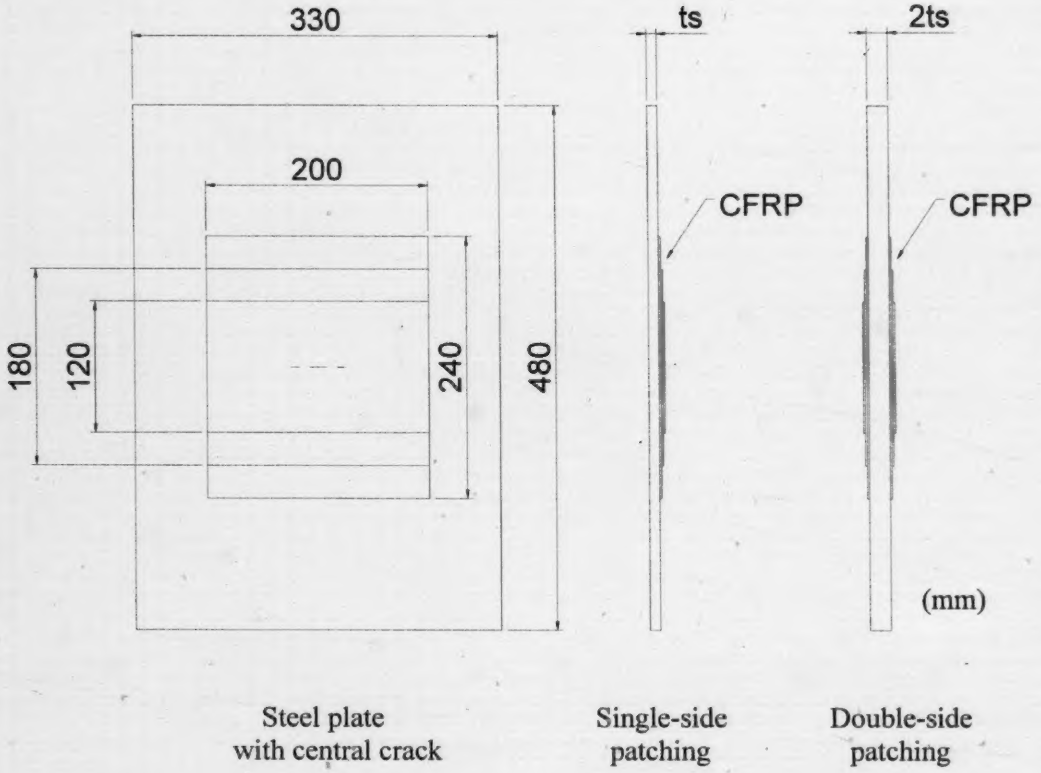
330
200
180
120
240
480
ts
2ts
CFRP
CFRP
(mm)
Steel plate with central crack
Single-side patching
Double-side patching

Figure 6.2 Steel plate with central crack, single-side / double-side CFRP patching

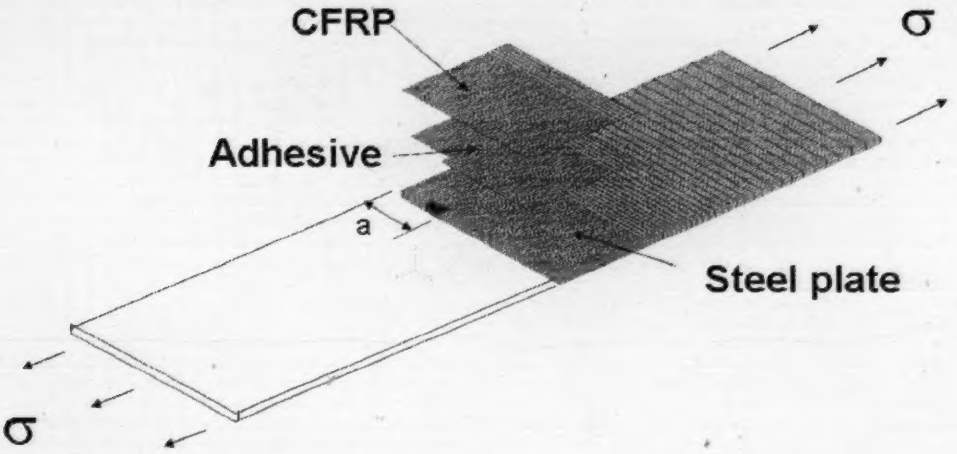
CFRP
σ
Adhesive
a
Steel plate
σ

Figure 6.3 Finite element model of edge cracked plate with single-side CFRP patching

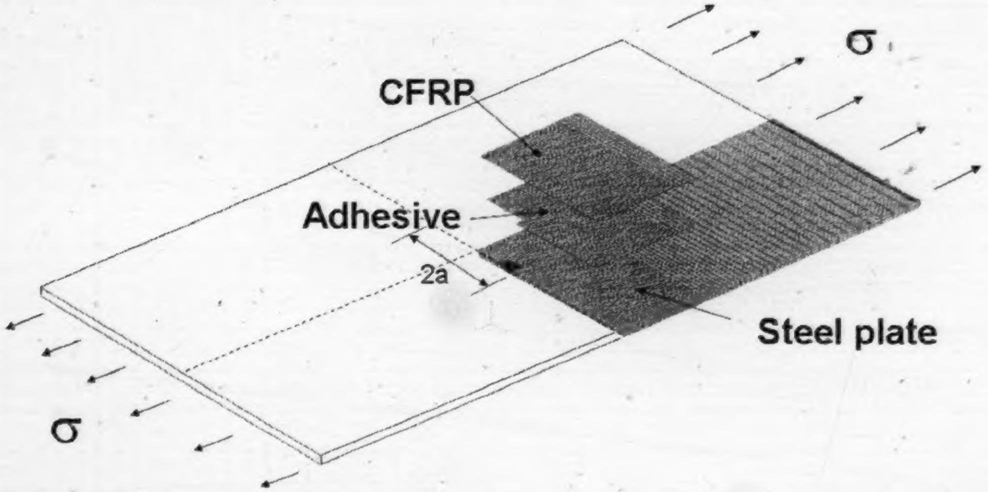
σ
CFRP
Adhesive
2a
Steel plate
σ

Figure 6.4 Finite element model of central cracked plate with single-side CFRP patching

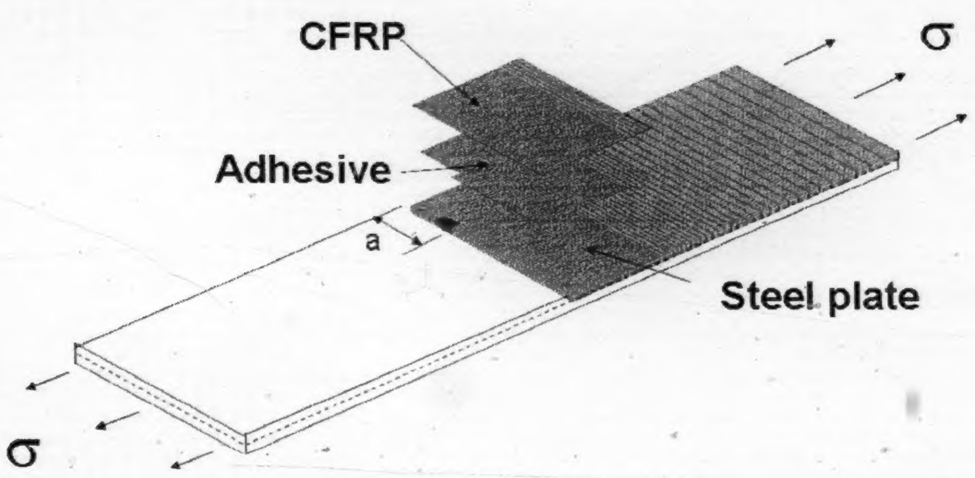
CFRP
σ
Adhesive
a
Steel plate
σ

Figure 6.5 Finite element model of edge cracked plate with double-side CFRP patching

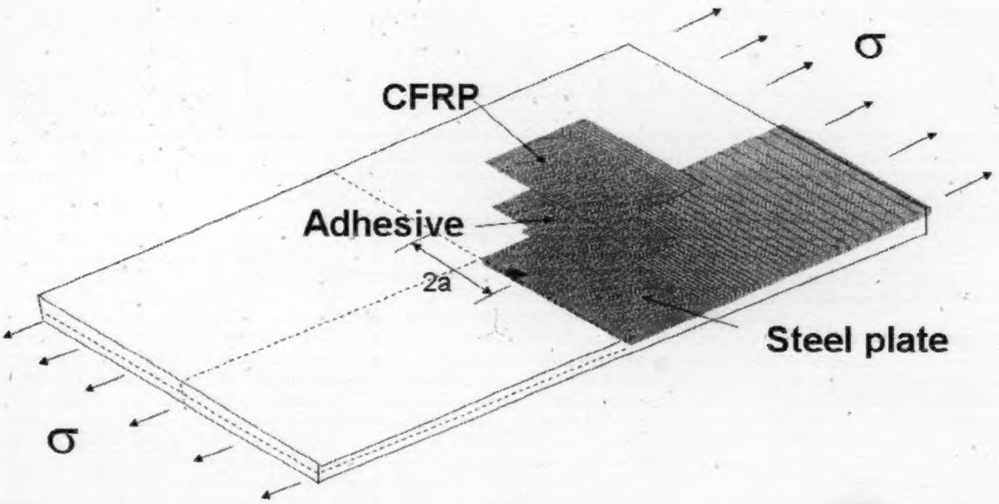
σ
CFRP
Adhesive
2a
Steel plate
σ

Figure 6.6 Finite element model of central cracked plate with double-side CFRP patching

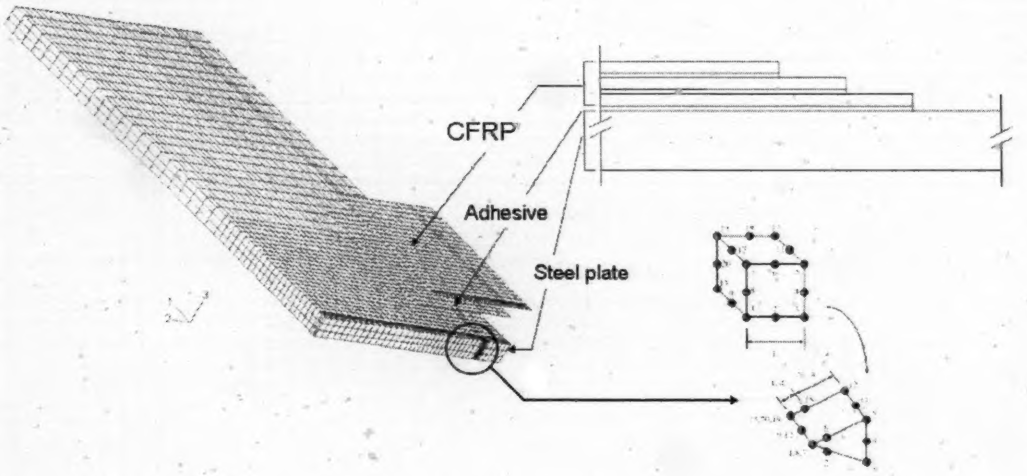
CFRP
Adhesive
Steel plate

Figure 6.7 Typical finite element mesh for the parametric study

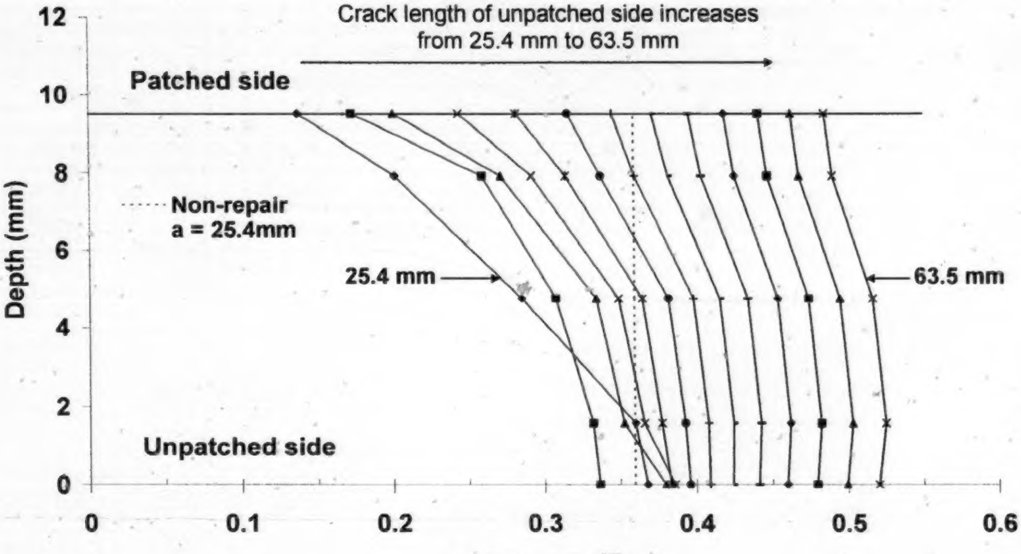

Figure 6.8 Through thickness normalized SIF (ΔK/Δσ) versus crack length of edge cracked FE model with single-side CFRP patching and ETR = 0.33

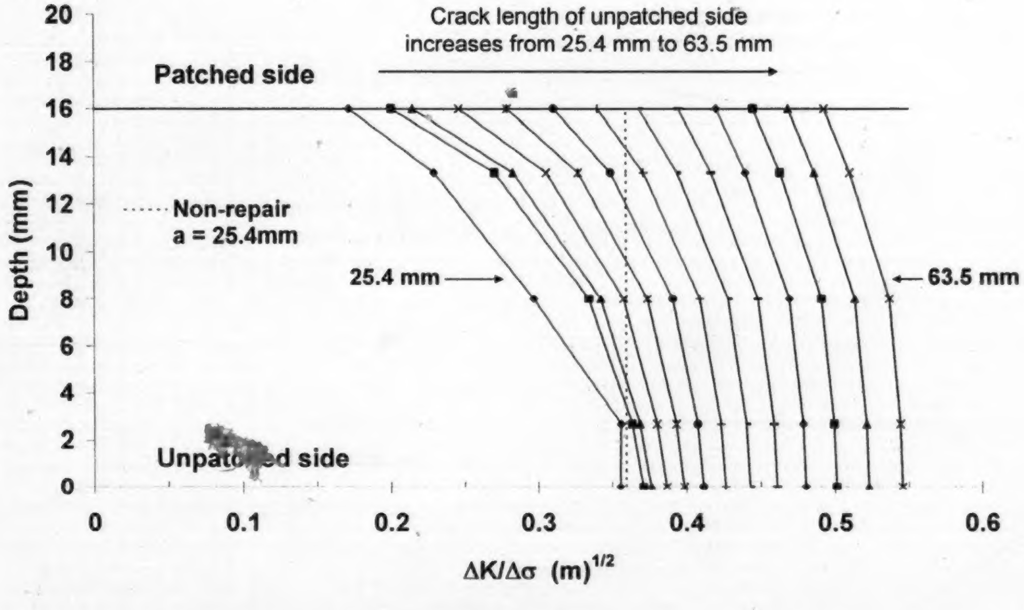

Figure 6.9 Through thickness normalized SIF (ΔK/Δσ) versus crack length of edge cracked FE model with single-side CFRP patching and ETR = 0.20

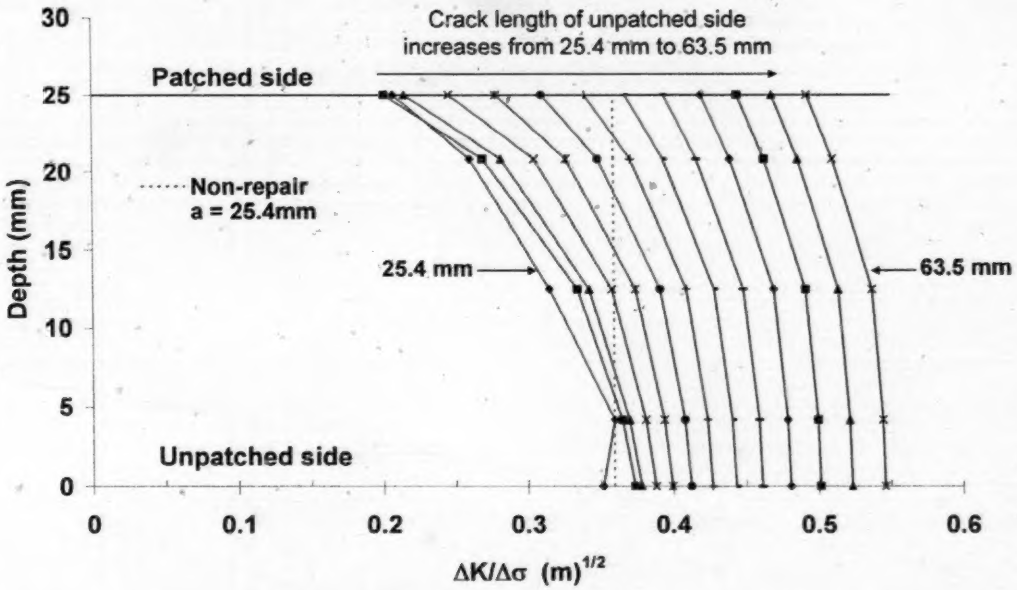

Figure 6.10 Through thickness normalized SIF (ΔK/Δσ) versus crack length of edge cracked FE model with single-side CFRP patching and ETR = 0.13

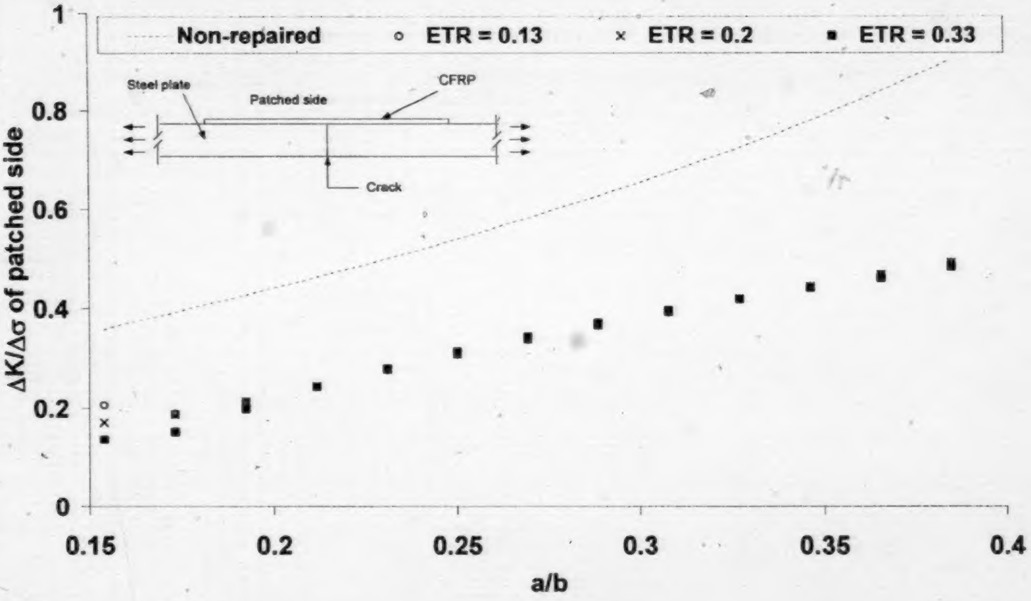

Figure 6.11 Normalized SIF (ΔK/Δσ) of patched side versus (a/b) of edge cracked FE model with single-side CFRP patching and ETR = 0.13, 0.20 and 0.33

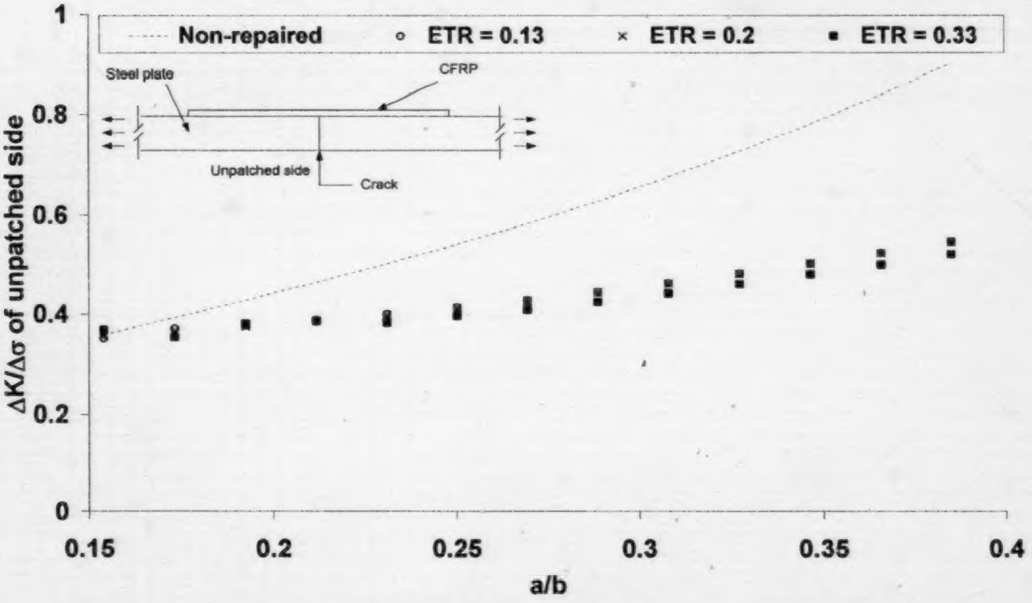

Figure 6.12 Normalized SIF (ΔK/Δσ) of unpatched side versus (a/b) of edge cracked FE model with single-side CFRP patching and ETR = 0.13, 0.20 and 0.33

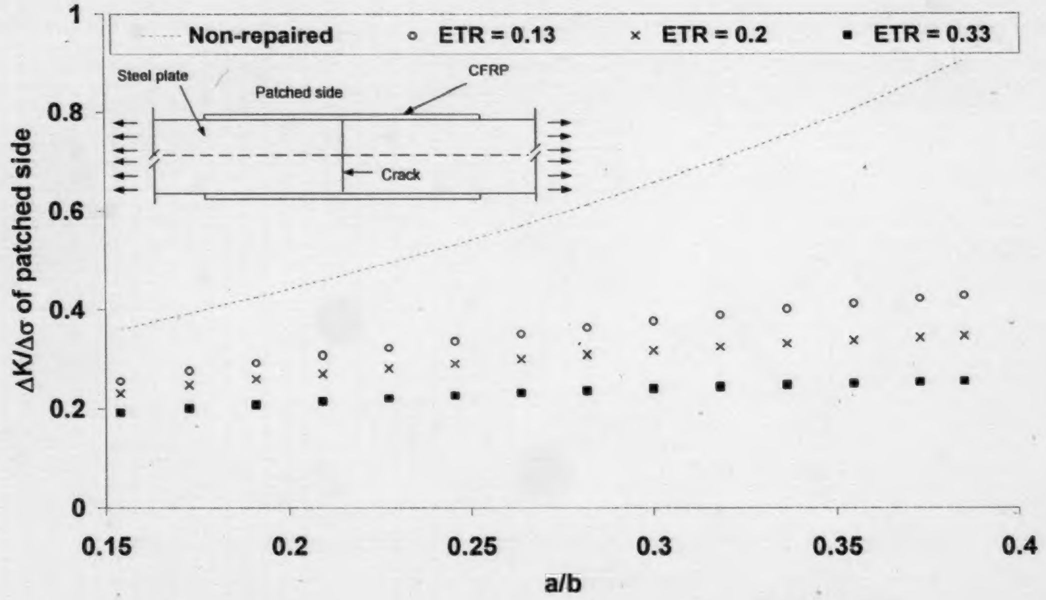

Figure 6.13 Normalized SIF (ΔK/Δσ) of patched side versus (a/b) of edge cracked FE model with double-side CFRP patching and ETR = 0.13, 0.20 and 0.33

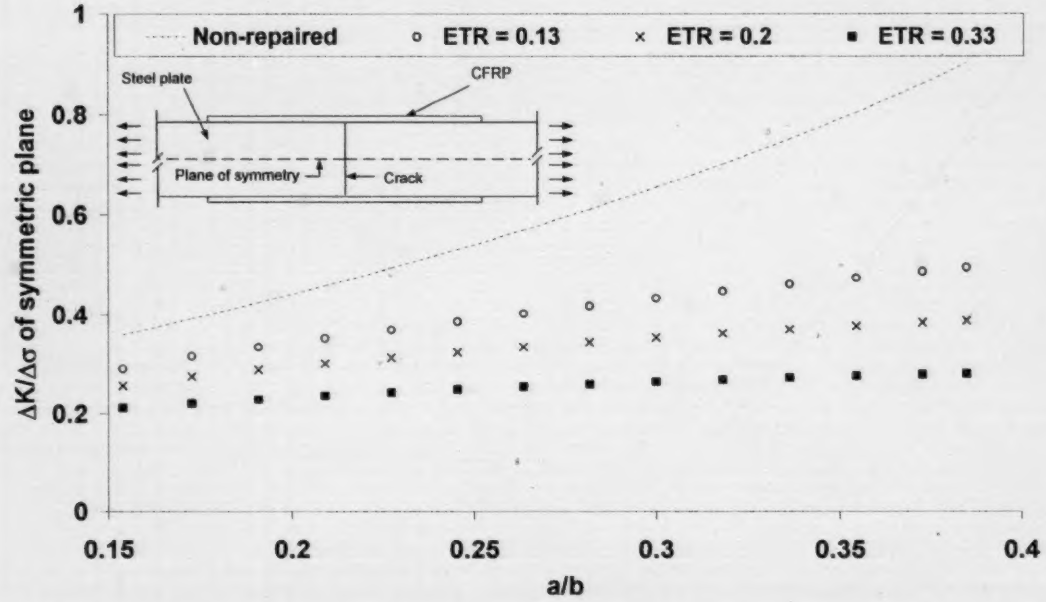

Figure 6.14 Normalized SIF (ΔK/Δσ) of plane of symmetry versus (a/b) of edge cracked FE model with double-side CFRP patching and ETR = 0.13, 0.20 and 0.33

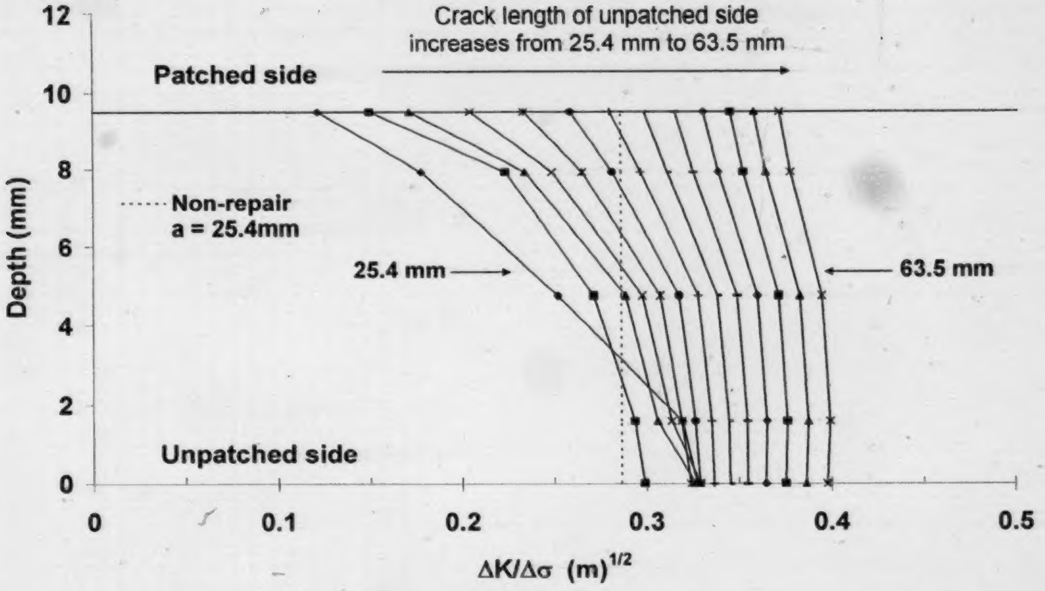

Figure 6.15 Through thickness normalized SIF ($\Delta K/\Delta\sigma$) versus crack length of central cracked FE model with single-side CFRP patching and ETR = 0.33

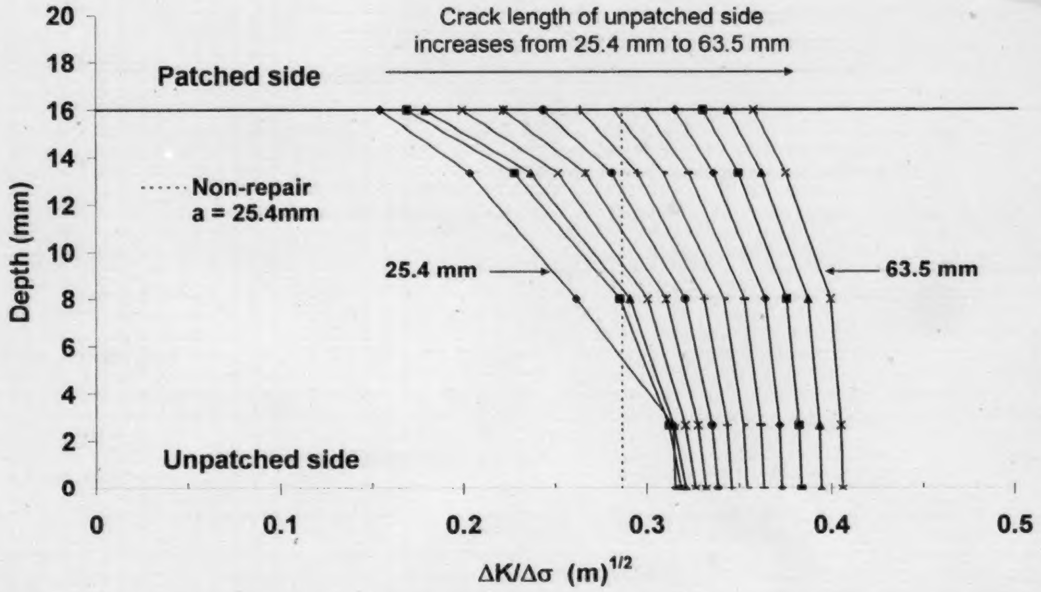

Figure 6.16 Through thickness normalized SIF ($\Delta K/\Delta\sigma$) versus crack length of central cracked FE model with single-side CFRP patching and ETR = 0.20

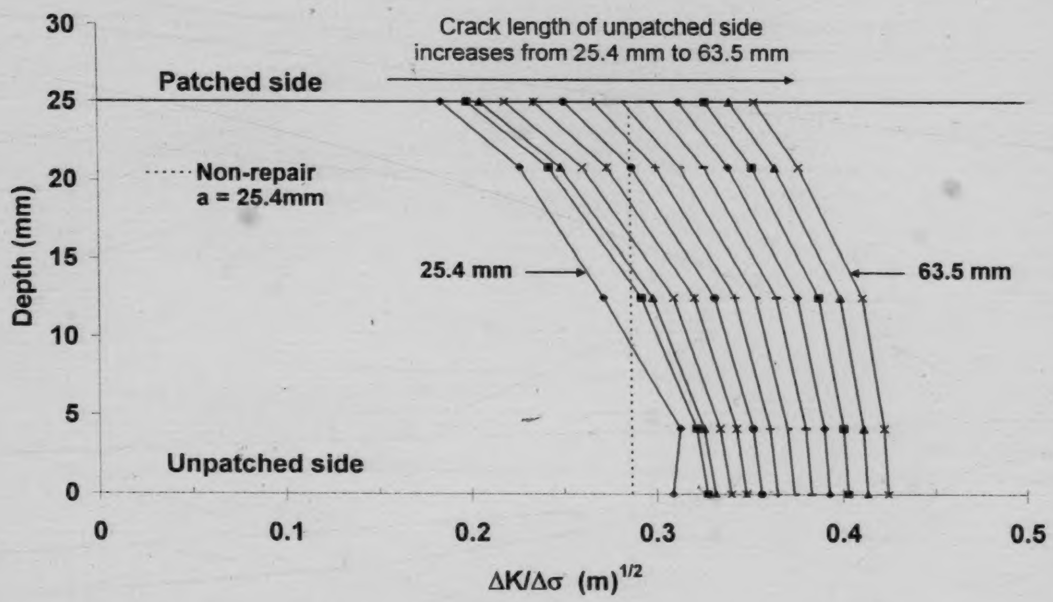

Figure 6.17 Through thickness normalized SIF (ΔK/Δσ) versus crack length of central cracked FE model with single-side CFRP patching and ETR = 0.13

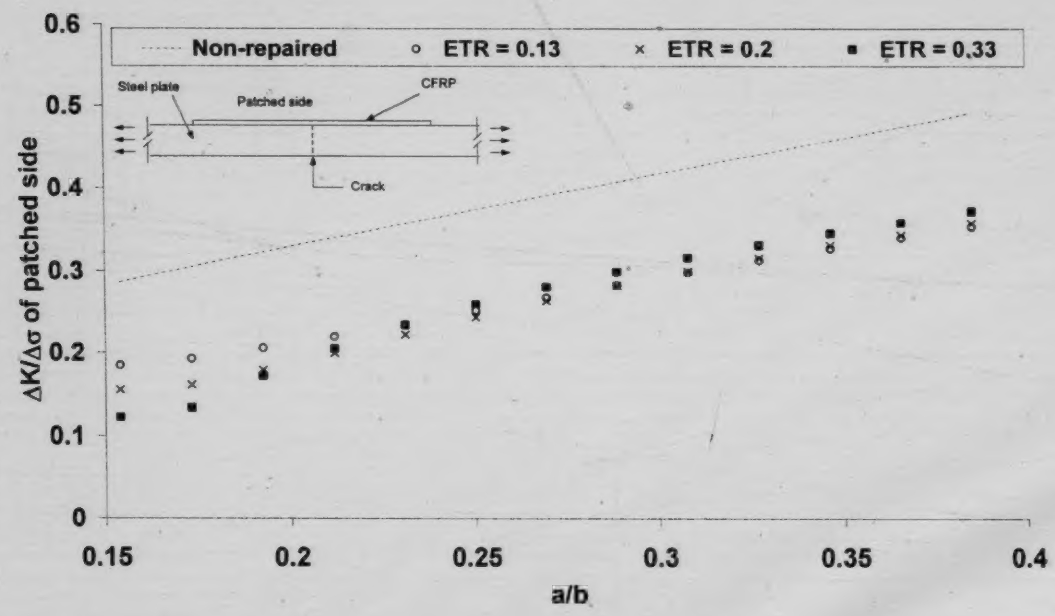

Figure 6.18 Normalized SIF (ΔK/Δσ) of patched side versus (a/b) of central cracked FE model with single-side CFRP patching and ETR = 0.13, 0.20 and 0.33

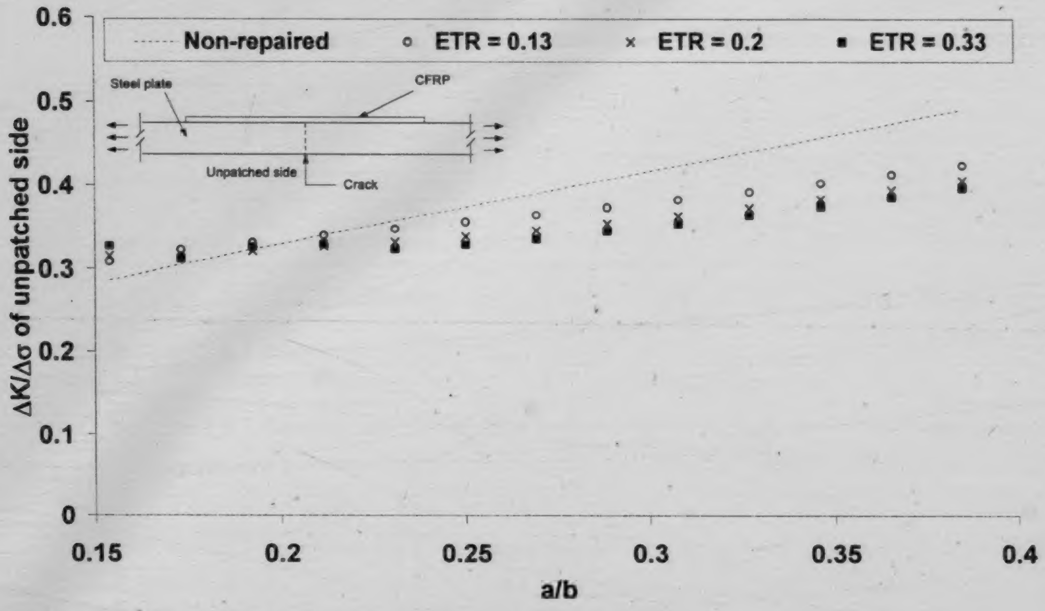

Figure 6.19 Normalized SIF (ΔK/Δσ) of unpatched side versus (a/b) of central cracked FE model with single-side CFRP patching and ETR = 0.13, 0.20 and 0.33

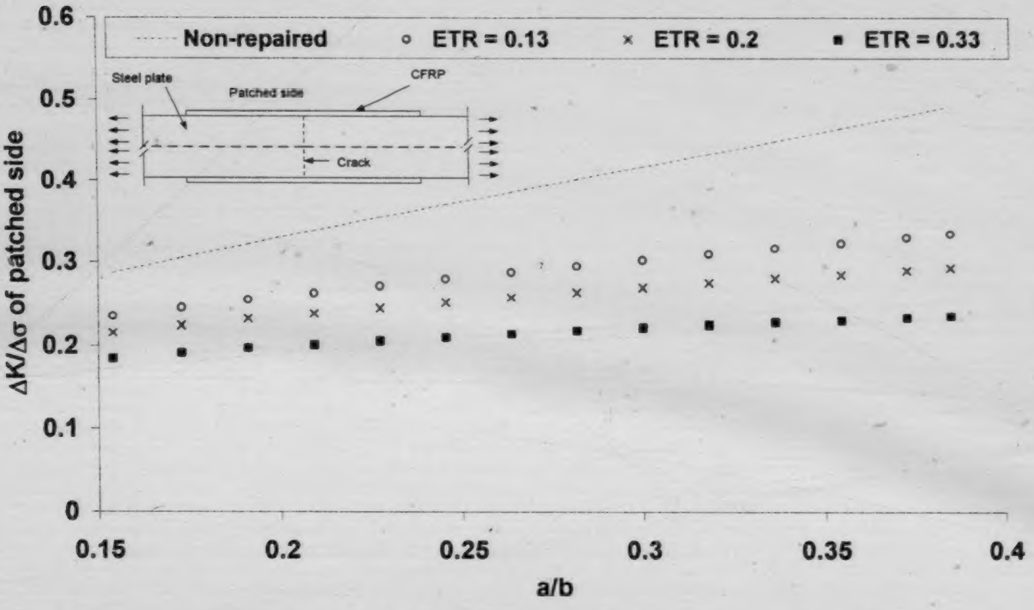

Figure 6.20 Normalized SIF (ΔK/Δσ) of patched side versus (a/b) of central cracked FE model with double-side CFRP patching and ETR = 0.13, 0.20 and 0.33

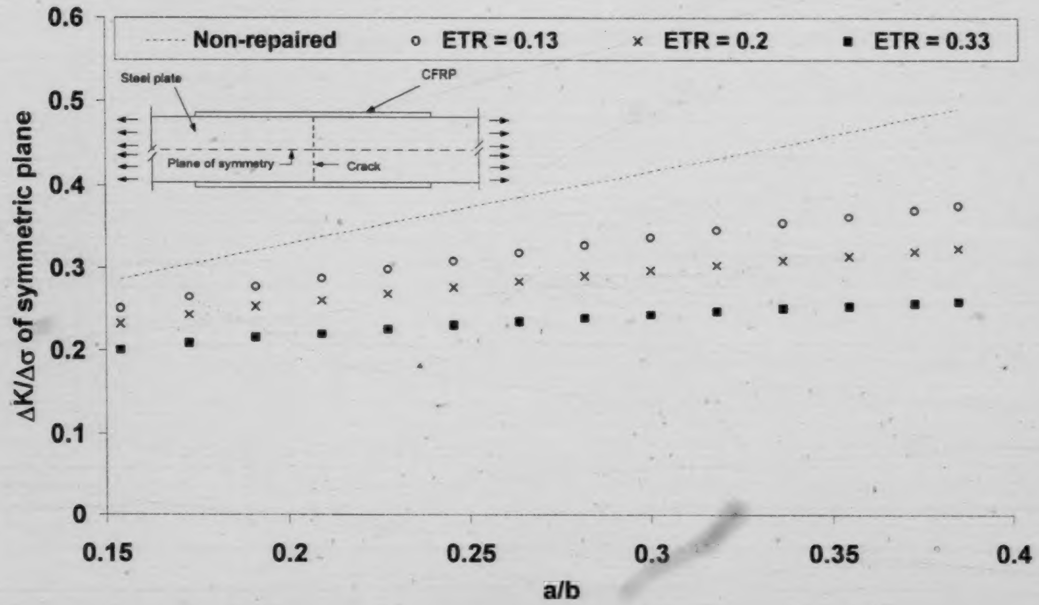

Figure 6.21 Normalized SIF (ΔK/Δσ) of plane of symmetry versus (a/b) of central cracked FE model with double-side CFRP patching and ETR = 0.13, 0.20 and 0.33

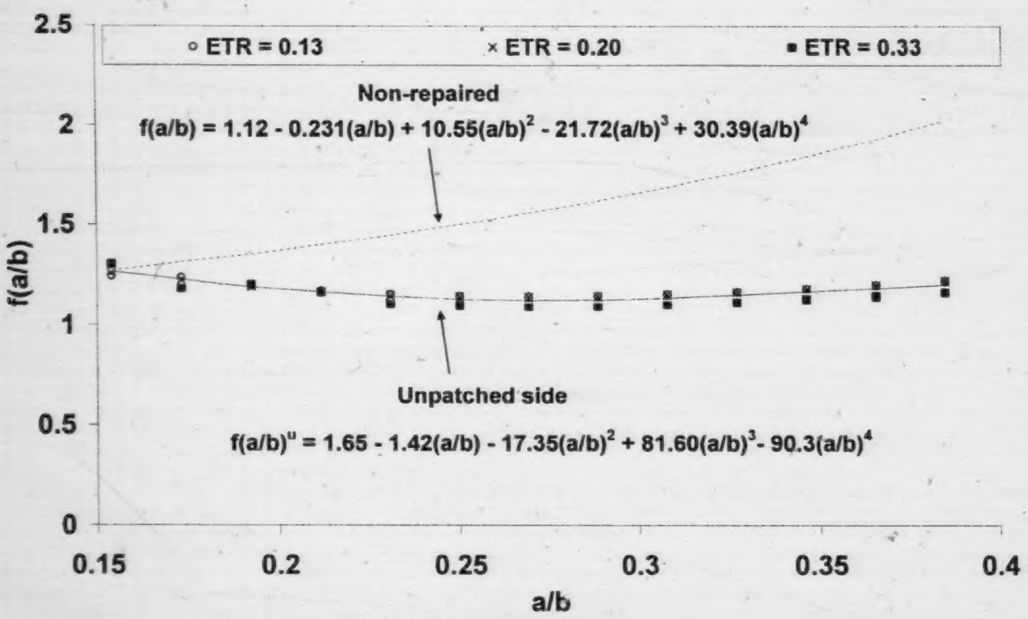

Figure 6.22 Value of f(a/b) versus crack length to plate width ratio (a/b) of edge cracked model with single-side CFRP patching

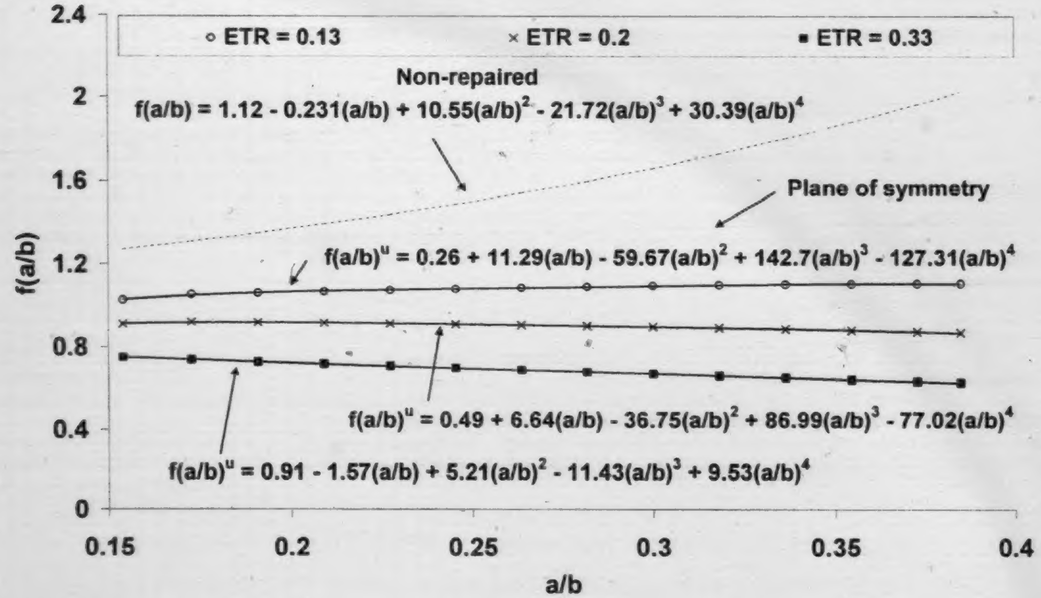

Figure 6.23 Value of f(a/b) versus crack length to plate width ratio (a/b) of edge cracked model with double-side CFRP patching

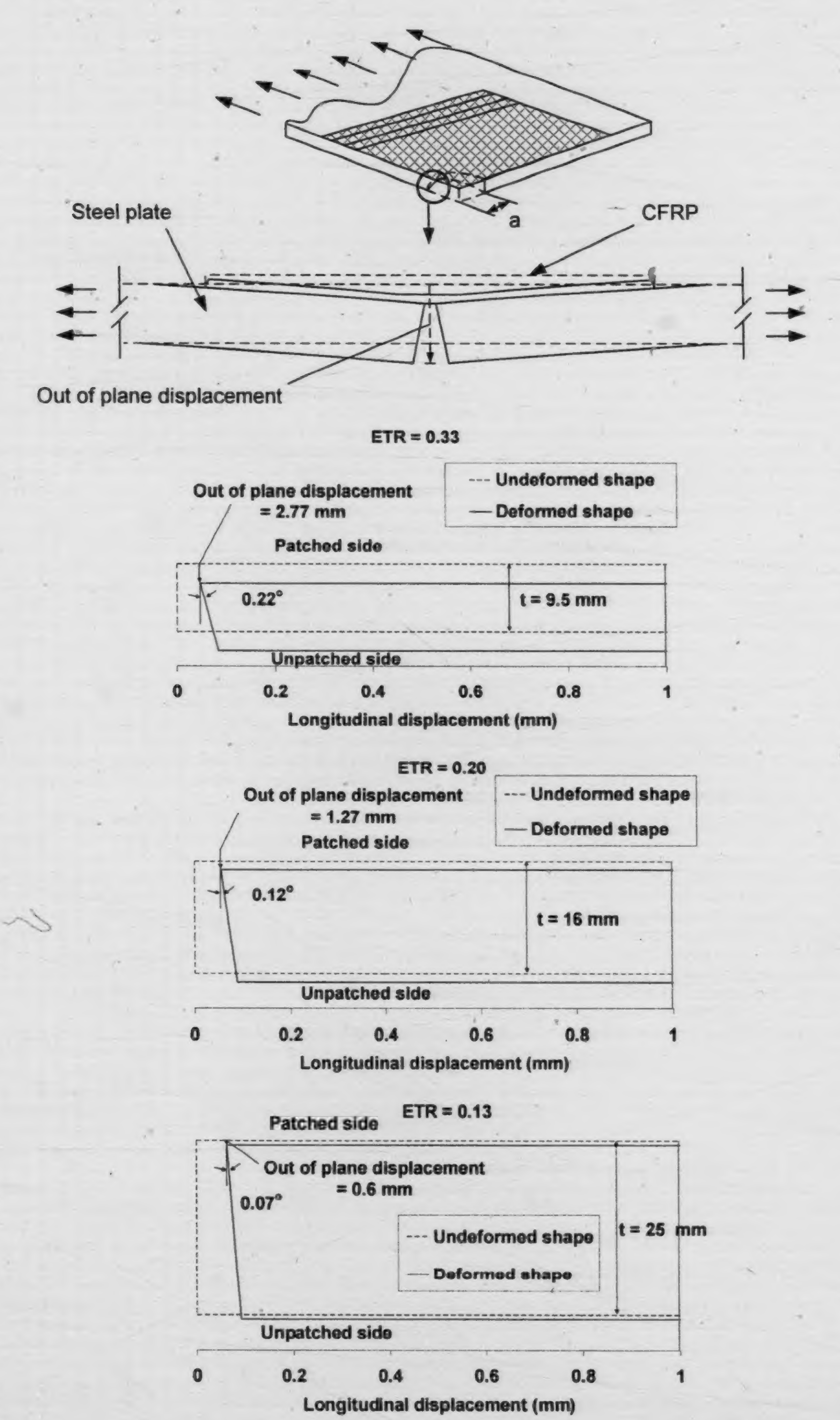

Figure 6.24 Crack mouth displacement of plate with single-side patching

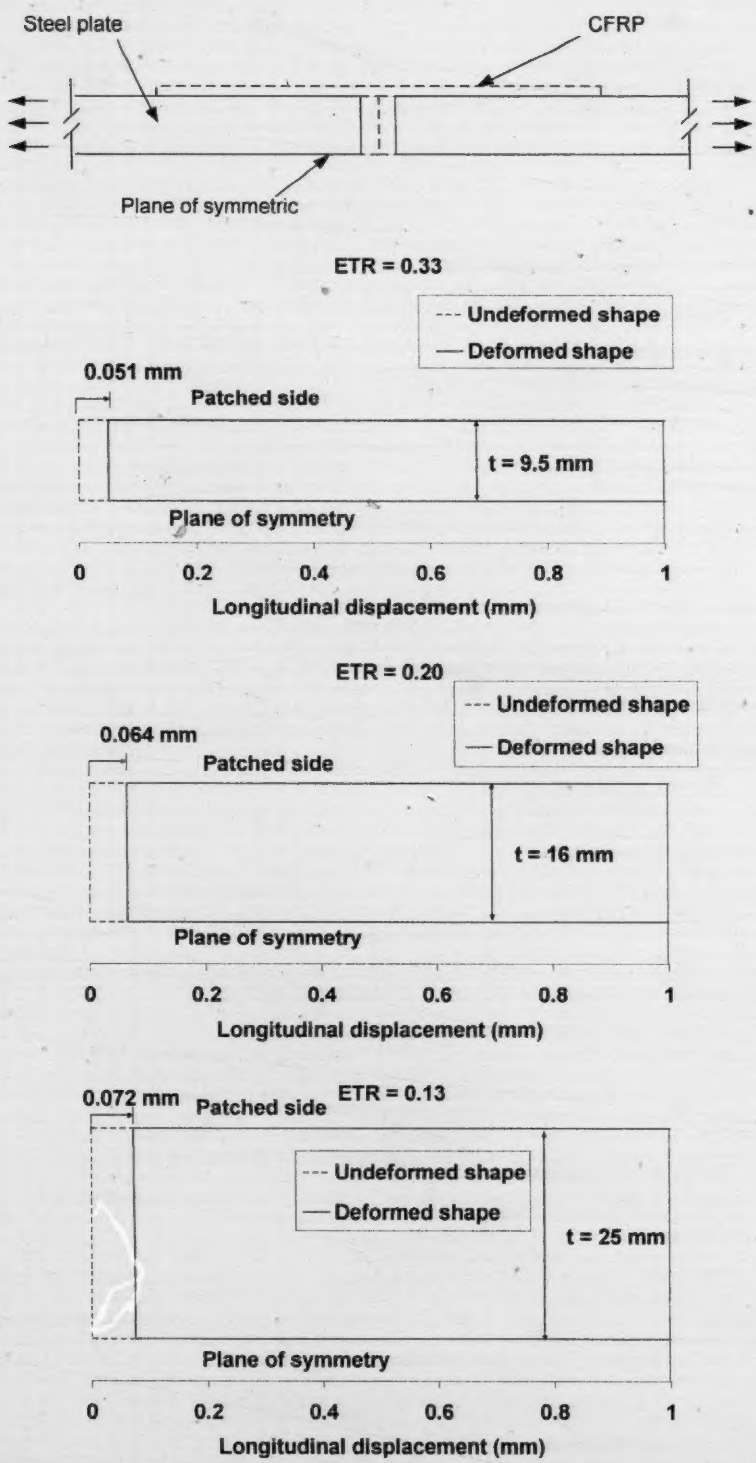

Figure 6.25 Crack mouth displacement of plate with double-side patching

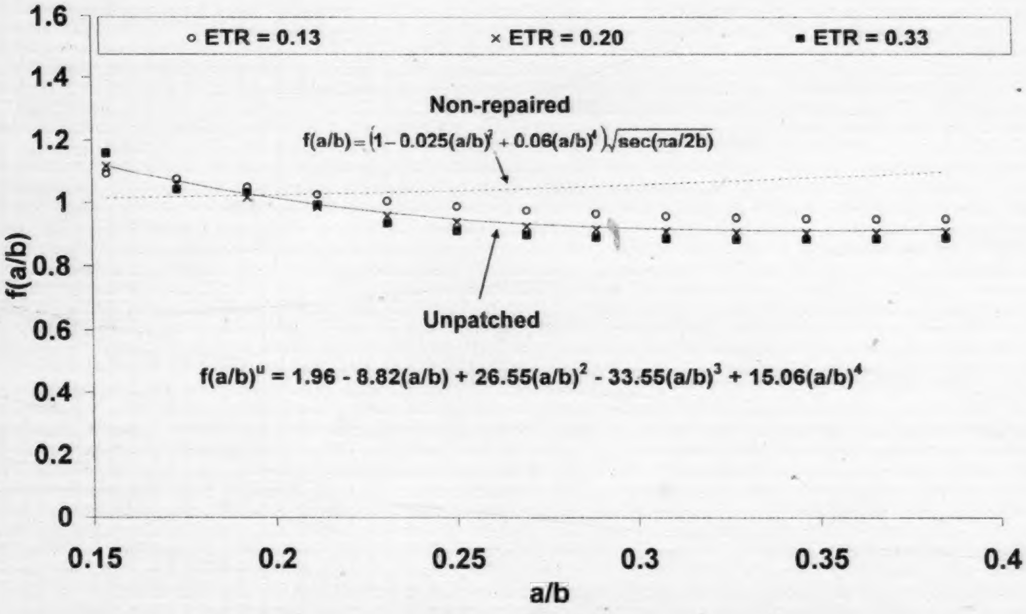

Figure 6.26 Value of f(a/b) versus crack length to plate width ratio (a/b) of central cracked model with single-side CFRP patching

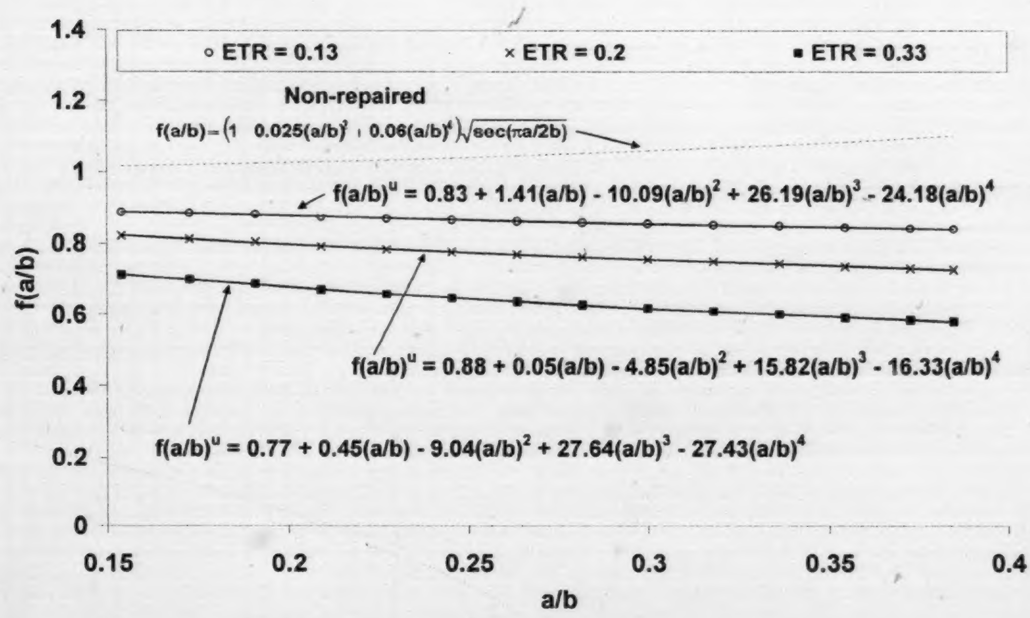

Figure 6.27 Value of f(a/b) versus crack length to plate width ratio (a/b) of central cracked model with double-side CFRP patching

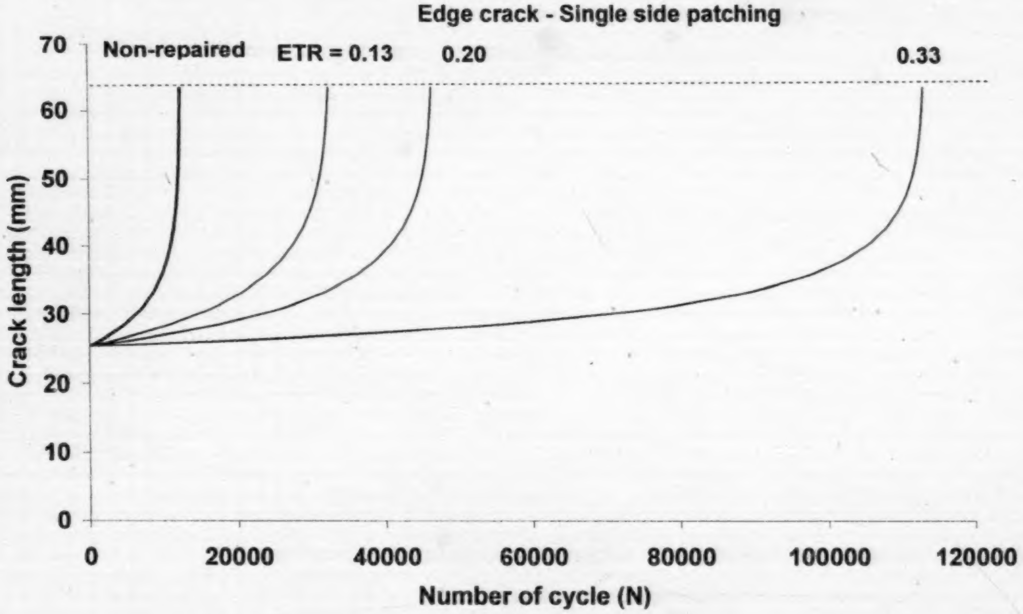

Figure 6.28 Number of cycle versus crack length of edge cracked model with single-side patching

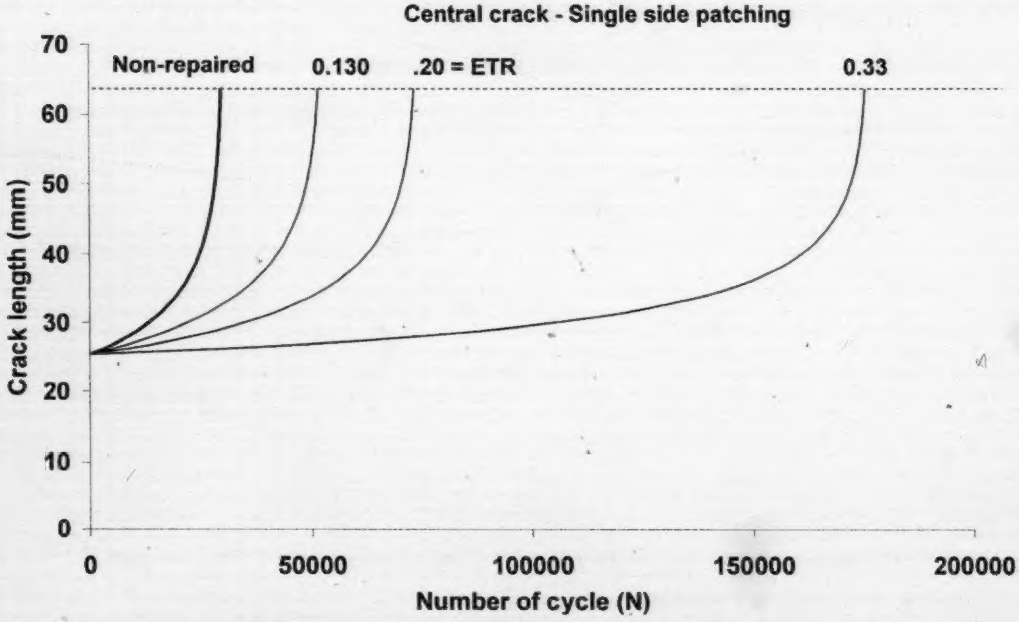

Figure 6.29 Number of cycle versus crack length of central cracked model with single-side patching

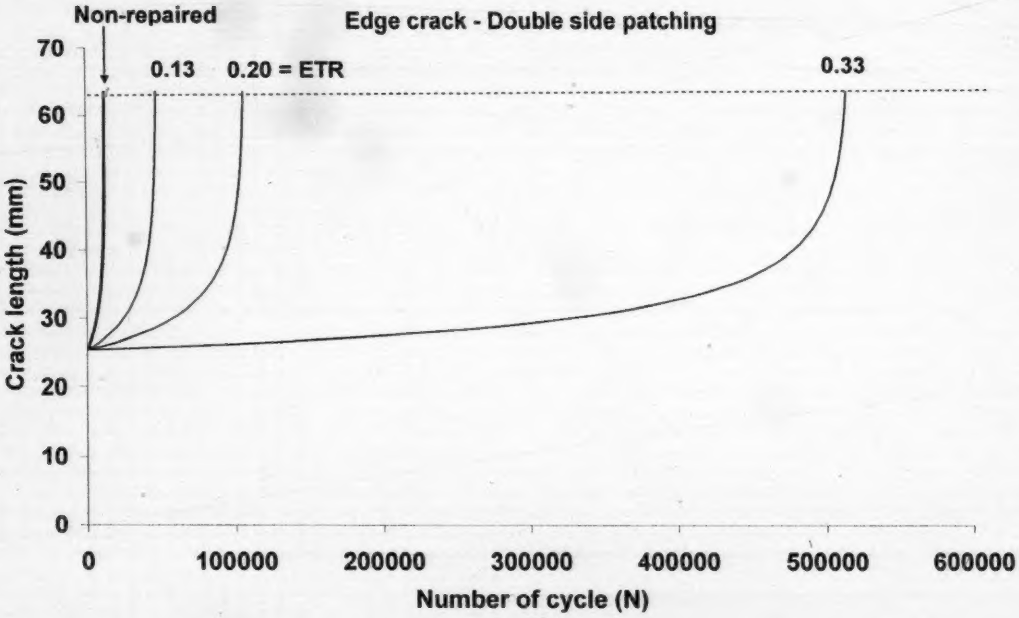

Figure 6.30 Number of cycle versus crack length of edge cracked model with double-side patching

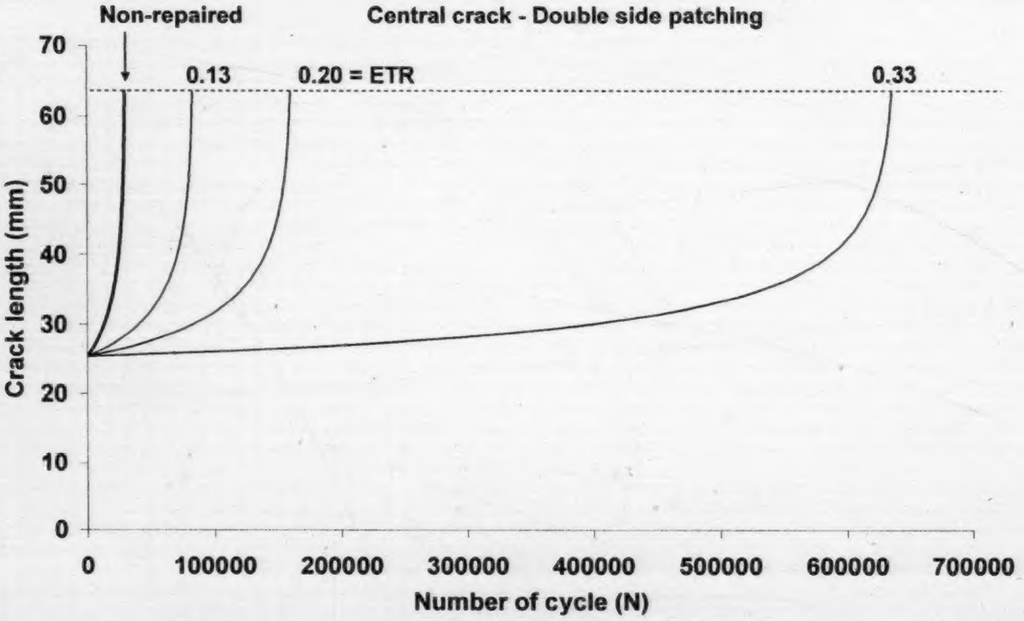

Figure 6.31 Number of cycle versus crack length of central cracked model with double-side patching

6.7 References

Barson, J. M. and Rolfe, S. T., 1999, Fracture and fatigue control in structures, ASTM manual series: MNL 41, pp. 213

Gross, B. and Srawley, J. E., 1964, "Stress intensity factors for a single notch tension specimen by boundary collocation of a stress function", NASA TN D-2395

Hibbitt, Karlsson & Sorenson, Inc., 2004, "ABAQUS Version 6.4", ABAQUS/Standard User's Manual Volumes I and II, Pawtucket, Rhode Island, U.S.A.

Paris, P.C. and Erdogan, F., 1960, "A critical analysis of crack propagation laws", Journal of Basic Engineering, Vol. 85, pp. 528-534

Sika Carbodur Technical Data Sheet. 2003. Sika Canada Inc. http://www.sika.ca/con-tds-sikacarbodur-ca.pdf

Tada, H., Paris, P.C., and Irwin, G.R., 1985, The stress analysis of cracks handbook (2nd Ed.), Paris Productions, Inc. St. Louis

Yin, Y., Grondin, G. Y. and Elwi, A. E. 2006. "Fatigue crack behaviour in Mine Excavator", Structural Engineering Report No. 265, University of Alberta, Department of Civil & Environmental Engineering, pp. 35

7 FINITE ELEMENT STUDY OF CRACKED CIRCULAR STEEL TUBE REPAIRED BY FRP PATCHING

7.1 Introduction

In Northern Alberta, Canada, the largest surface mining equipment in the world is used in oil sand mining operation. For example, the Syncrude mining site in Fort McMurray, Alberta is reliant on the operational reliability of heavy equipment. One of the heavy equipment used in the site is the draglines shown in Figure 7.1. In general, draglines are expected to remain in service for up to nine or more years, however, due to the increased loading on these structures and a harsh environment, cracking of boom members has become a major cause of unscheduled downtime of the equipment. Traditionally, repair of the crack is done by re-welding the cracked section. The method of re-welding the cracked section involves the removal of the fatigue crack by gouging of the material in the vicinity of the crack and subsequently replaces the material using a fill-weld process. However, in most instances, fatigue cracks reappear in the weld fill areas. As the application of FRP material to strengthen and repair of structures becoming more popular nowadays, FRP patching is considered as one of the possible alternative repair procedure for repairing the cracked steel members (Kennedy and Cheng 1998). A typical cluster in dragline boom is shown in Figure 7.2. In general, the dragline boom is in the form of circular tube structure and the crack is usually formed at a distance along the boom of approximately two-thirds the total boom length. A wall-thickness transition occurs 250 mm above the cluster and a typical diagram of the transition is shown in Figure 7.3.

7.2 Objectives

Test results have shown that it is effective to increase the fatigue life of cracked steel plate by applying FRP patching (Roberts 1995, Roach and Rackow 2005). FRP patching is considered as one of the possible alternative repair procedures for heavy steel equipment such as the boom members of draglines. In general, the dragline boom members are in the form of circular tube type structure. Therefore, FRP patching is usually bonded on one side (the outside surface) of the tube structure. Although the FRP material is applied on one side of the tube structure, the section will receive some support for out-of-plane bending after the application of the FRP material. In order to examine the efficiency of the repair by single-side patching of FRP material to tube structures, a finite element study of cracked steel tube structures was conducted and presented in this chapter. The objectives of this study are (1) to examine the reduction of SIF of cracked steel tube structure repaired with FRP patching using the finite element analysis; (2) to compare the finite element results of SIF of cracked tube structures with the finite element results obtained from the plates with single-side or double-side FRP patching; and, (3) to determine the fatigue life of welded steel tube member using the procedure discussed in Section 5.5.2.

7.3 Development of a finite element model for cracked circular tube structures

7.3.1 Dimension and finite element model of cracked steel tube

A section across the thickness of a dragline boom chord is shown in Figure 7.3. The diameter of the dragline boom is 660 mm and the thickness of the thinner part is about 16 mm. Therefore, the corresponding thickness-to-diameter ratio (t/D) is about 0.024. For the finite element model, the thickness of the steel tube was taken as 9.5 mm. This thickness is the same as the thickness of the plates used for fatigue analysis in Chapter 5. In order to achieve the thickness to diameter ratio (t/D = 0.024) of the dragline boom, the outside diameter of the steel tube was taken as 400 mm. The total length of the steel tube was taken as 4000 mm with a circumferential through-wall crack located at the mid-span. The initial half circumferential through-wall crack length was 25.4 mm and the final crack length was 63.5 mm. The initial half crack length, the final half crack length and the dimensions of patching were taken as the same as those used in previous finite element models of cracked steel plates with CFRP patching. The cross section dimension and an illustration of the circumferential through-wall crack are shown in Figure 7.4. Due to symmetry, only a quadrant of the steel tube was modeled. The modified three layers model technique, which was used in the previous chapter for modeling the cracked steel plate with CFRP patching was adopted for modeling the cracked steel circular tube with CFRP patching. As in the previous model, the cracked steel tube was modeled by 3-D brick elements (C3D20, 20 node brick element in ABAQUS) and the adhesive and CFRP patching were modeled using shell elements (S8R, 8 node general purpose shell element in ABAQUS). At the location of the crack tip, 3-D collapsed node elements were used and the SIF around the crack tip was obtained using the contour integral method. A typical finite element model of the cracked steel tube is shown in Figure 7.5. Symmetrical boundary conditions were assigned at the symmetrical plane along the longitudinal and circumferential direction and a uniform axial stress of 100 MPa was assigned at the far end of the steel tube.

7.3.2 Material properties of the steel tube, the adhesive and the CFRP patching

In the previous finite element parametric study of cracked steel plate with CFRP patching, the material properties of the 1.2 mm thick CFRP plate (Sika 2003) were assigned for the CFRP patching. In order to compare results of the plate model and the tube model, the same material properties of the CFRP plate were assigned for the cracked steel tube model with CFRP patching. The material properties of steel, CFRP plate and the corresponding adhesive are listed in Table 7.1. The number of layers assigned for the CFRP plate was 3. Therefore, the total thickness of CFRP plate was 3.6 mm and the corresponding adherend stiffness ratio of steel to CFRP (ETR) was 0.33. The corresponding thickness of the adhesive was 0.5 mm.

7.4 Finite element results of the cracked circular tube structure with and without CFRP patching

The finite element results of the SIF of cracked steel circular tube structure without FRP patching were compared to the prediction proposed by Lacire et al. (1999). According to Lacire et al. (1999), the SIF for a circumferential through-wall crack in a pipe under axial load and bending moment can be expressed by the following equations:

$$K_I = (F_t\sigma_t + F_b\sigma_b)\sqrt{\pi R_m \theta} \qquad (7.1)$$

where K_I is the SIF; F_t and F_b are the corresponding geometrical factors which represent the normalized stress intensity factor; R_m is the mean radius of the pipe; θ is half of the circumferential angle of crack (Figure 7.6); and, σ_t and σ_b are the applied tensile and bending stresses calculated by

$$\sigma_t = \frac{P}{2\pi R_m t} \quad \text{and} \quad \sigma_b = \frac{M}{\pi R_m^2 t} \qquad (7.2a, b)$$

where P is the applied axial force; M is the applied bending moment; and, t is the wall thickness of the tube. The geometrical factors for axial load (F_t) and bending moment (F_b) are calculated by the following equations:

Geometrical factor for axial load:

$$F_t = \left[A_t + B_t\left(\frac{\theta}{\pi}\right) + C_t\left(\frac{\theta}{\pi}\right)^2 + D_t\left(\frac{\theta}{\pi}\right)^3 + E_t\left(\frac{\theta}{\pi}\right)^4\right] \qquad (7.3)$$

where $A_t = 1$

$B_t = -1.040 - 3.1831\xi - 4.83\xi^2 - 2.369\xi^3$

$C_t = 16.71 + 23.10\xi + 50.82\xi^2 + 18.02\xi^3$

$D_t = -25.85 - 12.05\xi - 87.24\xi^2 - 30.39\xi^3$

$E_t = 24.70 - 54.18\xi + 18.09\xi^2 + 6.745\xi^3$

$\xi = \log\left(\frac{t}{R_m}\right)$

Geometrical factor for bending moment:

$$F_b = \left(1 + \frac{t}{2R_m}\right)\left[A_b + B_b\left(\frac{\theta}{\pi}\right) + C_b\left(\frac{\theta}{\pi}\right)^2 + D_b\left(\frac{\theta}{\pi}\right)^3 + E_b\left(\frac{\theta}{\pi}\right)^4\right] \qquad (7.4)$$

where $A_b = 0.65133 - 0.5774\xi - 0.3427\xi^2 - 0.0681\xi^3$

$B_b = 1.879 + 4.795\xi + 2.343\xi^2 - 0.6197\xi^3$

$C_b = -9.779 - 38.14\xi - 6.611\xi^2 + 3.972\xi^3$

$D_b = 34.36 + 129.9\xi + 50.55\xi^2 + 3.374\xi^3$

$E_b = -30.82 - 147.6\xi - 78.38\xi^2 - 15.54\xi^3$

$\xi = \log\left(\frac{t}{R_m}\right)$

The applicable range of the above equations are $1.5 < R_m / t < 80.5$ and $0 < \theta / \pi < 0.611$.

7.4.1 Finite element results of SIF of cracked circular tube structure with and without CFRP patching

For the finite element model, since only axial stress was assigned, based on Eq. (7.1) the normalized SIF is predicted by the following equation.

$$\frac{K_I}{\sigma_t} = F_t\sqrt{\pi R_m \theta} \qquad (7.5)$$

By assigning four different circumferential half crack lengths, a, equal to 25.4 mm, 38.1 mm, 50.8 mm and 63.5 mm, finite element models of a cracked steel circular tube with and without CFRP patching were formed and analyzed. As the mean radius of the tube is 195.25 mm, the corresponding R_m/t value is 20.55 and the θ/π values for the four circumferential crack lengths (a = 25.4 mm, 38.1 mm, 50.8 mm and 63.5 mm) are 0.042, 0.064, 0.085 and 0.106, respectively. These are within the applicable range of the equations proposed by Lacire et al. (1999). The finite element results of the normalized SIF and the results obtained by Lacire et al. (1999) are shown in Figure 7.7. As shown in the figure, the finite element results are generally in good agreement with the prediction of Lacire et al. (1999). Since 3-D brick elements were used for modeling the cracked circular tube, variation of the SIF across the thickness along the crack tip was obtained in the finite element analysis while the equations proposed by Lacire et al. (1999) did not reflect this variation.

Comparisons of the normalized SIF of a cracked tube of different crack lengths with and without CFRP plate patching are shown in Figure 7.8. For the tubes with CFRP plate patching, it is shown that the normalized SIF of the patched side of the tube with different crack lengths are all smaller than the SIF values of the tubes without CFRP patching when the crack length was equal to 25.4 mm. A plot of the normalized SIF versus crack length is shown in Figure 7.9. It is shown that for the tube without CFRP patching, the SIF increases significantly when the crack length increases. On the other hand, for the tube with CFRP patching, the increase of SIF is not as significant as the models without CFRP patching, especially for the patched side.

7.4.2 Finite element results of crack opening displacement of cracked circular tube structures with and without CFRP patching

The crack opening displacement of two cracked circular tubes (one without patching and one with CFRP plate patching) with half crack length of 63.5 mm is shown in Figure 7.10 (magnitude of displacement was magnified by 1000 times). Due to the presence of the crack only on one side of the tube, the section stiffness became non-symmetric about the out-of-plane axis (2-axis in the figure). This change of section stiffness causes the crack opening to displace not only along the longitudinal direction (the 1-axis), but also in the transverse direction (the 3-axis) as shown in Figure 7.10(a). With the presence of the CFRP patching on the cracked region, part of the reduced stiffness of the tube is recovered and the crack opening displacement was observed only along the longitudinal direction (the 1-axis), as shown in Figure 7.10(b). Numerical values of the longitudinal crack opening displacements of tubes with and without CFRP plate patching (crack length equals to 25.4 mm and 63.5 mm) are shown in Figure 7.11. As shown in the figure, even for the cracked tube with crack length of 63.5 mm, the maximum longitudinal crack opening displacement of tubes with CFRP plate patching is less than that of the cracked tube without CFRP patching and the crack length of 25.4 mm. Therefore, a significant reduction of the crack opening displacement could be obtained by applying CFRP patching on the crack region of circular tube structure.

7.4.3 Comparison of the finite element results of SIF of a circular tube structure and plate member

In the previous chapter, the results of parametric study of the SIF of cracked steel plates with single-side or double-side CFRP plate patching were presented and discussed. For plates with only single-side patching, bending of the plates occurs due to the un-symmetric application of patching. As a result, the SIF increases slightly for the side without patching. For the circular tube structure with crack only on one side, it was shown in the previous section that due to the presence of the crack only on one side of the tube, the crack opening displaced not only along the longitudinal direction, but also in the transverse direction when the tube was subjected to tensile stress only. When the crack was repaired by single-side FRP patching, part of the reduced stiffness of the tube was recovered and the crack opening displacement was observed only along the longitudinal direction. The normalized SIF values of a cracked tube member and a plate member with CFRP plate patching are shown in Figure 7.12. As shown in the figure, the values of the normalized SIF of cracked steel circular tube with single-side CFRP patching are close to the values of cracked steel plate with double-side CFRP patching. Therefore, due to the geometry of the tube structure, the application of single-side patching on cracked circular tube causes the SIF to reduce in a way similar to that of applying double-side patching to a cracked plate.

7.5 Reduction of SIF of cracked steel circular tube structure with different type of CFRP patching

In the previous section, the material properties of the CFRP composite were based on the material properties of a 1.2 mm thick pre-fabricated CFRP plate (Sika 2003). These pre-fabricated CFRP plates are very convenient for application on flat surfaces such as a beam flange, beam web, or slab. However, for the application of CFRP patching to tube structures with a curved surface, the CFRP sheet is more appropriate. Therefore, another set of finite element models were developed by assigning the material properties of CFRP sheets (Mitsubishi Chemical Co. 1999). Typical CFRP plate and CFRP sheet composites are shown in Figure 7.13. The material properties of CFRP sheet and corresponding adhesive are listed in Table 7.1. For the CFRP sheet, the average thickness per ply after applying the matrix is about 0.23 mm. In order to achieve a similar ETR value as in the previous analyses, the number of layers assigned for the CFRP sheet was 22 and the corresponding thickness and ETR value was 5.06 mm and 0.34, respectively. However, due to the different form of CFRP composite, the type and thickness of the corresponding adhesive are different. The thickness of the adhesive corresponding to the CFRP plate was 0.5 mm while the thickness of adhesive corresponding to the CFRP sheet was 0.06 mm.

The finite element results of SIF of a cracked steel tube with a different type of CFRP patching for a circumferential half crack length, a, of 25.4 mm are shown in Figure 7.14 along with the prediction by Lacire et al. (1999) and the finite element results of SIF of unpatched tube. It is shown that the reduction of the normalized SIF on the patched side is about 47% for the cracked tube with CFRP plate patching and 31% for the cracked tube with CFRP sheet patching. Although the ETR value for the tubes with CFRP plate patching and CFRP sheet patching is almost the same, it is shown that the reduction of the normalized SIF is more significant for model with CFRP plate patching with the material properties assigned in this study. The normalized SIF values across the thickness of the tube with different circumferential half crack length is shown in Figure 7.15 for tubes with CFRP sheet patching along with the results of the tubes without CFRP patching. Compare to the results of the tubes with CFRP plate patching (Figure 7.8), it is evident that the trend in the reduction of SIF for tubes with CFRP sheet patching is similar to that of the tubes with CFRP plate patching. It is also evident that the normalized SIF of the patched side of the tube with different crack lengths are all less than the values of the tube without CFRP patching with half crack length of 25.4 mm. A plot of the normalized SIF versus crack length for tubes with and without CFRP patching is shown in Figure 7.16. It is shown that the normalized SIF of tubes with CFRP sheet patching is about 20% and 24%, on average, higher than those obtained in the tubes with CFRP plate patching on the unpatched side and patched side, respectively. Nevertheless, it is evident that a significant reduction of the SIF is observed for tubes with either types of CFRP patching.

7.6 Fatigue life analysis of cracked steel tube structure with CFRP patching

In order to examine the increase of fatigue life of welded steel circular tube member due to the application of CFRP patching, prediction of the fatigue life of welded steel circular tube members with and without CFRP patching, was carried out. The analysis was based on the procedure discussed in Section 5.5.2. As in the previous study of welded steel plates with crack in welded region and with CFRP patching, the equation given in Chapter 5 for predicting the fatigue cycle (Eq. 5.29) was adopted here as well. The equation is repeated below:

$$N = \int_{a_i}^{a_f} \frac{1}{C(\Delta K_{eff})^m} da \qquad (5.29)$$

where N is the number of cycles, a_i is the initial half crack length; a_f is the final half crack length; ΔK_{eff} is the effective stress intensity factor range; and, C and m are the material constants of steel. The initial and final half crack lengths are taken as 25.4 mm and 63.5 mm respectively in this study. The C and m are taken as 8.88×10^{-12} m/cycle and 3.03 in this study according to the material constant of G40.12 350WT steel (Yin et al. 2006). The stress intensity factor (K) for a cracked circular tube without FRP patching subject to only axial load can be determined by the following equation (Lacire et al. 1999).

$$K = \sigma_t F_t \sqrt{\pi R_m \theta} \qquad (7.6)$$

where σ_t is the tensile stress range; F_t is the geometrical factor for axial load obtained from Eq. 7.3; R_m is the mean radius of the pipe; and, θ is half of the circumferential angle of crack. To account for the crack closure effect due to the presence of the residual stress in the welded region, the effective stress intensity factor range (ΔK_{eff}) is obtained from Eq. 7.7 below.

$$\Delta K_{eff} = (\sigma_{max} - \sigma_{op})F_t\sqrt{\pi R_m \theta} \tag{7.7}$$

where σ_{max} is the maximum tensile stress and σ_{op} is the opening stress, as defined in Eq. 5.28. Other terms have been previously defined. For cracked circular tube with CFRP patching, it was shown from the previous section that the SIF is reduced significantly. A plot of the finite element results of normalized SIF ($\Delta K/\Delta\sigma$) is shown in Figure 7.16 for tubes with and without CFRP patching. In order to obtain an equation for ΔK for cracked circular tubes with CFRP patching similar to Eq. 7.6, the geometrical factors $F_{t,\,CFRP}$ was calculated from the following equation.

$$F_{t,CFRP} = \frac{\Delta K}{\Delta\sigma\sqrt{\pi R_m \theta}} \tag{7.8}$$

where values of $\Delta K/\Delta\sigma$ were based on the finite element results of the unpatched side of cracked steel circular tube with CFRP sheet patching. A plot of F_t (based on Eq. 7.3) and $F_{t,\,CFRP}$ (based on Eq. 7.8) is shown in Figure 7.17. Based on the finite element results, an equation for $F_{t,\,CFRP}$ to the third order with respect to θ/π was developed and the equation is given below.

$$F_{t,CFRP} = 1.155 - 13.573\left(\frac{\theta}{\pi}\right) - 122.94\left(\frac{\theta}{\pi}\right)^2 - 401.18\left(\frac{\theta}{\pi}\right)^3 \tag{7.9}$$

Therefore, the corresponding effective stress intensity factor range ($\Delta K_{CFRP,eff}$) for cracked circular tubes with CFRP sheet patching is determined by the following equation.

$$\Delta K_{CFRP,eff} = (\sigma_{max} - \sigma_{op}{}^{P})F_{t,CFRP}\sqrt{\pi R_m \theta} \qquad (7.10)$$

where $\sigma_{op}{}^{P}$ is the opening stress for steel plates with patching, as defined in Eq. 5.31. Other terms have been defined previously.

In this study, the maximum stress (σ_{max}) was assigned as 283 MPa which was the maximum stress in the high stress range spectrum defined in the fatigue tests reported by Roach and Rackow (2005). The fatigue life of cracked steel circular tubes with and without CFRP sheet patching is shown in Figure 7.18. As shown in this figure, the number of cycles of loading of cracked steel circular tubes without and with CFRP sheet patching is 23262 and 503441, respectively. The number of cycles of loading is increased about 21.6 times for the cracked steel circular tube with CFRP sheet patching.

7.7 Summary and conclusions

In this chapter, a finite element study of the reduction of SIF of cracked steel circular tube repaired by CFRP patching was presented. The cracked steel circular tube was modeled using 3-D brick elements and the adhesive and CFRP patching were modeled by using shell elements. The finite element results for the SIF of the cracked steel circular tube without CFRP patching and with a half circumferential crack length of 25.4 mm, 38.1

mm, 50.8 m m and 63.5 mm were compared to the results obtained from equations proposed by Lacire et al. (1999). It was shown that the finite element results compared well with the results of Lacire et al. (1999). For the tubes with CFRP patching, two different types of CFRP materials (the plate type and sheet type) were used for modeling the cracked steel circular tubes with CFRP patching. A comparison of the SIF of cracked steel circular tubes with and without CFRP patching showed that the SIF was reduced significantly for the tubes with CFRP patching. Larger reduction of the SIF was observed for the tubes with CFRP plate patching (66% for model with CFRP plate patching and 54% for model with CFRP sheet patching) even though the adherend stiffness of the CFRP plate models was assigned almost the same as the CFRP sheet models in this study. However, the shear modulus of adhesive used in the CFRP plate model is about four times larger than that of the CFRP sheet model. Although the adherend stiffness of CFRP composite is one of the major parameters in this study, it is believed that other parameters such as the stiffness of adhesive also contributed to the reduction of the SIF.

The results of the normalized SIF of the cracked steel tube were compared to the results of cracked steel plate with single-side and double-side CFRP patching. Even though CFRP patching was applied only on one side of the cracked tube, due to the geometry of tube, the behaviour of the crack opening for the tube with CFRP patching was similar to that of the cracked steel plate with double-side CFRP patching. As a result, the reduction of SIF of the cracked steel tube with single-side CFRP patching was close to the values of the cracked steel plate with double-side CFRP patching.

The fatigue life of the welded steel circular tubes with and without CFRP patching was obtained using the procedure discussed in Section 5.5.2. It was shown that the increase of number of cycle of loading is about 21.6 times for the tubes with CFRP sheet patching compared to that of the model without CFRP patching when the circumference half crack length grew from 25.4 mm to 63.5 mm.

Table 7.1 Material properties of steel, adhesive and CFRP of tube model

Steel tube	Elastic modulus	E_s =	200,000 MPa
	Poisson's ratio	ν_s =	0.3
CFRP plate composite	Longitudinal elastic modulus	E_{frp1} =	175,000 MPa
	Transverse elastic modulus	$E_{frp\,2}$ =	9,000 MPa
	Poisson's ratio	ν_{frp} =	0.28
	Shear modulus	G_{frp} =	4,500 MPa
Adhesive for CFRP plate	Elastic modulus	E_a =	4,500 MPa
	Poisson's ration	ν_a =	0.34
	Shear modulus	G_a =	1,680 MPa
CFRP sheet composite	Longitudinal elastic modulus	E_{frp1} =	128,000 MPa
	Transverse elastic modulus	$E_{frp\,2}$ =	6,900 MPa
	Poisson's ratio	ν_{frp} =	0.17
	Shear modulus	G_{frp} =	4,480 MPa
Adhesive for CFRP sheet	Elastic modulus	E_a =	3,000 MPa
	Poisson's ration	ν_a =	0.34
	Shear modulus	G_a =	1,120 MPa

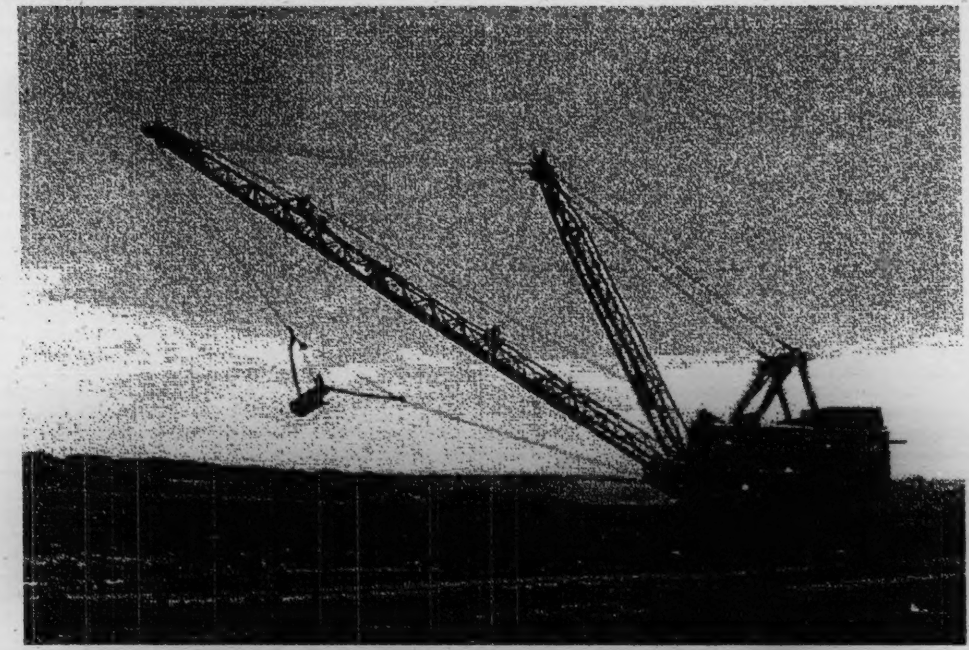

Figure 7.1 Dragline at Syncrude mining site (Courtesy Syncrude Canada Ltd.)

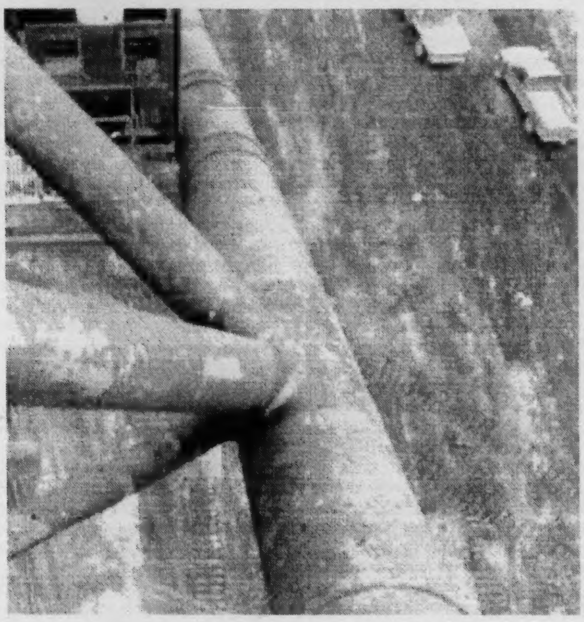

Figure 7.2 Cluster in dragline boom (Courtesy Syncrude Canada Ltd.)

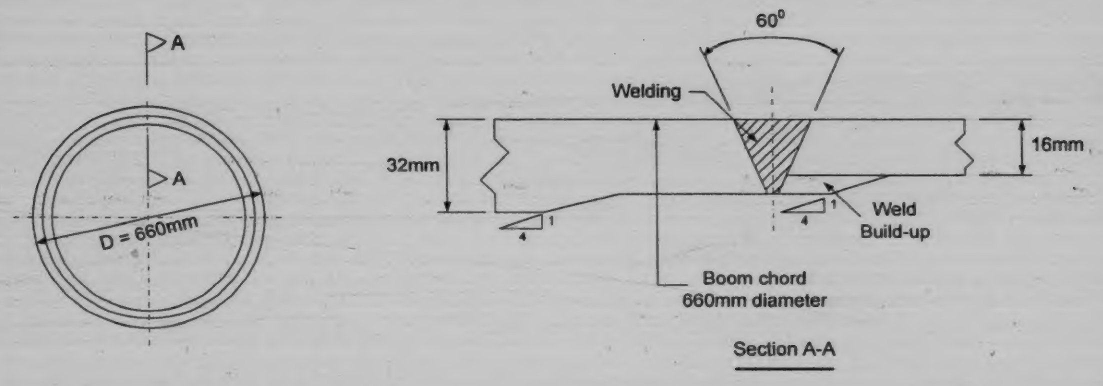
A
A
D = 660mm
60°
Welding
32mm
16mm
1
4
1
4
Weld
Build-up
Boom chord
660mm diameter
Section A-A

Figure 7.3 Wall-thickness transition in dragline boom chord (Courtesy Syncrude Canada Ltd.)

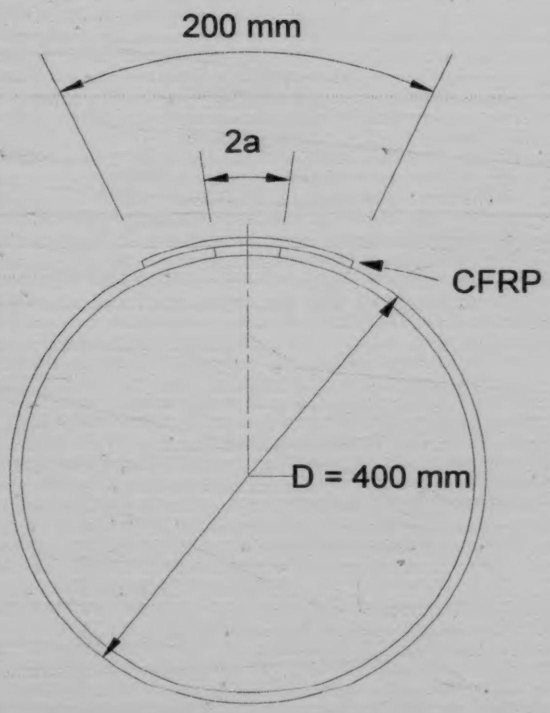
200 mm
2a
CFRP
D = 400 mm

Figure 7.4 Section dimension, crack and CFRP detail of tube member

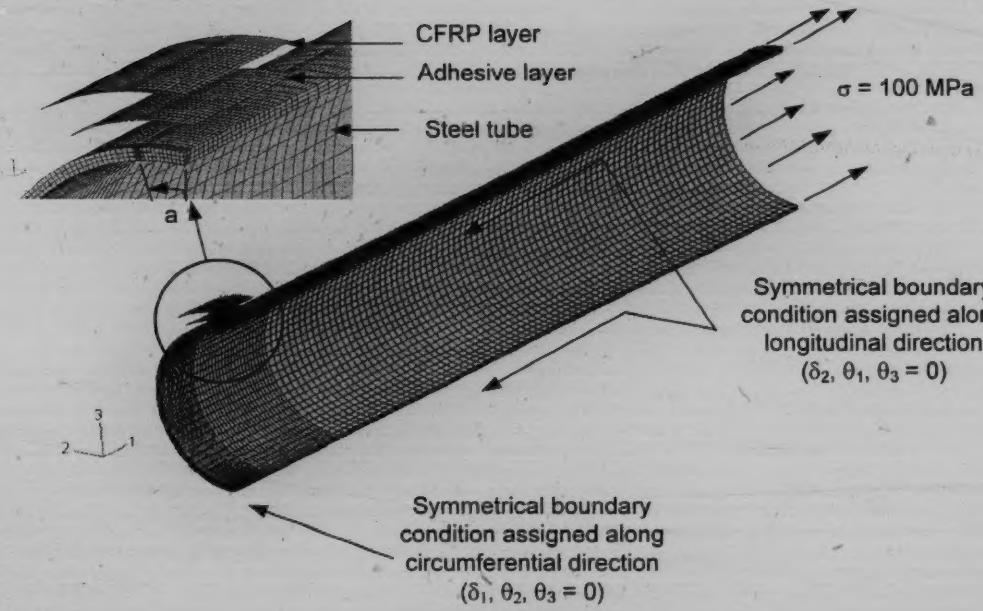
CFRP layer
Adhesive layer
Steel tube
a
σ = 100 MPa
Symmetrical boundary condition assigned along longitudinal direction (δ2, θ1, θ3 = 0)
Symmetrical boundary condition assigned along circumferential direction (δ1, θ2, θ3 = 0)
3
2
1

Figure 7.5 Typical finite element mesh of cracked steel circular tube member with CFRP patching

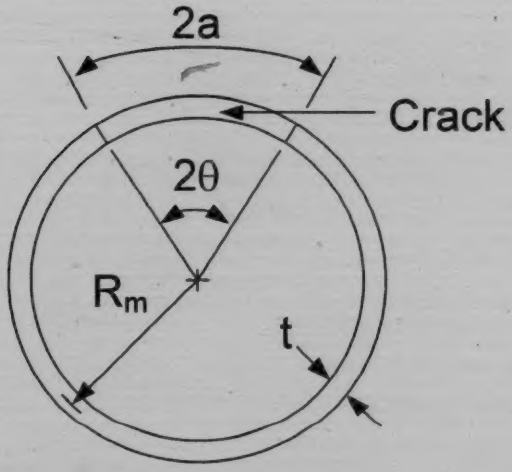
2a
Crack
2θ
Rm
t

Figure 7.6 Geometry of a circular tube with a circumferential through-wall crack

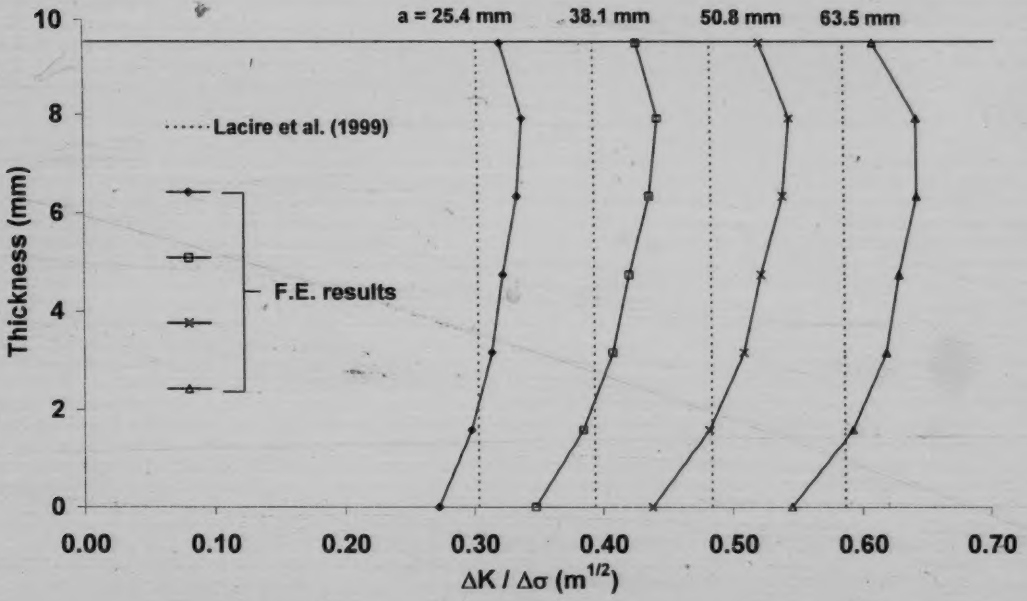

Figure 7.7 Comparison of F.E. results of normalized SIF of cracked steel circular tube without CFRP patching to the prediction of Lacire et al. (1999)

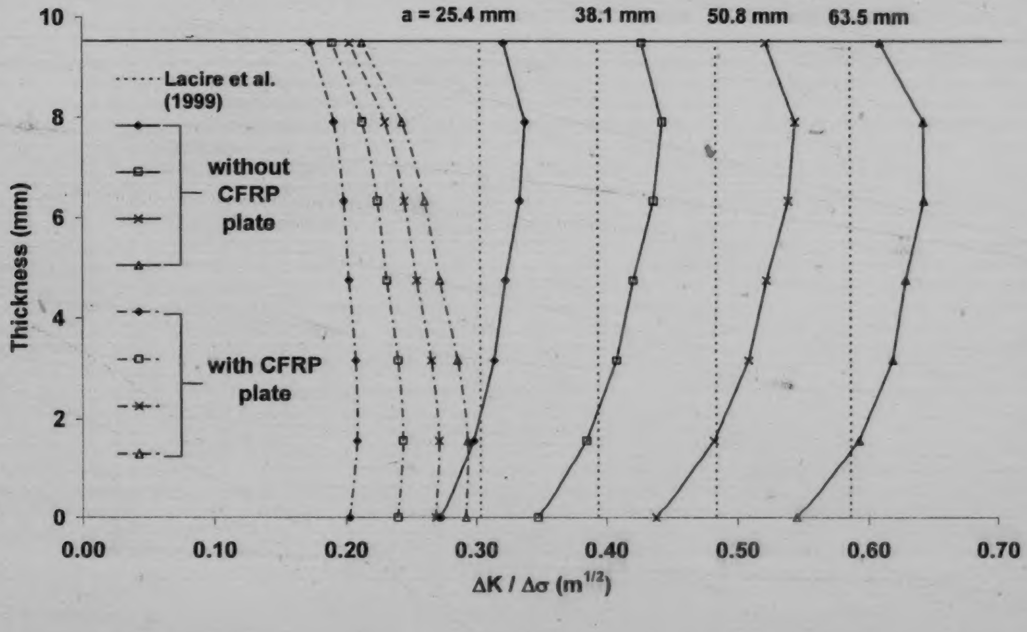

Figure 7.8 Comparison of F.E. results of normalized SIF of cracked steel circular tube with and without CFRP plate patching for various circumferential half crack length

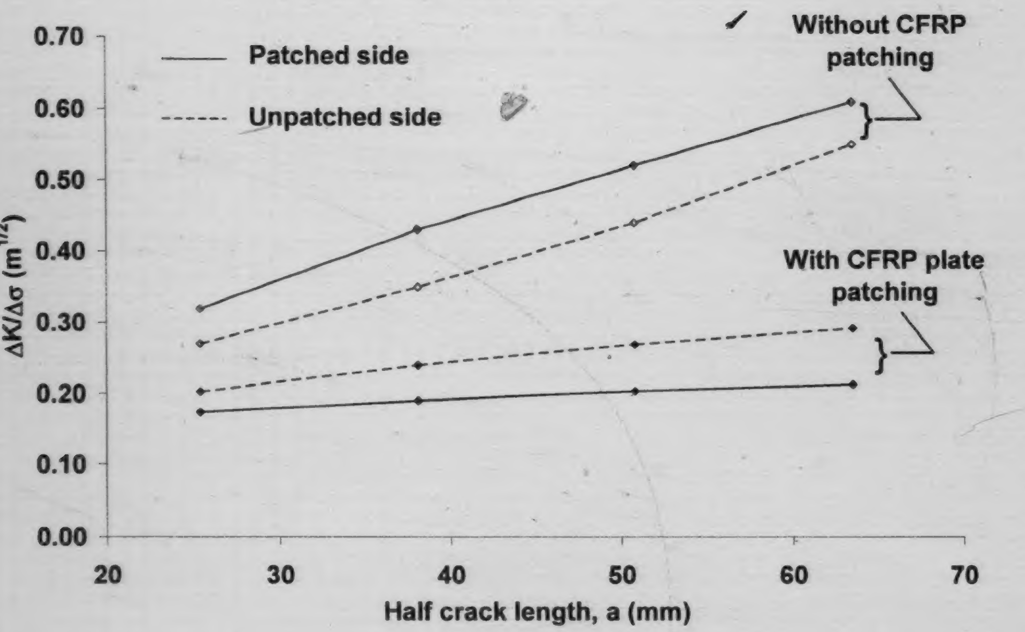

Figure 7.9 The normalized SIFs of cracked steel circular tube with and without CFRP plate patching versus half crack length

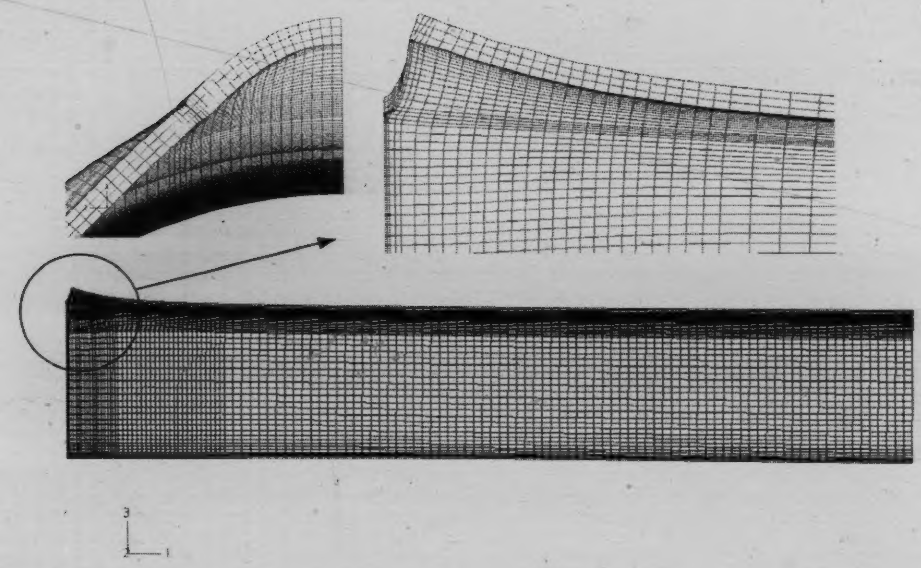

(a) crack opening displacement of crack steel circular tube without CFRP patching

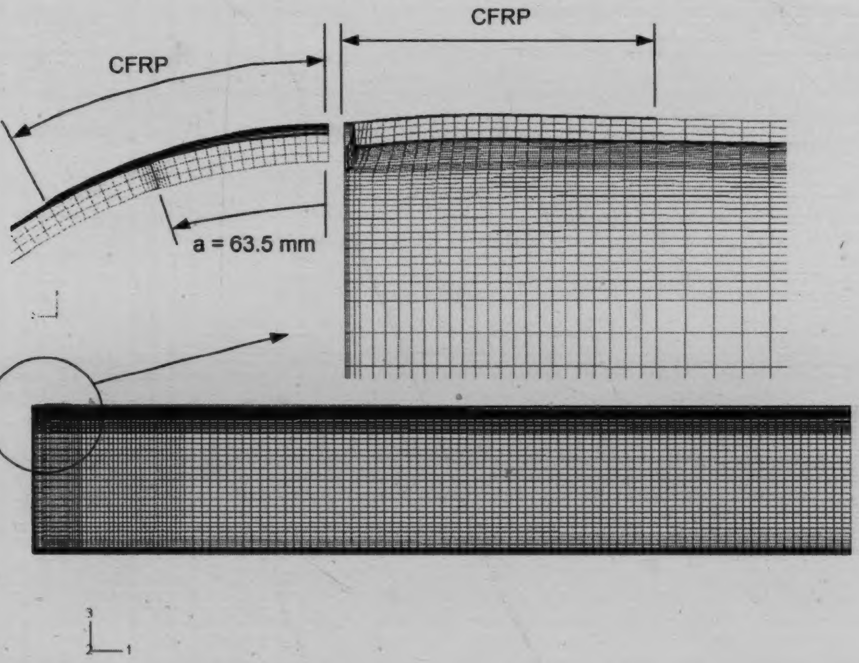

(b) crack opening displacement of crack steel circular tube with CFRP patching

Figure 7.10 Comparison of crack opening displacement of crack steel circular tube with and without CFRP plate patching

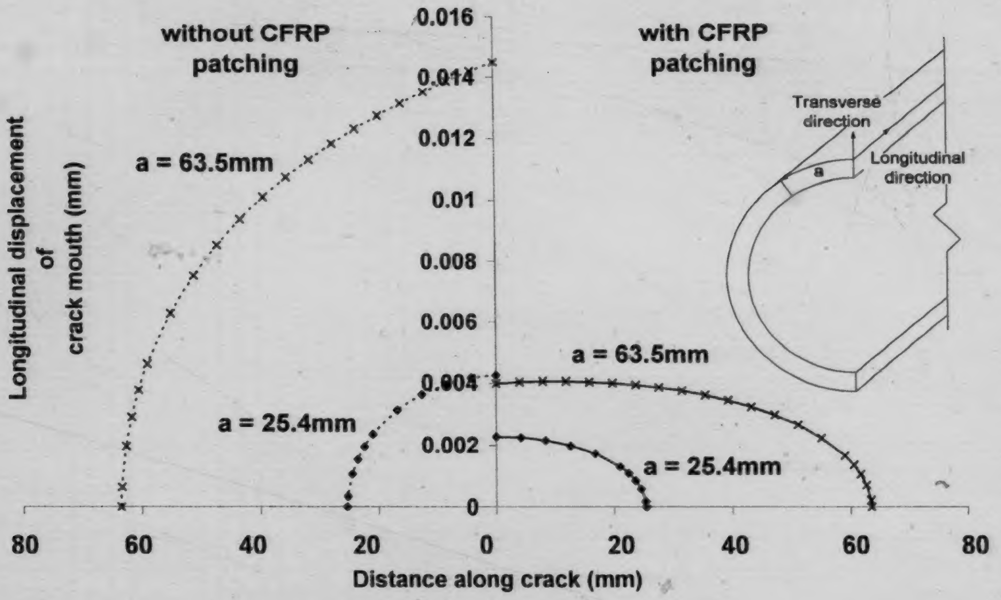

Figure 7.11 Longitudinal crack opening displacement of models with and without CFRP plate patching (half crack length of 25.4 mm and 63.5 mm)

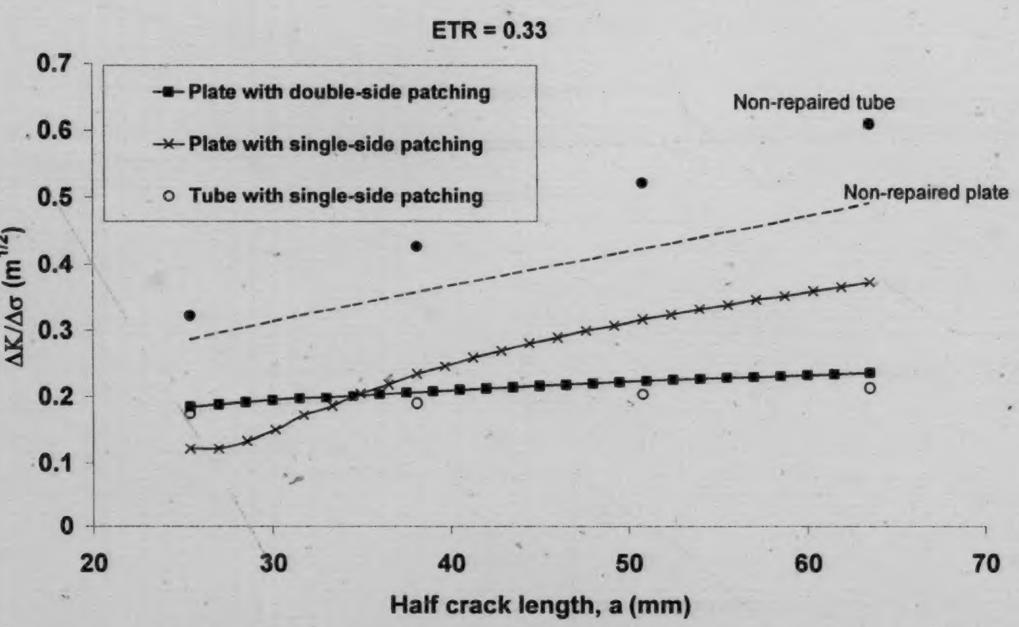

Figure 7.12 Comparison of normalized SIF of cracked steel circular tube and cracked plate with CFRP patching

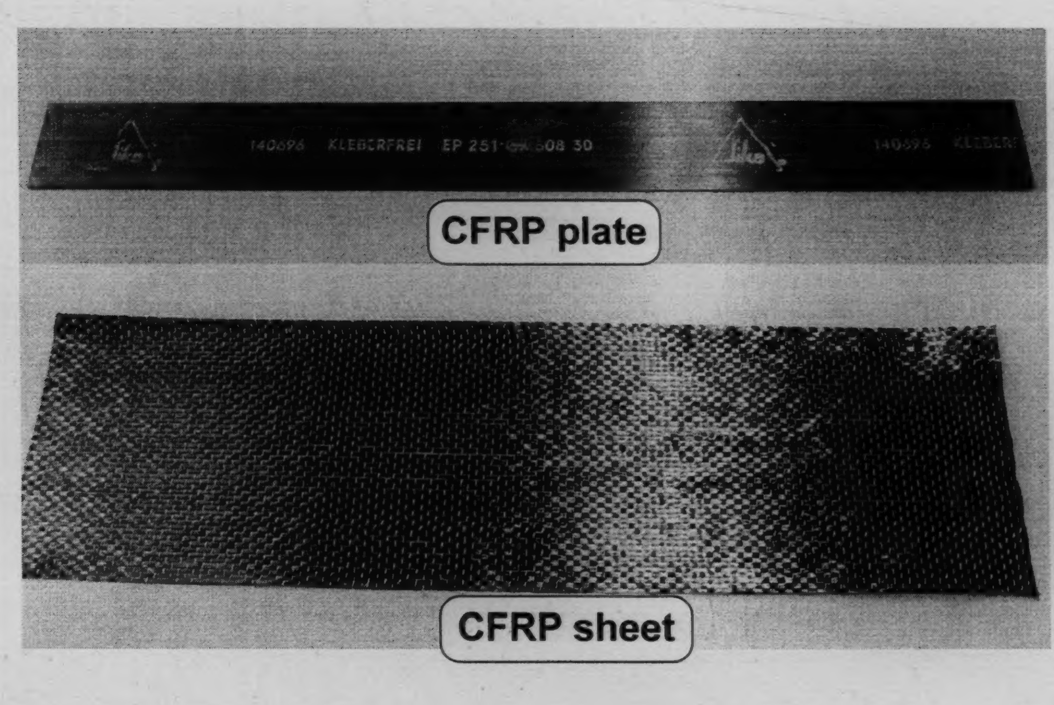
CFRP plate
CFRP sheet

Figure 7.13 Typical CFRP plate and CFRP sheet

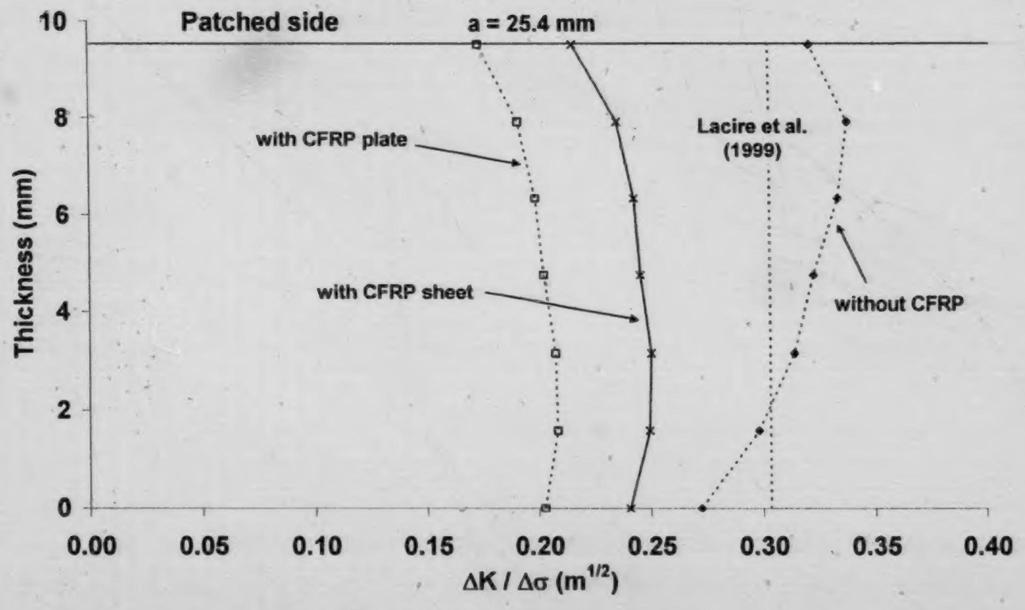

Figure 7.14 Comparison of F.E. results of normalized SIF of cracked steel circular tube with and without CFRP patching for circumferential half crack length, a, of 25.4 mm

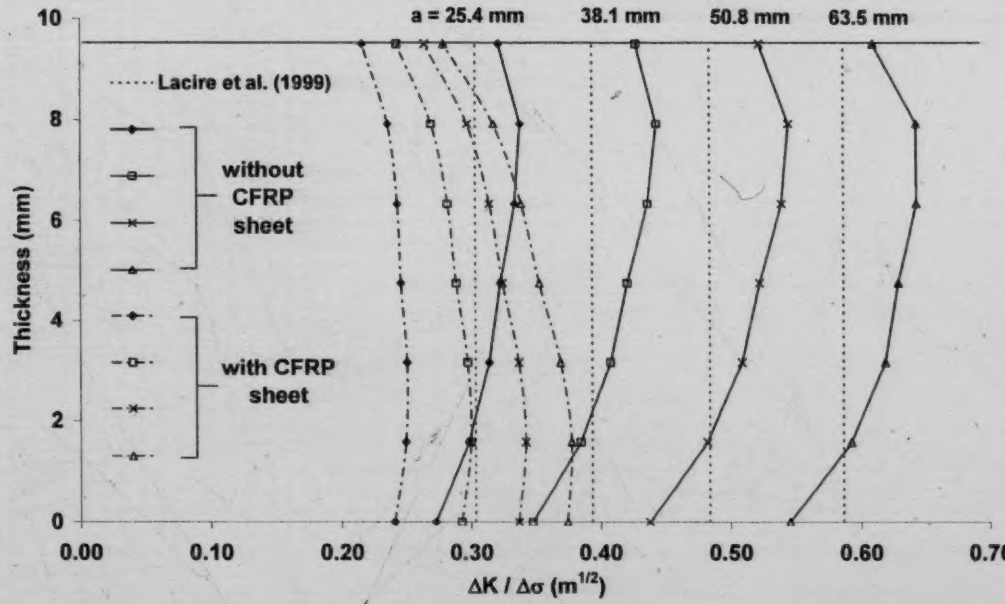

Figure 7.15 Comparison of F.E. results of normalized SIF of cracked steel circular tube with and without CFRP sheet patching for various circumferential half crack length

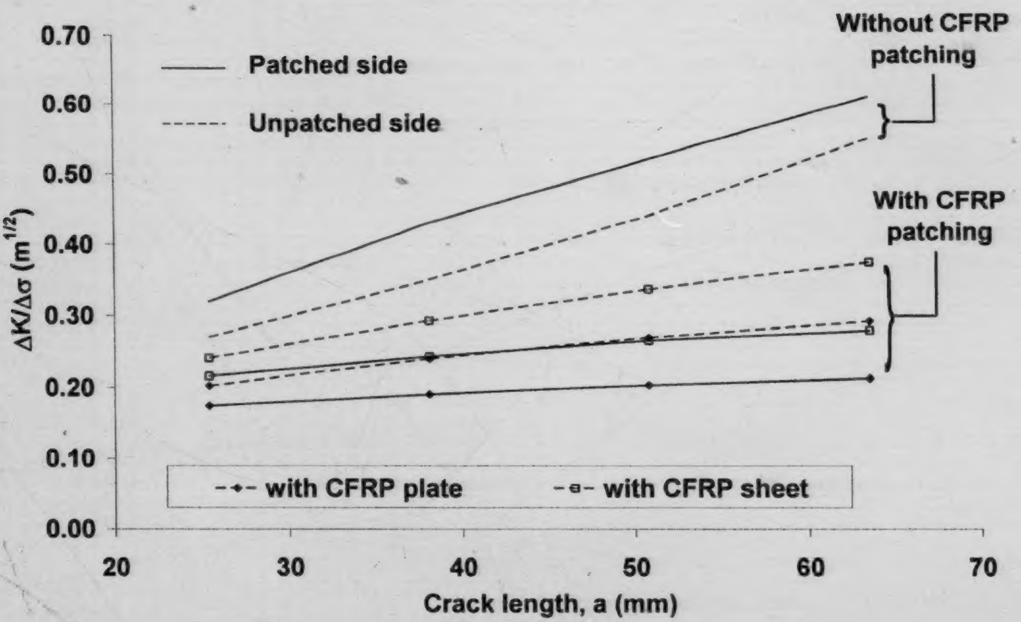

Figure 7.16 The normalized SIFs of cracked steel circular tube with and without CFRP patching versus half crack length

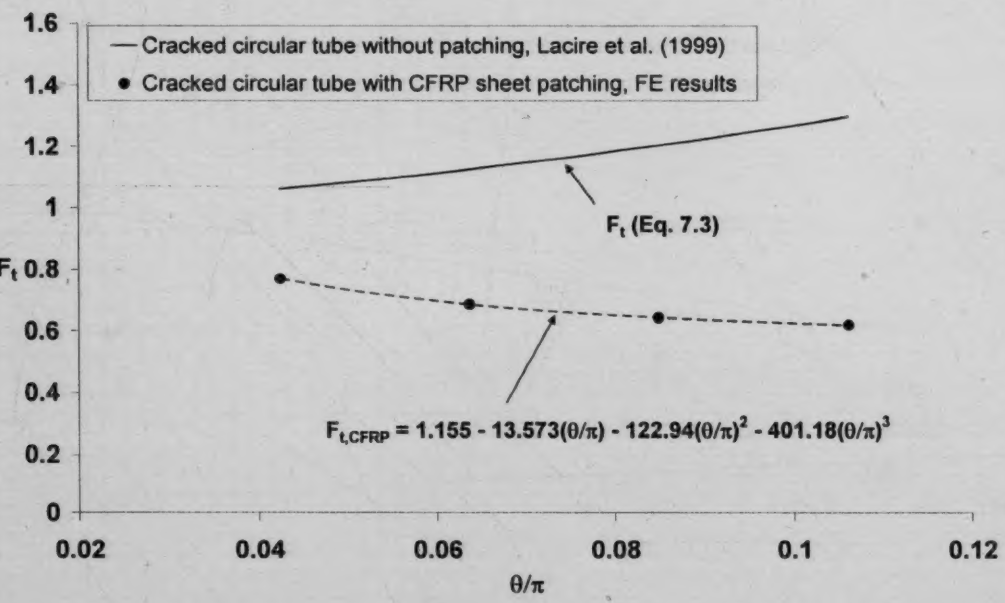

Figure 7.17 Geometrical factors of cracked steel circular tube with and without CFRP patching

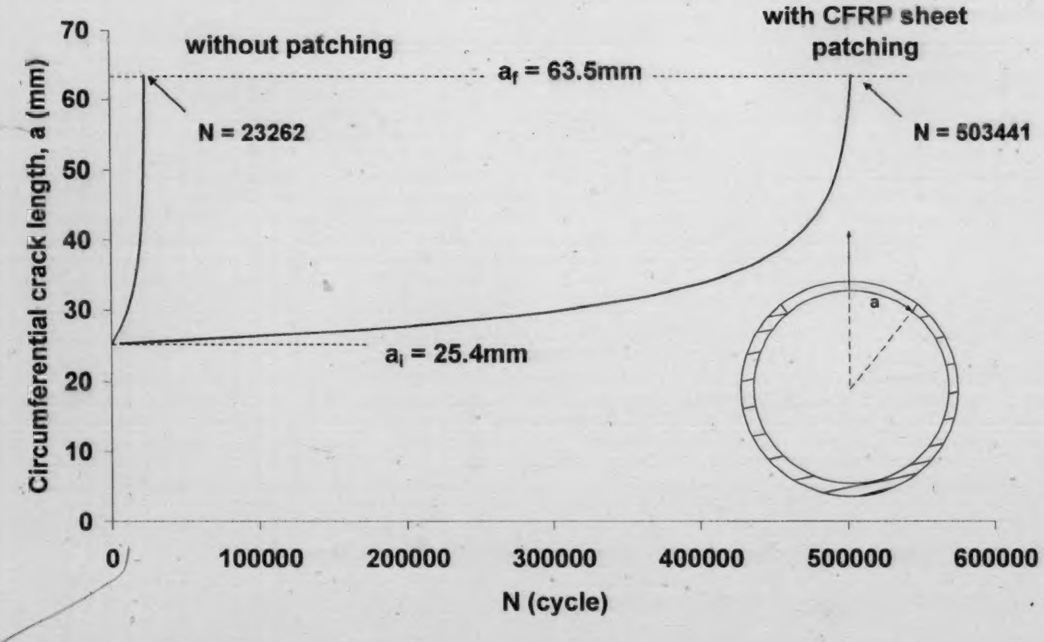

Figure 7.18 Comparison of the number of cycles of cracked steel circular tube with and without CFRP patching for circumference half crack length grew from 25.4 mm to 63.5 mm

7.8 References

Hibbitt, Karlsson & Sorenson, Inc. 2004. ABAQUS Version 6.4-1, ABAQUS/Standard User's Manual Volumes I and II, Pawtucket, Rhode Island, U.S.A.

Kennedy, G. D. and Cheng, J. J. R., 1998, "Repair of cracked steel elements using composite fiber patching", Structural Engineering Report No. 221, University of Alberta, Department of Civil & Environmental Engineering

Mitsubishi Chemical Co. 1999. Carbon fiber prepreg sheet (Replark^{TM}). Available from http://www.m-kagaku.co.jp/english/aboutmcc/division/prod/carbonfiber/r-products.htm

Roach, D. and Rackow, K., 2005, "Development of bonded composite doublers for the repair of oil recovery equipment", Sandia National Laboratories, Sandia report, Sand2005-3195

Roberts, P. D., 1995 "Crack growth retardation by carbon fiber composite patching: An application to steel pressure vessel repair", Master of Science Thesis, University of Alberta, Department of Mechanical Engineering

Sika Carbodur Technical Data Sheet. 2003. Sika Canada Inc. http://www.sika.ca/con-tds-sikacarbodur-ca.pdf

Lacire, M. H. , Chapuliot, S., and Marie, S., 1999, "Stress intensity factors of through wall cracks in plates and tubes with circumferential cracks", ASME PVP, 388, pp. 13 – 21

8 SUMMARY, CONCLUSIONS AND RECOMMENDATIONS

8.1 Summary

Due to the growing use of fiber reinforced polymer (FRP) composite materials to different engineering structures, FRP patching techniques are being considered as alternatives to traditional methods of strengthening and fatigue crack repair in steel structures. In order to understand the load transfer between composite patch and the base metal adherend, Kennedy and Cheng (1998) investigated the bond behavior of carbon fiber reinforced polymer (CFRP)/steel double lap joints. In their experiment, CFRP sheets with relatively thin thickness were used to form the CFRP/steel double lap joint. The corresponding adherend stiffness ratio (ETR) of CFRP to steel varied from 0.046 to 0.138. In order to study the bond behavior of CFRP/steel double lap joint with higher ETR value, additional experimental and numerical studies were carried out in the first study. Based on the experimental and the numerical results, analytical solutions proposed by Hart-Smith (1973) were adopted for predicting the minimum lap length and the corresponding maximum tensile strength of the CFRP/steel double lap joints.

The study of the tensile behavior of CFRP/steel double lap joint showed that loads could be transferred successfully from the steel plates to the CFRP composite materials through the adhesive. It is known that the fatigue behavior of a cracked member is related to the fracture properties of the crack tip, such as the magnitude of the stress intensity factor (SIF) of crack tip. Therefore, in the second study, investigation of the SIF of cracked members with FRP patching was carried out. Finite element models were developed to study the reduction of the SIF of cracked steel plates with single-side CFRP patching. Two types of finite element models: (a) the three layers finite element model (Naboulsi and Mall, 1996) which used shell elements to model the cracked steel plates, the adhesive and the CFRP patching and (b) a modified three layers finite element model proposed in this study which used shell elements to model the adhesive and the CFRP patching and brick elements to model the cracked steel plates were studied and the results of the SIFs obtained from these two finite element models were compared. It should be noted that a linear relationship of SIF through the plate thickness was assumed in the three layer model, whereas the SIF through the thickness of the plate of the modified three layer model could be obtained numerically since 3D brick elements were used to model the cracked steel plate. The strain results of the finite element analysis were compared to the experimental results obtained by Kennedy and Cheng (1998). Then, the SIF results obtained from the three layer model and the modified three layer model were compared. It was showed that the three layer model overestimated the SIF on the patched side and underestimated the SIF on the unpatched side. Based on the results of the modified three layer finite element model, it is shown that the SIF was reduced significantly on the patched side and the SIF values varied through the thickness of the cracked steel plate with single-side CFRP patching.

In the third study, the modified three layer finite element models were adopted to analyze the effect of single-side CFRP patching of cracked steel plates on the variation of the SIF across the thickness of the crack tip at different stages of crack propagation. The numerical procedure of crack propagation from Lee and Lee (2004) was applied in updating the crack tip shape and the corresponding SIF. The numerical results of the SIF were subsequently applied to the fatigue analysis and the results compared well with the fatigue test results of cracked steel plates with single-side FRP patching (Roach and Rackow, 2005).

In order to examine the effect of several parameters such as the adherent stiffness ratio, form of crack and patching, finite element parametric study of the stress intensity factor and prediction of fatigue life of cracked steel plates repaired by FRP patching was carried out in the forth study. Lastly, finite elements models were developed to study the reduction of the stress intensity factor of a cracked steel circular tube structure with FRP patching. Based on the finite element results, the extension of the fatigue life of a cracked steel circular tube member repaired by CFRP patching was determined.

8.2 Conclusions

A study of the repair of steel structures by bonding FRP composites was carried out by examining (1) the tensile strength of FRP composite/steel double lap joint; (2) the reduction of stress intensity factor of cracked steel plates with FRP patching; and, (3) the extension of fatigue life of cracked steel plates with FRP patching. The conclusions of the current study are as follows:

Tensile strength of CFRP/steel double lap joints:

The test parameters of the CFRP/steel double lap joint specimens subjected to tensile loading included: (a) the lap length; (b) the adherend stiffness ratio; and, (c) a tapered and a non-tapered lap joint pattern. Based on the experimental results, the following conclusions are drawn:

1. All of the specimens failed by debonding of the adhesive.
2. For specimens with the short lap length, brittle failure behavior was observed.
3. The axial capacity of the joint did not increase further once the lap length reached a certain limit. Once the lap length reached a certain limit, the axial load carrying capacity of the joint with the same adherend stiffness ratio could only be increased marginally by increasing the lap length. However, a larger failure deformation was observed before failure in specimens with longer lap length.
4. With the same inner adherend thickness, specimens with higher adherend stiffness ratio showed a higher axial load carrying capacity.
5. The axial capacity of joint with tapered lap and long lap length was almost the same as that of joint with non-tapered lap.

Based on the finite element results, the analytical solution which was developed by Hart-Smith (1973) was applied to determine the maximum axial strength and minimum required lap length of the lap joint (Eqs. 3.8 to 3.11). The corresponding minimum lap length of the joint can be obtained from the maximum joint strength. Both results for the maximum joint strength and the minimum lap length agree well with the test results.

Reduction of stress intensity factor (SIF) of cracked steel plates with CFRP patching

Based on the finite element results of the SIF using the modified three layers models, the following conclusions are drawn:

1. The finite element results showed that patch width, patch length and edge shape of patching have marginal effect on reducing the SIF.
2. The effect of adherend stiffness ratio (ETR = $E_{frp}t_{frp}/E_st_s$) on the reduction of SIF is more pronounced.
3. When compared to the non-patched patch, the average reduction of the SIF on the patched side was about 61% for specimens with ETR of 0.16 and 53% for specimens with ETR of 0.107
4. The SIF of the crack tip on the unpatched side was about 14% (at most) higher than the SIF value of plates without CFRP patching.

Extension of fatigue life of welded steel plates with the crack in welded region repaired with FRP patching

Based on the results of the finite element analysis, the following conclusions are drawn:

1. For plates with single-side patching only, it was found that the effect of adherend stiffness ratio (ETR) on the stress intensity factor of the unpatched side was not significant. However, the effective stress, which is defined as the difference between the maximum applied stress and the crack opening stress of plate with FRP patching, decreased with increasing ETR value.
2. It was shown that for an edge crack plate with single-side patching and with ETR of 0.13, 0.20 and 0.33, the fatigue life increased by 2.62, 3.76 and 9.2 times, respectively. Moreover, for the plates with a central crack and with

single-side patching; and, with ETR of 0.13, 0.20 and 0.33, the fatigue life was increased by 1.73, 2.46 and 5.90 times, respectively.

3. For plates with double-side patching, the increase in fatigue life was about 3.82, 8.59 and 41.7 times for plates with an edge crack and 2.79, 5.38 and 21.4 times for plates with a central crack with ETR of 0.13, 0.20 and 0.33, respectively.
4. It is shown that a higher efficiency of FRP patching was observed in plates with an edge crack than in plates with a central crack. It was also found that the increase in fatigue life was more pronounced for cracked plates with double-side patching.

Proposed procedures for determining the fatigue life of welded steel plates with a crack in the weld region were extended to determine the fatigue life of welded steel circular tube members. It was shown that for the welded steel circular tube member with CFRP patching, based on the numerical results, the increase in fatigue life was about 21.6 times for the tubes with CFRP sheet patching and an ETR of 0.34 when the circumference half crack length grew from 25.4 mm to 63.5 mm. Even though the CFRP patching was applied only on one side of the cracked tube, due to the geometry of the tube, the behavior of the crack opening displacement of the tube model with CFRP patching was similar to that of the cracked steel plate with double-side CFRP patching. As a result, the reduction of the SIF of the cracked steel tube with single-side CFRP patching was close to those of the cracked steel plate with double-side CFRP patching.

8.3 Recommendations for future work

In this study, a far end uniform stress was applied for both the numerical and the experimental studies and only two crack patterns (edge crack and central crack) were considered. Since the fatigue life of cracked elements with different geometry and loading patterns is highly dependent on the change of the stress intensity factor (SIF) at the crack tip, more studies (experimental and numerical) on the reduction of SIF of cracked element with different forms of crack and FRP patching should be conducted. The studies should consider parameters, such as the properties and orientations of FRP patching, the properties of adhesive, hybrid patching, geometry of crack pattern, loading pattern etc. Regarding the long term application of CFRP patching, durability of patching and adhesive should be examined since the efficiency of a repair would be reduced if significant debonding of FRP patching occurs.

8.4 References

Kennedy, G. D. and Cheng, J. J. R., 1998, "Repair of cracked steel elements using composite fiber patching", Structural Engineering Report No. 221, University of Alberta, Department of Civil & Environmental Engineering

Hart-Smith, L. J. 1973. Adhesive-bonded double-lap joints. National Aeronautics and Space Administration, CR-112235, Langley Research Centre

Lee, W-Y and Lee, J-J, 2004, "Successive 3D FE analysis technique for characterization of fatigue crack growth behavior in composite-repaired aluminum plate", Composite Structures, 66, pp. 513 - 520

Naboulsi, S. and Mall, S. 1996. Modeling of a cracked metallic structure with bonded composite patch using the three layer technique. Composite structures, Vol. 35, pp. 295-308

Roach, D. and Rackow, K., 2005, "Development of bonded composite doublers for the repair of oil recovery equipment", Sandia National Laboratories, Sandia report, Sand2005-3195

Appendix A Equations proposed by Wang et al. (1998) for determining SIF

Wang et al. (1998) proposed a modified equation for predicting the SIF of plate with only single side patching. Based on the assumption that the SIF at crack tip for plate with single side patching varies linearly across the thickness of the plate, the SIF at crack tip on patched and unpatched side are predicted by the Eqs. 5.18 and 5.19 which were repeated in following.

$$K^{*}_{\mathrm{unpatched}} = \left(\frac{3}{1+R_{SIF}+R_{SIF}^{2}}\right)^{1/2} K^{*}_{\mathrm{rms}} \qquad \text{(A1)}$$

$$K^{*}_{\mathrm{patched}} = \left(\frac{3}{1+R_{SIF}+R_{SIF}^{2}}\right)^{1/2} R_{SIF}K^{*}_{\mathrm{rms}} \qquad \text{(A2)}$$

where R_{SIF} is the ratio of the SIF of patched side to unpatched side and is depended on the geometry and material properties of the plate and reinforcement.

The calculation of the ratio of the SIF of patched side to unpatched (R_{SIF}) is as following:

$$R_{SIF} = \frac{K_{\min}}{K_{\max}} = \frac{I_t + (1+S)t_p(\Delta t)(\bar{z}-t_p)}{I_t + (1+S)t_p(\Delta t)\bar{z}} \qquad \text{(A3)}$$

where $I_t = I_p + nI_r$; $n = \frac{E_r}{E_p}$; $I_p = \frac{1}{12}t_p^3 + t_p(\bar{z}_p - \bar{z})^2$; $I_p = \frac{1}{12}t_r^3 + t_r(\bar{z}_r - \bar{z})^2$

$$\bar{z} = \frac{\bar{z}_p + S\bar{z}_r}{1+S}; \quad \Delta t = \bar{z} - \bar{z}_p; \quad S = \frac{E_r t_r}{E_p t_p}$$

E_r, E_p, t_r and t_p are the elastic modulus and thickness of reinforcement and plate; $\bar{z}_p$ and $\bar{z}_r$ are the distance defined in Fig. A1

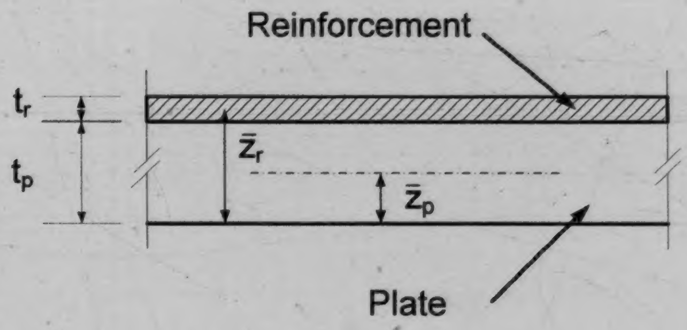

Figure A1 Definition of $\bar{z}_p$, $\bar{z}_r$, t_r and t_p

The K^*_{rms} is the root-mean-square SIF for plate with single patching (Eq. 5.20) which is repeated in following.

$$K^*_{rms} = K_r\omega \tag{A4}$$

where K_r denotes the SIF for two sided patching (Eq. 5.17) and ω is the bending correction factor which is related to the geometry and material properties of the plate and reinforcement also. The equation for calculating ω is shown in following.

$$\omega^2 = 2 + \frac{3t_p}{2t_r} + \frac{3\beta t_p}{kt_r}\left(1+\frac{t_p}{t_r}\right)(1-Q) + (1+S)\left(2+\frac{3t_p}{2t_r}\right)\left(\frac{\Delta t}{t_p}\right)^2 \frac{t_p^3}{I_t}$$
$$+ (1-Q)(1+S)\frac{\beta}{k}\left(1+\frac{t_p}{t_r}\right)\frac{t_p}{t_r}\frac{\Delta t}{t_p}\frac{t_p^3}{I_t}\left(\frac{3\bar{z}}{t_p}-1\right) \qquad \text{(A5)}$$

where $\beta = \left[\frac{\mu_a}{t_a}\left(\frac{1}{E_p t_p} + \frac{1}{E_r t_r}\right)\right]^{1/2}$; $k^4 = \frac{E_a}{4t_a}\left(\frac{1}{D_p}+\frac{1}{D_r}\right)$; $D_p = \frac{E_p t_p^3}{12}$; $D_r = \frac{E_r t_r^3}{12}$;

$$Q = \frac{\beta}{k(1+S)} \frac{(t_r/t_p + 3/4)(1 - St_r/t_p)}{1 + t_r/t_p}$$

E_a, t_a and μ_a are the elastic modulus, thickness and shear modulus of adhesive